STUDIA UNIVERSITATIS
BABEŞ-BOLYAI

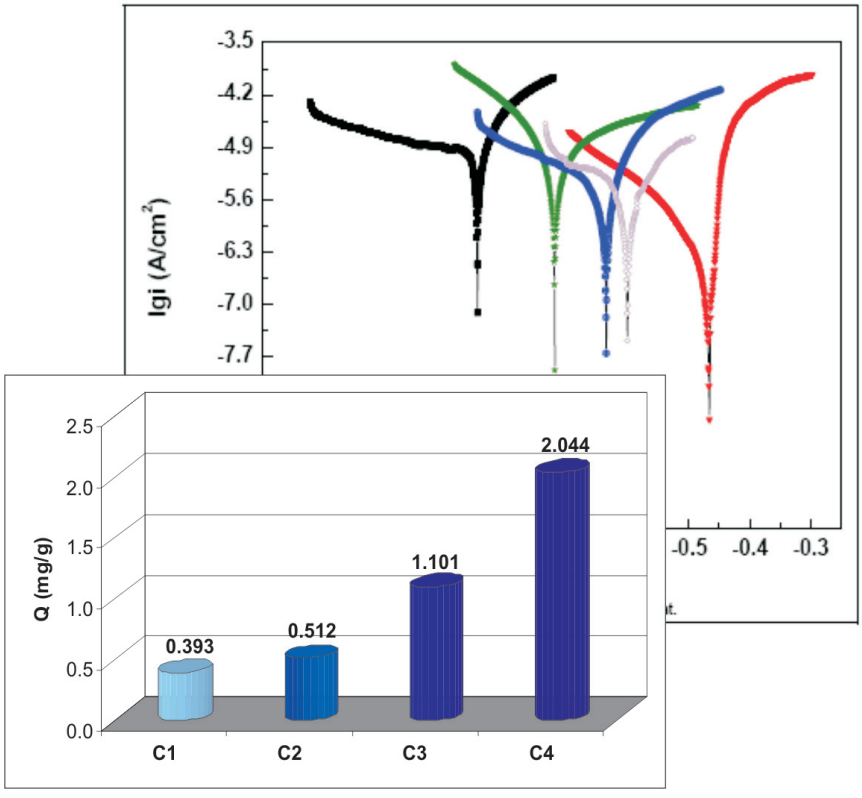

CHEMIA

1/2011

ANUL LVI **2011**

S T U D I A

UNIVERSITATIS BABEŞ–BOLYAI

CHEMIA

1

Volume dedicated to Professor SIMION GOCAN PhD.

Desktop Editing Office: 51ST B.P. Hasdeu, Cluj-Napoca, Romania, Phone + 40 264-40.53.52

CUPRINS – CONTENT – SOMMAIRE – INHALT

Studia Universitatis Babes-Bolyai Chemia has been selected for coverage in Thomson Reuters products and custom information services. Beginning with V. 53 (1) 2008, this publication is indexed and abstracted in the following:

- Science Citation Index Expanded (also known as SciSearch®)
- Chemistry Citation Index®
- Journal Citation Reports/Science Edition

Prof. Simion Gocan PhD.

Simion Gocan graduated from the Faculty of Chemistry, Research and Analysis Department of "Victor Babes" University, Cluj-Napoca in 1954. In 1969 he obtained his PhD under the supervision of Prof. Dr. Candin Liteanu. His teaching activity started at the Physical Department of the Polytechnic Institute and continued at the Pedagogical Institute as an assistant professor in Cluj-Napoca. In 1972 he joined the Faculty of Chemistry and Chemical Engineering, "Babes-Bolyai" University and from 1990 he was a full professor at the Analytical Chemistry Department. He was the head of the Department from 1990 to 1996, when he retired. His activity continued as a consulting professor and in 2009 he was granted the title of honorific consulting professor.

Professor Simion Gocan is among the first Romanian researchers who implemented and developed the analytical separation techniques based on chromatography. He introduced the new subject of "Separation Methods" in the faculty curriculum. Understanding the importance of modern data processing and interpretation he introduced the "Chemometrics" course, as a new course. In the position of PhD coordinator, he supervised ten doctoral theses in the field of separation methods, such as optimizing the chromatographic separation process, lipophilicity determinations, sample preparation for chromatographic analysis, immunoassay analysis, bioactive compound determination from different medicinal plants.

Professor Gocan is a member of many scientific societies of chemistry, analytical chemistry and chromatography, in the country and abroad. His academic activity is reflected in seven textbooks, collection of problems, practical work guides and courses for students or postgraduate training programs.

Professor Gocan has a rich publishing activity. He is co-author of ten scientific books such as “Fundamentals of Column Adsorption Chromatography” (1971), “Fundamentals of Ionic Exchange Chromatography on Paper and Thin Layers” (1972), “Liquid Chromatography”, Ed. Stiințifica (*printing house*), Bucharest, 1974. The last one was considered at the time a fundamental book for the training of researchers and teaching staff. Other reference books are “Gradient Liquid Chromatography”, Ed. Tehnică (*printing house*), Bucharest, 1976, “Analytical Separation”, Ed. Dacia (*printing house*), Cluj-Napoca, 1981, “Analytical Immunochemistry” (1995), “Modern Techniques for sample preparation” (2006).

His theoretical and experimental researches as well as his pedagogic experience were fructified into a series of books focusing on high performance chromatography: Gas Chromatography (1998), Liquid Chromatography (2002) and Thin Layer Chromatography (2005). He is co-author of the book “Gradient Liquid Chromatography” in the Series in Analytical Chemistry published by Ellis Horwood, Chichester, London, 1974. Professor Gocan published several chapters in scientific books such as: Chapter 2 “Stationary Phases in Thin-Layer Chromatography”; Chapter 3 “Mobile Phases in Thin-Layer Chromatography”; Chapter 4 “Theoretical Aspects of Thin-Layer Chromatography in Modern Thin-Layer Chromatography”, Marcel Dekker, N. Grinberg (Ed), New York, 1990 and Chapter 28 “Organophosphates”, in Handbook of Water Analysis, L.M.L. Nollet (Ed.) Marcel Dekker, New York, 2000. He had also brought his contribution in “Encyclopedia of Chromatography”, Marcel Dekker, New York, first edition in 2001, 2nd edition. 2005 and 3rd third edition in 2009.

The professor’s entire scientific activity is reflected in 105 peer-reviewed articles published in the country and 38 in prestigious international journals, of which 8 review papers. He was invited to sustain plenary presentations at many national and international meetings and conferences.

Cluj-Napoca, 24 March 2011

STUDIA UBB CHEMIA, LVI, 1, 2011

SPECTROSCOPIC STUDY OF ATMOSPHERIC PRESSURE ARGON/METHANE CAPACITIVELY COUPLED PLASMA

TIBERIU FRENTIU[a,*], MICHAELA PONTA[a], ALIN IRONIM MIHALTAN[b], EUGEN DARVASI[a], MARIA FRENTIU[b], E. CORDOS[b]

ABSTRACT. The emission spectrum (200 – 1000 nm) and discharge characteristics of an atmospheric pressure Ar/CH_4 capacitively coupled plasma, 275 W, 27.12 MHz, 0.7 L min^{-1} Ar and 0-7.5 mL min^{-1} CH_4 as collision/reaction gas were studied. The emission spectrum of pure Ar plasma is dominated by molecular bands of OH and N_2 second positive system in UV as well as Ar I ($4p \rightarrow 4s$) lines in VIS range. The addition of CH_4 results in the appearance of the C_2 Swan band and quenching of OH, N_2 and Ar emission. Quenching is the consequence of the second-kind collisions of CH_4 molecule with Ar, N_2 excited species and chemical reaction with OH radical, respectively. Processes were confirmed by the decrease of the excitation temperature of Ar and electron number density when adding CH_4 in Ar plasma. The Ar/CH_4 plasma is of great interest for applications in atomic spectroscopy due to the possibility to remove spectral interferences by the collision/reaction gas method and the use of low resolution microspectrometers.

Keywords: *capacitively coupled plasma, molecular emission, collision/reaction gas, plasma diagnosis*

INTRODUCTION

Progress in the atomic emission spectrometry (AES) relied *inter alia* on new spectral sources to guarantee the analytical performances required in the multielemental determinations of high sensitivity. The development of spectral sources began with flame, continued with arc and spark, than inductively coupled plasma (ICP), while in recent years microplasmas on a chip have become an important field of innovation [**1**]. Currently, ICP-AES is a mature technique with excellent analytical capabilities for the rapid multielemental determination as it benefits from the advantages of CCD technology and dual-viewing. ICP-AES was standardized for the determination of elements in water and soil [**2,3**]. The shortcomings of ICP-AES associated to acquisition

[a] *Babes-Bolyai University, Faculty of Chemistry and Chemical Engineering, 1, Kogălniceanu Street, RO-400084 Cluj-Napoca,Romania, ftibi@chem.ubbcluj.ro*

[b] *National Institute of Development for Optoelectronics, Bucharest – Research Institute for Analytical Instrumentation, 67 Donath Street, 400293 Cluj-Napoca, Romania.*

and maintenance high cost directed research towards the development of new plasma sources such as capacitively microwave plasma (CMP) [**4**], microwave induced plasma (MIP) [**5,6**], microwave plasma torch (MPT) [**7**] and radio-frequency capacitively coupled plasma (CCP) [**8,9**], less expensive and having several analytical performances similar to ICP. The advantages of the new plasma sources are related to the operation at atmospheric pressure, low consumption of Ar or He as support gas (< 1 L min^{-1}) and low operation power (< 300 W). This last feature enables the miniaturization to hand-held systems for in-situ analysis [**9**].

The results obtained in our laboratory have demonstrated that the atmospheric pressure CCP with tubular electrode operated at 275 W and below 1 L min^{-1} Ar is not only a relatively powerful excitation source in AES but also a promising atomization cell in atomic fluorescence spectrometry (AFS) [**10-13**]. The torch configuration favors the sample introduction right in the center of the plasma where most of the energy is dissipated. This ensures a better wet aerosol-plasma interaction and therefore the decrease of the matrix effects compared to MIP. Nevertheless, the emission spectrum is rich in molecular bands (OH, N_2) over a wide range (200-420 nm) because of the air diffusion in the Ar plasma. This raises problems of spectral interferences on analytes lines both in AES and AFS when using a low resolution microspectrometer. In a preliminary study it has been shown that the Ar/CH_4 plasma is suitable for Pb determination by AFS at 283.31 nm following circumventing spectral interferences by quenching of OH molecular emission [**13**].

Plasmas used for analytical purposes are usually developed in Ar and He, while those for thin film growth or surface treatment in mixtures of these gases with hydrocarbons (CH_4, C_2H_2) [**14**].

The aim of this work was the spectral characterization of an Ar/CH_4 plasma developed in the torch with tubular electrode and single ring electrode. The study presents the features of the background emission over the spectral range 200-1000 nm and physical and chemical processes in plasma responsible for quenching of OH and nitrogen molecular emission and argon lines. Results were corroborated with the electron number density (n_e) and excitation temperature (T_{ex}) of Ar lines. The study is of interest since the introducing CH_4 in the Ar plasma represents a simple method to remove spectral interference of the molecular emission on elements and allows the use of low-resolution microspectrometers in spectrochimical determinations.

RESULTS AND DISCUSSIONS

Study of background emission spectrum of Ar/CH_4 plasma

The main features of the emission of plasma developed in pure Ar and Ar/CH_4 mixture are shown in Table 1, while the background spectra in Figure 1.

Table 1. Main features of emission spectra of Ar and Ar/CH_4 plasmas

Species	System	Transition	Excitation energy (eV)
OH	282.90 nm (0,1) 308.90 nm (0,0)	$A^2\Sigma^+ \rightarrow X^2\Pi$	4.05
N_2 second positive system	337.13 nm (0,0) 357.69 nm (0,1) 380.49 nm (0,2)	$C^3\Pi_u \rightarrow B^3\Sigma_g$	11.05
C_2 Swan band	438.3 nm (0,2) 473.7 nm (0,1) 516.5 nm (0,0) 563.6 nm (1,0) 619.1 nm (2,0) 685.0 nm (3,0)	$D^3\Pi_g \rightarrow A^3\Pi_u$	2.40
Ar I	690-950 nm	4p→4s	12.90-13.50

The emission spectrum of the pure Ar plasma consists of OH bands, N_2 second positive system (SPS) and Ar I lines (690-950 nm) corresponding to 4p→4s transitions (E_{ex} up to 13.5 eV). Argon I lines related to 5p→4s transitions (415-430 nm) (E_{ex} above 14 eV) are much less intense, indicating low electron temperature values and a lower excitation capability. Results were similar to those reported by Yanguas-Gil et al. [**14**], who stated that the 5p→4s Ar I transitions were almost negligible in an Ar/CH_4 microplasma jet. Other emissions are those of atomic nitrogen (402.456 nm) and atomic oxygen (477.291 nm and 477.375 nm) with excitation energies similar to Ar I 4p→4s lines.

The OH radicals develop from H_2O molecules that dissociate following collisions with oxygen atoms resulted from O_2 traces diffused into plasma:

$$O + H_2O \rightarrow OH + OH \quad (1)$$

The molecular emission of OH radicals is the result of their excitation by collisions with electrons [**13**].

The emission of the N_2 SPS is principally due to second-kind collisions with metastable argon atoms [**15-17**]. Argon has 2 metastable energy levels for the 4s states ($^2P^0_{3/2}$ -11.55 eV; $^2P^0_{1/2}$ – 11.72 eV). The $C^3\Pi_u$ state of N_2 is similar in energy to Ar 4s metastable levels and therefore an energy transfer is possible [**18**]. The relatively strong band of N_2 SPS $C^3\Pi_u \rightarrow B^3\Sigma_g$ observed in our Ar plasma is the direct result of this energy transfer between a metastable Ar atom and a ground state N_2 molecule.

$$N_2 + Ar^* \rightarrow N_2^* + Ar \quad (2)$$

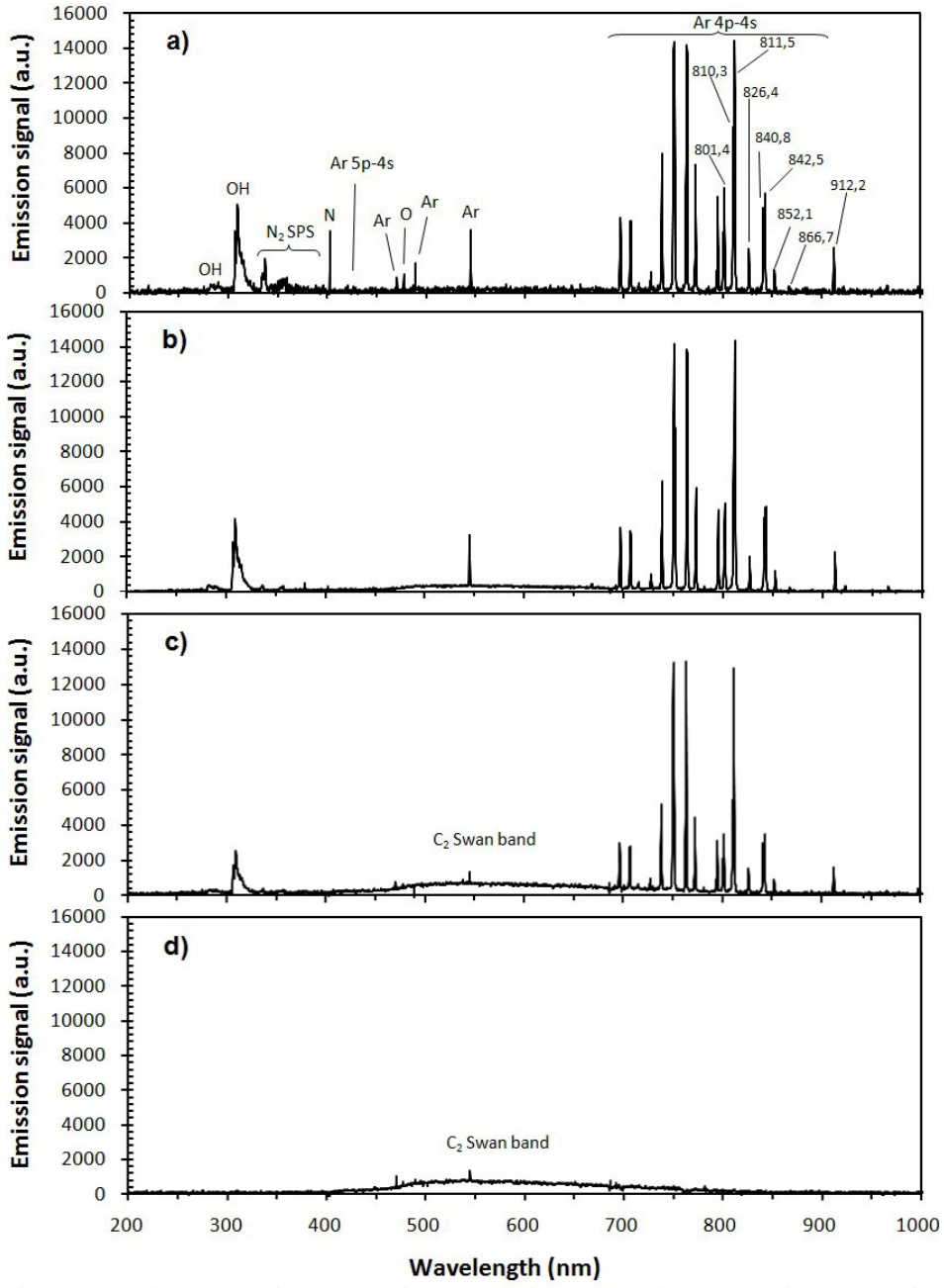

Figure 1. Background emission spectra of Ar and Ar/CH_4 plasmas. Experimental conditions: 275 W; 70 mm observation height; 0.7 L min^{-1} Ar; CH_4 flow rate (mL min^{-1}): (a) 0; (b) 2.5; (c) 5; (d) 7.5.

The emission spectra in Fig. 1 shows that the CH_4 content in the Ar plasma controls the emission intensity of OH, N_2 SPS and Ar I. The quenching of OH emission is the result of its photochemical reaction with CH_4 due to the radical affinity toward a hydrogen atom.

$$OH + CH_4 \rightarrow CH_3 + H_2O \quad (3)$$

The mechanism of this reaction is discussed in [**19-22**].

The quenching of the N_2 SPS is the result of the second-kind collision with CH_4 molecule and decrease of the population of Ar metastable atoms in the Ar/CH_4 plasma. Following this collision the N_2 molecule from $C^3\Pi_u$ goes to the ground state $A^3\Pi_u$ that remains unchanged in the presence of CH_4 [**23**]:

$$N_2^* + CH_4 \rightarrow N_2 + CH_4^* \rightarrow N_2 + CH_3 + H \quad (4)$$

The quenching of the Ar I emission in the visible spectral range is attributed to an energy transfer from Ar I excited state to the CH_4 molecule, which is dissociated according to the process:

$$Ar^* + nCH_4 \rightarrow Ar + nCH_4^* \rightarrow Ar + CH + CH_2 + CH_3 + H \quad (5)$$

This process is in agreement with a previous report in the literature [**24**]. For an addition of 7.5 mL min^{-1} CH_4 to 0.7 L min^{-1} Ar it occurred a complete quenching of OH and nitrogen molecular emission in UV and an almost complete one of Ar I 4p→4s in the visible range.

Interestingly, there is no evidence of the CN molecular emission ($B^2\Sigma^+ \rightarrow X^2\Sigma^+$; E_{ex} = 3.19 eV; 359.04 nm (0,1) and 388.34 nm (0,0)) in the spectrum of Ar/CH_4 plasma, which demonstrates that the chemical reaction between N_2 and methane is insignificant in the quenching of nitrogen molecular emission:

$$N_2^* + CH_3 \rightarrow N + HCN + H_2 \quad (6)$$

The lack of the CN emission was reported in other atmospheric pressure Ar/CH_4 microplasmas [**14**].

Another feature of the Ar/CH_4 plasma spectrum is the absence of the molecular emission corresponding to CH (CH 314.3 nm system $C^2\Sigma^+ \rightarrow X^2\Pi$; CH 390 nm system $B^2\Sigma^+ \rightarrow X^2\Pi$; CH 430 nm system $A^2D \rightarrow X^2\Pi$) and CH_2 (360-390 nm) as well as the presence of the intense C_2 Swan band ($D^3\Pi_g \rightarrow A^3\Pi_u$; 409-690 nm). Our finding is in agreement with that of Yanguas-Jil et al. [**14**] who reported the decrease of the CH/C_2 emissions ratio in the Ar/CH_4 plasma when increasing the CH_4 addition.

The approach of quenching the molecular emission by CH_4 addition in Ar plasma is superior to that based on oxygen-sheated plasma studied by Jin et al. [**7**] in Ar MPT. Whereas the method using CH_4 as reaction/collision

gas ensures quenching of both OH and N_2 SPS molecular emission, the approach using oxygen accomplishes only the removal of nitrogen emission signal, while that of OH increases.

Discharge parameters

Electron number density and excitation temperature of the Ar atoms were determined from the Ar emission spectrum. Spectroscopic data are summarized in Table 2 [**25**].

Table 2. Spectroscopic data for Ar I lines (4p→4s) [25]

□ (nm)	E_{ex} (eV)	gA 10^8 (s^{-1})
801.478	13.09	0.464
810.369	13.15	0.750
811.531	13.07	2.32
826.452	13.32	0.459
840.821	13.29	1.12
842.465	13.09	1.08
852.144	13.28	0.417
866.794	13.15	0.0729
912.297	12.90	0.567

Plasma diagnostics by optical emission spectrometry is a passive technique easy to implement but assumes that plasma is in local thermal equilibrium (LTE). In accord with the observation of Alder et al. [**17**] that electron temperature (T_e) is close to T_{ex} of species with high excitation energy, we considered that T_e could correspond to T_{ex} for Ar I (4p→4s). The gas temperature (T_g), n_e and T_e characterize the capability of atomization and excitation of a plasma source. Low T_g and high T_e recommend plasma as excitation source in atomic emission. The excitation temperature of Ar I (4p→4s) was estimated from the Bolzmann plot considering the convolution of the grating and detector efficiencies in conjunction with the wavelength. The excitation temperature of Ar I (4p→4s) *vs.* viewing height in the absence of CH_4 and with addition of 2.5 and 5 mL min^{-1} CH_4 in 0.7 L min^{-1} Ar is presented in Figure 2. The variation of electron number density under the same conditions is shown in Figure 3.

The excitation temperature of Ar I in pure Ar plasma is in the range 1210 – 1950 K and decreases to 780 – 1460 K and 580 – 1365 K when adding 2.5 and 5 mL min^{-1} CH_4 respectively. The error in the determination of T_{ex} evaluated from the standard deviation of the slope of the Bolzmann plot was in the range 5 – 15 %. The decrease of T_{ex} for Ar I confirms quenching of Ar emission caused by second-kind collisions between argon excited atoms and CH_4 molecules. The decline of the population of 4s Ar metastable atoms involved in the excitation of nitrogen SPS when adding CH_4 proves the decrease of the nitrogen molecular emission.

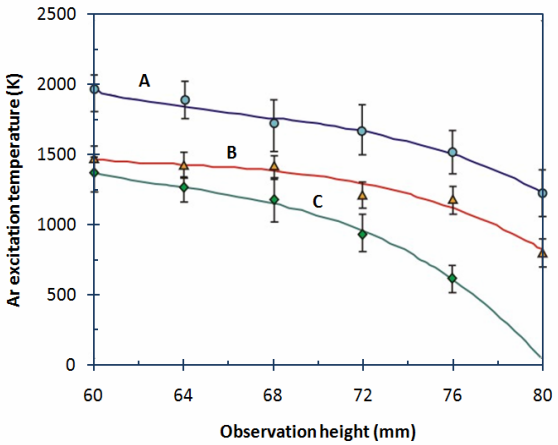

Figure 2. Dependence of the excitation temperature of Ar I (4p→4s) on the viewing height in plasma operated at 275 W and 0.7 L min^{-1} Ar. CH_4 flow rate (mL min^{-1}): A - 0; B - 2.5; C - 5. Error bars correspond to uncertainty in temperature determination

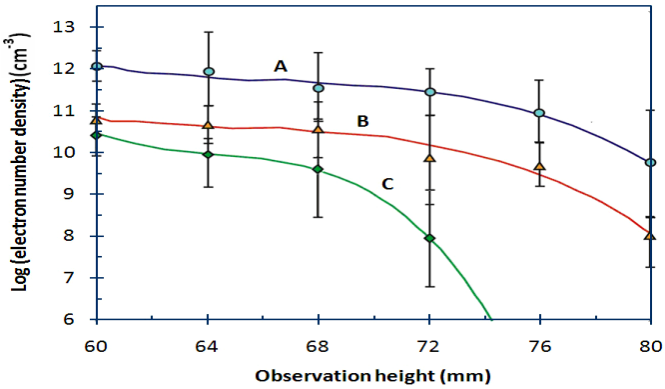

Figure 3. Electron number density *vs*. viewing height in plasma operated at 275 W and 0.7 L min^{-1} Ar. CH_4 flow rate (mL min^{-1}): A - 0; B - 2.5; C - 5. Error bars correspond to uncertainty in temperature determination

The value of n_e was calculated from the Saha's equation considering the statistical weights for electrons and ions (g_e=2 and g_i=6) and T_e equal to T_{ex} of Ar atoms.

$$\ln\left(\frac{hc}{I}\frac{gA}{\lambda}\right) = 51.72 - 2\ln n_e + \frac{3}{2}\ln T - \frac{E_i - E_{ex}}{kT} \qquad (7)$$

where: E_i – ionization energy of Ar (15.86 eV)
E_{ex} – excitation energy of Ar I lines

Thus, $\ln\left(\frac{hc}{I}\frac{gA}{\lambda}\right)$ was plotted *vs.* $\frac{E_i - E_{ex}}{k}$ (Fig.3) and n_e was calculated from the intercept.

The value of n_e in the plasma tail (60 – 80 mm) of pure Ar is in the range 6.34×10^9 – 1.37×10^{12} cm^{-3}, lower than in the inferior zone of the discharge (0 – 32 mm), of 4.35×10^{12} – 2.37×10^{13} cm^{-3} [**26**]. This parameter decreases at 1.21×10^8 – 7.70×10^{10} cm^{-3} and 1.06×10^8 – 3.79×10^{10} cm^{-3} when adding 2.5 and 5 mL min^{-1} CH_4, respectively. The error in n_e determination was in the range 5 – 15 %.

The decline of n_e in the presence of CH_4 in the Ar plasma suggests a sharp decrease of the ionization degree of the support gas. The gas temperature of Ar plasma was in the range 2330 - 2550 K [**26**]. The relatively high gas temperature and low electron temperature and n_e in the plasma tail are benefit for a good atomization of sample but provide low excitation capabilities, what is suitable as atoms cell in AFS [**11-13**].

CONCLUSIONS

The spectral characterization of an Ar/CH_4 plasma operated at low power and gas consumption was carried out. The emission spectrum of the pure Ar plasma was dominated by the OH, N_2 SPS band and Ar I lines 4p→4s transitions. Addition of CH_4 in Ar plasma resulted in quenching of the molecular emission and Ar I lines following chemical reactions with OH and second-kind collisions with nitrogen molecules and Ar atoms. In the Ar/CH_4 plasma molecular emission of CH_x (x=1, 2) is missing, while the C_2 Swan band is relative intense. The role of CH_4 in quenching of emission subsequent second-kind collisions was evidenced by the decrease of Ar I excitation temperature and electron number density. The low background spectrum and low excitation capability of the Ar/CH_4 plasma recommend it as an attractive atomization source in atomic spectrometry using low resolution microspectrometers.

EXPERIMENTAL SECTION

Instrumentation

The discharge was characterized by optical emission spectrometry using spectrum ranging from 200 – 1000 nm recorded with the low resolution HR4000 microspectrometer from Ocean Optics with FWHM of 1.5 nm. Detailed about the measurement settings are given in Table 3, while the experimental set-up in Figure 4. Under standard conditions, plasma was generated at a flow rate of 0.7 L min^{-1} Ar (5.0 quality). In the approach with CH_4 (4.5 quality) as collision/reaction gas, plasma was developed in a mixture using the same Ar flow rate as above and CH_4 in the range of 2.5-7.5 mL min^{-1}.

Table 1. Characteristics and operating conditions for the experimental system CCP torch-microspectrometer

Power supply	Free running generator, 275 W, 27.12 MHz (Research Institute for Analytical Instrumentation, Cluj-Napoca, Romania)
Plasma torch	Capacitively coupled with Mo tubular electrode (i.d. 3.5 mm) connected to the generator and grounded ring electrode of Cu spaced at 5 mm; 16 mm i.d. quartz tube, 10 cm length, GFC 17 model CH_4 mass flow meter (Aalborg Instr. and Controls, USA).
Sample introduction system	Meinhardt nebulizer equipped with impactor spray chamber (Perkin Elmer, Norwalk, USA) without desolvation, 5% nebulization efficiency; aerosol intake into the plasma *via* the tubular electrode.
Optics	HR4000 Microspectrometer Ocean Optics (200-1100 nm), 1200 grooves mm^{-1}, Toshiba TCD1304AP CCD array, 3636 pixels, focal length 101.6 mm, FWHM 1.5 nm, collimating system-74 UV, fibre optic QP 600 μm, 25 cm length (Ocean Optics, Dunedin, USA).
Data acquisition	Spectra Suite Soft (Ocean Optics); average of 10 successive measurements for 5 s integration time

Throughout the experiment a flow rate of 1 mL min^{-1} water with 5% nebulization efficiency was introduced into plasma. The emission signal was collected through the quartz tube with a collimating lens placed in the radial direction related to the plasma by means of the fibre optic of the microspectrometer. Measurements were performed in plasma tail at viewing heights greater than 60 mm above the tubular electrode, the zone considered as optimum for fluorescence measurements [**13**].

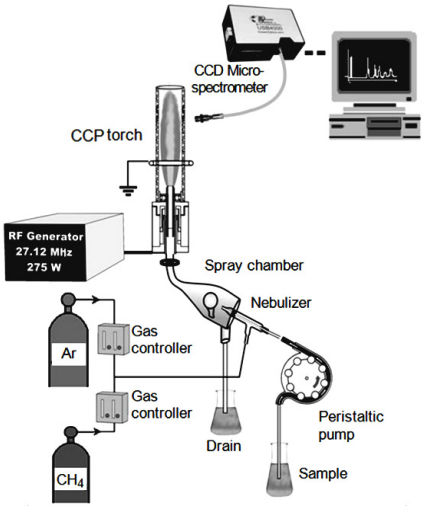

Figure 4. Experimental set-up of the capacitively coupled plasma torch and HR4000 Ocean Optics microspectrometer.

ACKNOWLEDGMENTS

The present investigations are supported by the Romanian Ministry of Education, Research and Innovation, PNCDI II Program (Project FLUOROSPEC no. 71019/2007.

REFERENCES

1. J.A.C. Broekaert, *Applied Spectroscopy*, **2008**, *62*, 227A.
2. ISO 11885: 2007, Water quality – Determination of selected elements by inductively coupled plasma optical emission spectrometry (ICP-OES).
3. ISO 22036 Soil quality - Determination of trace elements in extracts of soil by inductively coupled plasma - atomic emission spectrometry (ICP - AES).
4. A.E. Croslyn, B.W. Smith, J.D. Winefordner, *Critical Review Analytical Chemistry,* **1997**, *27*, 199.
5. D.L. Haas, J.A. Caruso, *Analytical Chemistry*, **1984**, *56*, 2014.
6. K. Jankowski, *Journal of Analytical Atomic Spectrometry*, **1999**, *14*, 1419.
7. Q. Jin, W. Yang, F. Liang, H. Zhang, A. Yu, Y. Cao, J. Zhou, B. Xu, *Journal of Analytical Atomic Spectrometry*, **1998**, *13*, 377.
8. M.W. Blades, *Spectrochimica Acta*, **1994**, *49B*, 47.
9. T. Frentiu, D. Petreus, M. Senila, A.I. Mihaltan, E. Darvasi, M. Ponta, E. Plaian, E.A. Cordos, *Microchemical Journal*, **2011**, *97*, 188.
10. E.A. Cordos, T. Frentiu, A.M. Rusu, S.D. Anghel, A. Fodor, M. Ponta, *Talanta,* **1999**, *48*, 827.
11. T. Frentiu, E. Darvasi, M. Senila, M. Ponta, E. Cordos, *Talanta,* 2008, **76**, 1170.
12. T. Frentiu, M. Ponta, M. Senila, A.I. Mihaltan, E. Darvasi, M. Frentiu, E. Cordos, *Journal of Analytical Atomic Spectrometry*, **2010**, *25*, 739.
13. T. Frentiu, M. Ponta, A.I. Mihaltan, E. Darvasi, M. Frentiu, E. Cordos, *Spectrochimica Acta*, **2010**, *65B*, 565.
14. A. Yanguas-Gil, K. Focke, J. Benedikt, A. von Keudell, *Journal of Applied Physics*, **2007**, *101*, 103307.
15. D.W. Setser, D.H. Stedman, J.A. Coxon, *Journal of Chemical Physics,* **1970***, 53*, 1004.
16. N. Bibinov, A. Fateev, K. Wiesemann, *Journal of Physics. D: Applied Physics,* **2001***, 34*, 1819.
17. J.F. Alder, R.M. Bombelka, G.F. Kirkbright, *Spectrochimica Acta*, **1980**, *35B*, 163.
18. W.K. McGregor, Proc. V Bienn. Gas Dynamics Symp., Evanson 1963, Chapter 8. Northwestern University Press (**1963**).
19. J.R. Dunlop, F.P. Tully, *Journal of Physical Chemistry*, **1993**, *97*, 11148.
20. F.P. Tully, A.R. Ravishankara, *Journal of Physical Chemistry*, **1980**, *4*, 3126.
21. J.G. Calvert, R. Atkinson, K.H. Becker, R.M. Kamens, J.H. Seinfeld, T.J. Wallington, G. Yarwood, "The Mechanisms of Atmospheric Oxidation of Aromatic Hydrocarbons", Oxford University Press, UK, **2002**.
22. T. Gierczak, R.K. Talukdar, S.C. Herndon, G.L. Vaghjiani, A.R. Ravishankara, *Journal of Physical Chemistry.* A **1997,** *101*, 3125.
23. M. Shimozuma, H. Tagashira, *Journal of Physics. D: Applied Physics*, **1981**, *14*, 1783.
24. A. Gicquel, M. Chenevier, Kh. Hassouni, A. Tserepi, M. Dubus, *Journal of Applied Physics*, **1998**, *83*, 7504.
25. NIST Atomic Spectra Database Lines Form http://physics.nist.gov/PhysRefData/ASD/lines_form.html (accessed November 2010)
26. T. Frentiu, M. Ponta, E. Darvasi, M. Frentiu, E. Cordos, *Acta Chimica Slovenica*, **2010**, *57*, 173.

STUDIA UBB CHEMIA, LVI, 1, 2011

PRODUCTION AND CHARACTERIZATION OF BIODIESEL FROM RAPESEED OILS

ADRIANA GOG[a], MIRCEA CHINTOANU*,[a], MARIUS ROMAN[a], EMIL LUCA[b], FLORIN-DAN IRIMIE[c]

ABSTRACT. The main objective of the present work was to investigate the influence of rapeseed oil type upon the biodiesel quality. For this purpose eleven types of rapeseed oil were used to obtain biodiesel by alkaline transesterification. The produced biodiesels were examined for several physico–chemical characteristics in order to evaluate and compare their quality with the specifications for biodiesel according to the EN 14214:2004 European standard.

Keywords: *rapeseed oil, biodiesel, alkaline transesterification*

INTRODUCTION

Biodiesel is gaining more and more importance as an attractive alternative fuel due to the depleting nature of fossil fuel resources. The most common method to produce biodiesel, industrially applied, is catalytic transesterification of vegetable oils and animal fats using a homogeneous acid or base catalyst (Fig. 1a). Alkaline-catalyzed transesterification process is normally adopted for biodiesel production because alkaline catalysts are the most effective transesterification catalysts compared to the acid catalysts and also for economic reasons [1, 2]. The basic catalyst reacts with methanol to form sodium methoxide (Fig. 1b) that reacts with the triglycerides to produce biodiesel (fatty acid methyl esters, FAMEs). The main by-product is glycerol which, after purification, can be used for pharmaceutical and cosmetic purposes. Free fatty acids, water and unreacted alkaline catalyst are also present. Thus, complicated purification steps are needed in order to obtain a pure biodiesel achieving the standard requirements. When the acidity of a feedstock is high the reaction between the free fatty acids and the basic catalyst produces soap (Fig. 1c). Since soap is a surfactant it forms emulsions and makes the separation between FAMEs and glycerol difficult. Thus, in the presence of a high content of free fatty acids an acid-catalyzed process is used.

[a] *INCDO-INOE 2000 Research Institute for Analytical Instrumentation - ICIA, 67 Donath St., 400293 Cluj-Napoca, Romania, *mircea.chintoanu@icia.ro*
[b] *University of Agricultural Sciences and Veterinary Medicine Cluj-Napoca, Faculty of Horticulture, 3 Calea Manastur St., 400372 Cluj-Napoca, Romania*
[c] *Babes-Bolyai University Cluj-Napoca, Faculty of Chemistry and Chemical Engineering, 11 Arany Janos St. 400028, Cluj-Napoca, Romania*

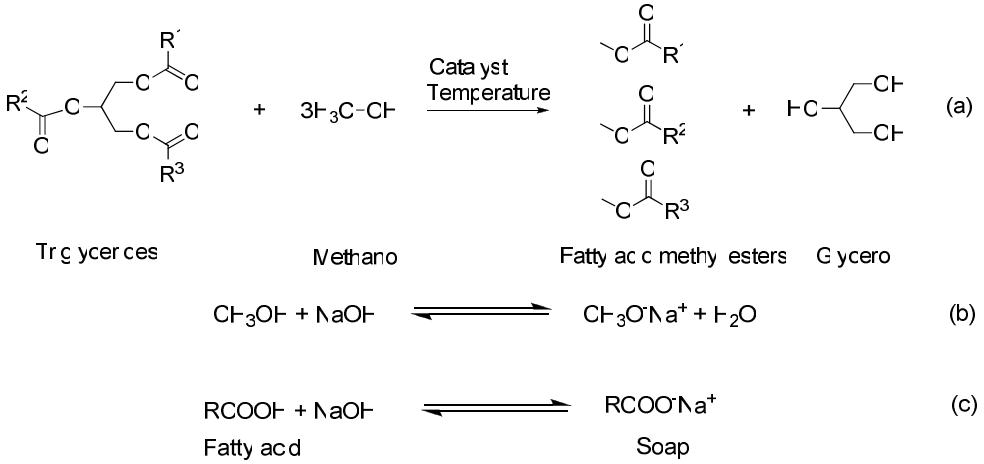

Figure 1. (a) Methanolysis reaction of triglycerides for the production of Fatty Acid Methyl Esters(biodiesel); (b) Methoxide formation; (c) Unwanted reaction of soap formation due to the presence of free fatty acids

Rapeseed (*Brassica napus*) is widely cultivated throughout the world for the production of animal feed, vegetable oil and biodiesel. Rapeseed oil is one of the preferred oil stocks for biodiesel production, partly because rapeseed produces more oil per unit of land area compared to other oil sources, ranking fourth in the world with respect to production, after soybean, palm and cottonseed [3]. The properties of the biodiesel fuel are strongly influenced by the structure and distribution of the component fatty acid methyl esters which vary depending on the source.

The main objective of the present work was to investigate the influence of rapeseed oil type upon the biodiesel quality. For this purpose eleven types of rapeseed oils were used to obtain biodiesel by alkaline transesterification. The reaction conditions used for methanolysis of rapeseed oils were: 1.5 % (w/w by oil weight) KOH as catalyst, methanol/oil molar ratio 6:1, reaction temperature 60℃, rate of mixing 300 rpm and a reaction time of 1 h. The produced biodiesel was examined for several physico–chemical characteristics in order to evaluate and compare its quality with the specifications for biodiesel according to the EN 14214:2004 European standard (Table 1) [4].

Table 1. Generally applicable requirements and related test methods for several physico-chemical characteristics necessary for FAME use as diesel fuel

Property	**Unit**	**Limits**		**Test method**
		Minimum	**Maximum**	
Density, 15℃	Kg/m^3	860	900	EN ISO 3675
Viscosity, 40℃	mm^2/s	3.50	5.00	ASTM D 2983-04a

Property	Unit	Limits		Test method
		Minimum	Maximum	
Acid value	mg KOH/g		0.50	EN 14104
Iodine value	gI_2/100g	-	120	EN 14111
Sulfur content	mg/Kg	-	10.0	prEN ISO 20846
Water content	mg/Kg	-	500	EN ISO 12937
Flash point	°C	120		prEN ISO 3679
Ester content	% (m/m)	96.5		EN 14103
Linoleic acid methyl ester	% (m/m)	-	12.0	EN 14103

RESULTS AND DISCUSSION

The biodiesel yield was considered as the ratio between the produced biodiesel weight and the initial rapeseed oil weight, % (w/w). The yields obtained for the transesterification of rapeseed oils are shown in Table 2.

Table 2. The yields obtained for the transesterification reactions of rapeseed oils

Rapeseed biodiesel	Martor I	Martor II	Aviator	Karibik	Formula	Nelson	Octans	Toccata	Petrol	Smart	Speed
Yield, wt %	93.2	93.9	92.9	90.6	57.3	91.3	92.4	92	91.2	93.3	93.4

As shown in the table above, the yields for the alkaline transesterification reactions were greater than 90 % except for FORMULA rapeseed oil, with a yield of only 57.3 %. The reason was the high content of free fatty acids which in the presence of potassium hydroxide determined the formation of soaps, making difficult the conversion of triglycerides to methyl esters and also the separation of reaction products.

The products of above transesterification processes were analyzed, taking into consideration several specifications for biodiesel as fuel in diesel engines. Most of these parameters comply with the limits prescribed in the EN 14214:2004 standard for biodiesel.

For each studied physico-chemical characteristic the values obtained were graphically presented compared with the minimum and/or maximum limits recommended by the quality specifications according to EN 14214:2004 (see Figure 2).

DENSITY

Density is an important property of biodiesel. It represents the weight of a unit volume of fluid. Fuel injection equipment operates on a volume metering system, hence a higher density for biodiesel results in the delivery of a slightly

greater mass of fuel. The density values for the rapeseed derived biodiesels are schematically presented in Figure 2a. It is noted that only the biodiesel obtained from FORMULA rapeseed oil has exceeded the maximum permissible. This was due to low yield of reaction; much of the oil remained untransformed. The density values for other rapeseed oils were comparable to those reported in the literature [5].

VISCOSITY

Viscosity is a measure of the internal friction or resistance of an oil to flow. As the temperature of oil is increased, its viscosity decreases and it is therefore able to flow more readily. Viscosity is the most important property of biodiesel since it affects the operation of fuel injection equipment, particularly at low temperatures when the increase in viscosity affects the fluidity of the fuel. High viscosity leads to poorer atomization of the fuel spray and less accurate operation of the fuel injectors. The viscosity may be used not only as the indicator of impurities in biodiesel, but also as the control parameter of the transesterification process [6].

The values of the kinematic viscosity at 40°C for the rapeseed oil biodiesels were represented in Figure 2b. Due to low conversion efficiency, the viscosity value for biodiesel obtained from FORMULA oil was higher than the maximum recommended (out of the plotting scale). Biodiesel produced from AVIATOR and MARTOR I oils have slightly exceeded the maximum, but in the literature the viscosity values for rapeseed biodiesel are up to 5.7 mm^2/s [7].

ACID VALUE

High fuel acidity is associated with corrosion and engine deposits, particularly in the fuel injectors. The acid number or acid value indicates the quantity of free fatty acids (FFA) and mineral acids (negligible) present in the sample. According to EN 14104, the acid value is expressed in milligrams (mg) potassium hydroxide (KOH) required to neutralize 1 g of sample.

The acid value of the analyzed biodiesels was ranged 0.09 – 0.42 mg KOH/g. The EN 14214:2004 biodiesel standard approved a maximum acid value for biodiesel of 0.5 mg KOH/g which was fulfilled by all of the produced rapeseed methyl esters (Figure 2c). The highest value of 0.42 mg KOH/g sample was obtained for the FORMULA oil biodiesel, indicating a high content of free fatty acids.

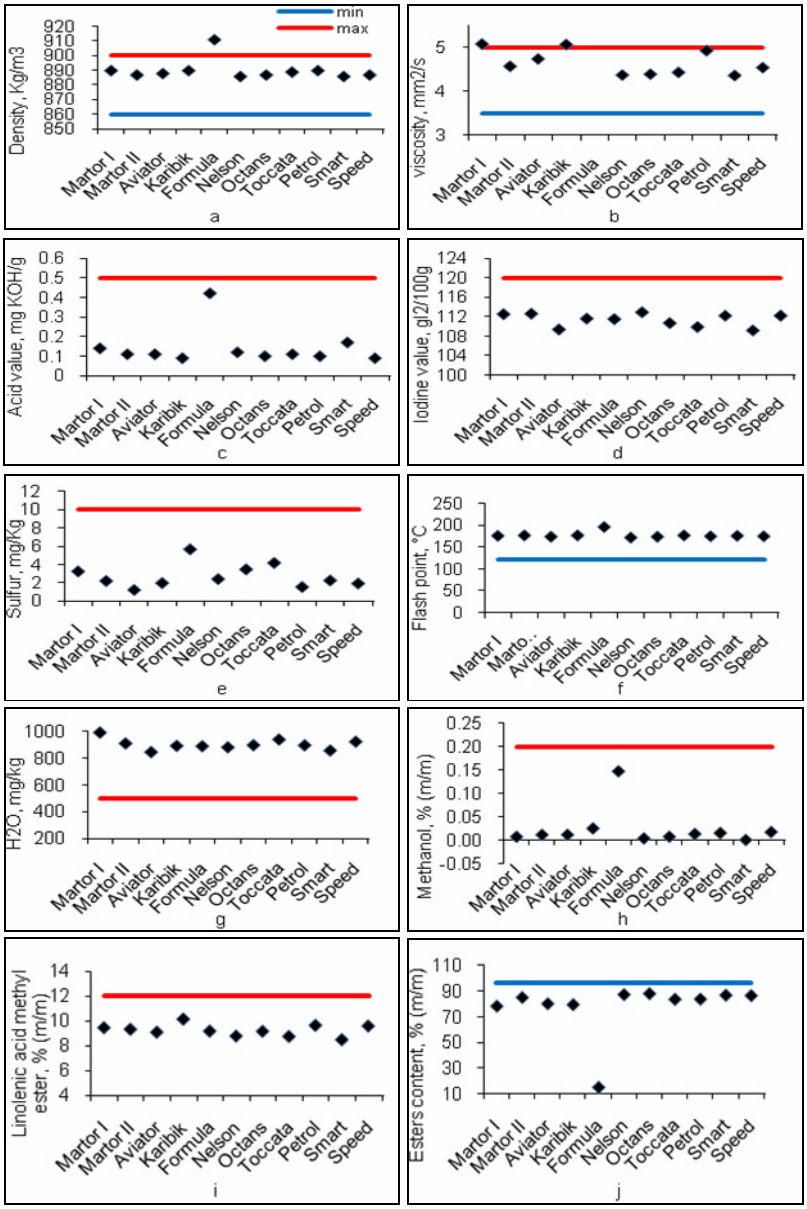

Figure 2. Physico-chemical characteristics of rapeseed derived biodiesels compared with the minimum and/or maximum limits recommended by the quality specifications according to EN 14214:2004 (minimum limit – blue line, maximum limit – red line); **a** - density; **b** - viscosity; **c** - acid value; **d** - iodine value; **e** - sulphur content; **f** - flash point; **g** - water content; **h** - methanol content; **i** - linoleic acid methyl ester content; **j** - ester content

IODINE VALUE

Iodine value depends on the feedstock origin and greatly influences fuel oxidation tendency. Consequently, in order to avoid oxidation, special precautions must be taken during the storage of biodiesel from rapeseed oil with high iodine values, According to EN 14214 European standard methyl esters used as diesel fuel must have an iodine value less than 120 g I_2 per 100 g of sample. Methyl esters obtained in this study had iodine value in the range 109.2 – 112.9 g I_2/100 g (Figure 2d), thus the variations were not considerable.

SULFUR CONTENT

The presence of sulfur in biodiesel samples may be from vegetable oils, for example, from phospholipids present in all vegetable oils or glucosinolates present in rapeseed derived biodiesel [8].The sulfur content of the biodiesels was analyzed by EN ISO 20846 test method, using ultraviolet fluorescence spectrometry. The values were ranged from 1.23–5.64 mg/Kg, as shown in Figure 2e. Values for sulfur content for the rapeseed biodiesels were all situated below the recommended maximum of 10.0 mg/Kg.

FLASH POINT

The flash point of a substance represents the lowest temperature at which it can vaporize to form flammable mixtures when exposed to air. It is a parameter to consider in the handling, storage and safety of fuels and flammable materials. A higher value of flash point decreases the risk of fire. In the case of biodiesel, the flash point (FP) decreases with increasing amounts of residual alcohol and other low-boiling solvents [9]. In this study, only residual methanol can be present in biodiesel. Therefore, the flash point was presupposed to be depending only on the methanol content. For all rapeseed biodiesel samples, the flash point was much higher than the minimum recommended value of 120 °C. The results are plotted in Figure 2f.

WATER CONTENT

The water content in biodiesel is an important factor in the quality control. Water can promote microbial growth, lead to tank corrosion, participate in the formation of emulsions, and cause hydrolysis or hydrolytic oxidation [8]. Therefore, the content of water is limited to 0.05 % (w/w) according to EN 14214. The water content of the rapeseed biodiesel samples was measured using EN ISO 12937 standard test method and in all experiments, the values were higher than the recommended maximum of 500 mg/Kg, as presented in Figure 2g. This indicates an incomplete purification process and the need for additional steps for biodiesel drying.

METHANOL CONTENT

The residual methanol in biodiesel can cause corrosion of metal, mainly of aluminium, and decreases the biodiesel flash point. Besides, it is responsible for cetane number and lubricity decreasing of fuel. The values for the methanol content were situated below the maximum recommended of 0.20% (w/w), for all the types of rapeseed biodiesel submitted to analysis (Figure 2h). The highest value of 0.1469 % (w/w) was obtained for FORMULA oil biodiesel that demonstrated once again the difficulties caused by the formed soaps on the conversion and purification processes.

ESTER CONTENT. LINOLENIC ACID METHYL ESTER CONTENT

The values for ester content of rapeseed biodiesels were all situated below the recommended minimum of 96.5% (w/w). This requires additional steps of purification and drying to achieve a more efficient removal of water and of by-products (mono-, di- triglycerides, and glycerol) to obtain a product that meets the quality specifications. Values for ester content are presented in Figure 2j. In the case of biodiesel obtained from FORMULA oil the ester content was only 14.9 % (w/w), indicating a very low conversion of triglycerides into methyl esters. The values for linolenic acid methyl ester content were all situated below the maximum recommended value of 12% (w/w) (Figure 2i).

A complete purification scheme of crude biodiesel in order to obtain a finished product that meets EN 14214 quality specifications is proposed in Figure 3.

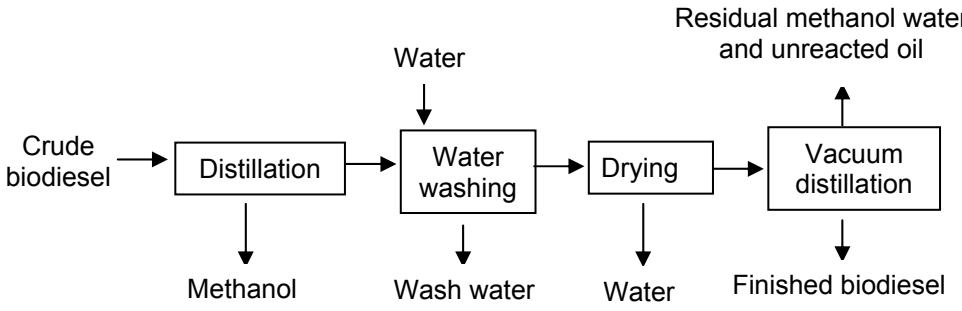

Figure 3. Purification scheme of crude biodiesel in order to obtain a finished product that meets EN 14214 quality specifications.

Crude biodiesel is first submitted to a distillation process in order to remove methanol from other components. Then a water washing step is used to remove remaining catalyst, soap, salts, methanol, or free glycerol from the biodiesel. After the wash process, the remaining water is removed from the biodiesel by a drying process. A final vacuum distillation is required to remove any residual methanol, water and

unreacted oil and to obtain a biofuel purity that meets EN 14214 specifications. Vacuum operating conditions are required in order to keep the temperature low enough to avoid the biofuel degradation.

HIGHER HEATING VALUE

Higher heating value (HHV) is an important property defining the energy content and thereby efficiency of fuels that determines in the case of biodiesel its suitability as an alternative to diesel fuels. As it can be observed from Table 3, the values were ranged from 38.8 to 40.1 MJ/kg. Higher HHVs were obtained for experiments in which the yields of ester were higher while the lowest value was obtained for FORMULA oil due to low conversion of triglycerides. For the other rapeseed biodiesels the variations were not considerable. The European standard EN 14214 approved a suitable heating value for biodiesel of 35 MJ/kg.

Table 3. High heating values for rapeseed derived biodiesels

Rapeseed biodiesel	Martor I	Martor II	Aviator	Karibik	Formula	Nelson	Octans	Toccata	Petrol	Smart	Speed
HHV, MJ/Kg	39.9	39.9	39.9	38.9	38.8	40.0	39.9	39.9	40.1	39.9	39.9

CONCLUSIONS

The results obtained in the present study regarding the production of biodiesel using alkaline transesterification of eleven varieties of rapeseed oil as feedstocks together with the physico-chemical characterization of the biodiesels obtained, showed that only the rapeseed oil from the FORMULA hybrid proved inadequate for the alkaline transesterification process due to high levels of free fatty acids that led to the formation of soaps. The consequence was a low yield for the transesterification process of only 57.3% due to incomplete conversion of triglycerides into esters. The formed soaps caused many difficulties also in the purification steps of crude biodiesel that included: separation, washing and drying, ester content of the final product being only 14.9% (w/w). The other rapeseed oils tested: control sample variety oils (MARTOR I, MARTOR II), AVIATOR, KARIBIK, NELSON, OCTANS, TOCCATA, PETROL, SMART, SPEED gave yields higher than 90% and the physico-chemical characterization of these biodiesels demonstrated that these rapeseed oils can be successfully used as feedstocks for biodiesel production using alkaline transesterification.

EXPERIMENTAL SECTION

Materials and methods

11 types of rapeseed oil: two rapeseed oils from DEXTER control sample variety named further MARTOR I and MARTOR II (obtained from Saaten-Union) and eight oils obtained from rapeseed hybrids: AVIATOR, KARIBIK, FORMULA, NELSON, OCTANS, TOCCATA, PETROL, SMART, SPEED (obtained from Syngenta). The fatty acid profiles of rapeseed oils are summarized in Table 4. Pure standards of fatty methyl esters (FAMEs) were obtained from Sigma Chemicals Co. (St. Louis, MO, USA). Methanol, n-hexane, potassium hydroxide, and anhydrous magnesium silicate were of Merck (Darmstadt, Germany). All the chemicals used were analytical reagent grade.

Table 4. Fatty acid composition for the rapeseed oils used for biodiesel production

Fatty acids Abr.		Cultivar										
		Dexter control sample variety (Saaten-Union)		Hybrids (Syngenta)								
		Martor I	Martor II	Aviator	Karibik	Formula	Nelson	Octans	Tocatta	Petrol	Smart	Speed
C10	%	0.014	0.013	0.013	0.015	0.013	0.013	0.016	0.014	0.016	0.017	0.015
C12	%	0.010	0.010	0.011	0.009	0.010	0.009	0.009	0.010	0.009	0.009	0.009
C14	%	0.057	0.058	0.065	0.055	0.056	0.056	0.051	0.058	0.051	0.051	0.051
C16	%	4.32	4.24	4.42	4.3	4.18	4.13	4.23	4.06	4.29	3.98	4.23
C16:1	%	0.186	0.191	0.185	0.197	0.176	0.184	0.186	0.174	0.186	0.17	0.193
C18	%	1.67	1.57	1.70	1.66	1.56	1.53	1.69	1.66	1.53	1.85	1.64
C18:1	%	58.2	58.9	59.1	59.17	57.5	58.8	58.3	59.8	59.1	61.4	59.5
C18:2	%	19.4	18.8	18.5	17.31	19.5	19.4	18.5	18.9	18.2	17.2	17.6
C18:3	%	9.27	9.26	8.98	10	8.46	8.67	9.01	8.65	9.5	8.28	9.51
C20	%	0.530	0.474	0.496	0.512	0.474	0.472	0.502	0.488	0.512	0.535	0.495
C22:0	%	0.261	0.220	0.227	0.236	0.224	0.23	0.226	0.224	0.275	0.225	0.229
C22:1	%	-	-	-	-	-	0.048	0.076	0.029	-	-	-
C24:0	%	0.093	-	0.071		0.069	0.091	0.078	0.071	0.096	0.076	-

Alkaline catalyzed transesterification

Single-stage laboratory esterification was carried out in a 250 ml conical flask equipped with a magnetic stirrer. 1.5 g potassium hydroxyde dissolved in 20 ml methanol was added to 100 g vigorously stirred oil. Stirring was continued for 1 h at 60°C. After this time the reaction was stopped, the mixture was transferred to a separatory funnel and the glycerol was allowed to separate for a minimum of 3 h. After separation of the two layers by sedimentation, the upper methyl esters layer was purified by distilling the residual methanol at 80°C. The remaining catalyst was removed by successive rinses with distilled water. Finally, the residual water was eliminated by treatment with anhydrous magnesium silicate at 60 °C for 60 min with stirring. After cooling, the biodiesel was filtered and its quality was tested.

Gas Chromatographic Analysis of Fatty Acid Methyl Ester

The fatty acid methyl ester contents in the reaction mixture were determined using an Agilent 7890A GC gas chromatograph equipped with a DB-WAX capillary column (30m × 0.25mm × 0.25μm) and a flame ionization detector. The column oven temperature was kept at 50 °C for 1 min, heated to 200 °C at 25°C/min, then to 230 °C at 3°C/min and finally maintained for 18 min. The injector and detector temperatures were set to 250 and 280 °C, respectively. Helium was utilized as a carrier gas. The gas chromatography calibration was conducted via the analysis of standard solutions of methyl esters and heptadecanoate methyl ester was used as internal standard.

ACKNOWLEDGMENTS

This work was financially supported by The Partnerships in Priority Domains Program of National Center of Programs Management from Romania, Project No. 22094/2008.

REFERENCES

1. U. Rashid, F. Anwar, *Fuel*, **2008**, *87*, 265–273.
2. G. Knothe, J.V. Gerpen, V. Krahl, “Basics of the Transesterification Reaction, the Biodiesel Handbook”, Champaign, III, AOCS Press, **2005**, 26-39.
3. FAO/WHO/UNU, World Health Organization, Geneva, **2002**.
4. EN 14214:2004
5. J.M. Encinar, J.F. Gonzalez, A. Rodryguez-Reinares A., *Ind. Eng. Chem. Res.,* **2005**, *44*, 5491–5499.
6. N. Ellis, F. Guan, T. Chen, C. Poon, *Chem. Eng. J.*, **2008**, *138*, 200–206.
7. http://www.brevardbiodiesel.org/viscosity.html
8. G. Knothe, *J. Am. Oil Chem. Soc.*, **2006**, *83*(10), 823–33.
9. M. Mittelbach, C. Remschmidt, “Biodiesel, the Comprehensive Handbook” Ist Ed. Martin Mittelbach, Graz, **2004**.

STUDIA UBB CHEMIA, LVI, 1, 2011

COMPARATIVE STUDY OF MERCURY DETERMINATION IN SOIL AND VEGETABLE BY METHODS BASED ON THERMAL DECOMPOSITION-AAS AND WET DIGESTION CV-AFS

MARIN ŞENILĂ[a], ERIKA LEVEI[a], LĂCRIMIOARA ŞENILĂ[a], OANA CADAR[a], GABRIELA OPREA[b], CECILIA ROMAN[a]

ABSTRACT. The aim of this study was to evaluate and compare the analytical parameters of two methods used for mercury determination from solid samples (soils and vegetables): direct determination from solid samples by thermal decomposition - atomic absorption spectrometry (TD-AAS) with gold amalgamation and determination using wet digestion followed by measurements by cold vapor atomic fluorescence spectrometry (CV-AFS). Two commercially available mercury (Hg) analyzers were used for the study. Using direct measurement in solid sample by TD-AAS, a detection limit of 1.2 μg kg^{-1} and a RSD of 3.8% for 1441 μg kg^{-1} Hg were obtained, while by using wet digestion and CV-AFS measurement, a detection limit of 2.5 μg kg^{-1} and a RSD of 4.5% for 1438 μg kg^{-1} Hg were calculated. The accuracy of the methods was verified by the determination of mercury in certified reference materials and good agreement between found concentrations and certified values was obtained for the both methods. Five real soil samples and five vegetable samples from Baia Mare area were analyzed. The Hg concentrations in soils ranged between 653–2004 μg kg^{-1} using TD-AAS method and between 644-1998 μg kg^{-1} using CV-AFS method, while in vegetables the concentrations ranged between 4,60-53,4 μg kg^{-1} using TD-AAS method and between 4,32-55,8 μg kg^{-1} using CV-AFS method. According to the t-Test and regression analysis, no significant statistical difference between the datasets obtained by the two methods was found.

Keywords: *mercury determination, soil samples, vegetable samples, TD-AAS, CV-AFS*

INTRODUCTION

As a consequence of natural and anthropogenic processes high amounts of mercury is released into the hydrosphere, atmosphere and biosphere. This element occurs naturally as the metallic form and/or its sulfide ores such as cinnabar (HgS) [1]. The earth's crust contains 0.5 mg kg^{-3}, ambient air may contain 0.002-0.02 pg dm^{-3}, and sea water contains about 0.03 mg dm^{-3}

[a] *INCDO-INOE Research Institute for Analytical Instrumentation, 67 Donath, 400293, Cluj-Napoca, Romania, e-mail: icia@icia.ro*
[b] *Faculty of Sciences, North University of Baia Mare, Victoriei 76, 430122 Baia Mare, Romania*

mercury. It is also found in trace amounts in most animal and plant tissues. Due to his volatility, elemental mercury is efficiently transported as a gas around the globe, and even remote areas [2, 3].

Hg poisoning may lead to damage in the central nervous system [4]. Due to its high toxicity, mercury (Hg) is considered one of the most dangerous pollutants, being in the lists of priority dangerous substances established by the United States Comprehensive Environmental Response, Compensation, and Liability Act (CERCLA) and the European Water Framework Directive (2000/ 60/EC) [5]. From 2011 export of mercury from the EU will be prohibited in order to further reduce its release [5]. As a consequence of its toxicity, it is very important to make accurate determinations of mercury in environmental samples.

A variety of analytical techniques can be used for mercury determination. The most popular methods for determining mercury in almost any type of sample are based on cold vapor atomic absorption spectrometry (CV-AAS) and cold vapor atomic fluorescence spectrometry (CV-AFS) [6-8]. The way of liberating mercury from aqueous or digested samples is reduction, followed by volatilization and introduction of the mercury by aid of a gas stream. A gold amalgamation method to purify the mercury vapor can be used [9]. Inductively coupled plasma mass spectrometry (ICP-MS) can be also successfully applied for mercury analysis [10, 11], including for mercury speciation, but not always under routine operating conditions.

The majority of analytical methods for the determination of mercury in solid samples are based on wet digestion [12, 13]. Ultrasound-assisted leaching is an alternative and effective way of extracting the analytes from samples [14]. The techniques using wet digestion followed by cold vapor generation are generally time-consuming and in addition, high amounts of harmful and expensive reagents are necessary. Also, the risk of contamination by supplementary pretreatment steps is high [15, 16]. A good alternative to wet digestion is the use of *reagent-free* methods, based on thermal decomposition of solid samples or extraction and preconcentration from liquid samples. These alternatives are in accord with new approach of use non-chemical methods leading to green analytical chemistry [17- 20].

Thermal decomposition (pyrolise) - atomic absorption spectrometry is a *reagent-free* analytical method in that decomposition products are carried to a catalyst by an oxygen flow, then sample oxidation is completed and halogens and nitrogen/sulphur oxides are trapped. The final decomposition products pass through a mercury amalgamator which collects Hg^0. The Hg amalgamator is heated at high temperature and the Hg^0 is released and quantified using the spectral method [21-26].

The aim of this study was to evaluate and compare the analytical parameters of the method based on thermal decomposition atomic absorption

spectrometry with those of wet digestion – cold vapor atomic fluorescence spectrometry, and to apply these methods for mercury determination in real solid samples (soils and vegetables) collected from Baia Mare (NW Romania) area.

RESULTS AND DISCUSSIONS

Performance parameters of analytical methods

Mercury determinations in soil and vegetable samples were carried out using two commercially available automated Hg analyzers. Direct measurements on solid samples were done using a TD-AAS analyzer, while the solutions obtained by wet digestion were analysed using a CV-AFS analyzer.

Limits of Detection (LOD) and Limit of Quantitation (LOQ) were calculated using the 3s criteria. For TD-AAS method, the SBR was determined for a concentration of 1400 $\mu g\ kg^{-1}$ Hg, while the relative standard deviation of the background (RSDB) was calculated from 10 successive measurements for the background signal, at analytical wavelength of 253.65 nm. The calculated value for detection limit was 1.2 $\mu g\ kg^{-1}$, using high sensitivity cell for measurement. Limit of quantitation was calculated as being 3.6 $\mu g\ kg^{-1}$ in solid samples (was considered to be three times the LOD). For CV-AFS method, the SBR was determined for a concentration in solution of 10 $\mu g\ L^{-1}$, while the RSDB was calculated from measurements of 10 independent black solutions at wavelength of 253.65 nm. The detection limit in liquid solution was 0.025 $\mu g\ L^{-1}$. For digestion of 1 g of sample, and dilution to 100 mL the detection limit in solid sample was calculated as being 2.5 $\mu g\ kg^{-1}$, while the limit of quantitation was 7.5 $\mu g\ kg^{-1}$.

Working ranges. In the Mercury Analyzer TD-AAS, the signal is measured in series by a high sensitivity cell followed by a low sensitivity cell. Using the two cells, a wider working range is obtained. For high sensitivity cell, the calibration curve was linear up to 50 ng Hg, and for low sensitivity cell, up to 600 ng Hg. If 10 mg sample is weighted and introduced in the system, the upper limit of working range is 600 mg kg^{-1}. Using the CV-AFS system the upper limit of working range is 250 $\mu g\ L^{-1}$ in liquid sample and 25 mg kg^{-1}, if 1g of solid sampled is digested.

According to the Romanian legislation the normal value for Hg concentration in soil is 100 µg kg^{-1}, the alert threshold for sensitive areas is 1000 µg kg^{-1}, and the intervention threshold 2000 µg kg^{-1}. All this values can be easily measured by TD-AAS and also by CV-AFS methods.

The **trueness** was studied by analyzing a Certified Reference Material in soil matrix, SRM 2709, and two CRMs in vegetable matrices, NCS 85 006 (Tomato) and IAEA-359 (Cabbage). The obtained results compared to certified values of mercury are presented in Table 1.

Table 1. Results of Mercury Determination in Various CRMs by TD-AAS and CV-AFS (mg kg^{-1})

CRM	*Certif. value*	*Found*	
		TD-AAS	*CV-AFS*
SRM 2709 soil	1.40±0.08	1.441±0.055	1.438±0.067
NCS ZC 85 006 tomato	0.14±0.022	0.152±0.006	0.144±0.014
IAEA-359 cabbage	0.013±0.002*	0.014±0.001	0.014±0.002

Values are reported with 95% confidence limit (n = 10).
* Information Values

For all analyzed CRMs: SRM 2709, NCS ZC 85006 and IAEA-359, good agreements of the results obtained by TD-AAS and CV-AFS with the certified values were obtained. No significant statistical differences were found at the significance level $p<0.05$ in all the cases.

Table 2. Mercury content in soil and vegetable samples measured by TD-AAS and CV-AFS ($\mu g\ kg^{-1}$), presented as confidence interval

Sample	**TD-AAS directly from solid sample**	**CV-AFS using microwave digestion**
Soil 1	1253±50	1143±79
Soil 2	653±28	644±47
Soil 3	983±32	985±63
Soil 4	2004±76	1998±97
Soil 5	1050±44	1071±65
Vegetable 1	19.7±1.0	18.8±2.2
Vegetable 2	53.4±3.4	55.8±5.2
Vegetable 3	4.92±0.42	4.96±0.58
Vegetable 4	20.8±1.5	20.0±1.8
Vegetable 5	4.60±0.44	4.32±0.38

Values are reported with 95% confidence limit (n = 10).

Precision of the method was evaluated in terms of repeatability. The repeatability was checked by carrying out 10 replicates on separate soil and vegetable subsamples, using the two methods: TD-AAS and CV-AFS, after microwave digestion. The results are presented as confidence interval, in Table 2.

In to compare the two sets of data obtained by the two methods, regression analysis and T-test for dependent samples were used. Using the T-test for dependent samples, and adopting the null hypothesis, no significant differences were found, the value of t_{calc} being lower than t_{tab} ($p=0.05$, $\nu=8$).

In the regression analysis, satisfactory agreement between the two sets of results was obtained, the correlation coefficient (r) and the slope (b) of the regression equation do not differ significantly from the unity and the intercept does not differ significantly from zero for a 95 % probability level considered within this study. The parameters of linear regression are presented in the Table 3.

Table 3. Linear regression parameters for a 95% confidence level for mercury determination in soil and vegetables by TD-AAS and CV-AFS

Regression analysis	Values
Intercept	-5.667±15.497
Slope	0.984±0.017
Correlation coefficient	0.9987

CONCLUSIONS

A comparison study of performance parameters of two methods used for Hg determination in solid samples: TD-AAS and wet digestion followed by CV-AFS was conducted. Detection limits in solid samples are lower in TD-AAS method, but in the same order of magnitude for the two methods. Working range of the both methods make possible the easily determination with a good accuracy of normal value, the alert threshold and the intervention threshold for Hg concentration in soil established by Romanian environmental legislation. The accuracy of methods was verified by the determination of mercury in the certified reference materials of soil and vegetables an no significant differences were found at the significance level $p<0.05$ in all the cases.

Differences between values measured in soil and vegetables by CV-AFS and TD-AAS were statistically evaluated using multiple regression and T-test for dependent samples. No significant differences between the two methods were found.

EXPERIMENTAL PART

Instrumentation

The direct measurements of mercury from solid samples were carried out using an Automated Direct Hg Analyzer Hydra-C (Teledyne Instruments, Leeman Labs, USA), based on thermal desorption atomic absorption spectrometry.

A Cold-Vapor Atomic Fluorescence Spectrometer Hydra-AF (Teledyne Instruments, Leeman Labs, USA) was used for mercury determination from digested samples.

A mortar grinder PM 100 Retsch (Germany) and a sieve shaker Fritsch Analysette 3 Spartan (Germany) were used for samples grinding and sieving.

A closed-vessel microwave system Berghof MWS-3+ with temperature control mode, (Eningen, Germany) was used for wet digestion.

Reagents, Standard Solutions and CRMs

Stock standard solutions of mercury (1000 mg L^{-1}) Merck (Darmstadt, Germany) was used for instruments calibration. For all dilutions ultrapure water (18 MΩ cm^{-1}) was obtained from a Millipore Direct Q3 (Millipore, France).

$SnCl_2 \cdot 2H_2O$ and 30% (v/v) HCl ultrapure both from Merck (Darmstadt, Germany) were used as reductant reagent for CV-AFS system.

Concentrated HNO_3 and HCl suprapure from Merck (Darmstadt, Germany) were used for samples digestion.

Soil CRM SRM 2709 San Joaquin Soil (New York, USA) and vegetable CRMs NCS ZC 85006 Tomato (Beijing, China) and IAEA-359 (Vienna, Austria) were used in the internal quality control of Hg determination.

Oxygen (4.5 quality) for Hydra-C Analyzer and Argon (5.0 quality) for Hydra-AF Analyzer supplying, both from Linde Gas SRL Cluj-Napoca, Romania were used.

Direct Hg determination in solid samples

Soil and vegetable samples were collected in Jully 2009 from Ferneziu, Baia Mare, NW of Romania. Ferneziu is a district of Baia Mare, situated in the north-east of it. This is located near to plant ROMPLUMB, whose activity has caused extensive pollution of the area with heavy metals [27-29].

Soils were sieved through a 2 mm sieve in order to eliminate stones and other materials extraneous to soil, and then stored in polyethylene bags for transport to the laboratory. The sieved soils were spread over a polyethylene sheet and air-dried at room temperature for one week. Samples were ground to a fine powder in a tungsten-carbide swing mill for 3 min and sieved through 100 micron mesh sieve. The fraction below 100 microns was further homogenised by mixing in a PVC drum for 1 h, then stored in brown glass bottles at room temperature until analysis. The vegetable samples were dried in oven, grounded using a grinder and sieved through 100 micron mesh sieve.

The Hydra-C Hg Analyzer includes a furnace module in that the sample is dried and decomposed at high temperature that assures a homogenous decomposition of sample. Decomposition products are carried to a catalyst by an oxygen flow, where sample oxidation is completed and halogens and nitrogen/sulphur oxides are trapped. The final decomposition products pass through a mercury amalgamator which collects Hg^0. By heating of amalgamation tube, mercury is released and carried to the atomic absorption spectrometer.

The transient signal is measured in series by two cells: a high sensitivity cell and a low sensitivity cell. The samples were weighted in nickel boats. Table 4 shows the instrument parameters employed for soils and vegetables.

Calibration was completed using aqueous standards prepared in 10% HNO_3. Working standards were blank, 0.1, and 1.0 ppm at six different injection weights. The calibration curve plots microabsorbance vs total mercury injected.

Table 4. Instrumental parameters of TD-AAS system

Parameter	*Setting*
Dry	300°C for 45 sec.
Decomposition	800°C for 150 sec.
Catalyst	600°C
Catalyst Wait Period	60 sec.
Gold Trap	700°C for 30 sec.
Measurement	90 sec.
Oxygen Flow Rate	300 mL min^{-1}

Determination of Hg by wet digestion and CV-AFS

Amounts of 1.000 g soil were digested with 10 ml *aqua regia* in closed PTFE containers of the microwave system. For vegetable, amounts of 1.000 g sample were digested with 6 ml concentrated nitric acid and 2 ml hydrogen peroxide in closed PTFE containers of the microwave system. After cooling to room temperature, the slurry was diluted to 100 ml with ultrapure water and then filtered under vacuum through a 0.45 µm cellulose membrane using the Sartorius vacuum filter equipment. At the end of this process, clear solutions were obtained. Digested samples were analyzed by CV-AFS method. Hydra AF is a continuous flow system where sample and reductant, in this case 2% $SnCl_2 \cdot 2H_2O$ in 3.6% (v/v) HCl ultrapure, are pumped into a gas/liquid separator. There the mercury in the sample is reduced to elemental mercury, which enters in the gas phase and is carried to the spectrometer. Instrument parameters are provided in the Table 5.

Table 5. Instrumental parameters of CV-AFS system

Parameter	*Setting*
Argon Flow Rate	700 mL min^{-1}
Sample Flow Rate	5 mL min^{-1}
Reductant Flow Rate	1 mL min^{-1}
Uptake time	20 sec.
Rinse time	60 sec.
Integration time	15 sec.

ACKNOWLEDGMENTS

The present investigations are supported by the Romanian Ministry of Education and Research, PNCDI II Program (Project CISPPA no. 52157/2008).

REFERENCES

1. M. Morita, J. Yoshinaga, J. Edmonds, *Pure & Appl. Chem*., **1998**, *70*, 1585.
2. F.M.M. Morel, A.M.L. Kraepiel, M. Amyot, *Annu. Rev. Ecol. Syst.,* **1998**, *29*, 543.
3. L.D. Hylander, M.E. Goodsite, *Sci. Total Environ*., **2006**, *638*, 352.
4. A.G. Bravo, J. Loizeau, L. Ancey, V. Ungureanu, J. Dominik, *Env. Sci. Pollut. Res.*, **2009**, *16-S1*, 66.
5. K. Leopold, M. Foulkes, P. Worsfold, *Anal. Chim. Acta*, **2010**, *663*, 127.
6. V.L. Dressler, E.M.M. Flores, D. Pozebon, L.E. Kaercher, *J. Anal. At. Spectrom.*, **2002**, *17*, 790.
7. P.R. Aranda, R.A. Gil, S. Moyano, I. De Vito, L.D. Martinez, *J. Hazard. Mater.*, **2009**, *161*, 1399.
8. H. Ashkenani, S. Dadfarnia, A.M.H. Shabani, A.A. Jaffari, A. Behjat, *J. Hazard. Mater.*, **2009**, *161*, 276.
9. M.J. Chang, R.L. McDaniel, J.D. Naworal, D.A. Self, *J. Anal. At. Spectrom.*, **2002**, *17*, 710.
10. I. López, S. Cuello, C. Camara, Y. Madrid, *Talanta*, **2010**, *82*, 594.
11. J.L. Rodrigues, S.S. de Souza, V.C. de Oliveira Souza, F. Barbosa, *Talanta*, **2010**, *80*, 1158.
12. A. Krata, E. Bulska, *Spectrochim*. *Acta Part B*, 2005, 60, 345
13. O.T. Butler, J.M. Cook, C.F. Harrington, S.J. Hill, J. Rieuwerts, D.L. Miles, *J. Anal. At. Spectrom*., **2007**, *22*, 187.
14. C. Lomonte, D. Gregory, A.J.M. Baker, S.D. Kolev, *Chemosphere*, **2008**, *72*, 1420.
15. F.X. Han, W.D. Patterson, Y. Xial, S.B.B. Maruthi, Y. Su, *Water Air Soil Pollut.,* **2006**, *170*, 161.
16. A. Collasiol, D. Pozebon, S.M. Maia, *Anal. Chim. Acta*, **2004**, *518*, 157.
17. A. Zierhut, K. Leopold, L. Harwardt, M. Schuster, *Talanta*, **2010**, *81*, 1529.
18. C. Fernandez, A.C.L. Conceicao, R. Rial-Otero, C. Vaz, J.L. Capelo, *Anal. Chem.*, **2006**, *78*, 2494.
19. Y. Li, C. Zheng, Q. Ma, L. Wu, C. Hu, X. Hou, *J. Anal. At. Spectrom.*, **2006**, *21*, 82.
20. K. Leopold, M. Foulkes, P.J. Worsfold, *Anal. Chem.*, **2009**, *81*, 3421.
21. Xun Li, Z. Wang, *Anal. Chim. Acta*, **2007**, *588*, 179.
22. Garcia-Sanchez, A. Murciego, E. Alvarez-Ayuso, I. Santa Regina, M.A. Rodriguez-Gonzalez, *J. Hazard. Mater*, **2009**, *168*, 1319.
23. M.J. Sierra, R. Millan, E. Esteban, *Food Chem. Toxicol.*, **2009**, *47*, 2761.
24. J. Canario, C. Vale, L. Poissant, M. Nogueira, M. Pilote, V. Branco, *J. Environ. Sci.*, **2010**, *22*, 1151.
25. A. Sahuquillo, G. Rauret, M. Bianchi, A. Rehnert, H. Muntau, *Anal. Bioanal. Chem.*, **2003**, *375*, 578.
26. *Teledyne Instruments Leeman Labs*, Hydra-C automated direct Hg Analyzer, Operations Manual.
27. E. Levei, M. Senila, C. Roman, M. Ponta, T. Frentiu, E. Cordos, *Studia UBB Chemia,* **2008**, *3*, 51.
28. M. Miclean, E. Levei, M. Senila, B. Abraham, C. Roman, E. Cordos, *Studia UBB Chemia,* **2008**, *3*, 57.
29. T. Frentiu, M. Ponta, E. Levei, E. Gheorghiu, M. Benea, E. Cordos, *Chem. Spec. Bioavailab.*, **2008**, *20*, 99.

STUDIA UBB CHEMIA, LVI, 1, 2011

ANALYSIS IN TERMS OF THE WILSON, NRTL (NON RANDON TWO LIQUIDS) AND UNIQUAC MODELS OF THE EXPERIMENTAL VAPOR - LIQUID EQUILIBRIUM DATA IN BINARY AND TERNARY SYSTEMS CONTAINING {(1*R*,4*S*)-(+)-FENCHONE, METHYL CHAVICOL AND *TRANS*-ANETHOLE}

IOAN BÂTIU[a]

ABSTRACT. The experimental vapor-liquid equilibrium data (VLE) in binary and ternary systems containing {(1R,4S)-(+)-fenchone, methyl chavicol and trans-anethole}, reported in previous papers, were correlated by means of Wilson, NRTL and UNIQUAC equation. The binary parameters of the corresponding models were calculated. The Wilson, NRTL and UNIQUAC parameters obtained from the isobaric T-x-y measurements at P=4000 Pa in binary systems were used to calculate the VLE data in the ternary system at the same pressure. A comparison with the experimental VLE data was done. The accuracy of the correlation is satisfactory. The Wilson, NRTL (Non Randon Two Liquids) and UNIQUAC models are the most useful models to correlate the experimental vapor – liquid equilibrium data.

Keywords: *Vapor - liquid equilibria, Terpenoids, Wilson, NRTL, UNIQUAC.*

INTRODUCTION

(1*R*,4*S*)-(+)-Fenchone [(1*R*,4*S*)-(+)-1,3,3-trimethylbicyclo[2.2.1]heptan-2-one], methyl chavicol [4-allyl-1-methoxybenzene] and *trans*-anethole [*trans*-1-methoxy-4(prop-1-en-1-yl) benzene] are the main components of the essential oil from the fruits of bitter fennel (*Foeniculum vulgare Mill, fam. Umbelliferae*). Both the raw essential oils and its isolated pure components are used in perfumery, cosmetics, pharmacy, aromatherapy and food industry [1].

Generally, essential oil components belong to the terpenoid class. Terpenoids are natural products comprising a large number of compounds with complicate chemical structures. Many essential oil components are monoterpenoids (C_{10}) and sesquiterpenoids (C_{15}), acyclic, monocyclic or bicyclic, saturated or unsaturated.

Batch distillation is an important unit operation frequently used for small scale production. Batch distillation is preferably to continuous distillation when small quantities of high value added chemicals and biochemicals need to separate. The main components of the essential oil are high value added chemicals.

[a] *Universitatea Babeş-Bolyai, Facultatea de Chimie şi Inginerie Chimică, Str. Kogălniceanu, Nr. 1, RO-400084 Cluj-Napoca, Romania, batiu@chem.ubbcluj.ro*

There are two basic mode of operating batch distillation column: constant reflux ration and variable product composition, respectively variable reflux ratio and constant key component composition. Also, there is the third mode of operation where neither the reflux ratio no the product composition is kept constant. This type of operation is possible in batch distillation and is known as the optimal reflux or the optimal control policy [2].

The second mode of operation is used to obtain the keys components of high purity. The main components separate function of their boiling points. The first key component distils at the lower temperature than the second key component. The third component distils at the higher temperature than the second key component. To reduce the energy consumes in the reboiler and to eliminate degradation of the key components it is necessary to adjust the pressure inside the batch distillation column.

Accurate isobaric vapor-liquid equilibrium data are necessary for the design and optimization of the batch distillation column. The literature [3, 4] is very poor in the vapor - liquid equilibrium data in the field of terpenoids.

The chemical structures of the main components of the essential oils of fennel are presented in Figure 1. The names of the components referred to in this paper are: (+)-fenchone, methyl chavicol and *trans*-anethole.

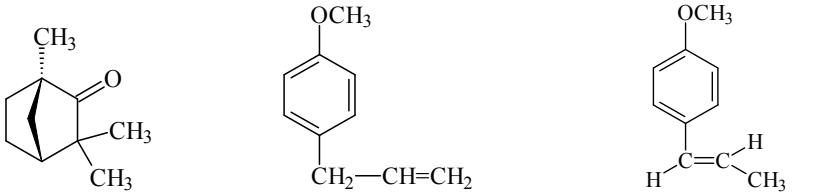

(1*R,*4*S*)-(+)-Fenchone Methyl chavicol t*rans*-Anethole

Figure 1. Chemical structure of (1*R,*4*S*)-(+)-fenchone, methyl chavicol and *trans*-anethole

RESULTS AND DISCUSSIONS

In the binary systems containing **{**(+)-fenchone, methyl chavicol and *trans*-anethole**}** the values of the experimental activity coefficients, γ_i are ranging from ca. 0.75 to ca. 1.08. The experimental fugacity coefficients, φ_i are very close to unity [5]. This means that a quasi-ideal behavior of the liquid phase and ideal behavior of the vapor phase can be considered.

Reduction of the experimental VLE data by non-electrolyte solutions models

The experimental VLE data of the all binary systems have been correlated by means of the Wilson [6], NRTL [7, 8] and UNIQUAC [9] activity coefficient, γ_i equations (eq. 1- 12).

The Wilson equations:

$$\ln\gamma_1 = -\ln\left(x_1 + \Lambda_{12}x_2\right) + x_2\left(\frac{\Lambda_{12}}{x_1 + \Lambda_{12}x_2} - \frac{\Lambda_{21}}{\Lambda_{21}x_1 + x_2}\right) \quad (1)$$

$$\ln\gamma_2 = -\ln\left(x_2 + \Lambda_{21}x_1\right) - x_1\left(\frac{\Lambda_{12}}{x_1 + \Lambda_{12}x_2} - \frac{\Lambda_{21}}{\Lambda_{21}x_1 + x_2}\right) \quad (2)$$

$$\Lambda_{12} = \frac{V_2^L}{V_1^L}\exp\left(-\frac{\lambda_{12} - \lambda_{11}}{RT}\right) \qquad \Lambda_{21} = \frac{V_1^L}{V_2^L}\exp\left(-\frac{\lambda_{21} - \lambda_{22}}{RT}\right) \quad (3)$$

where: γ_i is the activity coefficient of component *i*; x_i is the mole fraction of component *i*; in the liquid phase, V_i^L is the molar volume of component *i;* $(\Lambda_{12}, \Lambda_{21})$ and $\left[(\lambda_{12} - \lambda_{11}), (\lambda_{21} - \lambda_{22})\right]$ are two adjustable parameters of the Wilson model.

The NRTL equations

$$\ln\gamma_1 = x_2^2\left[\tau_{21}\left(\frac{G_{21}}{x_1 + x_2G_{21}}\right)^2 + \left(\frac{\tau_{12}G_{12}}{\left(x_2 + x_1G_{12}\right)^2}\right)\right] \quad (4)$$

$$\ln\gamma_2 = x_1^2\left[\tau_{12}\left(\frac{G_{12}}{x_2 + x_1G_{12}}\right)^2 + \left(\frac{\tau_{21}G_{21}}{\left(x_1 + x_2G_{21}\right)^2}\right)\right] \quad (5)$$

$$\tau_{12} = \frac{g_{12} - g_{22}}{RT};\tau_{21} = \frac{g_{21} - g_{11}}{RT}$$
$$G_{ij} = \exp(-\alpha_{ij}\tau_{ij});a_{ij} = (g_{ij} - g_{jj});\alpha_{ij} = \alpha_{ji} \quad (6)$$

where: γ_i is the activity coefficient of component *i*; x_i is the mole fraction of component *i*; in the liquid phase, (τ_{12}, τ_{21}) and $\left[(g_{12} - g_{22}), (g_{21} - g_{11})\right]$ are two adjustable parameters of the NRTL model; α is the third parameter of the NRTL model.

The UNIQUAC equations

The activity coefficient, γ_i is calculated as the sum of two terms (eq. 7):

$$\ln\gamma_i = \ln\gamma_i^C + \ln\gamma_i^R \quad (7)$$

where: the combinatorial part ($\ln\gamma_i^C$) accounts for entropic effects, while the residual part (γ_i^R) describes the interactions between the different groups from molecule. For a binary system:

$$\ln\gamma_1^{\,C} = \ln\frac{\phi_1}{x_1} + \left(\frac{z}{2}\right) q_1 \ln\frac{\theta_1}{\phi_1} + \phi_2\left(l_1 - \frac{r_1}{r_2} l_2\right) \tag{8}$$

$$\ln\gamma_2^{\,C} = \ln\frac{\phi_2}{x_2} + \left(\frac{z}{2}\right) q_2 \ln\frac{\theta_2}{\phi_2} + \phi_1\left(l_2 - \frac{r_2}{r_1} l_1\right) \tag{9}$$

$$\ln\gamma_1^{\,R} = -q_1 \ln\left(\theta_1 + \theta_2\tau_{21}\right) + \theta_2 q_1\left(\frac{\tau_{21}}{\theta_1 + \theta_2\tau_{21}} - \frac{\tau_{12}}{\theta_2 + \theta_1\tau_{12}}\right) \tag{10}$$

$$\ln\gamma_2^{\,R} = -q_2 \ln\left(\theta_1\tau_{12} + \theta_2\right) + \theta_1 q_2\left(\frac{\tau_{12}}{\theta_1\tau_{12} + \theta_2} - \frac{\tau_{21}}{\theta_1 + \theta_2\tau_{21}}\right) \tag{11}$$

$$\begin{gathered}\tau_{21} = \exp\left(-\frac{u_{21} - u_{11}}{RT}\right); \tau_{12} = \left(-\frac{u_{12} - u_{22}}{RT}\right) \\ l_1 = \left(\frac{z}{2}\right)\left(r_1 - q_1\right) - \left(r_1 - 1\right); l_2 = \left(\frac{z}{2}\right)\left(r_2 - q_2\right) - \left(r_2 - 1\right); z = 10 \\ \theta_i = \frac{q_i x_i}{\sum_j q_j x_j}; i = 1,2 \qquad \Phi_i = \frac{r_i x_i}{\sum_j r_j x_j}; i = 1,2\end{gathered} \tag{12}$$

where: x_i is the mole fraction of component i; in the liquid phase, θ_i is the area fraction of component i; Φ_i is the segment fraction of component i which is similar to volume fraction. Pure component parameters r, and q_i are measures of molecular van der Waals volumes and molecular surface area, respectively; (τ_{12}, τ_{21}) and $\left[\left(u_{12} - u_{22}\right), \left(u_{21} - u_{11}\right)\right]$ are two adjustable parameters of the UNIQUAC model.

The Wilson, NRTL and UNIQUAC adjustable parameters must be evaluated from experimental vapor-liquid equilibrium data. They are used to calculate vapor-liquid equilibrium data at other pressures than those from which were calculated. The pressure inside the batch distillation column is chosen taking into consideration the boiling points of the key components which successively separate at the top of the batch distillation column. Due to the high boiling points of the terpenoids the pressures inside the batch distillation column are adjusted at values smaller than the atmospheric pressure.

The Wilson, NRTL and UNIQUAC binary parameters were calculated from the isobaric *T-x-y* measurements and from the *T-P-x* measurements performed at the constant liquid phase compositions, x_i, respectively by minimizing the following objective functions (***S***):

- the maximum likelihood multimodel fitting method [10] (eq. 13)

$$S = \sum_{i=1}^{N} \left[\left(P_{ie} - P_{ic}\right)^2 / \sigma_P^2 + \left(T_{ie} - T_{ic}\right)^2 / \sigma_T^2 + \left(x_{ie} - x_{ic}\right)^2 / \sigma_x^2 + \left(y_{ie} - y_{ic}\right)^2 / \sigma_y^2 \right] \quad (13)$$

where: N is the number of experimental points, P_{ie}, T_{ie}, x_{ie} and y_{ie} are the experimental data and P_{ic}, T_{ic}, x_{ic} and y_{ic} are the corresponding calculated values for pressure, temperature, and the liquid and vapor phase compositions, respectively. In this paper, the standard deviation for pressure, temperature, and liquid and vapor phase compositions were set to σ_P = 60 Pa, σ_T = 0.05 K, σ_x = 0.003 mol. fr. and σ_y = 0.003 mol. fr., respectively.

- the boiling points condition, eq. (14):

$$S = \sum_{i=1}^{N} [1 - (P_1^0 / P) x_1 \gamma_1(A_{12}, A_{21}) - (P_2^0 / P) x_2 \gamma_2(A_{12}, A_{21})]_i = \min. \quad (14)$$

where: N is the number of experimental points, P is the total pressure, P_1^0 and P_2^0 are the vapor pressures of the pure components 1 and 2, A_{12} and A_{21} are, respectively, the binary parameters of the Wilson, NRTL and UNIQUAC models, γ_1 and γ_2 are the activity coefficients, x_1 and x_2 are the mole fractions of the pure components 1 and 2 in the liquid phase.

The purport of the calculated binary parameters, A_{12} and A_{21} (eq. 14) is: $[\Lambda_{12}, \Lambda_{21}]$ (Wilson); $[\tau_{12}, \tau_{21}]$ (NRTL) and $[(u_{12} - u_{22}), (u_{21} - u_{11})]$ (UNIQUAC), respectively B_{12} and B_{21} (eq. 13): $[(\lambda_{12} - \lambda_{11}), (\lambda_{21} - \lambda_{22})]$ (Wilson); $[(g_{12} - g_{22}), (g_{21} - g_{11})]$ (NRTL) and $[(u_{12} - u_{22}) / R, (u_{21} - u_{11}) / R]$ (UNIQUAC).

The binary parameters of each model (A_{12}, A_{21}, respectively B_{12}, B_{21}), the statistic criterion of the all experimental points (*global Ro*), the absolute mean deviations in the vapor phase compositions, *AMD(y)/*mol. fr. and in pressure, *AMD(P)*/Pa are reported in Tables 1 - 3.

It should be noted that the values of the binary parameters of the Wilson, NRTL and UNIQUAC models, for the same isobaric *T-x-y* measurements, are not identical when the two objective functions are used. Using the same objective function - the boiling points condition – the calculated binary parameters from the isobaric *T-x-y* measurements and from *T-P-x* measurements are different. This fact do not affect the VLE prediction if the binary parameters are used only to calculate VLE data at the same pressure or at others pressures. Consequently, the vapor phase compositions, y_i/mol. fr. at the pressure of P=4000 Pa and, respectively P=4270 Pa, calculated using the Wilson, NRTL and UNIQUAC binary parameters obtained from our *P-T-*x_i experimental data, are in good agreement with our *P-T-*x_i*-*y_i experimental data (Table 4). The absolute mean deviations, *AMD(y)* and *AMD(P)* for all the binary systems are less than 0.01 mol. fr. and respectively 100 Pa.

Table 1. Binary parameters of the Wilson, NRTL (α = 0.3) and UNIQUAC models for the binary systems containing (+)-fenchone, methyl chavicol and *trans*-anethole obtained from isobaric VLE data *T-x-y* (the object function - the maximum likelihood multimodel fitting method).

	Models								
	Wilson			NRTL (α=0.3)			UNIQUAC		
	B_{12}(*A_{12})	B_{21}(*A_{21})	Ro	B_{12}(*A_{12})	B_{21}(*A_{21})	Ro	B_{12}(*A_{12})	B_{21}(*A_{21})	Ro
Systems/Pressure									
(+)-fenchone (1) + methyl chavicol (2)/	-136.29	-143.99	0.804	-144.11	*-142.88	0.804	-3.784	-3.690	0.804
P=4000 Pa	*1.0198	*1.0725		*1.0471	*1.0467		*-31.412	*-30.664	
(+)-fenchone (1) + methyl chavicol (2)//	3421.28	-2021.48	0.712	21.18	24.17	0.799	0.395	0.543	0.798
P=4270 Pa	*0.3286	*1.9492		0.9932	*0.9923		*3.3240	*4.4874	
(+)-fenchone (1) + *trans* anethole (2)/	494.65	-506.98	1.003	-905.28	879.79	1.006	-1.396	-1.174	1.006
P=4000 Pa	*0.8439	*1.189		*1.329	*0.7585		*-11.634	*-9.7227	
methyl chavicol (1) + *trans* anethole (2)/	-1454.95	2272.61	0.783	3260.34	-2247.87	0.769	4.022	4.039	0.803
P=4000 Pa	*1.5695	*0.4972		*1.73669	*-0.8728		*33.4062	*33.5724	

Ro - the statistic criterion of the all experimental points (*global Ro*), $B_{12,}$ B_{21} - Wilson [$(\lambda_{12}-\lambda_{11})$, $(\lambda_{21}-\lambda_{22})$] and NRTL [$(g_{12}-g_{22})$, $(g_{21}-g_{11})$] parameters unit Jmol^{-1};UNIQUAC [$(u_{12}-u_{22})/R$,$(u_{21}-u_{11})/R$] parameter unit K; *$A_{12,}$ *A_{21} – Wilson and NRTL dimensionless parameters; UNIQUAC parameter unit Jmol^{-1}.

Table 2. Binary parameters of the Wilson, NRTL (α = 0.3) and UNIQUAC models for the binary systems containing (+)-fenchone, methyl chavicol and *trans*-anethole obtained from isobaric VLE data *T-x-y* (the object function - the boiling points condition).

	Models									
	Wilson			NRTL (α=0.3)			UNIQUAC			
	A_{12}	A_{21}	*AMD(y)*/ *AMD(P)*	A_{12}	A_{21}	*AMD(y)*/ *AMD(P)*	A_{12}	A_{21}	*AMD(P)*	*AMD(y)*
Systems/Pressure										
(+)-fenchone (1) + methyl chavicol (2)/ *P*=4000 Pa	1.3514	0.7041	01/ 45	-0.1946	0.2002	0.01/ 44	4.00	2.00		0.01/ 70
(+)-fenchone (1) + methyl chavicol (2)/ *P*=4270 Pa	0.1408	2.4010	0.0096/ 60	-1.1400	1.9458	0.0098/ 56	5.00	10.00		0.0089/ 100
(+)-fenchone (1) + *trans* anethole (2)/ *P*=4000 Pa	0.7713	1.3107	0.0066/ 71	0.1066	-0.1470	0.0067/ 72	1.00	0.50		0.0095/ 90
methyl chavicol (1) + *trans* anethole (2)/ *P*=4000 Pa	2.0602	0.2088	0.01/ 25	1.6781	-0.9667	0.01/ 26	5.00	1.00		0.002/ 117

Absolute mean deviations in the vapor phase composition, *AMD(y)*/mol. fr. and in pressure, *AMD(P)*/Pa, UNIQUAC parameter unit $Jmol^{-1}$.

Table 3. Binary parameters of the Wilson and NRTL (α = 0.3) and UNIQUAC models for the binary systems containing, (+)-fenchone, methyl chavicol and *trans*-anethole obtained from VLE data *T-P-x* (the object function - the boiling points condition)

	Models								
	Wilson			NRTL (α=0.3)			UNIQUAC		
	A_{12}	A_{21}	*AMD(P)*	A_{12}	A_{21}	*AMD(P)*	A_{12}	A_{21}	*AMD(P)*
Systems/Pressure									
(+)-fenchone (1) + methyl chavicol (2)	0.9898	1.0133	49	-0.6476	0.80038	53	0.50	1.00	57
(+)-fenchone (1) + *trans* anethole (2)	0.6707	1.5108	57	-0.5585	0.5574	58	-5.616	-7.955	54
methyl chavicol (1) + *trans* anethole (2)	2.1743	0.1585	40	19.258	20.2157	53	19.00	10.00	57

Absolute mean deviations in in pressure, *AMD(P)*/Pa, UNIQUAC parameter unit $Jmol^{-1}$.

Table 4. Comparison between experimental isobaric VLE data, *T-x-y* and calculated isobaric VLE data, *T-x-y* using the binary parameters of the Wilson, NRTL (α=0.3) and UNIQUAC models obtained from *T-P-x* measurements. Binary systems: (+)-fenchone + methyl chavicol (*P*=4000 Pa and, respectively *P*=4270 Pa*), (+)-fenchone + *trans*-anethole (*P*=4000 Pa) and methyl chavicol + *trans*-anethole (*P*=4000 Pa).

Models/Binary systems	*AMD(y)*/mol. fr.	*AMD(P)*/Pa
Wilson		
(+)-fenchone + methyl chavicol	0.010	45.00
*(+)-fenchone + methyl chavicol	0.005	100.00
(+)-fenchone + *trans*-anethole	0.009	78.00
methyl chavicol + *trans*-anethole	0.010	30.00
NRTL		
(+)-fenchone + methyl chavicol	0.010	45.00
*(+)-fenchone + methyl chavicol	0.004	100.00
(+)-fenchone + *trans*-anethole	0.009	80.00
methyl chavicol + *trans*-anethole	0.003	70.00
UNIQUAC		
(+)-fenchone + methyl chavicol	0.010	50.00
*(+)-fenchone + methyl chavicol	0.005	97.00
(+)-fenchone + *trans*-anethole	0.009	90.00
methyl chavicol + *trans*-anethole	0.010	60.00

AMD(y)/mol.fr. - Absolute mean deviations in the vapor phase*; AMD(P)*/Pa - Absolute mean deviations in pressure.

Calculated VLE data in the ternary system (+)-fenchone + methyl chavicol + trans-anethole using the binary parameters of the Wilson, NRTL and UNIQUAC models

The binary parameters of the Wilson, NRTL and UNIQUAC models, calculated from isobaric *T-x-y* data at *P*=4000 Pa, using the objective function (*S*) (eq. 13) - the maximum likelihood multimodel fitting method – have been used to calculate VLE data in the ternary system {(+)-fenchone + methyl chavicol + *trans*-anethole} (Table 5). The absolute mean deviations in the vapor phase composition, *AMD*(*y*)/mol.fr. are practicaly the same for all the models, while absolute mean deviation in temperature, *AMD*(*T*)/K exhibits rather small differences. We appreciate that, due to the same deviations in the vapor phase compositions and due to the small deviations in the temperature, the binary parameters of the Wilson, NRTL and UNIQUAC models present the same accuracy in calculating the vapor liquid equilibrium data.

In a previous paper [11] we checked the predictive capability of the neuronal networks in the ternary system {(+)-fenchone + methyl chavicol + *trans*-anethole}. The vapor phase compositions, y_i were calculated after training

the network considering the experimental liquid phase compositions, x_i of all the binary systems as inputs in each neuronal networks. The calculated vapor phase compositions, $y_{i,c}$ were compared with experimental vapor phase compositions, $y_{i,exp}$ at the liquid phase compositions, x_i of the ternary system. The absolute mean deviation in the vapor phase composition, *AMD*(*y*) was 0.01 mol. fr. (not calculated in paper) proving the better predictive capability of the VLE data using the neuronal network.

Table 5. Comparison between experimental isobaric VLE data *T-x-y* of the ternary system (+)-fenchone + methyl chavicol + *trans*-anethole and calculated isobaric VLE data *T-x-y* data using the binary parameters of the Wilson, NRTL (α=0.3) and UNIQUAC models obtained from the isobaric VLE data *T-x-y* of the binary systems at *P*=4000 Pa (objective function - the maximum likelihood multimodel fitting method).

Ternary system/Model	*AMD(y)*/mol. fr.	*AMD(T)*/K
(+)-fenchone + methyl chavicol + *trans*-anethole/		
Wilson	0.023	1.29
NRTL (α=0.3)	0.023	1.37
UNIQUAC	0.022	1.13

AMD(y)/mol.fr. - Absolute mean deviation in the vapor phase*;*
AMD(T)/K- Absolute mean deviation in temperature.

CONCLUSION

We have presented and correlated the experimental vapor-liquid equilibrium data (VLE) in binary and ternary systems containing **{**(1R,4S)**-**(+)-fenchone, methyl chavicol and trans-anethole} by means of Wilson, NRTL and UNIQUAC equation. The binary parameters of the corresponding models were calculated. The Wilson, NRTL and UNIQUAC parameters obtained from the isobaric *T-x-y* measurements at *P*=4000 Pa in systems which contain {(+)-fenchone, methyl chavicole and *trans*-anethole} were used to calculate the VLE data in the ternary system {(+)-fenchone + methyl chavicole + *trans*-anethole}. The calculated VLE data was compared with experimental VLE data. The accuracy is satisfactory.

EXPERIMENTAL SECTION

In previous papers [12, 13, 14] we reported experimental vapor-liquid equilibrium data for the following binary and ternary systems: {(+)-fenchone (1) + methyl chavicol (2)}; {(+)-fenchone (1) + *trans*-anethole (2)}; {methyl chavicol (1) + *trans*-anethole (2)}; {(+)-fenchone (1) + methyl chavicol(2) + *trans*-anethole (3)}.

A series of isobaric *T-x-y* measurements were performed at (4000±30) Pa [12, 13, 14]. Another series of *T-P-x* measurements were performed at three constant liquid-phase compositions [12, 13]. For the binary system (+)-fenchone (1) + methyl chavicol (2) a series of isobaric *T-x-y* measurements were performed at (4270±30) Pa [12].

VLE data in binary systems were found to be thermodynamically consistent as tested by using the maximum likelihood multimodel fitting method described by Panaitescu [10]. The thermodynamic consistency of the isobaric *T-x-y* measurements in the ternary system was checked using the McDermott-Ellis method [15] modified by Wisniak and Tamir [16].

REFERENCES

1. G. Radoias, A. Bosilcov, I. Batiu, "Odorante Naturale în Parfumeria Modernă" (Natural Fragrances in Modern Parfumery), Editura Casa Cărţii de Ştiinţă Cluj-Napoca, **2005**.
2. Urmila M. Diwekar, "BATCH DISTILLATION Simulation, Optimal Design and Control", Taylor & Francis Washington DC., **1995**.
3. I. Wichterle, J. Linek, Z. Wagner and H.V. Kehiaian, „Vapor-Liquid Equilibrium Bibliographic Database". 9th Ed. CD-ROM, ELDATA, Paris, France, **2004**.
4. I. Wichterle, J. Linek, Z. Wagner, J.-C. Fontaine, K. Sosnkowska-Kehiaian and H.V. Kehiaian, „Vapor-Liquid Equilibrium in Mixtures and Solutions. Landolt-Boernstein Numerical Data and Functional Relationships in Science and Technology, New Series". W. Martienssen, Ed.,Vol.IV/13A. Springer-Verlag, Berlin-Heidelberg, Germany, **2007**.
5. I. Bâtiu, Ph.D. Thesis "*Contributions to the separation process and high added value of the essential oils"* (*Contribuţii la tehnologia de separare şi valorificare superioară a uleiurilor volatile)* Cluj-Napoca, **1995**.
6. G.M. Wilson, *J. Am. Chem.Soc*., **1964**, *86*, 127.
7. H. Renon and J.M. Prausnitz, *A. I. Ch. E. Journal*, **1968**, *14*, 135.
8. H. Renon and J.M. Prausnitz, *Ind. and Eng. Chem. Process. Des. Dev*., **1969**, *8,* 413.
9. D.S. Abrams and J.M. Prausnitz, *A. I. Ch. Journal*, **1975**, *21*, 116.
10. G. M. Panaitescu, *Rev. Chim.*, **1982**, *33 (12),* 1110; *Ind. Chem. Eng*., **1985**, *25*, 68.
11. M. Cristea, I. Batiu, *Rev. Roumaine de Chimie*, **2005**, *50*,1009.
12. Batiu, E. Jurgea, G.M. Panaitescu, *ELDATA: Int. Electron. J. Phys.-Chem. Data,* **1995**, *1*, 39.
13. I. Batiu, G.M. Panaitescu, M. Peia, *ELDATA: Int. Electron. J. Phys.-Chem. Data*, **1995**, *1*, 117.
14. I. Batiu, *ELDATA: Int. Electron. J. Phys.-Chem. Data,* **1995**, *1*, 303.
15. C. Mc Dermott, S.R.M. Ellis, *Chem. Eng. Sci*., **1965**, *20*, 293.
16. J. Wisniak, A. Tamir, *J. Chem. Eng. Data,* **1977**, *22*, 253.

STUDIA UBB CHEMIA, LVI, 1, 2011

COMPARATIVE STUDY OF DIFFERENT OILS AND FATS IMPREGNATED THIN-LAYER CHROMATOGRAPHIC LAYERS FOR THE AMINO ACIDS LIPOPHILICITY ESTIMATION

DORINA CASONI[a]*, COSTEL SÂRBU[a]

ABSTRACT. The chromatographic behavior of a series of amino acids compounds was investigated on silica gel chromatographic plates impregnated with various oils (paraffin, olive, sunflower and corn) and different animal fats (pig, pullet, sheep and bear) using mixture of methanol-phosphate buffer in different proportions as mobile phase. The relevance of the obtained results was evaluated by a critical comparison of the lipophilicity parameters with different theoretical lipophilicity and solubility indices. Also some correlation matrices and diagrams were developed for a comparative evaluation of the studied impregnated stationary phases. The results indicated that the oils and some animal fats (pullet and bear) impregnated silica gel plates can be a good alternative in the field of chromatographic lipophilicity estimation of amino acids. In addition, the PCA methodology proved again to offer a realistic characterization of the impregnated plates, both from the retention mechanism and lipophilicity point of view.

***Keyords**: TLC, lipophilicity, amino acids, impregnated TLC plates*

INTRODUCTION

A problem that continues to evade researchers is a complete understanding of how proteins fold into their native state. The importance of this problem lies in the interactions of the individual amino acids that make up the tertiary structure. From the four types of involved interactions (hydrophobic/ lipophilic, electrostatic, hydrogen bonding, and van der Waals), the hydrophobic/ lipophilic ones are believed to be the most significant [1] giving considerable insights into how a protein is going to fold. A better understanding of these interactions can be provided by the lipophilicity concept that has been examined for many decades in absorption, permeability, toxicity and *in vivo* distribution of organic compounds [2]. Over the years, a vast amount of work has been done in measuring amino acids lipophilicity in order to find a universal amino acid lipophilicity scale that would be ideal in examining the interactions of

[a] *Babeş-Bolyai University, Faculty of Chemistry and Chemical Engineering, Arany Janos Str. No 11, RO-400028 Cluj Napoca, Romania, *casoni_dorina@yahoo.com*

transmembrane peptide segments with lipid bilayers (the natural environment of such peptides) [3]. The lipophilicity, defined as the tendency of a compound to partition between non-polar and aqueous environments, is most commonly measured directly using the shake-flask technique (when lipophilicity is expressed by log P_{ow} or log k_{ow} values) or indirectly using reversed-phase liquid chromatography (when lipophilicity is expressed by log k_w or R_{M0} values). Because of some advantages, nowadays the shake-flask technique has been successfully replaced by chromatographic methods such as high performance liquid chromatography RP-HPLC [4-7] and thin layer chromatography (RP-HPTLC) [8-10]. Concerning the experimental estimation of lipophilicity, the chromatographic procedures offer large possibilities, the combinations between both stationary and mobile phases being practically unlimited. Furthermore, the possibility of impregnation of the HPTLC plates with a series of oils more or less lipophilic may suggest the retention mechanism and may define them in the context of the strength of lipophilicity character. In addition, the chemical composition of vegetable oils (triglicerides, free fatty acids, lipophilic vitamins) and of animal fats (high concentration of saturated fatty acids and cholesterol) may enable their use as new realistic models for the mimesis of biological membranes. Over the years, the paraffin oil [11], silicon oil [12, 13] vegetable oils and different animal fats [14] were successfully used for the impregnation of TLC-plates in order to change the stationary phase characteristics and improve the chromatographic performance. Considering that the lipophilicity experiments are performed mainly to evidence in the *in vivo* behavior of active compounds, it may be appreciated that actually is still a need for continuously improvement of the stationary phases in order to offer a realistic alternative to the investigations of the biological membranes properties.

In the above considerations, the purpose of this work was to investigate the chromatographic behavior of the amino acids on different oils and fats impregnated TLC silica gel plates and evaluate their lipophilicity by using also different computed log P values.

THEORETICAL BACKGROUND

The most popular lipophilicity indices measured by RP-HPTLC are derived from the retention factor (R_F) according to Bate-Smith and Westall [15] equation:

$$R_M = \log (1/R_F - 1) \quad (1)$$

The direct influence of the organic modifier concentration from the mobile phase over the R_M values is described by the linear relationship expressed by the Soczewiński-Wachtmeister equation:

$$R_M = R_{M0} + bC \quad (2)$$

were R_{M0} is the extrapolated value to a zero fraction of organic component in the mobile phase composition, b is the regression slope frequently associated with the specific hydrophobic surface area of the stationary phase and C represents the volume fraction of the organic solvent in the mobile phase composition. Many studies suggested that the biological activity cannot be associated only with R_{M0} values, especially when polar interactions may take place. The specific hydrophobic surface area of the compounds plays an important role, a confirmed fact by the R_{M0} and b correlation [16]. Due to the advanced computerized procedures of multivariate data analysis, more recently, the Principal Component Analysis (PCA) has been successfully applied to develop new lipophilicity indices based on the R_F and R_M values [17,18]. The methodology based on PCA is not only more robust to different errors but it is also more informative. Usually, scatterplot of the first principal components produces charts in which the coordinates of the analytes reproduce the most variance of the input chromatographic data [19]. In addition, the first principal components can offer more efficient alternatives for characterization and ranking of investigated compounds and stationary phases including new insights into the chromatographic behavior of the compounds and the retention mechanism.

RESULTS AND DISCUSSION

For the studied amino acids, the use of different oils and animal fats impregnated silica gel plates revealed a linear dependence of retention parameters (R_M) with methanol fraction in the mobile phase, the regression determination coefficient being higher than 0.98 in all cases. These chromatographic regularities are supported by the profiles of retention parameters representation (Figure 1a and Figure 1b) that also illustrate high similarities in chromatographic behavior of compounds between oils impregnated stationary phases and also between animal fats impregnated stationary phases. This representation proves to be a very good way also for emphasizing the some specific interactions with stationary phases as it is highlighted for phenylalanine on RP-18W and oils impregnated plates (Figure 1a).

All the computed lipophilicity indices (Table 1 and Table 2) and the experimental ones (Table 3 and respectively Table 4) expressed by mean of retention parameters (mR_M), those obtained by extrapolation (R_{M0}), and respectively those obtained by applying PCA on the R_M values ($PC1/R_M$) show the histidine, arginine and respectively lysine as the most lipophilic compounds exception in case of RP-18W stationary phase were phenylalanine followed by tyrosine and respectively leucine seem to have the highest lipophilicity. The particular distinct behavior of lysine, arginine and histidine in case of the impregnated TLC stationary phases (Figure 2) might be attributed to possible specific (hydrogen bond or N-N pair) interactions with some of the principal constituents (lipids, triglycerides, fatty acids, lipoproteins) of the used fats and oils. These interactions seem to change the retention characteristics of the stationary phases and influence the behavior of the compounds containing

multiple amino groups. These considerations are very well supported by the new "lipophilicity charts" provided by the scores corresponding to R_M values onto the planes described by the first two principal components (PC1 and respectively PC2 obtained by applying principal component analysis to R_M values) (Figure 3). The applied methodology classified the specified compounds as outliers of the group in all cases.

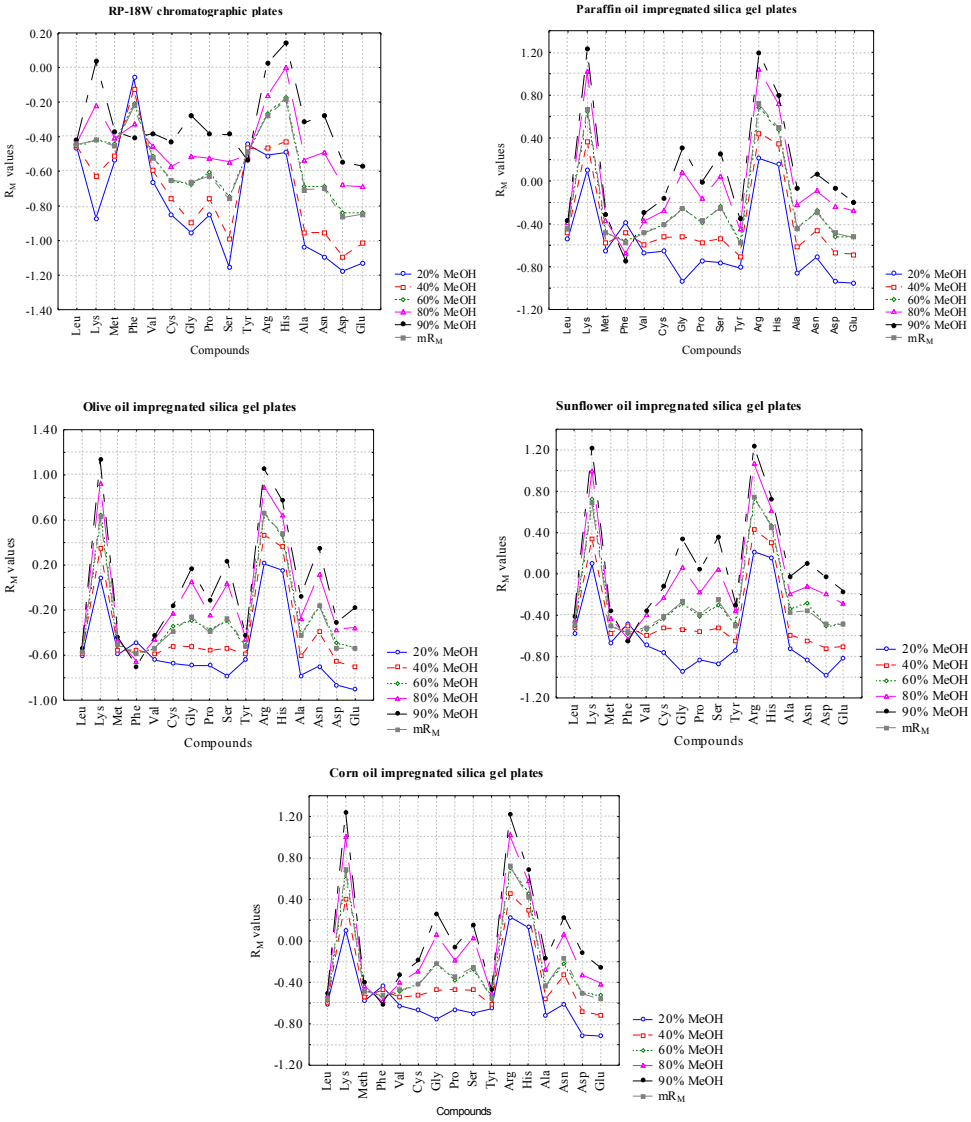

Figure 1a. Profiles of R_M values for all fraction of methanol on the investigated RP and oils impregnated stationary phases.

Table 1. The experimental log P_{ow} and computed lipophilicity descriptors of studied amino acids

No.	Abbr. Cpd.	Log P_{ow}	CLogP	ALOGP	MLOGP	ALOGPs	AC logP	AB/logP	miLogP	XLOGP2	XLOGP3
1	Leu	-1.52	-1.667	0.631	-1.677	-1.82	0.20	-1.77	-1.38	-1.39	-1.52
2	Lys	-3.05	-3.424	-0.680	-2.485	-3.76	-1.16	-2.00	-3.18	-2.95	-3.05
3	Met	-1.85	-1.730	-0.273	-2.055	-1.85	-0.43	-2.00	-2.24	-1.85	-1.87
4	Phe	-1.38	-1.556	0.955	-0.968	-1.35	0.21	-1.39	-1.23	-1.38	-1.52
5	Val	-2.26	-2.286	0.242	-2.055	-2.29	-2.26	-2.00	-1.91	-2.17	-2.26
6	Cys	-2.49	-2.347	-0.517	-2.918	-2.57	-0.94	-2.00	-2.71	-2.57	-2.49
7	Gly	-3.21	-3.210	-0.978	-3.437	-3.34	-1.47	-2.00	-2.55	-3.35	-3.21
8	Pro	-2.54	-2.413	-0.057	-0.232	-2.71	-0.35	-2.00	-1.7	-0.18	-2.50
9	Ser	-3.07	-2.811	-1.489	-3.726	-3.42	-2.02	-2.00	-3.67	-3.96	-3.07
10	Tyr	-2.26	-2.223	0.688	-1.508	-2.39	-0.09	-2.00	-1.71	-1.78	-2.26
11	Arg	-4.20	-3.517	-1.107	-2.934	-3.49	-2.41	-2.00	-3.63	-2.97	-4.20
12	His	-3.32	-4.367	-1.015	-3.057	-2.67	-1.64	-2.00	-3.00	-3.11	-3.56
13	Ala	-2.85	-3.124	-0.601	-2.918	-3.05	-1.06	-2.00	-2.69	-2.82	-2.96
14	Asn	-3.82	-3.544	-1.847	-3.762	-3.36	-2.49	-2.00	-2.81	-4.43	-3.41
15	Asp	-3.89	-2.411	-1.245	-3.356	-3.52	-1.95	-2.00	-3.52	-3.71	-2.76
16	Glu	-3.69	-2.694	-0.924	-2.946	-3.54	-1.49	-2.00	-3.25	-3.35	-3.69

Table 2. The solubility values for the studied amino acids

No.	Abbr. Cpd.	S_{exp} (mg/mL)	ALOGpS	AC logS
1	Leu	21.5	-0.27	-1.11
2	Lys	1000.0	-0.14	-0.79
3	Met	56.6	-0.80	-1.05
4	Phe	26.9	-1.60	-1.54
5	Val	58.5	0.26	-0.84
6	Cys	277.0	-0.72	-1.06
7	Gly	249.0	0.87	-0.03
8	Pro	162.0	0.50	-0.71
9	Ser	425.0	0.66	0.10
10	Tyr	0.5	-1.37	-1.25
11	Arg	182.0	-1.88	-0.16
12	His	45.6	-0.34	-0.38
13	Ala	164.0	0.70	-0.41
14	Asn	29.4	0.10	-0.23
15	Asp	5.4	0.03	-0.15
16	Glu	8.6	-0.26	-0.42

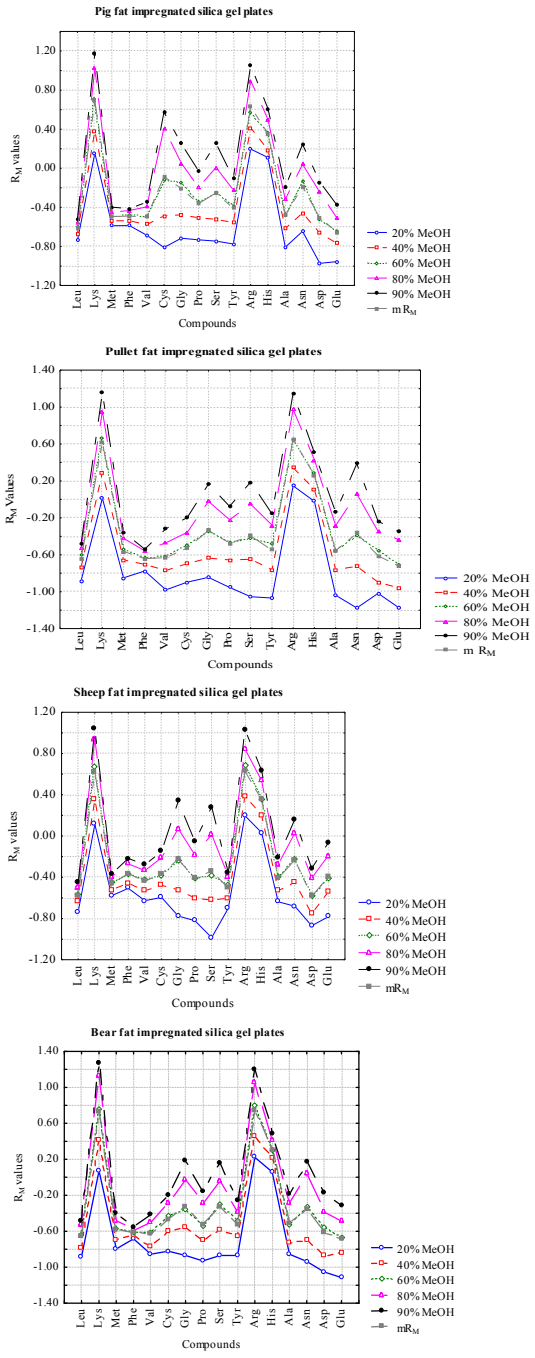

Figure 1b. Profiles of R_M values for all fraction of methanol on the investigated animal fats impregnated stationary phases.

Table 3. The lipophilicity indices of amino acids obtained on RP-18W and different oils impregnated TLC plates

No.	Abbr. Cpd.	RP-18W				Paraffin				Olive				Sunflower				Corn			
		mR_M	R_{M0}	b	PC1/ R_M	mR_M	R_{M0}	b	PC1/ R_M	mR_M	R_{M0}	b	PC1/ R_M	mR_M	R_{M0}	b	PC1/ R_M	mR_M	R_{M0}	b	PC1/ R_M
1	Leu	-0.445	-0.472	0.001	-0.341	-0.444	-0.581	0.002	0.534	-0.573	-0.636	0.001	0.790	-0.486	-0.617	0.002	0.627	-0.559	-0.651	0.002	0.791
2	Lys	-0.420	-0.930	0.012	-0.161	0.671	-0.256	0.016	-2.059	0.626	-0.229	0.015	-1.991	0.679	-0.259	0.016	-2.076	0.684	-0.234	0.016	-2.096
3	Met	-0.453	-0.554	0.002	-0.289	-0.483	-0.756	0.005	0.594	-0.512	-0.636	0.002	0.644	-0.506	-0.755	0.004	0.650	-0.483	-0.641	0.003	0.612
4	Phe	-0.226	-0.017	-0.005	-0.913	-0.569	-0.284	-0.005	0.881	-0.596	-0.427	-0.003	0.884	-0.567	-0.414	-0.003	0.852	-0.528	-0.386	-0.003	0.768
5	Val	-0.520	-0.681	0.004	-0.119	-0.486	-0.795	0.005	0.596	-0.531	-0.714	0.003	0.675	-0.515	-0.800	0.005	0.665	-0.477	-0.712	0.004	0.584
6	Cys	-0.654	-0.896	0.006	0.199	-0.408	-0.796	0.007	0.409	-0.384	-0.811	0.007	0.307	-0.417	-0.922	0.009	0.412	-0.420	-0.804	0.007	0.430
7	Gly	-0.663	-1.071	0.010	0.296	-0.262	-1.257	0.017	-0.015	-0.257	-0.994	0.013	-0.029	-0.271	-1.285	0.018	0.006	-0.225	-1.050	0.014	-0.082
8	Pro	-0.626	-0.897	0.007	0.155	-0.377	-0.973	0.010	0.305	-0.397	-0.870	0.008	0.327	-0.388	-1.063	0.012	0.321	-0.348	-0.823	0.008	0.255
9	Ser	-0.761	-1.214	0.011	0.527	-0.249	-1.088	0.015	-0.019	-0.270	-1.102	0.014	-0.020	-0.256	-1.220	0.017	-0.019	-0.251	-0.961	0.012	-0.004
10	Tyr	-0.490	-0.439	-0.001	-0.284	-0.577	-0.952	0.007	0.785	-0.527	-0.707	0.003	0.667	-0.506	-0.876	0.006	0.630	-0.558	-0.713	0.003	0.778
11	Arg	-0.278	-0.598	0.008	-0.551	0.715	-0.106	0.014	-2.137	0.658	-0.020	0.012	-2.029	0.736	-0.122	0.015	-2.190	0.726	-0.080	0.014	-2.164
12	His	-0.190	-0.586	0.009	-0.698	0.499	-0.046	0.009	-1.613	0.476	-0.006	0.008	-1.592	0.452	-0.016	0.008	-1.497	0.426	-0.022	0.008	-1.437
13	Ala	-0.705	-1.138	0.010	0.398	-0.441	-1.078	0.011	0.441	-0.432	-0.988	0.010	0.387	-0.372	-0.943	0.010	0.301	-0.427	-0.864	0.008	0.435
14	Asn	-0.700	-1.187	0.012	0.413	-0.295	-0.912	0.011	0.123	-0.154	-0.990	0.014	-0.274	-0.355	-1.130	0.013	0.230	-0.172	-0.836	0.012	-0.169
15	Asp	-0.867	-1.255	0.009	0.716	-0.489	-1.188	0.012	0.535	-0.539	-0.997	0.008	0.642	-0.488	-1.264	0.013	0.523	-0.509	-1.122	0.011	0.579
16	Glu	-0.849	-1.185	0.008	0.653	-0.530	-1.144	0.011	0.640	-0.536	-1.114	0.010	0.613	-0.489	-1.029	0.009	0.565	-0.564	-1.086	0.009	0.720

Table 4. The lipophilicity indices of amino acids obtained on different animal fats impregnated TLC plates

No.	Abbr. Cpd.	Pig				Pullet				Sheep				Bear			
		mR_M	R_{M0}	b	$PC1/R_M$	mR_M	R_{M0}	b	$PC1/R_M$	mR_M	R_{M0}	b	$PC1/R_M$	mR_M	R_{M0}	b	$PC1/R_M$
1	Leu	-0.615	-0.794	0.003	0.925	-0.644	-0.976	0.006	0.702	-0.574	-0.805	0.004	0.797	-0.663	-1.003	0.006	0.800
2	Lys	0.688	-0.173	0.015	-2.059	0.618	-0.331	0.016	-2.164	0.624	-0.166	0.014	-1.933	0.730	-0.283	0.018	-2.374
3	Met	-0.492	-0.642	0.003	0.657	-0.565	-0.961	0.007	0.521	-0.462	-0.640	0.003	0.555	-0.591	-0.913	0.006	0.642
4	Phe	-0.489	-0.635	0.003	0.652	-0.642	-0.843	0.004	0.711	-0.364	-0.609	0.004	0.329	-0.618	-0.719	0.002	0.728
5	Val	-0.499	-0.775	0.005	0.653	-0.632	-1.150	0.009	0.657	-0.438	-0.725	0.005	0.488	-0.631	-0.998	0.006	0.726
6	Cys	-0.085	-1.267	0.020	-0.402	-0.528	-1.083	0.010	0.422	-0.363	-0.735	0.006	0.309	-0.466	-0.970	0.009	0.343
7	Gly	-0.206	-0.998	0.014	-0.073	-0.337	-1.180	0.015	-0.030	-0.225	-1.122	0.016	-0.064	-0.325	-1.167	0.015	-0.009
8	Pro	-0.362	-0.912	0.010	0.308	-0.474	-1.179	0.012	0.288	-0.413	-1.041	0.011	0.388	-0.522	-1.148	0.011	0.452
9	Ser	-0.251	-1.056	0.014	0.023	-0.397	-1.382	0.017	0.092	-0.338	-1.351	0.018	0.172	-0.326	-1.161	0.014	-0.006
10	Tyr	-0.410	-0.949	0.009	0.416	-0.548	-1.295	0.013	0.451	-0.505	-0.798	0.005	0.635	-0.531	-1.015	0.008	0.489
11	Arg	0.628	-0.073	0.012	-1.901	0.653	-0.191	0.015	-2.235	0.629	-0.052	0.012	-1.929	0.749	-0.077	0.014	-2.392
12	His	0.355	-0.064	0.007	-1.256	0.261	-0.183	0.008	-1.323	0.353	-0.142	0.009	-1.293	0.295	-0.045	0.006	-1.326
13	Ala	-0.481	-0.972	0.009	0.581	-0.555	-1.287	0.013	0.468	-0.410	-0.768	0.006	0.415	-0.517	-1.088	0.010	0.448
14	Asn	-0.189	-0.917	0.013	-0.101	-0.368	-1.617	0.022	0.001	-0.233	-0.929	0.012	-0.021	-0.351	-1.302	0.016	0.035
15	Asp	-0.508	-1.179	0.012	0.612	-0.611	-1.291	0.012	0.594	-0.584	-1.052	0.008	0.788	-0.607	-1.324	0.012	0.631
16	Glu	-0.653	-1.103	0.008	0.966	-0.724	-1.429	0.012	0.846	-0.399	-0.971	0.010	0.364	-0.685	-1.314	0.011	0.814

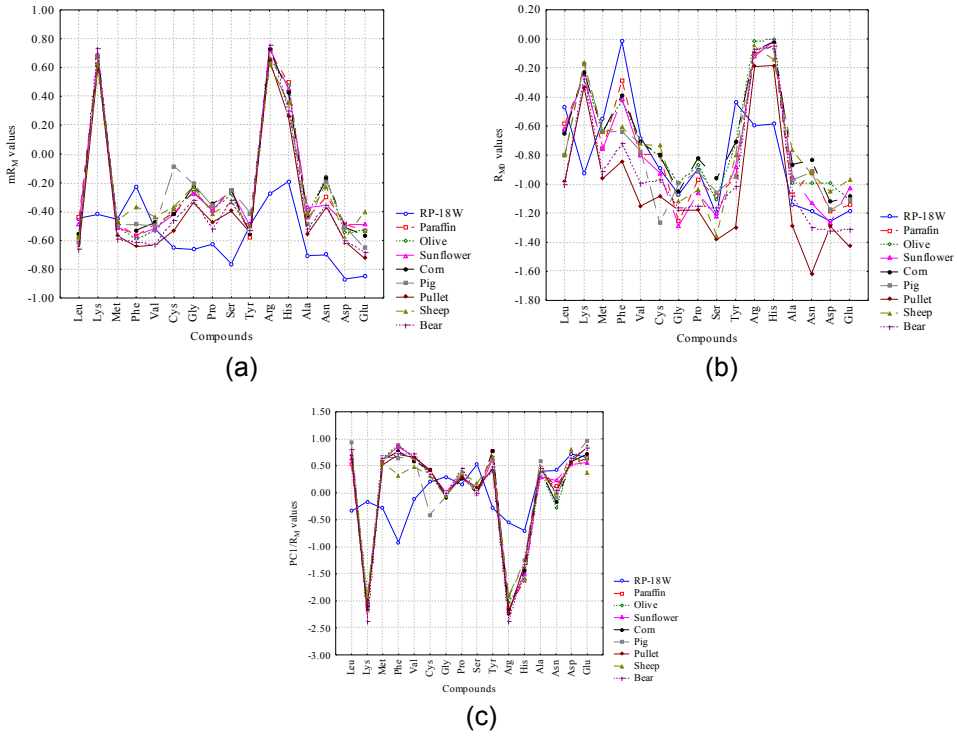

Figure 2. The correlation patterns of lipophilicity indices ((a) mR_M; (b) R_{M0}; (c) $PC1/R_M$) corresponding to the investigated stationary phases.

In order to evaluate the suitability of oils and animal fats impregnated plates as reversed phase for TLC determination of amino acids lipophilicity, the obtained results were compared with a series of theoretical lipophilicity indices. The correlation matrix of the experimental values versus theoretical ones is characterized by reasonable correlation coefficients (Table 5) in case of R_{M0} and b lipophilicity parameters in all cases. These correlations show in all cases that the specific surface area (b) of stationary phases is also a good alternative descriptor of amino acids lipophilicity. The mean (mR_M) of retention parameter R_M proved to be a good lipophilicity parameter only in case of RP-18 stationary phases ($r_{log\ Pow}$ = 0.92 and r_{ALOGPs} = 0.95) having low statistical significance in case of all impregnated stationary phases. By a careful examination, it can observe that in case of pig and respectively sheep fat impregnated stationary phases the correlations between theoretical and experimental lipophilicity indices are not statistically significant. Among the used different calculated lipophilicity indices, the best correlations were obtained with ALOGPs, log P_{ow} and respectively XLOGP3 values for all the RP-18W,

oils and respectively pullet and bear fat impregnated stationary phases. These correlations illustrate that the substructure of molecule and both topological and valence states of atoms have an important contribution on the lipophilicity of the amino acids compounds.

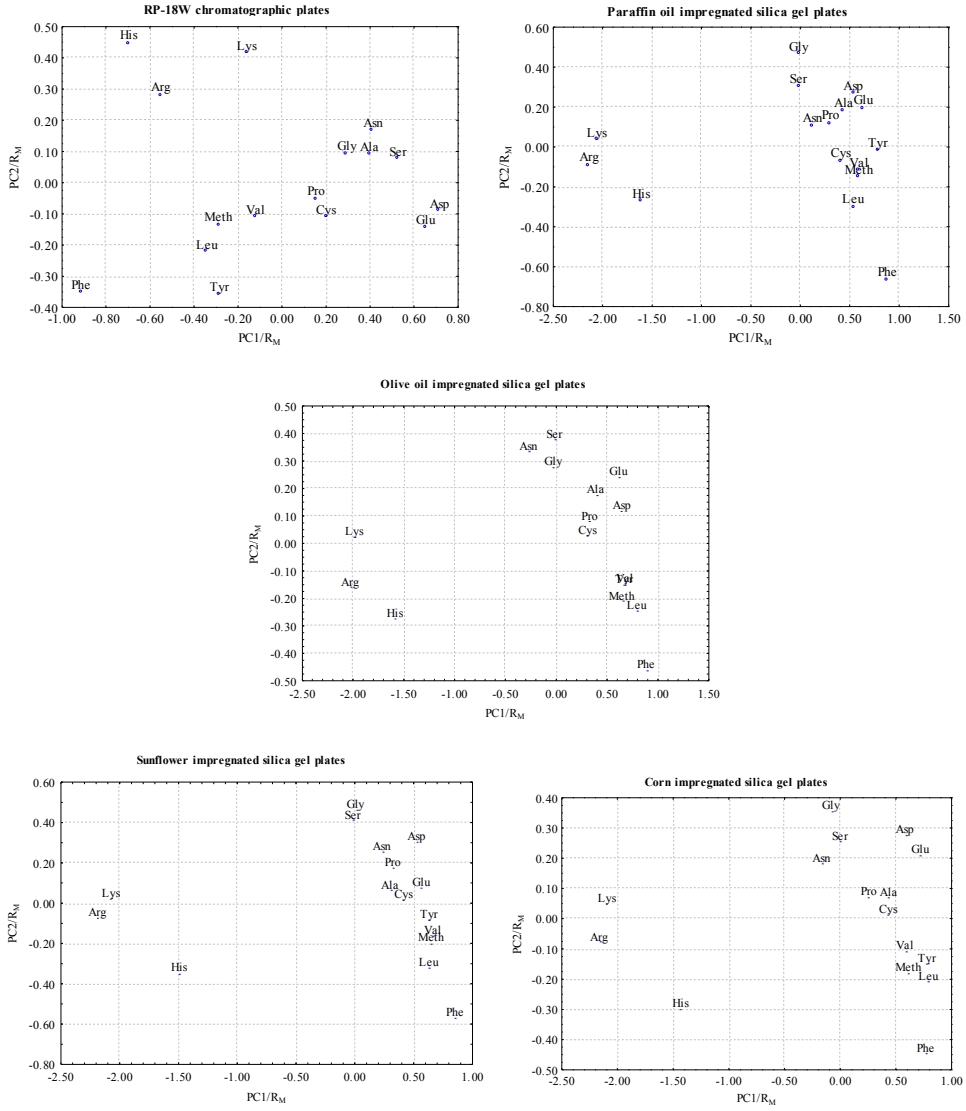

Figure 3a. Lipophilicity charts corresponding to R_M values in case of RP-18W and different oils impregnated silica gel plates.

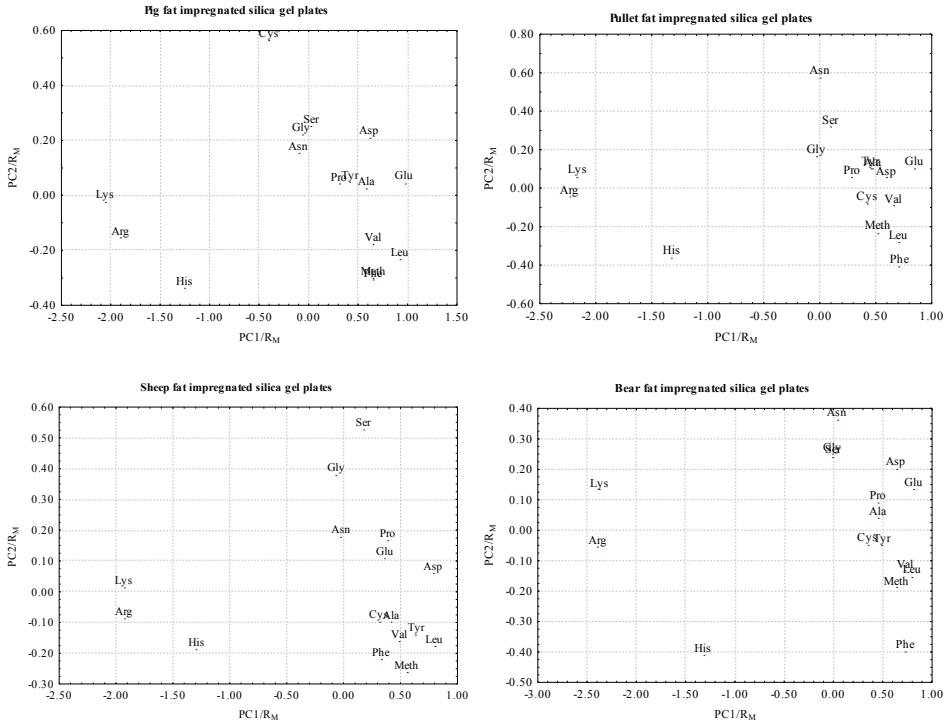

Figure 3b. Lipophilicity charts corresponding to R_M values in case of different animal fats impregnated silica gel plates.

Statistically significant correlations were obtained also with solubility parameter AClogS for almost of the used stationary phases, exception being in case of pig and pullet fat impregnated stationary phases (Table 5). These results indicate that newly ALOGPs version of log P computing module, based on associative neutral networks method, seems to cover, in the most efficiently way, the lipophilic character of amino acids.

Surprisingly, the log D and log P_n values, calculated by correctly adjust for charged parts of molecules are not so well statistically correlated with experimental lipophilicity indices in some cases. The best correlations coefficients are r = 0.91 and r = -0.93 between log P_n and $R_{M0RP18W}$ and respectively b_{RP-18W}; r = -0.91 between log P_n and b_{bear}; r = 0.92 and r = -0.94 between log D(IP) and $R_{M0RP18W}$ and respectively b_{RP-18W}; r = -0.92 between log D(IP) and b_{corn}; r = -0.92 between log D(IP) and b_{bear}.

These results are in good agreement with the properties of amino acids that having both amine and carboxylic acid functional groups, at a certain pH (known as isoelectric point -IP) they can have both positive and negative

charges (zwitterions). Amino acids can exist as zwitterions in polar solutions such as water [20] this fact being supported by the corelations of experimental lipophilicity indices and log D(IP) values in most of the cases. In order to getting more information concerning the similarities and differences between the oils and animal fats impregnated layers, PCA was applied to the matrices resulted by considering the experimental lipopilicity indices mR_M and respectively R_{M0} obtained for all RP-18W and impregnated stationary phases. According to the "lipophilicity space" obtained by 3D representation of scores corresponding to the first three principal components (Figure 4), the RP-18W stationary phases lipophilicity appears in the group of outliers including pig fat (in case of mR_M values) and respectively pullet fat (in case of R_{M0} values) impregnated silica gel plates. The different lipophilicity of RP-18W stationary phase is very well supported also by PC1/R_M representations provided by Figure 2.

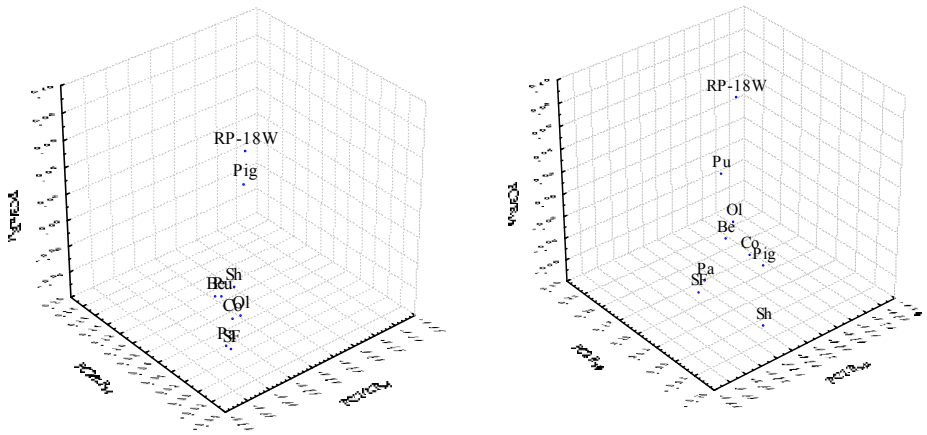

(a) (b)

Figure 4. The "lipophilicity space" provided by score plots of the first three principal components (PC1, PC2, PC3) obtained by applying PCA on the: (a) mR_M lipophilicity indices; (b) R_{M0} lipophilicity indices.

Table 5. The correlation between the theoretical and experimental lipophilicity indices of amino acids (Marked correlations are statistically significant)

Stationary Phases	Lipophilicity indices	log P_{ow}	log P_n	log D (pH=7)	log D (IP)	ClogP	ALOGP	MLOGP	ALOGPs	AC log P	miLogP	XLOGP2	XLOGP3	S_{exp}	ALOGpS	AClogS
RP-18W	mR_M	**0.92**	**0.83**	**0.89**	**0.84**	0.71	**0.83**	0.69	**0.95**	0.70	**0.89**	0.68	**0.86**	-0.29	-0.63	**-0.84**
	R_{M0}	**0.91**	**0.91**	**0.84**	**0.92**	**0.82**	**0.91**	0.74	**0.96**	0.76	**0.88**	0.72	**0.89**	-0.39	-0.76	**-0.92**
	b	**-0.86**	**-0.93**	-0.76	**-0.94**	**-0.87**	**-0.92**	-0.75	**-0.91**	-0.77	**-0.82**	-0.71	**-0.86**	0.46	0.83	**0.93**
	PC1/R_M	**-0.92**	**-0.87**	**-0.88**	**-0.88**	-0.75	**-0.87**	-0.72	**-0.96**	-0.73	**-0.89**	-0.70	**-0.88**	0.33	0.68	**0.88**
Paraffin Oil	mR_M	-0.41	-0.73	-0.28	-0.74	-0.66	-0.67	-0.52	-0.52	-0.49	-0.42	-0.45	-0.49	0.73	0.73	0.71
	R_{M0}	**0.82**	0.69	0.70	0.71	0.73	0.70	0.58	**0.91**	0.58	0.73	0.55	**0.82**	-0.32	-0.68	**-0.83**
	b	**-0.81**	**-0.81**	-0.66	**-0.82**	**-0.81**	-0.79	-0.64	**-0.91**	-0.63	-0.74	-0.60	**-0.83**	0.50	0.79	**0.91**
	PC1/R_M	0.52	0.79	0.38	0.79	0.72	0.73	0.57	0.63	0.55	0.51	0.50	0.58	-0.72	-0.78	-0.79
Olive Oil	mR_M	-0.54	-0.77	-0.32	-0.77	**-0.81**	-0.73	-0.57	-0.59	-0.55	-0.45	-0.55	-0.63	0.59	0.57	0.66
	R_{M0}	**0.91**	**0.88**	**0.84**	**0.89**	**0.83**	**0.86**	0.71	**0.98**	0.70	**0.86**	0.71	**0.94**	-0.41	-0.72	**-0.92**
	b	**-0.85**	**-0.93**	-0.71	**-0.94**	**-0.92**	**-0.91**	-0.73	**-0.92**	-0.72	-0.78	-0.72	**-0.91**	0.54	0.74	0.91
	PC1/R_M	0.60	**0.81**	0.39	**0.81**	**0.85**	0.78	0.61	0.65	0.59	0.51	0.59	0.69	-0.60	-0.61	-0.71
Sunflower oil	mR_M	-0.49	-0.73	-0.32	-0.74	-0.76	-0.68	-0.55	-0.65	-0.45	-0.51	-0.48	-0.62	0.80	0.76	0.77
	R_{M0}	**0.88**	**0.84**	0.73	**0.86**	0.78	**0.84**	0.65	**0.93**	0.69	0.78	0.64	**0.82**	-0.43	-0.70	**-0.90**
	b	**-0.82**	**-0.86**	-0.66	**-0.87**	**-0.82**	**-0.84**	-0.66	**-0.90**	-0.66	-0.75	-0.63	**-0.81**	0.56	0.76	**0.91**
	PC1/R_M	0.58	0.78	0.40	0.78	**0.80**	0.73	0.59	0.72	0.51	0.58	0.53	0.68	-0.77	-0.78	**-0.82**
Corn Oil	mR_M	-0.46	-0.71	-0.24	-0.71	-0.74	-0.68	-0.48	-0.51	-0.54	-0.37	-0.47	-0.53	0.61	0.62	0.65
	R_{M0}	**0.89**	0.78	**0.86**	0.79	0.68	0.77	0.67	**0.94**	0.64	**0.83**	0.64	**0.84**	-0.29	-0.66	**-0.86**

Stationary Phases	Lipophilicity indices	log P_{ow}	log P_n	log D (pH=7)	log D (IP)	ClogP	ALOGP	MLOGP	ALOGPs	AC log P	miLogP	XLOGP2	XLOGP3	S_{exp}	ALOGpS	AClogS
	b	**-0.87**	**-0.91**	-0.75	**-0.92**	**-0.85**	**-0.89**	-0.72	**-0.94**	-0.73	-0.78	-0.70	**-0.87**	0.50	0.78	**0.95**
	PC1/R_M	0.54	0.77	0.33	0.78	0.79	0.74	0.54	0.60	0.59	0.45	0.53	0.61	-0.61	-0.67	-0.72
Pig Fat	mR_M	-0.24	-0.45	-0.01	-0.45	-0.49	-0.44	-0.37	-0.28	-0.30	-0.25	-0.31	-0.30	0.66	0.21	0.28
	R_{M0}	0.69	0.60	0.64	0.60	0.51	0.58	0.57	0.75	0.42	0.72	0.52	0.65	-0.40	-0.31	-0.53
	b	-0.58	-0.63	-0.41	-0.64	-0.60	-0.61	-0.56	-0.63	-0.44	-0.59	-0.50	-0.58	0.62	0.32	0.49
	PC1/R_M	0.29	0.48	0.05	0.48	0.51	0.46	0.39	0.33	0.32	0.29	0.34	0.34	-0.67	-0.22	-0.30
Pullet Fat	mR_M	-0.33	-0.56	-0.07	-0.57	-0.64	-0.53	-0.38	-0.40	-0.34	-0.25	-0.35	-0.39	0.61	0.49	0.53
	R_{M0}	**0.86**	0.76	0.69	0.77	**0.83**	0.75	0.61	**0.85**	0.71	0.67	0.71	**0.86**	-0.08	-0.46	-0.72
	b	-0.79	**-0.82**	-0.55	**-0.82**	**-0.90**	-0.79	-0.62	**-0.82**	-0.69	-0.61	-0.68	**-0.82**	0.32	0.55	0.77
	PC1/R_M	0.38	0.60	0.12	0.60	0.68	0.57	0.41	0.45	0.38	0.29	0.39	0.44	-0.60	-0.51	-0.57
Sheep Fat	mR_M	-0.31	-0.48	-0.15	-0.48	-0.64	-0.47	-0.38	-0.33	-0.39	-0.21	-0.41	-0.53	0.48	0.31	0.38
	R_{M0}	0.65	0.71	0.60	0.73	0.56	0.66	0.47	0.77	0.50	0.64	0.48	0.64	-0.55	-0.67	**-0.83**
	b	-0.66	-0.77	-0.55	-0.78	-0.72	-0.73	-0.54	-0.76	-0.56	-0.61	-0.56	-0.73	0.64	0.66	**0.83**
	PC1/R_M	0.37	0.54	0.21	0.54	0.68	0.52	0.42	0.39	0.43	0.27	0.44	0.57	-0.52	-0.37	-0.45
Bear Fat	mR_M	-0.39	-0.63	-0.14	-0.62	-0.69	-0.60	-0.52	-0.48	-0.41	-0.38	-0.49	-0.48	0.71	0.46	0.57
	R_{M0}	**0.93**	**0.82**	**0.88**	**0.83**	0.73	0.79	0.59	**0.92**	0.68	0.73	0.63	**0.84**	-0.05	-0.62	**-0.83**
	b	**-0.88**	**-0.91**	**-0.71**	**-0.92**	**-0.88**	**-0.88**	-0.69	**-0.91**	-0.70	-0.72	-0.71	**-0.86**	0.40	0.68	**0.90**
	PC1/R_M	0.45	0.67	0.20	0.66	0.73	0.64	0.55	0.53	0.45	0.43	0.52	0.53	-0.69	-0.49	-0.61

CONCLUSIONS

Different lipophilicity indices of amino acids on RP-18W and different oils (paraffin, olive, sunflower and corn) and respectively animal fats (pig, pullet, sheep and bear) impregnated silica gel plates were determined using methanol-phosphate buffer as mobile phase. The obtained results indicate no significant differences, in terms of lipophilicity, between oils and animal fats impregnated silica gel plates. The correlation between the theoretical and chromatographic lipophilicity indices revealed that all oils and some animal fats (pullet and bear) can be a good alternative in the field of chromatographic lipophilicity estimation of amino acids. From the lipophilicity used indices, the R_{M0} and b values showed, in all cases, the most significant correlations. The PCA methodology proved to be again a useful tool that can offer a realistic characterization of impregnated plates, both from the retention mechanism and lipophilicity point of view.

EXPERIMENTAL SECTION

Chemicals

The amino acids Leucine (Leu), Lysine (Lys), Methionine (Met), Phenylalanine (Phe), Valine (Val), Cysteine (Cys), Glycine (Gly), Proline (Pro), Serine (Ser), Tyrosine (Tyr), Arginine (Arg), Histidine (His), Alanine (Ala), Asparagine (Asn), Aspartic acid (Asp) and Glutamic acid (Glu) of analytical grade were obtained from Merck or Fluka. Analytical - grade methanol was purchased from Chemical Company (Iasi, Romania). The oils (paraffin, olive, sunflower and corn) and fats (from pig, pullet, sheep and bear), used for silica gel plates impregnation, were from local markets. Ninhydrin, used as visualization reagent, was from Riedel-de Haen (Seelze, Germany).

Thin-Layer Chromatography

The chromatographic behavior of series of amino acids compounds was studied on eight different impregnated silica gel layers (10 x 20 cm) and on RP-18W (10 X 20 cm) chromatographic plates. The silica gel plates were impregnated with 10% of oil and respectively 5% of animal fat in diethyl ether solution in all cases, by ascendant development. The animal fats used as raw material were extracted from the natural membranes by heating to melting point followed by filtration. The standard solutions of amino acids (2 mg/mL) were prepared in methanol and respectively water and 2µL of which were applied manually, in duplicate, on the plate by means of a 10 µL Hamilton (Switzerland) microliter syringe. The mobile phase consisting of different proportions of methanol and phosphate buffer (pH = 7) mixture was from

20% to 90% methanol in all cases. Chromatography was performed in a normal developing chamber, saturated for 15 min at room temperature (~22 ^{0}C), by ascendant development and a developing distance of 8 cm in all cases. The amino acids were visualized by using a 0.2% ninhydrin solution prepared in ethanol and heating the plates at 110 ^{0}C for 10 minutes.

Computation of lipophilicity indices

Nowadays, it is well known that many software and internet modules are able to calculate different lipophilicity values applying various algorithms based on structural, atomistic, topological or electrotopological considerations. All of them require a previously molecule drawing that is usually performed by Hyperchem [21] and optimized using the MM+ molecular mechanics force field. On the basis of obtained geometry, software like Chem3D Ultra 8.0 [22] and Dragon Plus version 5.4 [23] calculate various lipophilicity descriptors. In the present study, one log P value (Clog P) was calculated by Chem3D Ultra and two log P values (MLOGP-Moriguchi method and ALOGP- Ghose-Crippen method) by the Dragon Plus software. Another five lipophilicity descriptors (ALOGPs, AC logP, miLogP, XLOGP2, XLOGP3) were computed by the internet module ALOGPS 2.1 [24]. By using this free internet module we derived also a set of three solubility indices (ALOGpS, AC logS, AB/logS). The experimental solubility in water and octanol-water partition coefficient of studied compounds are from the Human Metabolome Project database [25].

In some cases, the distribution coefficient (log D) of a compound at a given pH may be used as an appropriate descriptor for lipophilicity estimation. Because of the nature of studied compounds, we derived log D values for two different pH (log D (pH = 7) and log D (PI) -at isoelectric point of each compound) and respectively log P for nonionic species of amino acids (log P_n) by using a new and improved log P calculator available as free internet module Marvin Sketch 5.3.2 [26].

ACKNOWLEDGMENTS

The financial support of the Ministry of Education and Research of Romania (CNCSIS, IDEI 560/2007) is gratefully acknowledged.

REFERENCES

1. K.A. Dill, *Biochemistry*, **1990**, *29*, 7133.
2. W.P. Walter, M.A. Ajay Murcko, *Curr. Opin. Chem. Biol*., **1999**, *3*, 384.
3. K.M. Biswas, D.R. DeVido, J.G. Dorsey, *J. Chromatogr. A*, **2003**, *1000*, 637.
4. K. Valkó, *J. Chromatogr. A*, **2004**, *1037*, 299.

5. X. Liu, H. Tanaka, A. Yamauchi, B. Tesa, H. Chuman*, J. Chromatogr. A,* **2005**, *1091*, 51.
6. R.D/ Briciu, A. Kot-Wasik, J. Namiesnśik, C. Sârbu, *J. Sep. Sci*., **2009**, *32*, 2066.
7. D. Casoni, A. Kot-Wasik, J. Namiesnśik, C. Sârbu, *J. Chromatogr. A,* **2009**, *1216*, 2456.
8. T.L. Djakovic, C. Sârbu, N.U. Perišic-Janjic, *J. Planar Chromatogr.,* **2005**, *18*, 432.
9. A. Pyka, D. Gurak, *J. Planar Chromatogr*., **2007**, *20*, 373.
10. D. Casoni, C. Sârbu, *Chromatographia*, **2009**, *70*, 1277.
11. N.U. Perišić-Janjić, T.L. Djaković-Sekulić, *J. Planar Chromatogr*., **2006**, *19*, 438.
12. T. Csermely, G. Petroianu, K. Kuca, J. Fûrész, F. Darvas, Z. Gulyás, R. Laufer, H. Kalász, *J Planar Chromatogr*., **2007**, *20*, 39.
13. J. Kresta, P. Kastner, J. Klimeš, V. Klimešová, *J. Planar Chromatogr.,* **2005**, *18*, 450.
14. C. Sârbu, R.D. Briciu, *J. Liq. Chromatogr. Rel. Technol.,* **2010**, *33*, 1.
15. E.C. Bate-Smith, R.G. Westall, *Biochim. Biophys. Acta*, **1950**, *4*, 427.
16. S. Gocan, G. Cimpan, J. Comer. "Lipophilicity measurements by liquid chromatography. In: Grushka E., Grinberg N. (eds), "Advances in chromatography", Oxford, UK, **2005**, chapter 2.
17. C. Sârbu, S. Todor, *J. Planar Chromatogr*., **1998**, *11*, 123.
18. C. Sârbu, S. Todor, *J. Chromatogr. A*, **1998**, *822*, 263.
19. R. Kaliszan, *Chem. Rev*., **2007**, *107*, 3212.
20. M. Remko, B.M. Rode, *J. Phis. Chem. A,* **2006**, *110*, 1960.
21. HyperChem, release 7.5 for Windows, Molecular Modeling System; Hypercube, Inc. and Autodesk, Inc.
22. Chemical Structure Drawing Standard, ChemDraw Ultra 8.0.3 (2003) http://www.cambridgesoft.com.
23. Talete SRL, DRAGON for windows (software for molecular descriptor calculations). Version 5.4-2006. http://www. talete.mi.it.
24. Virtual Computational Chemistry Laboratory. http://www.vcclab.org/lab/alogps/.
25. The Human Metabolome Project. http://www.metabolomics.ca.
26. Marvin Sketch 5.3.2 free internet module. http://www.chemaxon.com.

STUDIA UBB CHEMIA, LVI, 1, 2011

SIMPLE AND COST-EFFECTIVE MULTISPECTRAL IMAGING SYSTEM FOR REFLECTANCE MEASUREMENT USING LED LIGHT SOURCES AND INTEGRATING SPHERE

EUGEN DARVASI[*,a] AND CSONGOR MÁTYÁS[a]

ABSTRACT. In the developed multispectral imaging system the sample is illuminated diffusely by monochromatic light with an integrating sphere. The LEDs are used for monochromatic light source. The wavelengths of the 11 different type of LEDs are uniformly covering the 380–670nm wavelength range. For calibration we use gray standards placed on the wall of the sphere. The detector is a digital camera. From the multispectral image after calibration the reflectance spectra of any region can be represented.

Keywords: *multispectral imaging, image spectroscopy, LED light source, integrating sphere, reflectance spectra*

INTRODUCTION

Multispectral imaging is an imaging technology that can simultaneously record spectral and spatial information of a sample. A multispectral image consists of a set of gray images, each registered at a desired narrow band of wavelengths [1]. New forms of multispectral imaging are now appearing: spectrum imaging (or a variant of it: image-spectroscopy), where a complete spectrum is recorded for each pixel in the image, combines the useful properties of spectroscopy and imaging [2]. Multispectral imaging techniques have been adopted in many disciplines, such as airborne remote sensing, environmental monitoring, medicine, military operations, factory automation and classification or sorting of agricultural products.

Traditionally the images are produced using the light filters or scanning spectrometers. Ariana et al. assembled an imaging system to capture images of apples under different lighting modes and seven band pass filters [3]. Lu used the spectral images of the backscattering of light at the apple surface, which were generated from a focused broadband beam, obtained for five selected spectral bands [4]. Guo, et al. used a multispectral imaging microscope for White Blood Cell segmentation. The apparatus consists of a microscope, a Liquid Crystal Tunable Filter (LCTF) device and a cooled monochrome Charge Coupled Device (CCD) camera [5]. Vila et al. described

[a] *Babeş-Bolyai University, Faculty of Chemistry and Chemical engineering, Str. Arany János 11, 400028 Cluj-Napoca, Romania, * edarvasi@chem.ubbcluj.ro*

a smart multispectral system for industrial, environmental and commercial applications. The system acquires multispectral images by means of an optical tunable filter (six spectral bands in the range 400–1000 nm) in front of a monochrome camera [6].

In the developed imaging system the sample is illuminated by monochromatic light of LEDs. Light emitting diodes (LEDs) were first used for chemical analysis three decades ago. They are finally making their appearance in commercial analytical systems and dedicated detectors [7]. Light emitting diodes (LEDs) are used very often in analytical photometric methods as extremely cheap, low-power, most energy-efficient sources of nearly monochromatic light. Pokrzywnicka et al. described a very simple photometric system dedicated for simultaneous photometric and fluorometric detection [8]. More advanced absorbance detectors are presented for chromatography [9–10] and for flow injection analysis [11–12]. Darvasi et Kekedy describe the application of integrating sphere in imaging spectroscopy [13]. The light source used was a halogen bulb. Commercial digital cameras were used to calculate the color characteristics of 16 pepper powder samples. No reference was found regarding the use of LEDs as monochromatic light sources in multispectral systems. Thus the system presented below can be considered a novelty.

In the present article the preliminary testing results are presented, with the possibility of future improvement.

The measuring system can have numerous applications in the non-invasive study of biological and geological samples.

RESULTS AND DISCUSSION

In the developed multispectral imaging system the sample is illuminated diffusely with an integrating sphere. Eleven images from different wavelength range of the visible region were acquired. The photo detector was a commercially available digital camera.

Measuring geometry

The diffuse measuring geometry was realized with the help of a self designed integrating sphere having a diameter of 106 mm. (Fig.1). The experiments were carried out with an integrating sphere cast in a gypsum cubic block, having a spherical inner hole. The inner wall was covered with $BaSO_4$ powder (used as white reference material for reflectance measurements). The sphere was provided with 2 apertures. The aperture on the upper side served as observation hole for camera. The second aperture, on the lower side, opposite to the first, served for sample introduction. The samples were put on a plastic support, and lifted upwards till they reached a tangential position to the sphere. The support also served as a light trap, as it is painted black in the inside. The trap has three holes, serving as the black reference.

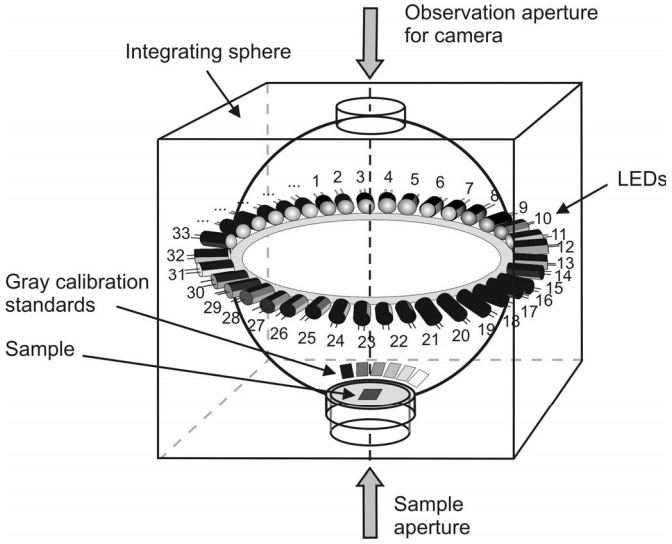

Figure 1. The multispectral imaging system with an integrating sphere and LEDs

Light sources

For lighting the integrating sphere eleven different type of LEDs were used. (Table 1)

Table 1. LEDs data

LED	Type	Color	Central wavelength (nm)	Position in sphere
a	L-7113UVC[1]	UV	400	1, 12, 23
b	L-53MBC[1]	Blue	430	2, 13, 24
c	OSUB5111A-RS[2]	Blue	471	3, 14, 25
d	OSBG5121A-TU[2]	Blue	505	4, 15, 26
e	OSPG5111P[2]	Green	525	5, 16, 27
f	L-53SGC[1]	Green	565	6, 17, 28
g	LL-503UGC-2BC[3]	Green	568	7, 18, 29
h	OSYL5111P[2]	Yelow	590	8, 19, 30
i	OSOR5111P[2]	Red	605	9, 20, 31
j	OSHR5111P[2]	Red	625	10, 21, 32
k	L-53SRC/F[1]	Red	660	11, 22, 33

Manufacturer: [1] Kingbright Elec. Co., Ltd, [2]Optosupply Ltd, [3]Lucky Light Co. Ltd

The wavelengths of the LEDs are uniformly covering the 380–670nm wavelength range (Fig.2).

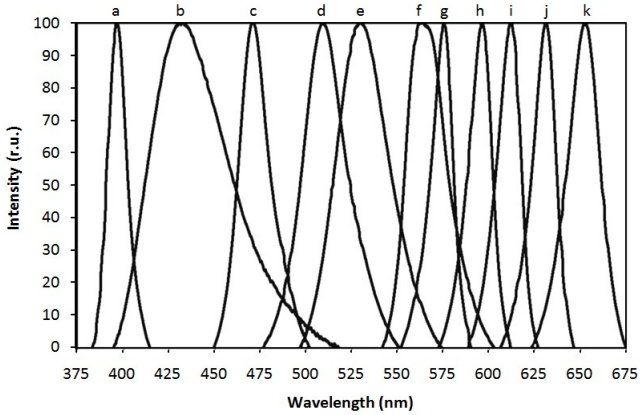

Figure 2. The spectral characteristics of the LEDs used

The LEDs were positioned in 11 groups of 3 inside the sphere along the great circle. The intensity of the LEDs was set individually for each group. The selection of the wavelength range was possible in 11 steps by turning on the appropriate LED groups. For operating the LED groups a switchboard was used.

Photo detector

The photo detector was a commercially available CS330 VGA digital camera (manufacturer: Intel Co). The exposure parameters of the camera were set manually (saturation, brightness, white balance and hue). The digital image was saved as .jpg file and transferred to the PC for processing. As reflectance reference 6 gray standards were photographed together with each sample.

CONCLUSIONS

The developed multispectral imaging system is simple and cost-effective. After calibrating the system the reflectance spectrum of any image detail can be determined based on the multispectral images of small samples. The measurement results are close to the values determined by a spectrophotometer. The system can be further developed by the use of a professional camera and specific software.

EXPERIMENTAL SECTION

Procedure

The samples were put on a plastic support, and lifted upwards till they reached a tangential position to the sphere. The sample was sequentially lit by the different wavelengths LED groups while images were recorded. 11 images of identical size were made, these containing the spectral information.

Calibration and data processing

Six gray calibration standards with known reflectance placed close to the lower aperture of the sphere were used for calibration (Fig.1). A function was established between the calibration standards in the sphere wall and the same standards in sample support (Fig.3a). The images of the samples were calibrated based on the corrected grey standards' value (Fig.3b). The image calibration curve was used for calculating the reflectance value of selected sample pixels. In order to attain the best signal/noise ratio in the case of a, b, LEDs B image parameters were used, in the case of c, d, e, f, g, h LEDs G image parameters were used and in the case of i, j, k LEDs R image parameters were used. The RGB image parameters were determined using ColorPilot 4.80.01v software package (Two Pilots™, USA, Germany, Russia). The rest of data processing and graphical representation was made in Microsoft Office Excel program.

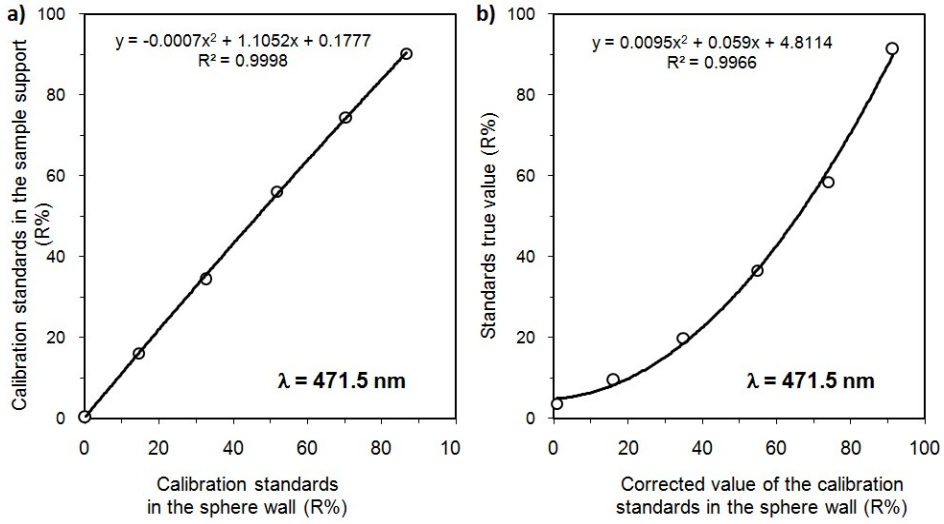

Figure 3. The calibration a) The calibration of the standards in the sphere wall; b) The image calibration curve

Measurements

The testing of the system was made using gray and colored standards (Macbeth ColorChecker). The reflectance value of the used standards was determined with a Jasco V-670-ILN725 spectrophotometer. These values were considered reference values in error determination. Figure 4 represents the measured and reference reflectance values of the 1 cm^2 surface gray standards depending on the wavelength.

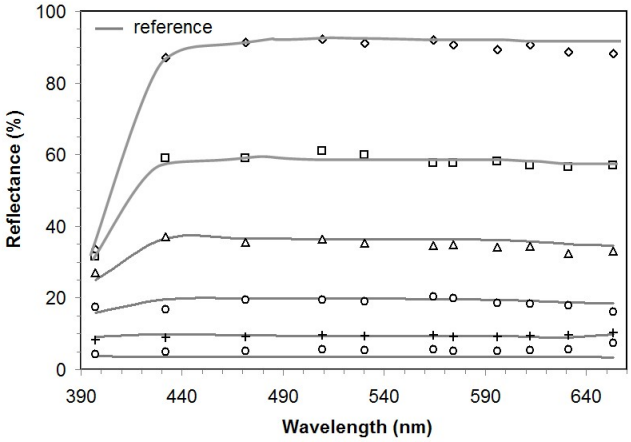

Figure 4. The measured and reference reflectance values of the gray standards

The measurement errors in the case of gray standards do not exceed 4%R. The measurement results of the colored samples are shown in figure 5. In the case of colored standards the measurement errors are greater than those of gray standards but they do not exceed 7%R.

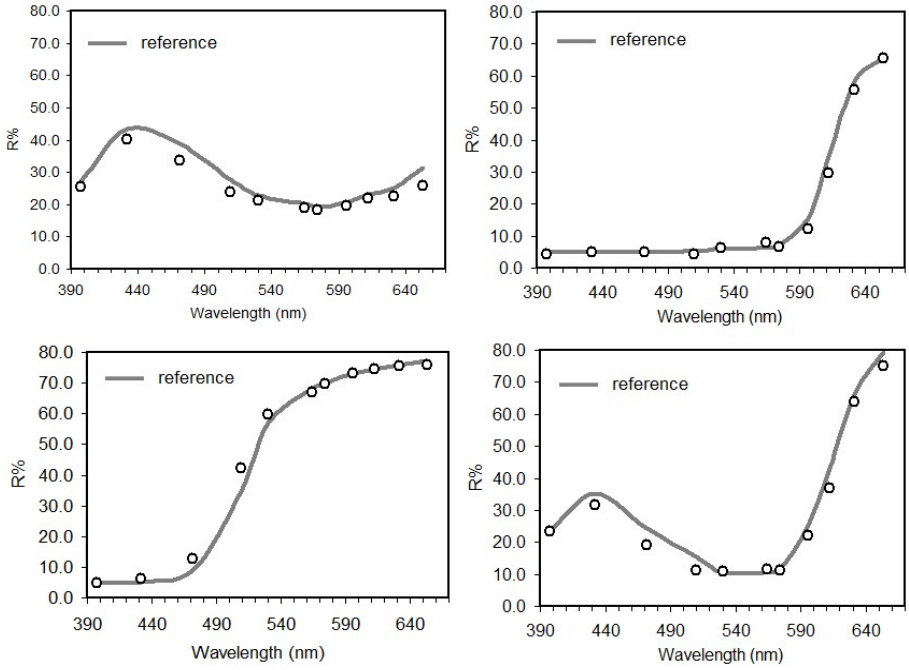

Figure 5. The measured and reference reflectance values of the color standards

REFERENCES

1. R.M. Levenson, C.C. Hoyt, *American Laboratory*, **2000**, November, 26–33.
2. N. Bonnet, *Micron,* **2004***, 35*, 635.
3. D. Ariana D.E. Guyer, B. Shrestha, *Computers and Electronics in Agriculture,* **2006**, *50*, 148.
4. R. Lu, *Postharvest Biology and Technology,* **2004**, *31*, 147.
5. N. Guo, L. Zeng, Q. Wu, *Computers in Biology and Medicine,* **2006**, *37*, 70.
6. J. Vila et al., *Real-Time Imaging,* **2005**, *11,* 85.
7. P.K. Dasgupta, I.-Y. Eom, K. J. Morris, J. Li, *Analytica Chimica Acta*, **2003**, *500*, 337.
8. M. Pokrzywnicka, R. Koncki, Ł. Tymecki, *Talanta,* **2010**, *82*, 422.
9. L. Barron, P.N. Nesterenko, D. Diamond, M. O'Toole, K.T. Lau, B. Paull, *Anal. Chim. Acta,* **2006**, *577*, 32.
10. L. Barron, M. O'Toole, D. Diamond, P.N. Nesterenko, B. Paull, *J. Chromatogr. A,* **2008**, *1213*, 31.
11. M. O'Toole, K.T. Lau, D. Diamond, *Talanta,* **2005**, *66*, 1340.
12. M. O'Toole, K.T. Lau, R. Shepherd, C. Slater, D. Diamond, *Anal. Chim. Acta*, **2007**, *597*, 290.
13. E. Darvasi, L. Kekedy N., *Studia UBB Chemia,* **2009**, 54(3), 49.

STUDIA UBB CHEMIA, LVI, 1, 2011

BIODIESEL PRODUCTION FROM SUNFLOWER OIL WITH *CANDIDA ANTARCTICA* LIPASE B

GOG ADRIANA[a], MIRCEA CHINTOANU[a], MARIUS ROMAN[a], EMIL LUCA[b], PAIZS CSABA[c], FLORIN-DAN IRIMIE[c]

ABSTRACT. In this paper, we have evaluated the efficacy of an enzymatic method for the transesterification process of sunflower oil with methanol in the presence of *tert*-butanol. *tert*-Butanol was used as the reaction medium to eliminate both negative effect caused by excessive methanol and glycerol resulted as by product. Using the following reaction conditions: 1% Novozym 435 based on oil weight, methanol / oil molar ratio 6:1, *tert*-butanol/ oil volume ratio 6:1, the FAME reached its maximum level after 3h, with a value of 78.6% (m/m).

Keywords: *biodiesel, tert-Butanol, Novozym 435, enzymatic transesterification*

INTRODUCTION

Biodiesel, having a chemical structure of fatty acid alkyl esters (usually fatty acid methyl ester, FAME), has recently become an alternative to petroleum-based diesel fuel. It is renewable, biodegradable, non-inflammable, and non-toxic. It also has a favorable combustion emission profile, producing much less carbon monoxide, sulphur dioxide and unburned hydrocarbons than petroleum-based diesel [1]. Biodiesel is derived from abundant and renewable substances such as vegetable oils, animal fats, algae, industrial acid oil, waste cooking oil etc. In conventional chemical processing, synthesis of these esters is achieved by an alkaline esterification reaction encountered with lowered selectivity, leading to undesirable side reactions. Moreover, the process is not environmentally friendly. The disadvantages caused by chemical catalysts are largely prevented by the lipases which allow mild reaction conditions and easy recovery of glycerol without purification, avoiding in this way the formation of chemical waste [2, 3]. Because of the high energy cost of the conventional chemical process and additional purification step of glycerol, application of lipase in

[a] *INCDO-INOE 2000 Research Institute for Analytical Instrumentation - ICIA, 67 Donath St., 400293 Cluj-Napoca, Romania*
[b] *University of Agricultural Sciences and Veterinary Medicine Cluj-Napoca, Faculty of Horticulture, 3 Calea Manastur St., 400372 Cluj-Napoca, Romania*
[c] *Babes-Bolyai University Cluj-Napoca, Faculty of Chemistry and Chemical Engineering, 11 Arany Janos St., 400028 Cluj-Napoca, Romania*

the oleo chemical industry has become more attractive. Although enzymatic approaches have become more and more attractive, their use at industrial scale has not been realized yet, due to the relatively high price of lipases and their short operational life caused by the negative effects of excessive methanol and by-product glycerol [4, 5].

It has been demonstrated that more than 1/2 molar equivalent methanol are insoluble in vegetable oils and the immobilized lipases are easily inactivated by contacting with insoluble methanol existing as drops in the oils [6]. For example, Shimada et al. [7] found that immobilized *Candida antarctica* lipase was inactivated in a mixture containing greater than 1.5 molar equivalents of methanol in oil when using a solvent-free system. Stepwise addition of methanol or using some hydrophobic solvents such as *n*-hexane or petroleum ether as reaction media have been proposed to reduce the negative effect of methanol on lipase activity [8, 9]. But in another study, although n-hexane was used as reaction medium for the methanolysis of salad oil with *Candida* sp., Nie et al. [10] found that the lipase was denatured when methanol/oil molar ratio exceeded 1:1. This was caused by methanol poor solubility in this hydrophobic solvent, so the negative effects of methanol on lipase activity and stability could not be eliminated. Several hydrophilic organic solvents have also been tested for lipase-catalyzed biodiesel production and proved much less useful, as strongly interact with the essential water layer coating enzyme molecules [4, 11]. Other studies reported that when using hydrophilic 1,4-dioxane and *tert*-butanol the enzymatic process was improved [4, 9, 11-13].

In our study, we conducted the enzyme-catalyzed methanolysis of sunflower oil using Novozym 435, a well-known lipase that facilitates reactions between a wide variety of substrates and a remarkably heat-tolerant enzyme. A moderate polar solvent, *tert*-butanol, was adopted as reaction medium for lipase-catalyzed methanolysis of sunflower oil in order to eliminate the negative effect caused by methanol and glycerol on lipase activity [11, 12].

RESULTS AND DISCUSSION

In this study, *tert*-butanol was used as reaction medium for lipase-catalyzed methanolysis of sunflower oil because it dissolves both methanol and glycerol and is not a substrate for lipases (lipases do not act on tertiary alcohols). Moreover, *tert*-butanol is a non-toxic solvent of relative low cost.

The influence of *tert*-butanol was examined for the enzymatic methanolysis of sunflower oil and the result was shown in Figure 1. Total methyl ester content was very low in solvent-free system due to the toxicity of excessive methanol on lipase activity. But when *tert*-butanol was added into the reaction mixture the ester content significantly increased. The highest content of methyl esters of 70% was obtained when the volume ratio of *tert*-butanol/oil reached 6:1 therefore this ratio was used for further studies.

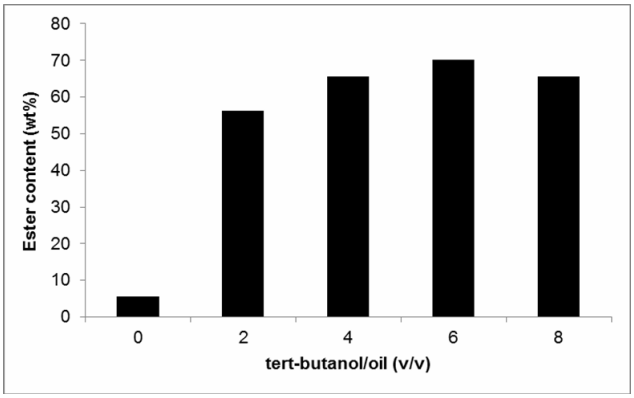

Figure 1. Effect of *tert*-butanol quantity on the methanolysis of sunflower oil. Reaction conditions: methanol/oil molar ratio 6:1, 10% Novozym 435 based on oil weight, 8 h reaction time.

Effect of molar ratio of methanol/oil was studied and the results are shown in the Figure 2. It can be seen that total methyl ester content increased with the increasing of methanol/oil molar ratio and that the presence of *tert*-butanol as solvent allowed the use of methanol in high excess without lipase deactivation.

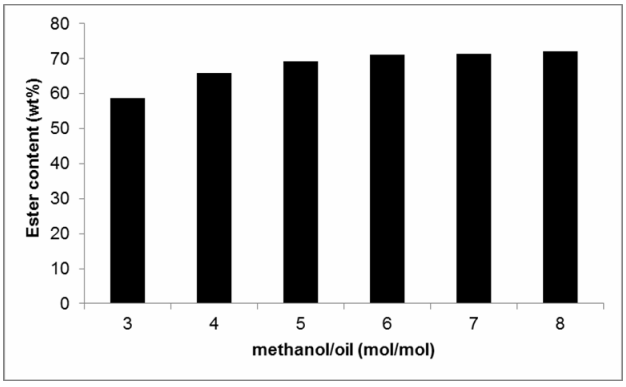

Figure 2. Effect of methanol to oil molar ratio on the methanolysis of sunflower oil. Reaction conditions: 10% Novozym 435 based on oil weight, *tert*-butanol/ oil volume ratio 6:1, 8 h reaction time.

The effect of Novozym 435 dosage on the methanolysis of sunflower oil was shown in Figure 3. The methyl ester content was increased by increasing lipase dosage and when lipase dosage reached 10%, a content of 72% could be given at 8 h. Further increase of lipase dosage did not have that much effect on ester content.

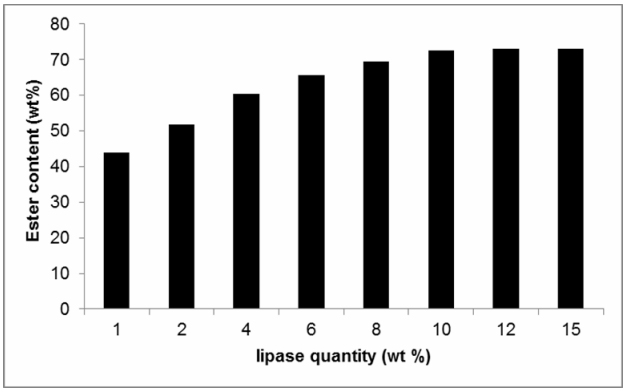

Figure 3. Effect of lipase dosage on the methanolysis of sunflower oil. Reaction conditions: methanol /oil molar ratio 6:1, *tert*-butanol/oil volume ratio 6:1, 8 h reaction time.

These optimized conditions (10% Novozym 435 based on oil weight, *tert*-butanol/oil volume ratio 6:1, methanol/oil molar ratio 6:1) were further used for the enzymatic methanolysis of sunflower oil for 12 h reaction time. The results obtained are summarized in Table 1 and the time course methanolysis of sunflower oil was shown in Figure 4.

Table 2. Fatty acid methyl ester content resulted for the enzymatic methanolysis of sunflower oil using *tert*-butanol as reaction medium

Time [min]	Total methyl ester content [wt %]
15	9.19
30	34.78
45	50.21
60	56.14
90	63.76
180	78.60
360	77.06
480	76.71
540	70.74
660	55.40

It was observed that the FAME content reached its maximum after 3h, with a value of 78.6% (m/m). After reaching this point the FAMEs content was maintained almost constant for another 2h and in the end a decrease of FAMEs content was observed.

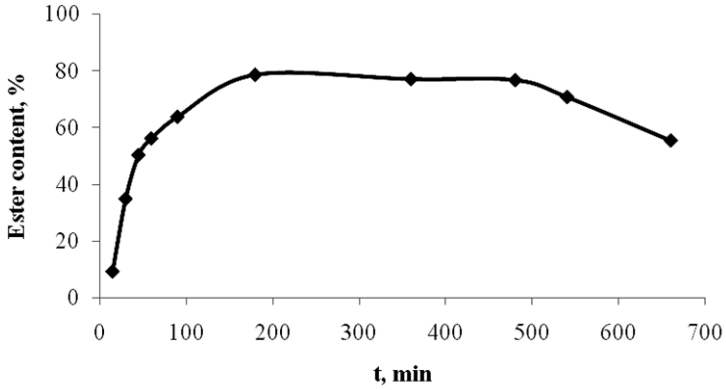

Figure 1. Time course methanolysis of sunflower oil. Reaction conditions: 10 % Novozym 435 based on oil weight; methanol /oil molar ratio 6:1; tert-butanol/ oil volume ratio 6:1

This decrease was caused by the mechanical disruption of the enzyme due to the physical agitation of the reaction mixture with the magnetic stirrer. Thus, the particles resulted from the enzyme and from the carrier determined a dilution effect for the samples withdrawn after 8h. The results obtained showed a high activity of the lipase even in the presence of methanol in high excess and this high activity was maintained because of the *tert*-butanol used as reaction medium. However, disruption of the enzyme carrier by the physical agitation force may not promise the use of immobilized lipase for a long period of time. Thus, in case of immobilized lipases the solution would be the use of mechanical shakers instead of magnetic stirrers, or other reactor configurations such as packed-bed reactor.

The widely accepted mechanism for triglycerides alcoholysis follows a Ping-Pong Bi Bi mechanism, as each product is released between addition of the substrates [14-16]. When fitting to experimental results, simplifications such as Michaelis–Menten kinetics can also be applied [17]. The effect of substrate concentration on the initial reaction rate (V) catalyzed by the Novozym 435 lipase was studied using sunflower oil as the substrate. Thus, using Michaelis–Menten model, Michaelis constant (K_m) and the maximum reaction rate (V_{max}) of Novozym 435 were calculated from the Lineweaver-Burk plot given in Figure 2. The experiment was run using substrate concentration in the range of 0.1 –0.6 M, at a constant methanol concentration of 3 M and in the presence of *tert*-butanol as reaction medium. The values obtained for initial reaction rate V_{max} and the Michaelis constant K_m were 0.0165 M min^{-1} and 0.7118 M respectively.

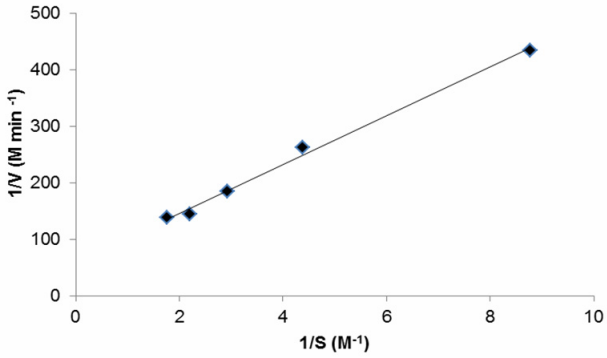

Figure 2. Lineweaver-Burk plot of sunflower oil methanolysis reaction for variation in triglycerides concentration in the range of 0.1 –0.6 M. The value of R^2:0.9893

CONCLUSIONS

For the enzymatic methanolysis of sunflower oil a batch reactor was used and the reaction was performed under continuous agitation using a magnetic stirrer. The enzyme used was Novozym 435 and the reaction was performed in the presence of *tert*-butanol in order to avoid the inactivation of enzyme caused by methanol or by the glycerol formed during the reaction. The FAME content was 78.6% (m/m) after 3h, when the following optimized conditions have been used: 10% Novozym 435 based on oil weight, *tert*-butanol/oil volume ratio 6:1, methanol/oil molar ratio 6:1. The effect of substrate concentration on the initial reaction rate was studied using sunflower oil concentration in the range of 0.1 –0.6 M and the values obtained for initial reaction rate V_{max} and Michaelis constant K_m were 0.0165 M min^{-1} and 0.7118 M respectively.

The main disadvantage of the batch reactor used was the enzyme denaturation in time caused by mechanical degradation produced by the magnetic stirring but the presence of *tert*-butanol improved the solubility of methanol in the reaction mixture, and thus lipase retained a high level of activity with all methanol added for lipase-catalyzed methanolysis.

EXPERIMENTAL SECTION

Materials

The Novozym 435, lipase B from *Candida antarctica*, immobilized on macroporous acrylic resin, 1–2% water content, 10,000 propyl laurate units/g) was purchased from Novozymes (Vienna, Austria). The sunflower oil was obtained locally and its characteristics are summarized in Table 1. Methyl

ester standards (palmitic acid methyl ester, stearic acid methyl ester, oleic acid methyl ester, linoleic acid methyl ester, linolenic acid methyl ester, arachidic acid methyl ester, eicosane acid methyl ester, docosane acid methyl ester and heptadecanoic acid methyl ester) were obtained from Sigma-Aldrich (St. Louis, MO, USA) and were chromatographically pure; other chemicals and solvents were of the highest purity.

Table 1. Fatty acid composition for the sunflower oil used for biodiesel production

Systematic name	Common name	Abbr.	Content [%] (m/m)
Hexadecanoic acid	Palmitic acid	C16:0	6.2
Octadecanoic acid	Stearic acid	C18:0	3.9
cis-9-Octadecenoic acid	Oleic acid	C18:1n9	26.3
cis,cis-9,12-octadecadienoic acid	Linoleic acid	C18:2n6	62.7
6,9,12-octadecatrienoic acid	γ-Linolenic acid	C18:3n6	0.1
Icosanoic acid	Arachidic acid	C20:0	0.2
Docosanoic acid	Behenic acid	C22:0	0.6

GC-FID analysis

The fatty acid methyl ester contents in the reaction mixture were determined using an Agilent 7890A GC (Agilent Technologies) gas chromatograph equipped with a DB-WAX capillary column (30m × 0.32mm × 0.5μm) and a flame ionization detector. The instrumental configuration and the experimental conditions are given in Table 2.

Methanolysis of sunflower oil

Methanolysis reaction was carried out under continuous stirring in a 50 mL round-bottomed flask, maintained at room temperature. In order to avoid the direct contact of lipase with methanol drops, methanol was mixed with *tert*-butanol and oil first, followed by the addition of lipase into the mixture. The reaction conditions were the following: 10% Novozym 435 based on oil weight; methanol /oil molar ratio 6:1; tert-butanol/ oil volume ratio 6:1.

The methanolysis reaction using a batch reactor was monitored for 12 h. Samples from reaction mixture were withdrawn at specific periods of time and analyzed to determine the ester content. Before analysis, the samples were processed as the following: a volume of 100 μL sample was introduced in a mixture that contained 400 μL hexane, 400 μL methyl heptadecanoate (used as internal standard) and 100 μL water, and the solution obtained was centrifuged at 1000 rpm for 15 min. 1 μL from the organic phase was injected in the gas chromatograph to determine the FAME content (m/m).

Tabel 2. Instrumental configuration and experimental conditions used for GC-FID analysis of fatty acid methyl esters

Instrumental configuration	Agilent 7890N GC - FID
GC Parameters	
Injector	Split/Splitless
Column	DB-WAX 30 m x 0,25 mm(i.d.), 0,25µm
Detector	FID
Experimental conditions	
Inlet temperature	250°C
Injection mode	Split (Split ratio: 1/50)
Injection volume	1 µl
Carrier gas	He
Pressure	53 kPa
Oven temperature	50, 1 min 25°C/min to 200°C 3°C/min to 230°C, 18 min
Detector temperature	280°C
Detector gases	H2:40 ml/min; Air: 450 ml/min; He make-up: 30 ml/min

ACKNOWLEDGMENTS

This work was financially supported by The Partnerships in Priority Domains Program of National Center of Programs Management from Romania, Project No. 22094/2008.

REFERENCES

1. D. Bajpai, V.K. Tyagi, *J. Oleo. Sci*., **2006**, *55*, 487.
2. G. Knothe, J.V. Gerpen, V. Krahl, “Basics of the Transesterification Reaction, The Biodiesel Handbook”, Champaign, III, AOCS Press, **2005**, 26.
3. L.C. Meher, D.V. Sagar, S.N. Naik, *Renew. Sustain. Ener. Rev.*, **2004**, 1.
4. M. Iso, B. Chen, M. Eguchi, T. Kudo, S. Shrestha, *J. Mol. Catal. B: Enzym*., **2001**, *16*, 53.
5. S. Shah, S. Sharma, M.N. Gupta, *Indian J. Biochem. Biophys*., **2003**, *40*, 392.
6. G.-T. Jeong, D.-H. Park, *Appl. Biochem. Biotechnol.*, **2008**, *148*, 131.
7. Y. Shimada, Y. Watanabe, A. Sugihara, Y. Tominaga, *J. Mol. Catal. B: Enzym*., **2002**, *17*, 133.

8. L.A. Nelson, T.A. Foglia, W.N. Marmer, *J. Am. Oil Chem. Soc*., **1996**, *73*, 1191.
9. M.M. Soumanou, U.T. Bornscheuer, *Enzyme Microb. Technol*., **2003**, *33*, 97.
10. K. Nie, F. Xie, F. Wang, T. Tan, *J. Mol. Catal. B Enzym*., **2006**, *43*, 142.
11. D. Royon, M. Daz, G. Ellenrieder, S. Locatelli, *Bioresour. Technol.,* **2007**, *96*, 767.
12. L. Li, W. Du, D. Liu, L. Wang, Z. Li, *J. Mol. Catal. B: Enzym.*, **2006**, *43*, 58.
13. J.W. Chen, W.T. Wu, *J. Biosci. Bioeng.*, **2003**, *95*, 466.
14. A.L. Paiva, V.M. Balcao, F.X. Malcata, *Enzyme Microb. Technol.,* **2000**, *27*, 187.
15. T. Garcia, A. Coteron, M. Martinez, J. Aracil, *Chem. Eng. Sci.*, **1996**, *51,* 2841.
16. V. Dossat, D. Combes, A. Marty, *Enzyme Microb. Technol.,* **2002**, *30,* 90.
17. X. Xu, "Modification of oils and fats by lipase-catalyzed interesterification: Aspects of process engineering" in: U. T. Bornscheuer, (Ed.), Enzymes in lipid modification, Wiley-VCH, Weinheim, Germany, **2000**, 190.

STUDIA UBB CHEMIA, LVI, 1, 2011

ORGANICS REMOVAL FROM AQUEOUS SOLUTIONS USING SUSPENDED AND IMMOBILIZED ROMANIAN BENTONITES

ANDRADA MĂICĂNEANU[a,*], CERASELLA INDOLEAN[a], SILVIA BURCĂ[a], MARIA STANCA[a], HOREA BEDELEAN[b], MAJDIK CORNELIA[a]

ABSTRACT. This work presents experimental results obtained in the process of phenol and Fastac pesticide removal from aqueous solutions using batch technique (immobile phases, 3D shaker, magnetic stirring) on Romanian bentonites (Oraşul Nou and Petreşti deposits). Bentonite samples were used in suspension and immobilized in alginate beads. Influences of bentonite provenience and quantity, batch contact type and phenol concentration over the process efficiency were studied. The most effective bentonite proved to be the one from Oraşul Nou. Removal efficiencies up to 80% were reached in case of phenol solutions with concentrations smaller then 50 mg/L on immobilized bentonite and Fastac (100 mg/L) on suspended bentonite. Also, adsorption capacity increased with the decrease of the bentonite quantity and the increase of the initial phenol concentration.

Keywords: *bentonite, suspension, alginate beads, phenol, pesticide, adsorption*

INTRODUCTION

Phenolic compounds, which are released into the aquatic environment by industries such as coke ovens in steel plants, petroleum refineries, petrochemical, phenolic resin, and fertilizer, pharmaceutical, chemical, and dye industries and have been reported in hazardous wastes sites, are considered to be hazardous wastes [1].

The utilization of phenol-contaminated waters causes protein degeneration, tissue erosion, paralysis of the central nervous system and also damages the kidney, liver and pancreas in human bodies [2].

According to the recommendation of World Health Organization (WHO), the permissible concentration of phenolic contents in potable waters is 1g/L [3] and the regulations by the Environmental Protection Agency (EPA), call for lowering phenol content in wastewaters less than 1mg /L [4].

[a] *Universitatea Babeş-Bolyai, Facultatea de Chimie şi Inginerie Chimică, Str. Kogălniceanu, Nr. 1, RO-400084 Cluj-Napoca, Romania, * andrada@chem.ubbcluj.ro*

[b] *Universitatea Babeş-Bolyai, Facultatea de Biologie şi Geologie, Str. Kogălniceanu, Nr. 1, RO-400084 Cluj-Napoca, Romania, horea.bedelean@ubbcluj.ro*

According to Romanian legislation the maximum allowable concentration of phenol in surface waters and municipal sewer system is 0.3 and 30 mg/L, respectively [5], therefore elimination of phenol becomes a necessity in order to preserve water quality [6]. In case of drinking water Romanian legislation states values of 0.001 to 0.1 mg phenol/L for waters that are used for drinking water production [5].

Fastac is one of the many commercial names for alpha-cypermethrin, which is a compound from synthesis pyrethroid pesticide group. It is used on a large scale as an insecticide and acaricide. It behaves as neurotoxin (non-systemic insecticide) in insects (e.g. cockroaches, mosquitoes, flies). Alpha-cypermethrin is highly toxic to fish, bees and aquatic insects; it can produce acute poisoning in humans (tingling, burning dizziness, itching, nausea, tiredness) by contact inhalation or ingestion [7]. According to Romanian legislation the maximum allowable concentration of pesticide as total pesticides varies from 0.5 μg/L for potable water to 1-5 μg/L for waters subjected to various treatments in order to obtain potable water [5].

Various methods have been proposed for the treatment of wastewaters containing organic and inorganic pollutants. These processes are based on the principles of precipitation and coagulation, chemical oxidation, sedimentation, filtration, adsorption, osmosis, ion exchange, etc. Adsorption technology is currently being used extensively for the removal of organic and inorganic micro pollutants from aqueous solutions. There are many absorbents in use. Activated carbon is the most widely used for the removal of a variety of organics from waters, but the disadvantage associated with it is the high regeneration cost and the generation of carbons fines, due to the brittle nature of carbons used for the removal of organic species [8].

Adsorbents from low-cost materials, such as fertilizer wastes [9], wood [10], and rice husk [11], by several chemical treatments are currently developed for phenol removal. The use of sawdust for the removal of phenol from aqueous solution was also studied by Sivanandam and Anirudhan [12].

Natural zeolites gained a significant interest among scientist, mainly due to their valuable properties such as ion exchange ability and high surface areas. Large deposits of natural zeolites in many countries such as Greece, UK, Italy, Mexico, Iran, and Jordan, provide local industries some promising benefits such as cost efficiency since they are able to treat wastewater contaminated with organic solutes at low-costs [8,13].

Clay is one of the potential alternatives to activated carbon as well. Similar to zeolites, clay minerals are important inorganic components in soil. Their sorption capabilities come from high surface area and exchange capacities. The negative charge on the structure of clay minerals gives clay the capability to be modified by surfactant. USA, Lithuania, Georgia, Romania and Kazakhstan are well known for their large deposits of natural clay minerals [6,8,14].

Bentonite is a member of 2:1 clay minerals (meaning that it has two tetrahedral sheets sandwiching a central octahedral sheet) which consists essentially of clay minerals of montmorillonite group. Bentonite is characterized by an Al octahedral sheet between two Si tetrahedral sheets. It has a negative surface charge created by the isomorphous substitution of Al^{3+} for Si^{4+} in tetrahedral layer and Mg^{2+} for Al^{3+} in octahedral layer. The bentonite surface is hydrophilic in nature because inorganic cations, such as Na^{+} and Ca^{2+}, are strongly hydrated in presence of water. As a result, the adsorption efficiency of natural bentonite for organic molecules is low. The adsorption properties of bentonite can be improved by the modification of clay mineral surface with a cationic surfactant. [15,16].

The aim of this work was to investigate, the potential of two Romanian bentonites from Oraşul Nou, (ON), Satu Mare County, and Petreşti (P), Cluj County, used in suspension, and immobilized in calcium alginate to adsorb phenol and Fastac pesticide from aqueous solutions, in batch conditions (Influences of bentonite provenience and quantity, batch contact type and phenol concentration over the process efficiency were studied). The considered bentonites were used without any chemical modification of their structure.

RESULTS AND DISCUSSION

Bentonite samples

In order to realise the proposed adsorption study, two bentonite samples were collected from two deposits located in Transylvania, Romania, namely, Oraşul Nou, (ON), and Petreşti (P). Bentonite samples were collected as representative bulk rock sample from the open pits.

The bentonite deposit from Oraşul Nou (Satu Mare County) is located about 30 km north-west of the city of Baia Mare. The bentonites were formed by alteration of rhyolites and perlites, due to the solutions' complex circulation through the rocks. They are white in colour, fine grained or compact, the perlitic fabric being more or less preserved. The mineralogical composition of raw material was analysed using XRD and indicates the presence of montmorillonite, as the main clay mineral (subordinately kaolinite, illite), cristobalite, carbonates, clinoptilolite, iron oxi-hydroxides and quartz and feldspar (as relics of primary minerals). According to the transformation degree of the primary rock, the amount of montmorillonite varies between 20-85% [17].

The bentonite deposit from Petreşti (Cluj County, Romania) is located at about 30 km south from Cluj-Napoca (north-western part of Romania). The bentonite deposit was formed at then contact of the carbonate rocks (Upper Jurassic age) and basaltic andesites and basalts rock, generated by circulating hydrothermal fluids. The main rocks are represented by Ca-bentonites white and white-yellowish in color. Mineralogical composition of clay raw material resulting from X-ray diffraction analyses is represented by smectite (montmorillonite) 65-72%, mica/illite, quartz, cristobalite, feldspars and clinoptilolite [14].

Suspended bentonite – phenol removal

In figure 1 are presented the results obtained for the two bentonite samples in batch conditions, immobile phases and magnetic stirring. It can be observed that the highest increase of the removal efficiency is in the first 24 hours, respectively in the first 15 minutes from the beginning of the experiment depending on the contact type (immobile vs. stirring).

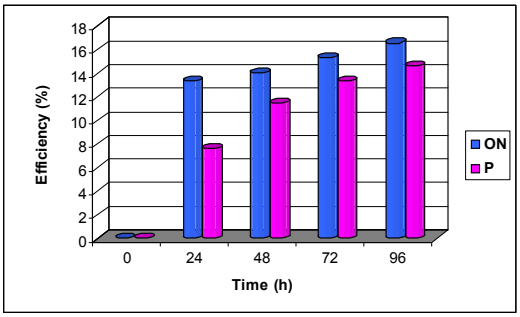

(a).

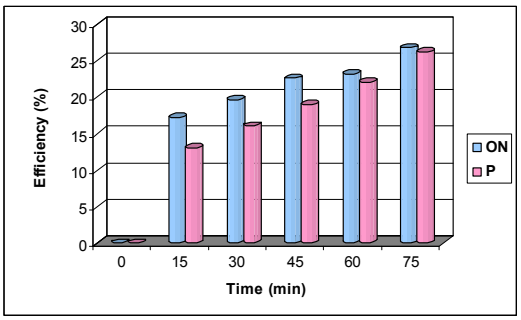

(b).

Figure 1. Time evolution of phenol removal efficiency on bentonite samples (suspended) from Oraşul Nou (ON) and Petreşti (P) in batch conditions, solid : liquid ratio = 1:10, C_i = 100 mg phenol/L; (a) immobile phases, and (b) magnetic stirring.

Also the equilibrium was reached after 96 hours, respectively after 75 minutes (diffusion limitations are reduced with stirring intensification) for both bentonite samples. If we compare the values obtained for ON and P samples it is easy to observe that in all cases the ON sample proved to be more efficient, results that can be correlated with the specific surface area of the bentonite sample, which is higher in case of ON (72 m^2/g) by comparison with 64 m^2/g for P.

In case of the batch conditions realised using a 3D shaker, exemplified for P sample in figure 2, equilibrium was reached after 150 minutes suggesting that external diffusion limitation are diminished by comparison with immobile

phases, but they still have a great influence taking in account that the equilibrium was reached in 150 minutes by comparison to 75 minutes for the magnetic stirring. Another aspect observed in case of 3D shaker by comparison with magnetic stirring was that the increase of the adsorption efficiency (decrease of the phenol quantity in solution) takes place more slowly.

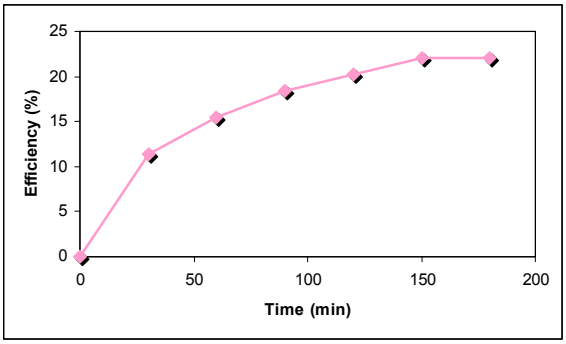

Figure 2. Time evolution of phenol removal efficiency on bentonite sample (suspended) from Petreşti (P) in batch conditions – 3D shaker, solid : liquid ratio = 1:10, C_i = 100 mg phenol/L.

The influence of the contact type in batch conditions for phenol adsorption in suspension is presented in figure 3, for ON sample. As the intensity of the mass transfer increases due to a more intense stirring, the removal efficiency also increases.

The influence of the bentonite quantity (solid : liquid ratio) over the removal process efficiency is exemplified in figure 4, for P sample when 2 and 4 grams of bentonite were suspended in 20 ml of phenol solution. An increase in the adsorbent quantity led to only a small increase in the removal efficiency, suggesting that an increase of the bentonite quantity (more than 2 grams) is not economically feasible.

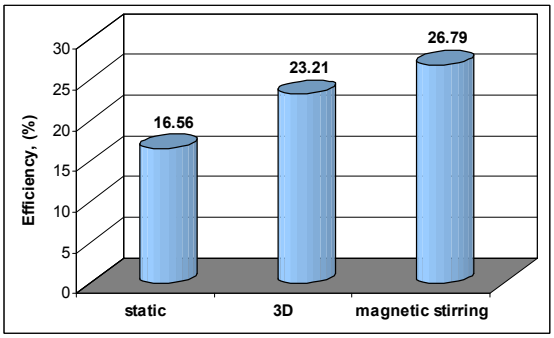

Figure 3. Maximum phenol removal efficiency on ON bentonite sample (suspended), obtained in batch conditions, solid : liquid ratio = 1:10, C_i = 100 mg phenol/L.

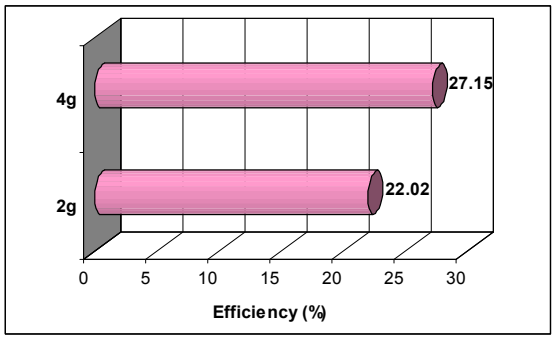

Figure 4. Bentonite quantity influence over the maximum phenol removal efficiency on the P bentonite sample (suspended) in batch conditions – 3D shaker, corresponding to a solid : liquid ratio of 1:10 and 2:10 respectively, C_i = 100 mg phenol/L.

Suspended bentonite – Fastac (alpha-cypermethrin) removal

Adsorption of Fastac pesticide was realised in similar conditions on the ON and P samples. In case of immobile phases (static), as for phenol, the adsorption equilibrium was reached in 96 hours, again with better removal efficiencies on the ON sample, 65.78% (ON) by comparison with 57.22% (P). In case of magnetic stirring, figure 5, adsorption efficiency increased very much in the first 15 minutes, after that a slowly increase until equilibrium (75 minutes) being observed. A direct comparison between the batch conditions, figure 6, showed that magnetic stirring is more efficient due to a more intense stirring leading to a more intense mass transfer. The highest adsorption efficiency was calculated to be 78.61% in case of ON bentonite sample.

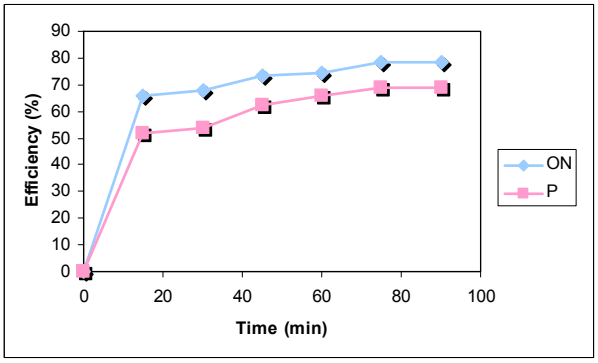

Figure 5. Time evolution of Fastac removal efficiency on bentonite samples (suspended from Oraşul Nou (ON) and Petreşti (P) in batch conditions – magnetic stirring, solid : liquid ratio = 1:10, C_i = 100 mg Fastac/L.

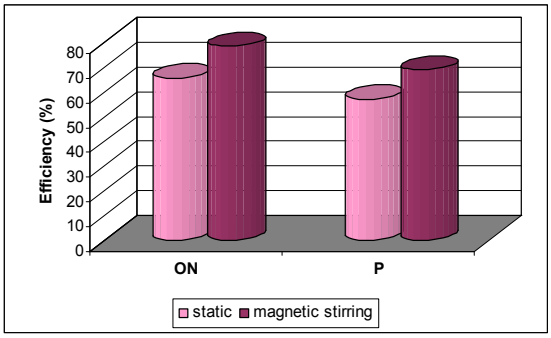

Figure 6. Maximum Fastac removal efficiencies on Oraşul Nou (ON) and Petreşti (P) bentonite samples (suspended), obtained in batch conditions, solid : liquid ratio = 1:10, C_i = 100 mg Fastac/L.

Immobilized bentonite – phenol removal

In the first stage of the experiment, phenol adsorption was realised in a batch reactor with mobile phases, benonite-alginate beads, ON and P samples, being contacted with the phenol solution using a magnetic stirrer. The obtained results are presented in terms of adsorption capacity evolution in time, figure 7, and maximum adsorption efficiency, figure 8, for the same quantity of bentonite present in the beads (8g) and the same phenol initial concentration (103.77 mg/L). From figure 7 it can be observed that in the first 15 minutes from the beginning of the experiment the highest quantity of phenol is removed. Also at the beginning of the experiment P sample looks to be more efficient, while towards the end of the experiment ON sample will retain a higher quantity of phenol. This fact can be attributed to the internal diffusion limitation for ON sample which has a higher specific surface area as was mentioned before. Adsorption capacity was calculated to be 0.708 mg/g and 0.629 mg/g for ON and P samples respectively. The adsorption equilibrium was reached after 180 minutes. If we compare this value with that obtained when the bentonite was suspended (75 minutes) it can be observed that the time for reaching equilibrium is more than double (due to diffusion limitation in the alginate bead). Maximum values for adsorption efficiencies, figure 8, showed also that ON immobilized bentonite sample is more efficient in phenol removal process. Taking into account the fact that ON bentonite sample proved to be the most efficient one in the phenol adsorption process, this sample was next considered for the rest of adsorption experiments.

For a better use of the adsorbent (optimisation of the adsorbent quantity) the next stage of the experiment was to study the evolution of the adsorption process for different ON bentonite quantities immobilized in calcium alginate beads (2-8g) at different initial concentrations of phenol in solution. In figures 9 and 10 the results obtained for C_i = 157.23 mg phenol/L and all considered bentonite quantities are presented. Evolution of the adsorption efficiency in

time, figure 9, showed that in the first 15 minutes from the beginning of the experiment, the highest quantity of phenol was adsorbed, after that the adsorbed quantity increase very slowly in case of 2 and 4 g of bentonite and increase slowly in case of 8g benotnite. Equilibrium was reached in about 60 minutes.

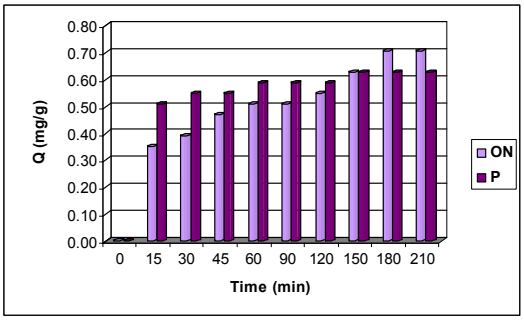

Figure 7. Time evolution of phenol adsorption capacities for Oraşul Nou (ON) and Petreşti (P) bentonite samples (immobilized), 8g bentonite, C_i = 103.77 mg phenol/L.

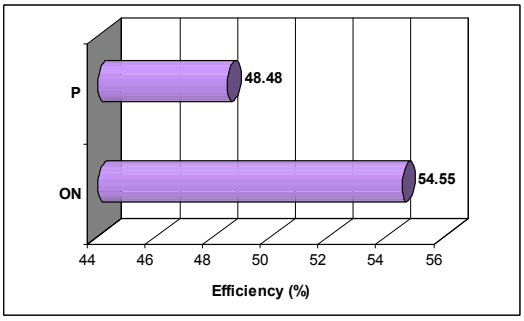

Figure 8. Maximum adsorption efficiency obtained on bentonite samples (immobilized) from Oraşul Nou (ON) and Petreşti (P), 8g bentonite, C_i = 103.77 mg phenol/L.

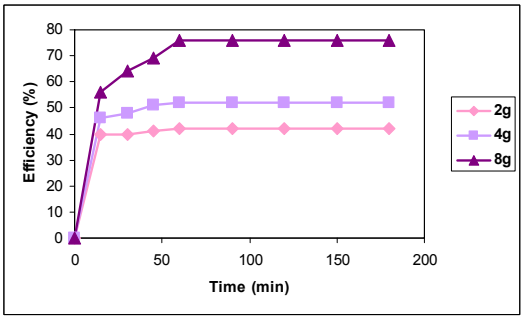

Figure 9. Influence of the bentonite quantity over the time evolution of phenol removal efficiency, 4g ON bentonite (immobilized), C_i = 157.23 mg phenol/L.

To have a more complete image of the adsorption process on the chosen bentonite sample, adsorption capacities were calculated in order to include into the numerical values also the bentonite quantities we used, figure 10. From the values in figure 10, it is easy to observe that as the bentonite quantity increases, the adsorption capacity decreases. Therefore if an adsorption process of this type is considered for practical uses, it will be necessary to take into consideration the initial phenol concentration and water quantity that need to be treated, in order to establish the appropriate bentonite quantity. Also adsorption efficiency should be calculated and evaluated along with bentonite quantity from the economic point of view. As our results show, an increase of the bentonite quantity will lead to an increase of adsorption efficiency, which will finally lead to an increase of the operating cost.

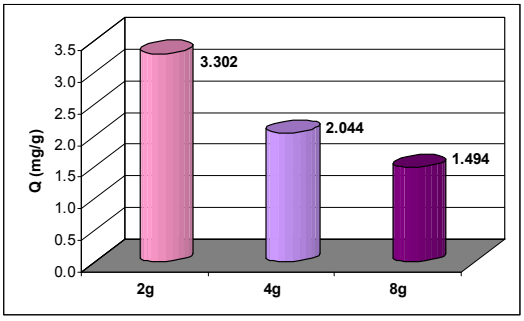

Figure 10. Bentonite quantity influence over the adsorption capacity values for phenol removal, ON bentonite (immobilized), C_i = 157.23 mg phenol/L.

In the final part of the study, the influence of the initial phenol concentration over the adsorption process was studied. Were used solutions containing between 31 and 160 mg phenol/L and as adsorbent 4g of ON bentonite immobilized in calcium alginate beads. Influence of phenol initial concentration over the evolution of phenol concentration in time is presented in figure 11.

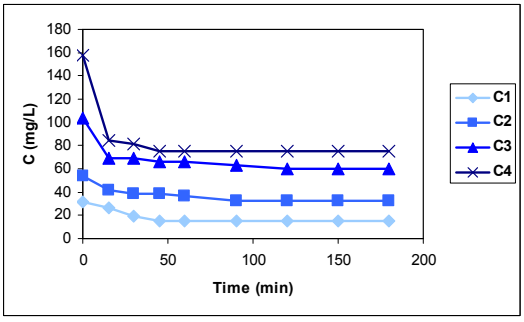

Figure 11. Influence of the phenol initial concentration over the removal process kinetics on 4g ON bentonite (immobilized), C_1 = 31.35, C_2 = 53.46, C_3 = 103.77, C_4 = 157.23 mg phenol/L.

As the initial concentration decreases, the quantity of phenol retained in the first 15 minutes decreases also, due to the smaller difference that exist between the concentration of phenol on the adsorbent surface and in the solution. Therefore the adsorption capacity of the immobilized ON, increases with an increase of the phenol initial concentration, from 0.393 to 2.044 mg phenol/L, figure 12.

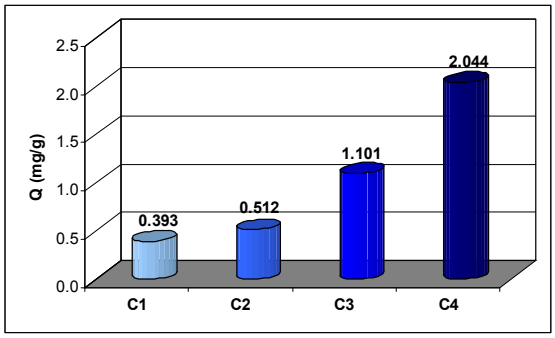

Figure 12. Adsorption capacity values for phenol removal for different initial concentrations, 4g ON bentonite (immobilized), C_1 = 31.35, C_2 = 53.46, C_3 = 103.77, C_4 = 157.23 mg phenol/L.

CONCLUSIONS

This work presents experimental results obtained in the process of phenol and Fastac pesticide removal from aqueous solutions using batch technique (immobile phases, 3D shaker and magnetic stirring) and suspended and alginate immobilized bentonite as adsorbent. Influences of bentonite provenience (Oraşul Nou and Petreşti samples) and quantity (2-8 grams), batch contact type and phenol concentration (31-160 mg/L) over the process efficiency were studied.

The most effective bentonite sample proved to be the one from Oraşul Nou in suspended and alginate immobilized form as well. Removal efficiencies up to 80% were reached. Also, adsorption capacity increased with a decrease in the bentonite quantity and an increase of the initial phenol concentration showing the capacity of this adsorbent to retain organic compounds.

EXPERIMENTAL SECTION

In this study two bentonite samples collected from two deposits, Oraşul Nou, (ON), Satu Mare County, and Petreşti (P), Cluj County, were used as adsorbents for phenol and Fastac (alpha-cypermethrin). The two bentonite samples were used suspended or immobilized in Ca-alginate beads. The bentonite samples were used as powder, (d < 0.2 mm), without any chemical treatment.

Phenol solutions with concentrations ranging from 31 to 160 mg/L were prepared. Fastac working solution, 100 mg/L, was obtained from commercial available pesticide vials. Fastac is one of the many commercial names for alpha-cypermethrin, which is a compound from synthesis pyrethroid pesticide group, containing more than 90% the most active pair (Scheme 1, (*RS*)-α-ciano-3-fenoxibenzil (1*RS*)-*cis*-3-(2,2-diclorovinil)-2,2-dimetilciclopropan carboxilat) from the 4 cis isomers of cypermethrine, as racemic mixture [7].

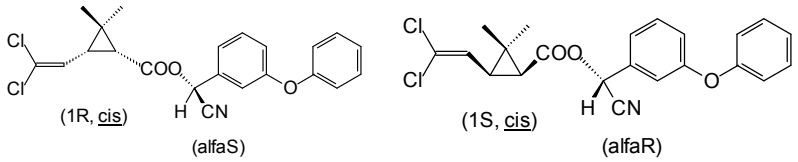

Scheme 1

Beside Fastac which was used in its commercial available form, all chemicals used in this study were analytical reagent grade (phenol, alginic acid sodium salt, ethanol and $CaCl_2$).

Removal efficiencies (E, %), equation (1), and adsorption capacities (Q, mg/g), equation (2), were calculated in order to establish the effectiveness of the considered samples in the organics removal process (the calculated values of removal efficiencies and adsorption capacities should be regarded according to the precision of the determination methods we used). Q was calculated just in case of immobilized bentonite where phenol was determined using the spectrophotometric procedure.

$$\mathbf{E} = \frac{\mathbf{C_i - C_t}}{\mathbf{C_i}} \cdot \mathbf{100} \tag{1}$$

$$\mathbf{Q} = \frac{\mathbf{C_i - C_t}}{\mathbf{m}} \cdot \frac{\mathbf{V}}{\mathbf{1000}} \tag{2}$$

where,

C_i, initial organic concentration in solution, in mg/dm^3
C_t, organic concentration in solution at time t, in mg/dm^3
V, sample volume, 100 cm^3
m, bentonite quantity, in g.

Suspended bentonite

Bentonite samples were suspended in phenol or Fastac solutions and contacted in three ways in batch conditions: immobile phases (static), mobile phases 3D shaker (GFL 3012) and magnetic stirring (FALC F60, 825 rpm) with a

solid liquid ratio of 1:10 and 2:10. In order to determine organics concentration in the aqueous solutions, water samples were collected every 24 hours, every 15 minutes and every 30 minutes for batch conditions realised in static, 3D and magnetic stirring conditions respectively. The experiments were conducted in isothermal conditions at room temperature until equilibrium was reached. Organics concentration in solution was determined as chemical oxygen demand COD, using $KMnO_4$ standard procedure. Prior to this determination a centrifugation procedure at 5000 rpm (Hettich EBA21) was realised in order to remove solid particles from solution. We studied the influence of the bentonite provenience and quantity, and working conditions over the process efficiency.

Immobilized bentonite

ON and P bentonite samples powder were immobilized in alginate beads using the entrapment procedure with calcium alginate [18,19]. Thus, various quantities of bentonite (2, 4, 8, g) were immobilized in Ca-alginate beads. For phenol adsorption study we used aqueous solutions containing between 31 and 160 mg phenol/L. Concentration of phenol in solution was determined using a Jenway 6305 UV/VIS spectrophotometer (UV, 270 nm) after a preliminary centrifugation (14000 rpm, Mikro 200R Hettich centrifuge). Phenol adsorption process was realized in batch conditions under magnetic stirring (FALC F60, 825 rpm) using 100 ml phenol solution of different concentrations, in which Ca-alginate bentonite beads obtained from the desired quantity of adsorbent were suspended. In order to determine the exact concentration of phenol and establish the evolution of the removal process, water samples from the supernatant, diluted as required, were collected at different time intervals, every 24 hours when we used immobile phases, and every 15 minutes for the first hour and next every 30 minutes when we used mobile phases (magnetic stirring), until equilibrium was reached. We studied the influence of the bentonite provenience and quantity, and phenol concentration in solution over the process efficiency in batch conditions.

REFERENCES

1. M. Ahmaruzzaman, D.K. Sharma, *Journal of Colloid and Interface Science*, **2005**, *287*, 14.
2. A. Knop, L.A. Pilato, *Phenolic Resins-Chemistry. Applications and Performance*, **1985**, Springer-Verlag Ed.
3. WHO (World Health Organization), *Guidelines for Drinking Water Quality: Health Criteria and Supporting Information,* World Health Organization, Geneva, Switzerland, **1984**, volume 2.

4. N.N. Dutta, S. Brothakur, R. Baruaha, *Water Environmental Resources*, **1998**, *70*, 4.
5. *** Romanian Government decision, HG 188/2002 modified with HG 352/2005; law 458/2002 modified with law 311/2004 (NTPA-001, -002, -013).
6. C. Majdik, A. Măicăneanu, C. Indolean, S. Burcă, M. Stanca, *Studia UBB Chemia,* **2010**, *LV*, 115.
7. A. Măicăneanu, H. Bedelean, M. Stanca, *Zeoliți naturali. Caracterizare şi aplicații în protecția mediului*, **2008**, Presa Universitară Clujeană, Cluj-Napoca.
8. S.-H. Lin, R.-S. Juang, *Journal of Environmental Management*, **2009**, *90*, 1336.
9. S.K. Srivastava, R. Tyagi, N. Pal, D. Mohan*, Journal of Environmental Engineering*, **1997**, *123*, 842.
10. H.M. Asfour, O.A. Fadali, M.M. Nassar, M.S. El-Geundi, *Journal of Chemical Technology and Biotechnology*, **1985**, *35a*, 21.
11. K. Srinivasan, N. Balasubramanian, T.V. Ramakrishna, *Indian Journal of Environmental Health*, **1988**, *30*, 376.
12. A.V. Sivanandam, T.S. Anirudhan*, Indian Journal of Chemical Technology*, **1995**, *2*, 137.
13. M. Spysnskyy, T. Ligor, B. Buszewski, *Journal of Hazardous Materials*, **2008**, *151*, 570.
14. H. Bedelean, A. Măicăneanu, S. Burcă, S., M. Stanca, *Clay Minerals*, **2009**, *44*, 486.
15. H.B. Senturk, D. Ozdes, A. Gundogdu, C. Duran, M. Soylak, *Journal of Hazardous Materials*, **2009**, *172*, 353.
16. Q. Zhou, H.P. He, J.X. Zhu, W. Shen, R.L. Frost, P. Yuan, *Journal of Hazardous Materials*, **2008**, *154*, 1025.
17. A. Măicăneanu, H. Bedelean, S. Burcă, M. Stanca, *Studia UBB Chemia*, **2009**, *54*, 127.
18. S. Schiewer, E. Fourest, K.H. Chong, B. Volesky, *Biohydrometallurgical Processing*, **1995**, *2*, 219.
19. Sz. Tonk, A. Măicăneanu, C. Indolean, S. Burcă, C. Majdik, *Journal of Serbian Chemical Society*, **2010***, in press*.

STUDIA UBB CHEMIA, LVI, 1, 2011

THE INFLUENCE OF TiO_2 NANOPARTICLES ON MORPHO-STRUCTURAL AND ANTI-CORROSION PROPERTIES OF ELECTRODEPOSITED Zn-Ni COATINGS

DIANA BLEJAN[a], DANIEL MARCONI[b], AUREL POP[b], LIANA MARIA MURESAN[a*]

ABSTRACT. Composite Zn-Ni coatings incorporating TiO_2 nanoparticles were obtained by electrodeposition on steel from alkaline solution containing triethanolamine (TEA) as complexing agent for Ni^{2+} and polyethyleneglicol (PEG) in combination with vanillin, as leveling/brightening agents. The influence of TiO_2 nanoparticles on phase composition and structure of Zn- Ni coatings were investigated by X-ray diffraction and SEM-EDAX methods. By using polarization measurements, the corrosion behaviour of the nanocomposite coatings was examined and the corrosion process on Zn-Ni-TiO_2 composite coatings was found to be slower than on pure Zn-Ni surface.

Keywords: *Corrosion; Electrodeposition; Zinc-Nickel alloy; alkaline electrolyte*

INTRODUCTION

Considerable efforts have been devoted over the years to provide improved corrosion protection to metallic surfaces. Zn alloys with Ni have attracted much attention because Zn-Ni coatings possess higher corrosion resistance and better mechanical characteristics than pure zinc and other zinc alloy coatings [1-4]. Corrosion studies have also indicated that Zn-Ni alloys may be useful as a substitute for cadmium deposits in marine environments [5].

A relatively recent way for enhancing the corrosion resistance of zinc coatings consists in generating composite layers by electrolysis of plating solutions in which micron or sub-micron size inert particles (i.e. TiO_2, Al_2O_3 etc.) are suspended [6,7]. The electrodeposition of metallic coatings containing inert particles produces corrosion resistant coatings with enhanced mechanical and tribological properties. The advanced physical properties of composite coatings quickly became clear during the 1990s, when new areas such as electrocatalysis and photoelectrocatalysis were considered [8]. However, till now, there are only few papers focused on zinc-nickel composite coatings incorporating nanoparticles [9].

[a] *Department of Physical Chemistry, Babes-Bolyai University, 11 Arany Janos St., 400028 Cluj-Napoca, Romania*

[b] *Department of Physics, Babes-Bolyai University, M. Kogalniceanu St.1, 400084 Cluj-Napoca, Romania *limur@chem.ubbcluj.ro*

In this context, the aim of this work is to investigate the combined effect of Ni and TiO_2 nanoparticles on the corrosion resistance of zinc coatings. Zn-Ni and Zn-Ni-TiO_2 coatings were obtained by electrodeposition from an alkaline bath containing triethanolamine (TEA) as complexing agent for Ni^{2+} and polyethyleneglicol (PEG) in combination with vanillin, as leveling/ brightening agents, selected based on our previous work [10].

X ray diffraction (XRD) and SEM-EDAX methods were used to determine the structure and the surface topography of the deposits. Polarization measurements were carried out in order to characterize the corrosion behavior of the coatings by using Tafel method.

RESULTS AND DISCUSSION

Electrodeposition

As it can be seen from the polarization curves recorded during the electrodeposition of Zn-Ni coatings (Fig. 1), no significant changes are observed in the kinetically controlled region of the curves, when adding TiO_2 nanoparticles or when modifying their concentration, while a slight increase of the current density is noticed in the mixed-control region. This could be due to a catalytic phenomenon initiated by defects and dislocations or to chemical heterogeneities generated in the metallic matrix by the embedded particles at high overpotentials.

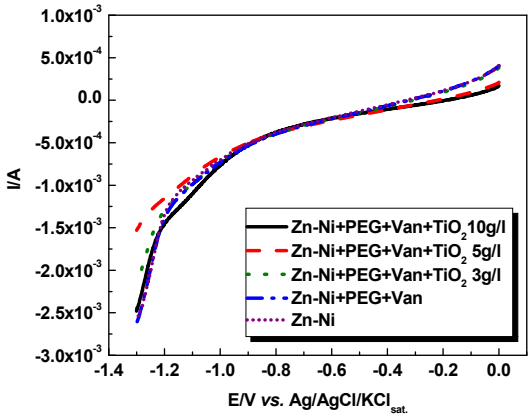

Figure 1. Polarization curves obtained during Zn-Ni electrodeposition in the absence and in the presence of TiO_2 nanoparticles.

Structural and morphological analysis

Figure 2 shows XRD pattern for four Zn-Ni coated samples: S_{01} (in the absence of brightening agents and of TiO_2), S_0 (obtained in the presence of brightening agents but in the absence of TiO_2), S_5 and S_{10} (obtained in the presence of brightening agents and with 5 g/l and 10 g/l TiO_2 nanoparticles, respectively, in the plating bath).

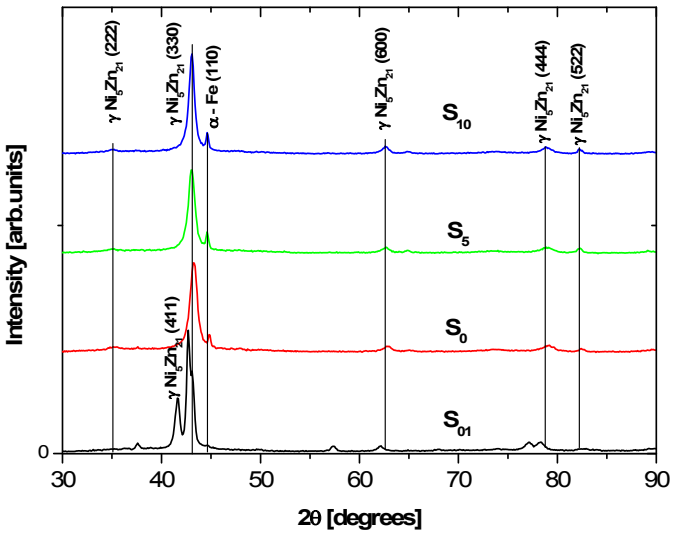

Figure 2. XRD of samples S_{01} (in the absence of brightening agents and of TiO_2), S_0 (in the absence of TiO_2 nanoparticles, x=0), S_5 and S_{10} (for x = 5 g/l and x = 10 g/l TiO_2 nanoparticles).

As can be seen from figure 2, the diffraction peaks for all samples obtained by using brightening agents and TiO_2 nanoparticles correspond only to γ-phase (Ni_5Zn_{21}). It is well-known that, the high corrosion resistance of the Zn–Ni coatings might primarily be attributed to the existence of this phase. The absence of TiO_2 peaks in the XRD spectra suggests that the concentration of phases associated with the nanoparticles is under the limit of detection of XRD method. The obtained results are in accordance with those reported for alloys containing 19–20 at. % Ni [11] and with the zinc–nickel phase diagram for γ-Ni_5Zn_{21} [12].

Another aspect that should be emphasized is related to the crystal orientation in the deposit, which is considered to be an important factor in the corrosion process. It is common knowledge that the intensity of XRD peaks (characterized by Miller indices (hkl)) is proportional to the density of oriented lattice planes. Consequently, the change of the grain orientations in presence of nanoparticles is indicated by changes of peak intensities. In the same time, the metal local coordination is correlated with planar packing densities.

In the case of investigated Zn-Ni coatings, the small change in the intensities ratio $I_{(330)}/(I_{(330)}+I_{(600)})$, presented in Table 1, shows the absence of textural modifications of deposits in the presence of TiO_2 nanoparticles. The packing density decreased in this order: ρ (110) > ρ (100), as in reference [13]. The high value of the intensities ratio $I_{(330)}/(I_{(330)}+I_{(600)})$ suggests a good packing

density associated to more closely packed (330) (or (110)) planes. The XRD pattern of sample S_{10} is similar with the result reported for pure γ-phase deposits obtained from alkaline solutions [14].

Previous investigations using XRD [15] indicated that deposition of bcc zinc–nickel on a mild steel substrate with a {110} texture resulted initially in the nucleation of {110} orientated grains of bcc zinc–nickel at the substrate/ deposit interface. Because the mild steel substrate has a {110} texture and the interplanar spacing of the mild steel {110} and of the zinc–nickel {330} are almost identical, the nickel and zinc atoms in the bcc {110} planes can fit very closely to the recesses between atoms in the mild steel {110}. This process explains the high value of $I_{(330)}/(I_{(330)}+I_{(600)})$ ratio in our samples.

Crystallite size calculations were made by using the full width at half maximum (FWHM) of (110) peak, in the Scherer equation:

$$D = \frac{0{,}9\lambda}{B\cos\theta}$$

where *D* is the grain size [nm], $\lambda = \lambda_{CuK\alpha 1} = 0{,}15406$ nm), *B* is the line width and *θ* is the position for (110) peak. For all coatings, the profile of (110) peak exhibits Lorentz type behavior

The calculated value for D (see Table 1) shows that the grain size decreases with increasing concentration x of TiO_2 nanoparticles up to 5g/l TiO_2, and slightly increases for x =10 g/l. The decrease of grain dimensions is due to the fact that the nanoparticles influence the competitive formation of metal nuclei and crystal growth. The TiO_2 nanoparticles disturb the regular growth of metallic crystals and causes new nucleation sites to appear.

Table 1. Parameters obtained from XRD and EDAX measurements.

Sample	$\frac{I_{(330)}}{I_{(330)}+I_{(600)}}$ %	D [nm]	Ni wt.%
S_{01}	92	14.0	15.7
S_0 (x=0 g/l TiO_2)	94	11.4	16.0
S_5 (x=5 g/l TiO_2)	95.5	10.7	16.5
S_{10} (x=10 g/l TiO_2)	95	11.9	17.0

Morphological observation of Zn-Ni nanocomposite coatings and their chemical composition were carried out by SEM and EDAX methods. Figure 3 shows the scanning electron micrographs of Zn–Ni deposits with different concentration of TiO_2 nanoparticles.

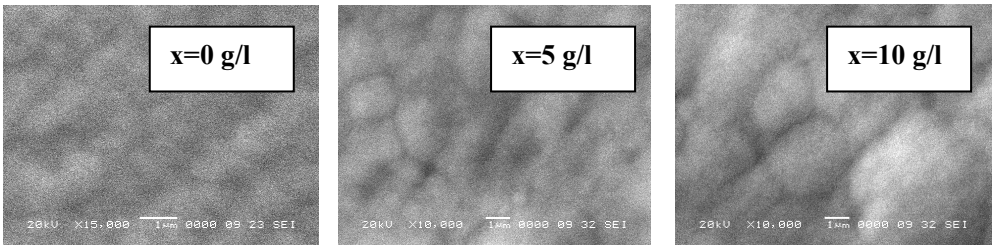

Figure 3. SEM micrographs of the Zn–Ni deposits, showing the change of morphology with TiO_2 nanoparticle concentration.

Thus, the plate-like shape morphology of the electrodeposits slowly changes by increasing the concentration x of TiO_2 nanoparticles. Similar results were obtained by Felloni *et al.* [16], who found that the platelet-type grains are closely related to the (330) (or (110)) component, and the pyramidal microstructure coincided with a preferential (600) orientation. The crystallographic preference for the (330) orientation that occurs in the presence of TiO_2 nanoparticles coincides with the formation of platelet-type structures.

Figure 4 shows the results of EDAX analysis for Zn-Ni alloy samples with x = 0 g/l, 5 g/l and 10 g/l TiO_2, respectively. The corresponding Ni content in the deposits (wt %) is presented in Table 1.

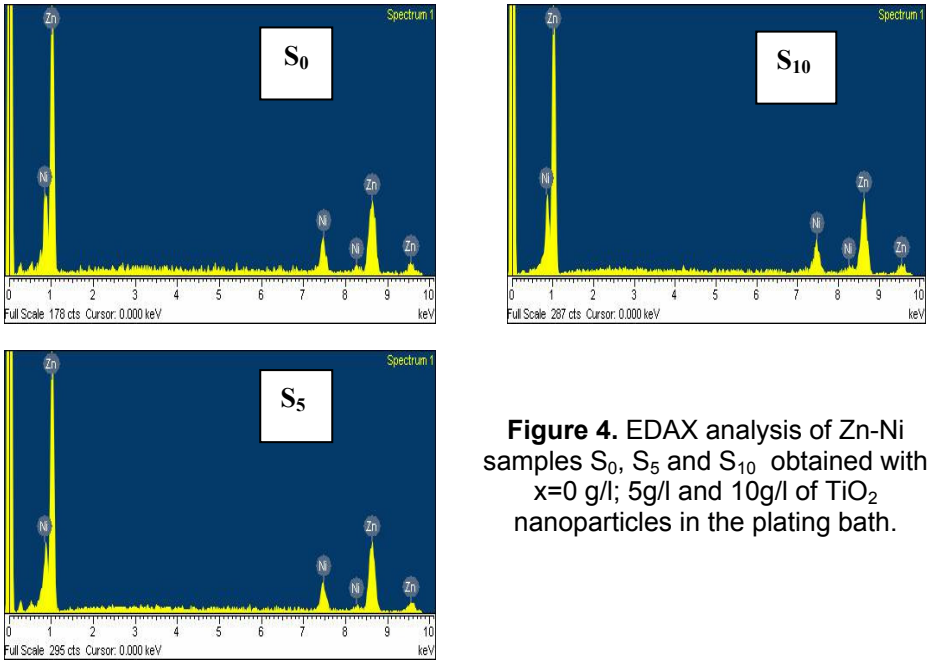

Figure 4. EDAX analysis of Zn-Ni samples S_0, S_5 and S_{10} obtained with x=0 g/l; 5g/l and 10g/l of TiO_2 nanoparticles in the plating bath.

It was observed that the Ni content increases from 16% to 17% with increasing concentration of TiO_2 nanoparticles. Literature reports mention that Ni–Zn alloy coatings on Fe substrates are relatively rich in Ni at the substrate/ deposit interface [17].

Electrochemical corrosion measurements

Open circuit potential

The open-circuit potentials (*ocp*) evolution in time for Zn-Ni and Zn-Ni-TiO_2 samples recorded after their immersion in Na_2SO_4 solution (pH 5) is presented in Fig. 5.

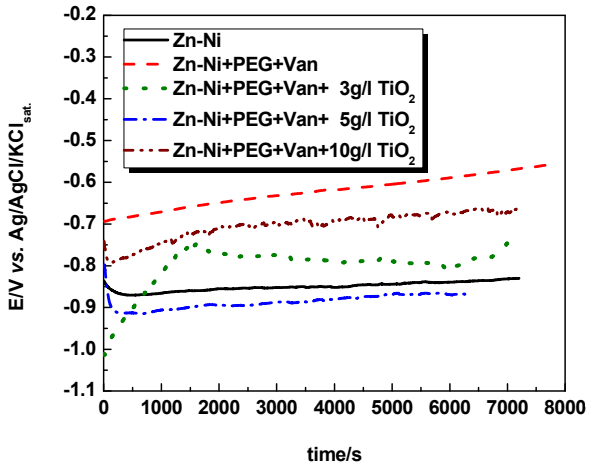

Figure 5. Evolution of open circuit potentials for Zn-Ni coatings obtained in the absence and in the presence of TiO_2 nanoparticles, after immersion in 0.2 g/l Na_2SO_4 (pH 5).

As expected, the *ocp* values noticed for Zn-Ni alloy are more positive than those observed in the same conditions for pure Zn coatings [18] suggesting a more noble character of the deposit, which could be associated to an inhibition of the anodic reaction and consequently to a higher corrosion resistance. The most positive shift was recorded in the case when only PEG and Vanillin were used, due, probably, to the smaller roughness of the surface. The fact that Zn-Ni alloys became nobler with the immersion time could be attributed to a dezincification process [19].

A shift of the *ocp* values towards more positive potentials is observed in some cases when TiO_2 nanoparticles were present in the plating bath, as compared to Zn-Ni coatings obtained without additives, suggesting an interaction of TiO_2 with the anodic reaction of the corrosion process.

Polarization curves

Polarization measurements performed in a potential range of ± 20 mV *vs. ocp* allowed the evaluation of the polarization resistance, R_p (Table 2). The higher values noticed in the presence of TiO_2 are probably due to lowering of the surface area of the electrode by embedded particles [20]. However, it should be mentioned that an increase of TiO_2 concentration beyond 3 g/l does not lead to further increase of R_p, probably due to defects and dislocations generated by the inclusion of nanoparticles in the metallic matrix.

Table 2. Polarisation resistance values calculated as the reciprocal of the slope of polarization curves (ΔE/Δi) recorded in a potential range of E = E_{corr} ± 20 mV.

Nr. crt.	Electroplating solution	R_p (Ohm)
S_{01}	Zn-Ni	8138
S_0	Zn-Ni+PEG+Van	8305
S_3	Zn-Ni+PEG+Van+TiO_2 3g/L	9995
S_5	Zn-Ni+PEG+Van+TiO_2 5g/L	9411
S_{10}	Zn-Ni+PEG+Van+TiO_2 10g/L	9033

The results of the polarization tests, carried out in a potential range of ± 200 mV *vs. ocp* using the Zn-Ni coated steel electrodes prepared in presence of different TiO_2 concentrations in the plating bath, are presented in Fig.6.

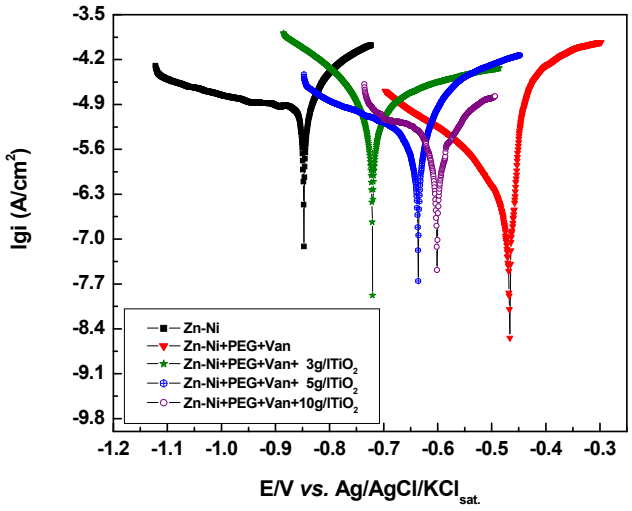

Figure 6. Polarization curve for the Zn-Ni coated steel obtained from a bath containing additives and TiO_2 nanoparticles in different concentrations. Experimental conditions: electrolyte Na_2SO_4 0.2g/l (pH=5); scan rate 0.166 mV/s; PEG, 3ml/l; Vanillin, 10 mg/l.

The corresponding corrosion reaction equations are:

$$Zn \rightarrow Zn^{2+} + 2e^-$$
$$Ni + ½\ O_2 \rightarrow NiO$$

for the anodic process, and

$$½\ O_2 + 2H^+ + 2e^- \rightarrow H_2O$$

for the cathodic one.

The values of the corrosion parameters of the coatings were calculated from the polarization curves based on the Stern - Geary theory [21], and by using Tafel interpretation (Table 3).

As it can be observed, the addition of PEG and Vanillin in the plating bath gives rise to significant decrease of corrosion current density as compared to Zn-Ni obtained without additives. This indicates that, as expected, the organic compounds strongly modified the quality of the cathodic deposit in terms of structure and morphology, producing more compact, fine-grained and consequently more corrosion resistant coatings.

In what the effect of TiO_2 nanoparticles is concerned, the addition of inert nanoparticles led to a decrease of corrosion current densities only in comparison with the pure Zn-Ni coating obtained from solution without additives. The decrease of corrosion currents could be due either to grain refinement of the deposit (see D values in Table 1), or to the fact that the incorporation of inert TiO_2 nanoparticles in the coatings isolates them from the corrosion medium and distracts the corrosion current [22].

Table 3. Kinetic parameters of the corrosion process obtained by non-linear regression using the Stern-Geary equation for interpretation of the polarization curves

Electrode	Zn-Ni	Zn-Ni +PEG+ Vanillin	Zn-Ni +PEG+ Vanillin+ 3g/l TiO_2	Zn-Ni +PEG+ Vanillin+ 5g/l TiO_2	Zn-Ni +PEG+ Vanillin+ 10g/l TiO_2
i_{corr} (A/cm^2)	$4.0*10^{-5}$	$6.3*10^{-6}$	$5.0*10^{-5}$	$2.0*10^{-5}$	$1.0*10^{-5}$
b_a* (V^{-1})	25.13	11.86	2.00	17.07	13.37
$-b_c$* (V^{-1})	2.30	2.18	10.46	4.26	13.18
E_{corr} (V/SCE)	-0.848	-0.469	-0.717	-0.646	-0.601

*b_a and b_c are the Tafel anodic and cathodic activation coefficients, respectively.

A decrease tendency of corrosion current densities of the coatings was noticed with increasing TiO_2 concentration in the plating bath. However, it should be mentioned that the differences between i_{corr} values for the samples obtained from baths containing different amounts of TiO_2 are not significant, being situated within limits of experimental errors. The acceleration of the corrosion process on Zn-Ni with additives and nanoparticles in comparison with the case of pure Zn-Ni could be due to defects and dislocations or to chemical heterogeneities generated in the metallic matrix by the embedded particles.

CONCLUSIONS

The analysis of the results led to the following conclusions:

(i) A correlation between preferred crystallographic orientation and surface morphology and of the electrodeposits was put on evidence. The platelet type grains are closely related to the (330) (or (100)) orientation.

(ii) the corrosion process on Zn-Ni-TiO_2 composite coatings is only slightly slower than on pure Zn-Ni surface and no significant decrease of corrosion current densities of the coatings were noticed with increasing TiO_2 concentration in the plating bath; this behaviour could be explained by the balance occurring between two contrary effects: on one side, the embedded inert oxide particles diminish the active surface in contact with the corrosive environment and, on the other side, they disturb the electrocrystallization process, by generating dislocations and defects in the metallic matrix which act as chemical heterogeneities and favour the corrosion process.

EXPERIMENTAL SECTION

Electrodeposition

Zn-Ni alloys were deposited from alkaline electrolytes (pH 13-14) containing 15 g/l ZnO (Merck, Germany), 130 g/l NaOH (Merck, Germany), 80 g/l triethanolamine (TEA) (Sigma-Aldrich, Germany) and 6 g/l $Ni_2SO_4*6H_2O$ (Reactivul Bucuresti). 3 ml/l Polyethylene glycol (PEG) and 10 mg/l vanillin (Sigma-Aldrich, Germany) were used as brightening agents. TiO_2 nanoparticles (99.5%, 21 nm, Degussa) were added into the plating bath in order to obtain composite Zn-Ni-TiO_2 coatings. The concentrations of TiO_2 nanoparticles were x =0 (sample S_0), x = 3 g L^{-1} (sample S_3), x = 5 g L^{-1} (sample S_5) and x=10 g L^{-1} (sample S_{10}), respectively.

Experiments were carried out in a two compartments glass cell, with the capacity of 250 ml, under magnetic stirring. The working electrode was a steel (OL 37) disk electrode, (S = 0.502 cm^2) Ag/AgCl/KCl_{sat} was used as reference electrode and a Pt foil as counter electrode. Before using, the working electrode was wet polished on emery paper of different granulation

and finally on felt with a suspension of alumina. Then, the electrode was ultrasonicated during 2 minutes, washed with acetone and distilled water in order to remove the impurities from the surface.

Corrosion measurements

For corrosion studies, a solution of 0.2 g L^{-1} $(Na)_2SO_4$ (Riedel–de Haën, Germany) (pH 5) was used.

Electrochemical measurements (open circuit potential and polarization curves) were carried out using a PC controlled potentiostat PARSTAT 2273 (Princeton Applied Research, USA). Before the polarization measurements, the open circuit potential (ocp) was recorded during 1 hour, until it was stabilized.

For evaluation of corrosion resistance, polarization measurements were carried out in 0.2g/l Na_2SO_4, using a three electrode cell. The scan rate was 0.166 mV s^{-1}, and the sweep direction was from cathodic to anodic region. Corrosion tests were conducted at room temperature.

Morphological and structural analysis

The deposit structure and the preferred orientation of crystallites were determined by X-ray diffraction (XRD) analysis, using a Brucker X-ray diffractometer with a Cu K_α (λ = 0,15406 nm) at 45 kV and 40 mA. The 2θ range of 20–100º was recorded at the rate of 0.02º and 2θ /0.5 s. The crystal phases were identified comparing the 2θ values and intensities of reflections on X-ray diffractograms with JCP data base using a Diffrac AT-Brucker program. The deposit morphology was determined with a scanning electron microscope (SEM) (Philips XL-30). The chemical composition of the nanocomposite films was determined by using an EDAX NEW XL30 (Philips) X-ray dispersive energy analyzer attached to the SEM.

ACKNOWLEDGMENTS

The authors gratefully acknowledge the financial support within the projects **POSDRU/88/1.5/S/60185** – "Innovative doctoral studies in a Knowledge Based Society" Babeş-Bolyai University, Cluj-Napoca, Romania and **PN II INOVARE No. 261/2008 (ZINITECH).**

REFERENCES

1. M.G. Hosseini, H. Asassi-Sorkhabi, H.A.Y. Ghiasvand, *Surface & Coatings Technology,* **2008**, *202*, 2897.
2. M.G. Hosseini, H. Asassi-Sorkhabi, H.A.Y. Ghiasvand, *Iranian Corrosion; ICA International Congress, Tehran: May 14-17,* **2007**.

3. G. Roventi, R. Fratesi, *Surface & Coatings Technology,* **1996,** *82*, 158.
4. M. Musiani, *Electrochimica Acta*, **2000**, *45*, 3397.
5. M. Pushpavanam, S.R. Natarajan, K. Balakrishnan, and L.R. Sharma, *Journal of Applied Electrochemistry*, **1991**, *21*, 642.
6. J. Fustes & A. Gomes & M.I. da Silva Pereira, *Journal Solid State Electrochem.,* **2008**, *12*, 1435.
7. B.M. Praveen, T.V. Venkatesha, *Applied Surface Science*, **2008**, *254*, 2418.
8. R. Ramanauskas, *Appllied Surface Science,* **1999**, *153*, 53.
9. C.G. Fink, J.D. Prince, *Transactions of the American Electrochemical Society*, **1928**, *54*, 315.
10. M. Sider, C. Fan, D.L. Piron, *Journal of Applied Electrochemistry,* **2001**, *31*, 313.
11. L.S. Tsybulskaya, T.V. Gaevskaya, O.G. Purvskaya, T.V. Byk, *Surface & Coatings Technology*, **2008**, *203*, 234.
12. Metals Handbook, 9th ed., *ASM International*, **1992**, 3.
13. F. Mansfeld, S. Gilman, *Journal of the Electrochemical Society*, **1970**, *117*, 588.
14. M.S. Chandrasekar, S. Srinivasan, M. Pushpavanam, *Journal of Solid State Electrochemistry*, **2009**, *13*, 781.
15. D.B. Lewis, C.E. Lehmberg, G.W. Marshall, *Transactions of Institute of Metal Finishing*, **2004**, *82* (1–2), 64.
16. L. Felloni, R. Fratesi, E. Quadrini, *G.* Roventi, *Journal of* Applied *Electrochemistry*, **1987**, *17,* 574.
17. E. Raub, F. Elser, Metalloberflache **1957**, *11* (5), 165.
18. M.S. Chandrasekar, S. Srinivasan, M. Pushpavanam, *Journal of Solid State Electrochemistry,* **2009**, *13*, 781.
19. D.E. Hall, *Plating & Surface Finishing*, **1983**, *70*, 59.
20. O. Kardos, D.G. Foulke, "Applications of mass transfer theory. Electrodeposition on small-scale profiles" in Advances in Electrochemistry and Electrochemical Engineering; Tobias, Ch.W.; Ed.; Publisher: Interscience New York, NY, **1966**, *2*, 145.
21. L.M. Muresan, S.C. Varvara, "Leveling and Brightening mechanisms in Metal Electrodeposition" in Metal Electrodeposition, Ed. M. Nunez, Nova Science Publishers, Inc. New York, **2005**, chapter 1.
22. M. Stern, A. L. Geary, *Journal of Electrochemical Society,* **1957**, *104*, 56.

STUDIA UBB CHEMIA, LVI, 1, 2011

IN DEPTH VARIATION OF WATER PROPERTIES FOR ST. ANA LAKE – ROMANIA RELATED TO SEDIMENTS IN SUSPENSION

RAMONA FLAVIA CÂMPEAN[a], NELI KINGA OLAH[b*], CLAUDIA TOMA[c], RISTOIU DUMITRU[d], GEORGE ARGHIR[e]

ABSTRACT. The minerals identified in the sand shore and mud from the bottom of St. Ana Lake is: biotite, potassic feldspar, hornblende, potassic muscovite, and hydrate silicate mixed with amorphous andesite. Such mineral particles were observed suspended in the water from an average depth of 2 m to the bottom. The suspended particle average diameter and density increases along with the water depth, which may affect water properties. We found that the electrical conductivity is close to the distilled water in the upper layers and increases to the bottom due to the dissolved mineral ions. The turbidity is very low, at the surface and progressively increases at 4 meter depth, because of the particle density variation in lower water layer. The pH has an acid range. The pH values are slowly decreasing with the water depth due to the acid pH of phylosilicates. The main metal found is Fe, the concentration is considerably below the standard limit. It increases with water depth due to the increased concentration of biotite and hornblende particles floating in the water. There were also identified traces of Zn and Cu in very low concentrations and no traces of Pb and Cd. All measurements performed in July 2010 prove that the St. Ana Lake presents a normal state for a closed water system with no pollution trace.

Keywords: *volcanic lake, turbidity, electrical conductivity, pH, heavy metals*

INTRODUCTION

St. Ana Lake is situated in Romania in the area of volcanic mountain chain Călimani - Gurghiu – Harghita. It represents the unique crater lake in the Eastern Europe formed by water accumulation in the Ciomadu Mare volcano cone. The earliest scientific reports on the volcanic origin of the lake were

[a] *Babeş-Bolyai University, Faculty of Environment Science, Str. Fântânele, No. 30, RO-400294 Cluj-Napoca, Romania and SC PlantExtrakt SRL, 407059 Rădaia*
[b] *"Vasile Goldis" West University of Arad, Faculty of Pharmacy, Department of Pharmaceutical Industry, 1 Feleacului Street, 300041, Romania and SC PlantExtrakt SRL, 407059 Rădaia*
[*] *correspondent author*
[c] *"Vasile Goldis" West University of Arad, Faculty of Pharmacy, Department of Pharmacognosy, 1 Feleacului Street, 300041, Romania*
[d] *Babeş-Bolyai University, Faculty of Environment Science, Str. Fântânele, No. 30, RO-400294 Cluj-Napoca,Romania*
[e] *Technical University of Cluj-Napoca, Faculty of Materials Science and Engineering, Muncii Ave., No. 103 – 105, RO-400641 Cluj-Napoca, Romania*

published in 1956 and 1964 [1, 2]. Further the area presents a great geological interest. Some of the newest studies affect the geology of the area to Later Tertiary and Quaternary [3, 4].

Geological drillings revealed two petrologic formations: the deeper layer containing amorphous volcanic glass with andesites and pyroxenes. The second formation is situated at the surface containing amorphous volcanic glass with andesite, hornblende and biotite [5]. However, pyroxene degradation forms several minerals such hornblende and biotite [6, 7] which could be found in the crater soil and gravel. Such soil and gravel forms the sand shore of St. Ana Lake and also covers the formation in the crater depth.

St. Ana Lake was formed exclusively by accumulation of precipitation having no other water sources. The structure of volcano cone is formed by pyroclastic rocks e.g. andesite, and pyroxenes binded with volcanic glass covered with sand and gravel resulted from upper formation's erosion. This structure of the lake's bottom is permeable due to the cracks in pyroclastites causing some water loss. Actually the water level is 6.4 m varying according to the precipitation amount [8, 9]. The average level of 6 m is sustained by an impermeable layer of mud deposed at the lake bottom having the maximum thickness of 4 m [8]. The variation of water level is related only to the infiltration in the shore pyroclastite, gravel and sand.

The rain water presents a high level of purity very close to distilled water with a slighter acid pH due to CO_2 dissolving from atmosphere and this unless there are some pollution traces [10, 11]. St. Ana lake has no other water sources than precipitations so the water in the lake must have physical – chemical properties similar to the distilled water. By natural way there are involved some interactions with shore sand, gravel and respectively with the mud from the bottom of the lake that could affect the water's properties. On the other hand some research mentions some alteration of the local environment due to the intense touristy traffic mainly increased rates of lead pollution [8].

The aim of present article is to investigate the mineralogical composition of St. Ana Lake shore and bottom related to the measured water properties at different depths.

RESULTS AND DISCUSSION

Assuming all considerations concerning closed water systems results that the single minerals involved at St. Ana Lake are the sand shore and the mud from the bottom. The mineral composition was identified by X-ray diffraction analysis. The obtained diffractograms are presented in Figure 1. Both spectra presents well developed diffraction peaks corresponding to the crystalline minerals and a curved baseline due to the amorphous volcanic glass. There were found the following minerals (in order of their amount): potassic feldspar, biotite, hornblende, potassic muscovite, and hydrate silicate for both investigated samples.

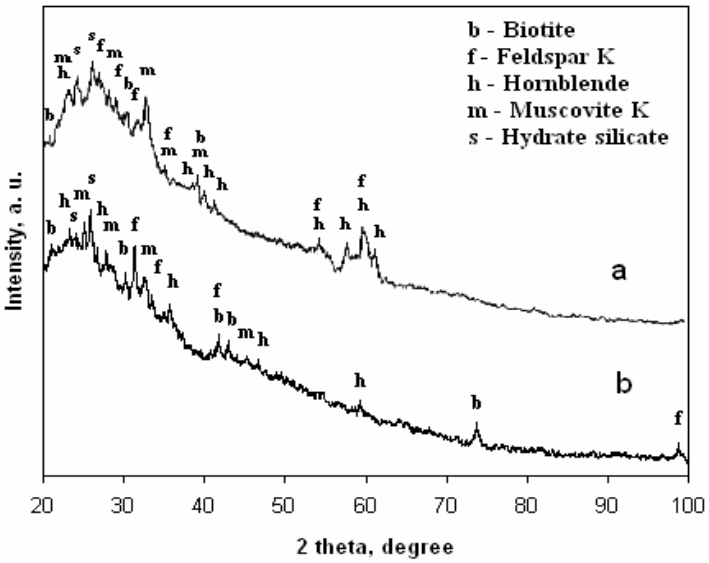

Figure 1. The X ray diffraction spectra for samples collected from St. Ana Lake: a) sand collected from the shore, and b) dry mud from the bottom of lake.

Potassic feldspar is a tectosilicate based on tetrahedral $[SiO_4]^{4-}$ structure with a ¼ amount of Al^{3+} ions which forms extra bounds $[AlO_4]^{5-}$ which fix alkaline ions such K^+ or Na^+. The chemical formula for identified potassic feldspar is: $K(AlSi_3O_8)$. It has a triclinic crystal structure and appears in a bright white color in cross polarized light [6, 12]. This structure is more stabile than inosilicates and phylosilicates. There were found some altered form of potassic feldspar as hydrate silicate which have the chemical formula $K_4(H_4Si_4O_{12})$ [13].

Another important mineral found is the hornblende. It is an inosilicate having simple or double infinite chains of tetrahedral $[SiO_4]^{4-}$ mixed with extra bounds $[AlO_4]^{5-}$. The free valence of Al^{3+} in the chains structure bonds several ions such Mg^{2+}, Ca^{2+}, Fe^{2+}, Fe^{3+}, and others [6]. The chemical formula for identified hornblende is: $Ca_2(Fe_2,Mg)_4Al(Si_7Al)O_{22}(OH,F)_2$. The double chains are very resistant due to SiO_2 units in the tetrahedral silica meanwhile Mg^{2+}, Ca^{2+}, Fe^{2+}, Fe^{3+} ions have weaker bonds [14]. The hornblende sheets appear in a greenish color in cross polarized light.

It was also found a new class of silicate - phylosilicates. They are the result of decomposed tectosilicates and inosilicates. In this case are formed very resistant pseudo-hexagonal planes of tetrahedral $[SiO_4]^{4-}$ bonded by 3 common oxygen molecules. The free valences resulted are perpendicularly oriented to the planes which bounds ions such Al^{3+}, Fe^{2+}, Fe^{3+}, Mg^{2+}, K^+ which assure a monoclinic crystal structure [6]. One of the most important phylosilicate found is the biotite. The chemical formula of biotite is $KFeMg_2(AlSi_3O_{10})(OH)_2$ [15]. We notice the presence of Mg^{2+} and Fe^{2+} ions which gave a shiny black color

of biotite crystals, which is also known as black mica. In cross polarized light it features an orange – red color with pleochroism. Similar to biotite we found muscovite, the common mica. The chemical formula is $H_2KAl_3Si_3O_{12}$ [16]. The crystal structure is similar to biotite and the microscopic aspect is bright featuring a yellow colour in cross polarized light.

Figure 2a presents the optical transmitted light microphotograph for the sand shore sample. We observe a wide range of particle size. The occurrence of crystals in the sand is observed in cross polarized light microphotograph. There are revealed large green hornblende particles having at least 75 μm diameter, reddish biotite and yellow muscovite particles with a planar average dimension of almost 100 μm, and several potassic feldspar particle featured in a bright white color having around of 50 μm diameter. There are also observed some traces of fine particles of similar occurrence having at least 10 μm.

In Figure 2b are presented the optical microphotographs for the mud collected from the bottom of the lake. There are revealed formations of very fine particles having the average diameter between 5 and 10 μm. The particle refinement influence the color of cross polarized light where the formations appear in a diffuse light due to the small particle mixture. However there are observed some of bigger reddish biotite and potassic feldspar particles having around of 20 μm diameter [28].

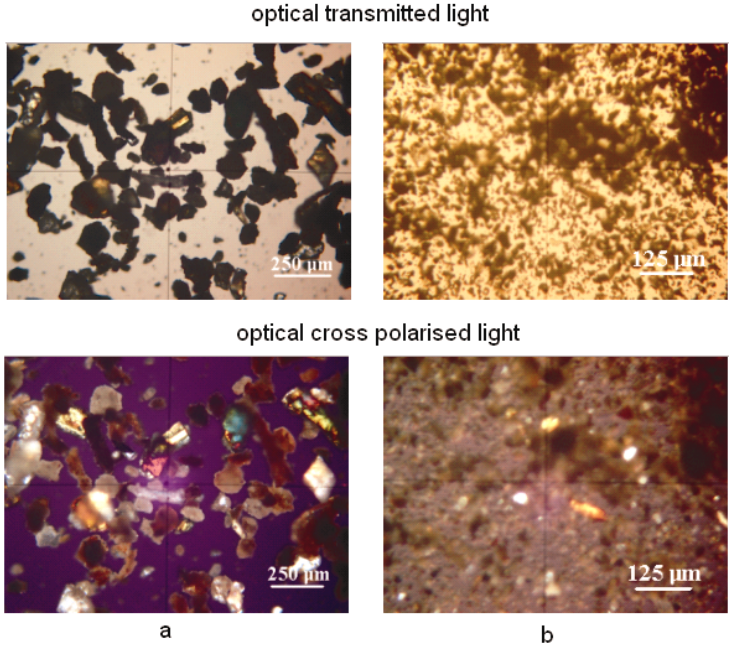

Figure 2. Optical microphotographs for samples collected from St. Ana Lake: a) sand collected from the shore, and b) dry mud from the bottom of lake.

Optical microscopy reveals that the particles of sand are rough micro-scaled particles instead of small particles which are rather found in the mud from the bottom and they have similar mineralogical structure. Small particles of clays and inosilicates are able to release ions at longer exposure in wet environment [17, 18]. Some recent studies evaluate the clays ability of ions releasing in some pH controlled environment. There were noticed the releases of Al^{3+}, Fe^{2+}, Ti^{2+}, and Zn^{2+} in acid environment [19, 20].

We identify the following minerals that which release ions: the biotite, the muscovite, and the hornblende due to their lamellar structure and weaker bonds between lamellae. The main released ions are Fe^{2+}, K^{+}, and Mg^{2+} because of their positions as bonds between pseudo-hexagonal lamellae. Assuming the ions releasing as an emergent hypothesis the water properties of St. Ana Lake will vary according to the particles distribution at different depths.

The quantitative particle distribution measure is given by the average diameter and average percentage density unit. Optical microscopy investigation prove that the water from the surface to 2 m depth is free of micro-scaled particles, but they were found dispersed in water samples from 2 m to the bottom of the lake (4 m), Figure 3.

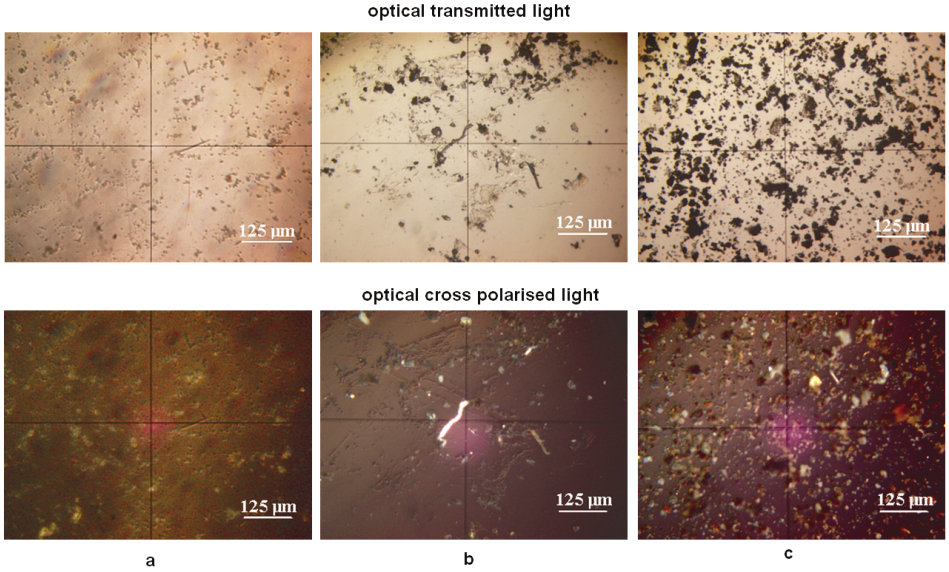

Figure 3. Optical microphotographs for water sample collected from different depths: a) 2 m, b) 3 m and c) 4m.

The optical transmitted light microphotographs of water sample collected from 2, 3, and 4 m depth are presented in Figure 3. At 2 meters we observe, Figure 3a, several very small micro-scaled particles, at 3 m they are bigger

and finally at 4 m they are the biggest. In cross polarized light at 2 meters, particles are so small that appears as a low diffused light which could not allow identifying of certain mineral. At 3 and 4 m depth there could be observed in cross polarized light, Figure 3 b and c, some potassic feldspar, biotite and hornblende particles. The quantitative analysis on optical microphotographs was performed by Image J processing soft and the results are plotted in Figure 4.

The particles average diameter variation with water depth, Figure 4a, was correlated with particle density distribution presented in Figure 4b. In the water layer from 0 to 2 m depth were found no micro-scaled particles proving that they are dispersed. At 2 m depth we found an average particle size of 5.53 μm related to a density of 7 %, at 3 m depth the particle average diameter became 10.60 μm related to a density of 25 % meanwhile at 4 m depth the average particle diameter is 14.58 μm corresponding to a density of 55 %. The situation observed at 4 m depth is very close to the mud from the bottom, the observed particle diameter is in good agreement. This difference is due to a lower particle density than in the mud layer.

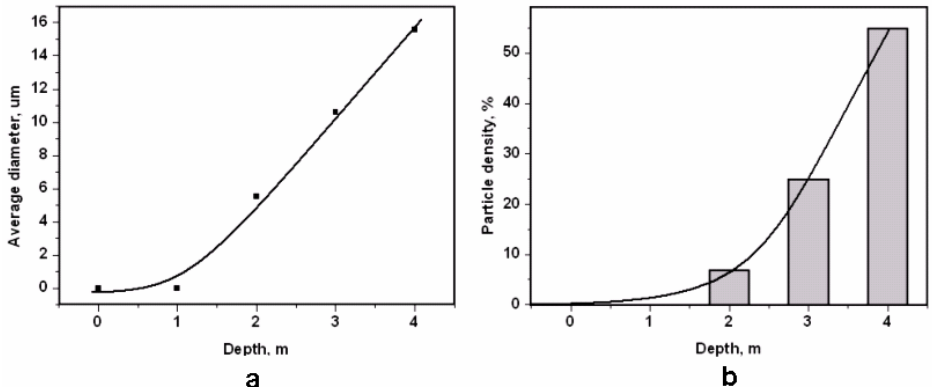

Figure 4. Particle distribution versus water depth:
a) Average diameter and b) Particle density.

Particle size distribution feature a parabolic shape related to a half – Gaussian distribution of density which means a possibly exponential increasing of water turbidity with water depth. Smallest particles related to a low density, case at 2 m depth, assure a low dispersion of light radiant flux in a turbidity nephelometer, respectively a low amount of scattered light. This situation leads to a low turbidity. Increased particle sizes and their density lead to an average scattered light in a nephelometer, case of 4 m depth, which gave an average turbidity. The usual turbidimeters have two ranges of measurements: for very low turbidity between 0 – 40 NTU (the sensor is set for scattered light) and for high turbidity between 40 – 4000 NTU. For high turbidity measurements it is used the direct light beam attenuation [21, 22].

In Figure 5a is presented the resulted variation of water turbidity versus depth. We observe that all obtained values are below the limit of 40 NTU which means that the water in St. Ana Lake is clear. At the surface and at 1 m depth were obtained turbidity values 2.18 and 2.55 NTU, very low values induced by possible nano - suspensions (e.g. particles with diameter under 100 nm which could not appear at common optical microscopy inspection). The turbidity increases sensibly at 2 m resulting 3.03 NTU, a value still very low. The notable increasing turbidity is between 3 and 4 m depth where it increases from values of 3.55 to 25.7 NTU. This strong increasing is due to the proximity of mud layer. The turbidity variation features a part of a logarithmic shape which probably leads to a constant value in the compact mud layer (a high turbidity domain). Based on the observation in Figure 5a, water turbidity is rather affected by the particle density in the water layers than their size.

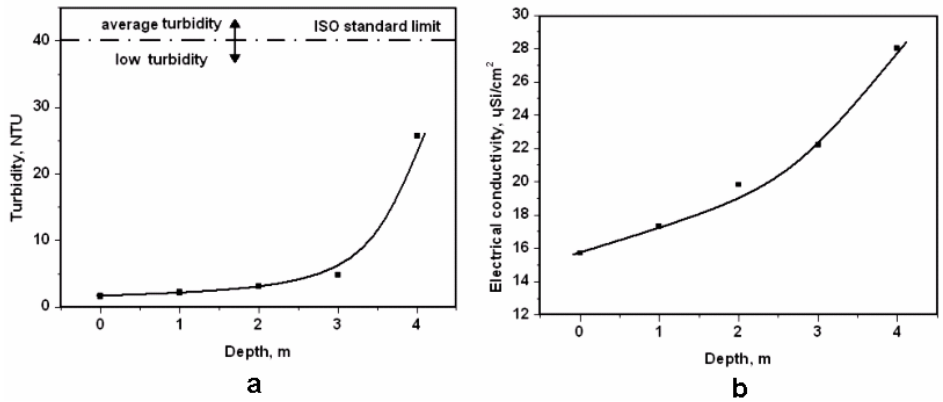

Figure 5. Physical properties of water versus water depth:
a) Turbidity and b) Electrical conductivity.

The other main physical property of water is the electrical conductivity. It is affected by salts dissolved in water such carbonates and chlorides. The electrical conductivity increases proportionally to the amount of dissolved solids [23, 24]. Minerals identified for St. Ana Lake shore and bottom mud are not soluble in water so the electrical conductivity must be preserved. However, as mention before minerals such biotite, hornblende and feldspar are able to release ions at longer contact with water, fact favored by a lower pH value [17 – 20].

The only water source of St. Ana Lake is the precipitation (e.g. rainfall and snow) which leads to an electrical conductivity similar to the rain water. This hypothesis is confirmed by the value obtained at the water surface 13.5 μS/cm. The electrical conductivity increases progressively with the suspended particle density resulting 26.8 μS/cm at 4 m depth, value comparable to the well water.

The observed electrical conductivity variation proves the hypothesis of ions releasing, fact confirmed also by the variation of pH and Fe content.

In Figure 6a is presented the variation of pH versus water depth. The measurements points out a pH of 6.82 at water surface close to the neutral value. The pH value is typical for rain water which is slightly lower than neutral because of CO_2 dissolved from atmosphere during the raining [10, 11]. In the precipitation samples, the pH values range from 5.18 to 7.30 [29] and we observed similar values. The pH decreases directly proportional with the water depth resulting at 4 m an acidic value of 5.80. Resulted values are in good agreement with the observations for other inactive volcanic crater lakes [25], while the active ones presents a lower pH due to intensive emission of SO_2 [26, 27].

The observed acidic pH in the lower water layer of St. Ana Lake favors a slow and continuous releasing of Al^{3+}, Fe^{2+}, and Zn^{2+} from biotite, hornblende, and potassic feldspar proving the variation of electrical conductivity without solids dissolvation.

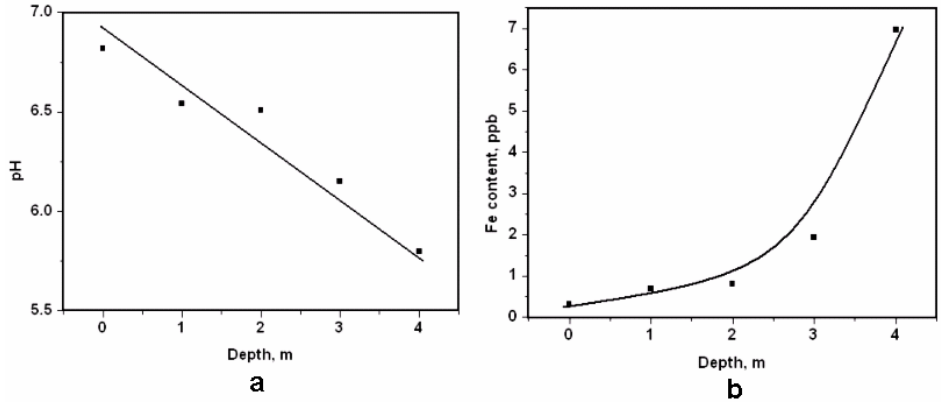

Figure 6. Chemical properties of water versus water depth: a) pH and b) Fe content.

We want it to prove that St. Ana lake has no pollution. The determined heavy metals were chosen according to the environmental criteria. These heavy metals have a relevant impact on the environment and their absence is a sign that the lake is not polluted.

The most important element involved in identified minerals is the Fe due to its belonging of heavy metals which could be traced. The performed measurements pointed out significant amounts of Fe, but situated far below the maximum admitted level, Figure 6b. At the water surface and 1 m depth the Fe content is under the detection limit which is 2,02 ppm. The Fe content has an increasing tendency with water depth. The strongest increase is observed

between 3 and 4 m depth from values of1.94 ppb to 6.96 ppb. Comparing with the turbidity evolution, the water with higher turbidity in St. Ana Lake features also a higher content of Fe.

Heavy metals measurements found traces of Cu and Zn, resulted average values are Cu = 0.03 ppb and Zn = 0.05 ppb. The performed measurements show that in St. Ana Lake at investigation period (July 2010) are no traces of Cd and Pb, the samples results were: Cd is under the detection limit which is 0,17 ppm and Pb is under the detection limit which is 0,084 ppm. This situation is very good for the environment condition and proves a very good improvement from the state reported in 2008 by Duliu et al. [8]

Cu and Zn traced in identified minerals are in very low amounts. Because Cd and Pb are missing, the observed traces of Cu and Zn are rather found by natural reasons (similar to Fe content) than due to some pollution sources.

All measurements prove that the water properties of St. Ana Lake varies with water depth in a naturally manner due to the distribution of mineral particles suspended in water layer. At the investigation time, July 2010 results that there are no traces of pollution in aquatic environment.

CONCLUSIONS

The minerals identified in the sand shore and mud from the bottom of St. Ana Lake is: biotite, potassic feldspar, hornblende, potassic muscovite, and hydrate silicate mixed with amorphous andesite. Such mineral particles were observed suspended in the water from an average depth of 2 m to the bottom. We found that the electrical conductivity is close to the distilled water for the upper layers and increases to the bottom due to the dissolved mineral ions, mainly Fe^{2+}, released by phylosilicates and tectosilicates (e.g. biotite and hornblende). The turbidity is very low at the surface and progressively increased at 4 meter depth, because of the particle density variation in lower water layers. The pH is in an acid range having a slight decreasing with the water depth due to the acid pH of phylosilicates. The main metal found is Fe, the concentration is considerably under the standard limit. It increases with water depth due to the increasing of biotite and hornblende particles floating in water. There were also identified traces of Zn and Cu in very low concentrations and no traces of Pb and Cd. All measurements performed in July 2010 prove that the St. Ana Lake presents a normal state for a closed water system with no pollution trace.

EXPERIMENTAL SECTION

The sand samples were collected from all exposed shore and mixed into an average sample representative for all regions. Mud samples were taken with a manual dredge from several points and mixed into a representative sample which was naturally dried.

Representative average water samples were extracted with a specific device from top of water and from 1, 2, 3 and 4 m depth. Water samples were transported to the lab in proof well sealed plastic bottles. Water samples were preserved with 1% HNO_3 until conductivity and pH measurements were taken.

The sand and mud samples were investigated by X – ray diffraction analysis using a DRON 3 diffractometer improved with registering module and professional analyzing soft. It was used a Co k_{α} monochrome radiation. Diffraction peaks identification was done using standard database MATCH edited and compiled by Crystal Impact.

Sand, mud and water samples were inspected by optical transmission light and cross polarized light using a Laboval 2 mineralogical microscope produced by Carl Zeiss Jena.

Electrical conductivity and pH were measured with HI 255 Combined Meter & EC/TDS/NaCl Hanna Instruments. Turbidity was measured with a turbidity meter 4193414, Hanna Instruments. Water samples were preserved with 1% HNO_3 until conductivity and pH measurements.

The metal content was measured by emission spectrometry / flame atomic absorption AAS Sens Spectrophotometer, GBC Australia. For the heavy metals determination, water samples were prepared as following: take 50 ml of water and bring to dry, then resume with 10 mL 0.5 M HNO_3. The used wavelengths are: for Cu - 324,70 nm, for Fe - 248,30 nm, for Zn - 213,90 nm, for Pb - 217,00 nm and for Cd - 228,00 nm. Each sample determination is repeated three times by the device. The results are the average readings. The quantitative determination is made based on calibration curves constructed with standards.

REFERENCES

1. D. Slavoaca, C. Avramescu, *Academia R.P.R., Comunicari,* **1956**, *VI.* 3.
2. A. Lazar, E. Arghir, *Comunicari Geologice,* **1964**, *vol L/2*, 87-101.
3. S. Szakacs, I. Seghedi, *Acta Vulcanologica*, **1995**, *7*, 145–153.
4. D. Karatson, *Zeitschrift fur Geomorphologie*, **1999**, *114*, 49–62.
5. I. Seghedi, A. Szakacs, M. Kovacs, E. Rosu, Z. Pecskay, Sed inst. Geol. Geof., **1995**, *76*, no.7, 49-50.
6. G. Arghir, L.M. Ghergari, Cristalografie – Mineralogie Indrumător de lucrări de laborator, Litografia Institutului Politehnic din Cluj – Napoca,**1983**.
7. I. Seghedi, H. Downes, Z. Pecskay, M.F. Thirlwall, A. Szakacs, M. Prychodko, D. Mattey, *Lithos*, **2001**, *57*, 237.
8. O. Duliu, T. Brustur, Ş. Szobotka, G. Oaie, C. Ricman, V. Alexe, M. Iovea, S. Hodorogea, *Geo-Eco-Marina,* **2008**, *14, supliment nr. 1,* 181.

9. A.G. Pilbath, Z. Pal, Microregiunea Ciomad-Balvanyos, Ed. Green Steps România, **2007**.
10. I. Haiduc, Chimia mediului ambiant. Controlul calității apei, Ed. Universității Babeş-Bolyai, Cluj-Napoca, **1996**, 61.
11. G. B. Lawrence, *Atmospheric Environment*, **2002**, *36*, 1589.
12. ***, Feldspat potassic, Match Diffraction Database, Match PDF # 89-8572, Crystal Impact, **2008**.
13. ***, Potassic Hydrate Silicate, Match Diffraction Database, Match PDF # 72-1101, Crystal Impact, **2008**.
14. ***, Hornblende, Match Diffraction Database, Match PDF # 71-1060, Crystal Impact, **2008**.
15. ***, Biotite, Match Diffraction Database, Match PDF # 80-1106. Crystal Impact, **2008**.
16. ***, Muscovite, Diffraction Database, Match PDF # 02-1019. Crystal Impact, **2008**.
17. F. Tateo, V. Summa, M.L. Giannossi, G. Ferraro, *Applied Clay Science*, **2006**, *33*, 181.
18. F. Tateo, V. Summa, *Applied Clay Science,* **2007**, *36*, 64.
19. J.R.O. Kikouama, K.L. Konan, A. Katty, J.P. Bonnet, L. Baldea, N. Yagoubi, *Applied Clay Science*, **2009**, *43*, 135.
20. F. Tateo, A. Ravaglioli, C. Andreoli, F. Bonina, V. Coiro, S Degetto, A. Giaretta, A. Menconi Orsini, C. Puglia, V. Summa, *Applied Clay Science*, **2009**, *44*, 83.
21. ***, EPA, Quality criteria for water, *Office of Water Regulations and Standards*, Washington DC 20460, U.S., **1986**.
22. ***, Water Quality – Determination of turbidity, *ISO European Standards*, EVS-EN ISO 7027:2000, **2000**.
23. D. Masterman, K. Redding, Water Quality with Vernier*, Vernier Software & Technology Guidelines*, **2006**.
24. I. Chicinaş, N. Jumate, V. Pop, Fizica materialelor metode experimentale, Presa Universitară Clujeană, Cluj-Napoca, **2001**.
25. J.C. Varekamp, G.B. Pasternack, G.L. Rowe Jr, *Journal of Volcanology and Geothermal Research*, **2000**, *97*, 161.
26. B.W. Christenson, *Journal of Volcanology and Geothermal Research*, **2000**, *97*, 1.
27. M. Martınez, E. Fernandez, J. Valde, V. Barboza, R. Van der Laat, E. Duarte, E. Malavassi, L. Sandoval, J. Barquero, T. Marino, *Journal of Volcanology and Geothermal Research*, **2000**, *97*, 127.
28. Ramona-Flavia Câmpean, Dumitru Ristoiu, George Arghir, Aspects Concerning the Nano-Sediments Compozition and Distribution in St Ana Lake-Romania, *Studia UBB Ambientum*, **2009**, LIV, 1-2, p. 11.
29. ***, Raport privind starea factorilor de mediu în județul Harghita, Semestru II, 2010, Ministerul Mediului şi Pădurilor, Agenția Națională pentru Protecția Mediului Bucureşti, Agenția pentru Protecția Mediului Harghita Miercurea Ciuc.

STUDIA UBB CHEMIA, LVI, 1, 2011

ELECTROCHEMICAL BEHAVIOUR OF $YBaCo_4O_7$ IN NEUTRAL AQUEOUS SOLUTION

MIRCEA DAN*[a], NICOLAE VASZILCSIN[a], ANDREA KELLENBERGER[a], NARCIS DUTEANU[a]

ABSTRACT. Considering the possibility to use $YBaCo_4O_7$ as oxygen sensor in different environments, the study of electrochemical behaviour of this compound was extended for neutral aqueous solution. Cyclic voltammetry and electrochemical impedance spectroscopy have shown that the compound behaviour in neutral solution is different than that in alkaline one. Compound porosity was determined using BET technique and the results are in accordance with thermogravimetric studies carried out in oxygen flow for $YBaCo_4O_7$ compound, emphasizing the oxygen intake / release by $YBaCo_4O_7$. Correlating all these results, an electrochemical mechanism for $YBaCo_4O_7$ oxidation in neutral aqueous solution has been proposed.

Keywords: *mixed oxides, $YBaCo_4O_7$, electrochemical behaviour of $YBaCo_4O_7$, cyclic voltammetry, electrochemical impedance spectroscopy, BET technique.*

INTRODUCTION

Recent studies have revealed special structural, electrical and magnetic properties of Y-114 mixed cobalt oxide. Due to these properties the mixed cobalt oxides can be used as membranes with high oxygen permeability, oxygen sensors and also as cathodic material in fuel cells [1-5].

The compound $YBaCo_4O_7$, also named Y-114, has been extensively studied since 2002 by Valldor et al. [6,7].

The electrochemical behaviour of Y-114 mixed oxide has been studied in alkaline solutions [8] and had as starting point the electrochemical intercalation the oxygen inside of transitional metal oxide network, presented by J.C. Grenier et al. [9,10] as well as the experimental results regarding the electrochemical cobalt behaviour studied by cyclic voltammetry and electrochemical impedance spectroscopy [11].

The aim of the present paper is to study the electrochemical behaviour of Y-114 mixed oxide in neutral aqueous solution (Na_2SO_4 0.5 mol L^{-1}) and to give an insight of its anodic oxidation mechanism. To the best of our knowledge, there are no studies devoted to the electrochemical behaviour of $YBaCo_4O_7$ in aqueous neutral solutions.

[a] *University "POLITEHNICA", Faculty of Industrial Chemistry and Environmental Engineering, P-ta Victoriei, Nr.6, RO- 300006 Timisoara, Romania, * mircea.dan@chim.upt.ro*

RESULTS AND DISCUSSION

Due to Y-114 structural and morphological complexity, the shape of polarization curves depends on the working conditions; a critical parameter is represented by the polarization rate.

Cyclic voltammograms recorded starting from -1.8 V versus Ag/AgCl are depicted in Fig. 1. All these curves were recorded after a prior polarization at -1.8 V (versus Ag/AgCl) for 300 seconds in order to remove the superficial adsorbed oxygen.

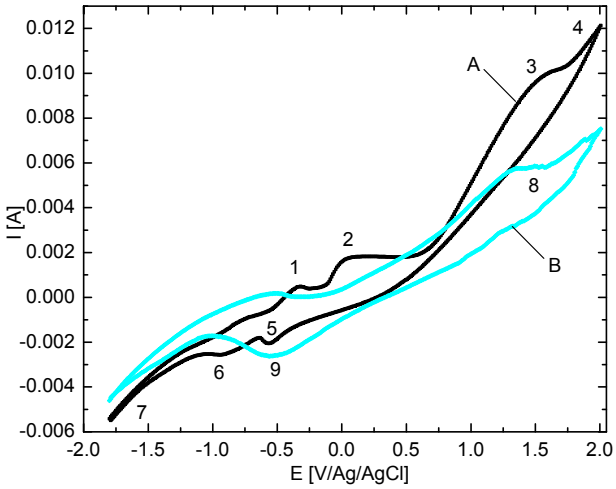

Figure 1. Cyclic voltammograms (A-first cycle; B-fifth cycle) on $YBaCo_4O_7$ working electrode in 0.5 mol L^{-1} Na_2SO_4 solution at 10 mV s^{-1} scan rate.

Analyzing the voltammograms presented in Fig. 1, one can observe the appearance of an anodic peak (1) in the first cycle. This peak can be associated with oxidation of superficial adsorbed hydrogen or of absorbed hydrogen inside the mixed oxide network during cathodic polarization. At more positive electrode potential an anodic wave (2) appears. This wave is associated with cobalt oxidation ($Co \rightarrow Co^{II} + 2e^-$). When the electrode potential becomes more positive a second anodic wave (3) associated with oxidation of Co (II) ions ($Co^{II} \rightarrow Co^{III} + e^-$) can be observed. Like in alkaline media, anodic oxidation of Co (II) ions consists in oxygen insertion into the mixed oxide crystalline structure. When the electrode potential is over 1.17 V versus Ag/AgCl oxygen evolution on electrode surface can be noticed.

On the backward scan a cathodic peak (5) associated with reduction of Co (III) ions to Co (II) ions was noticed, followed by a small current plateau (6) associated with reduction of Co (II) ions to Co. When the electrode potential becomes more negative the hydrogen evolution reaction was observed (7).

The insertion of oxygen ions into the Y-114 crystalline structure leads to its compaction, resulting in the inhibition of redox processes at the Y-114 / electrolyte solution interface. Therefore, the peak height and also the limiting currents decrease during electrochemical polarization. In the fifth cycle, the polarization curves details are fading, except the anodic wave (8) associated with oxidation of Co (II) ions and also the reduction peak (9) associated with the reduction of Co (III) ions to Co (II).

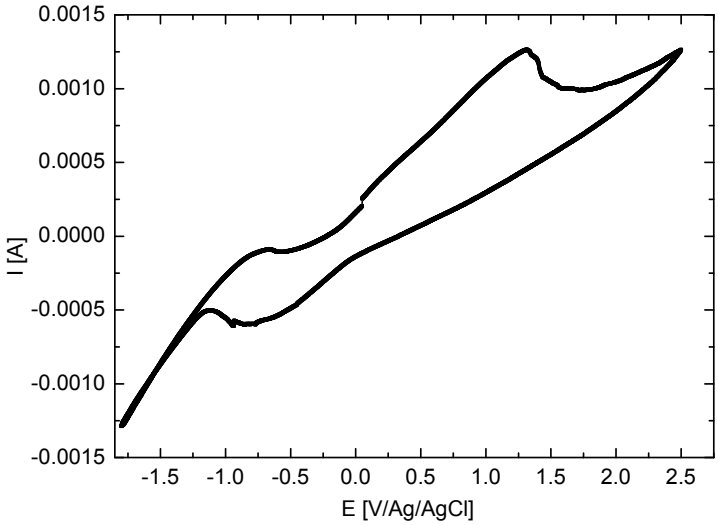

Figure 2. Cyclic voltammogram on $YBaCo_4O_7$ working electrode in 0.5 mol L^{-1} Na_2SO_4 solution at 5 mV s^{-1} scan rate.

When the cyclic voltammograms were recorded at lower polarization rate (5 mV s^{-1}), starting from open circuit potential (OCP) with polarization at OCP for 300 s (Fig. 2), the first peak 1 (Fig. 1) corresponding to the oxidation of Co to Co (II) was not obtained. The lower polarization rate, leads to higher quantities of electricity crossing the interface during the experiment. A further analysis of the CV shown in Fig. 2, reveals a net oxidation peak related to the oxidation of Co (II) ions to Co (III) ions, instead of the plateau recorded at higher polarization speed (Fig. 1). This process is controlled by the diffusion of O^{2-} ions inside of Y-114 mixed oxide and not by the diffusion of different ionic species presented in the adjacent electrolyte solution. Quasi-irreversible nature of the oxidation of Co (II) ions is distinguishable both by the higher difference between potentials related with the oxidation and reduction peak potentials and also by the attenuation with almost 50% of the reduction peak height in comparison with the oxidation peak.

When cyclic voltammograms were recorded at higher polarization scan rate (100 mV s^{-1}) the anodic wave associated with the oxidation of the Co (II) ions is indistinct and overlapped over the oxygen evolution curve as is depicted in Fig. 3.

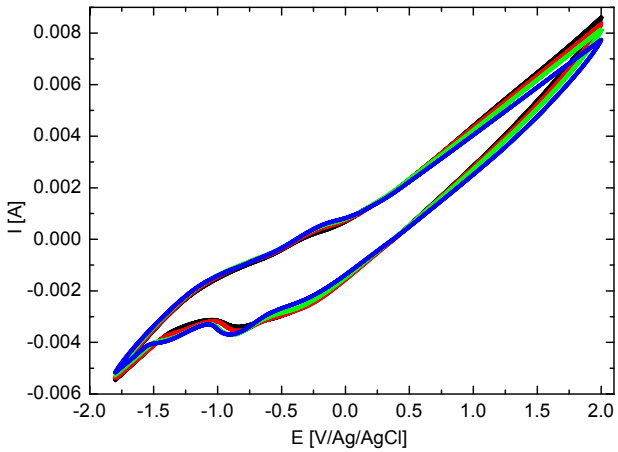

Figure 3. Cyclic voltammogram (5 cycles) on $YBaCo_4O_7$ working electrode in 0.5 mol L^{-1} Na_2SO_4 solution at 100 mV s^{-1} scan rate.

The compound porosity was determined by the BET technique and the results are presented in Table 1.

Table 1. BET surface area, pore diameter, and pore volume of the $YBaCo_4O_7$ sample

Parameter	Value
BET Surface Area	0.3108 m^2 g^{-1}
BJH Desorption average pore diameter (4V/A)	11.0584 nm
BJH Desorption cumulative volume of pores between 1.7000 nm and 300.0000 nm diameter	0.000786 cm^3 g^{-1}

This will lead to large specific surface and provide channels favouring adsorption and desorption of oxygen in time of electrochemical polarization. Compared with dense bulk sample, this porous balls show fast oxygen adsorption and desorption rates.

SEM images obtained for $YBaCo_4O_7$ bar electrode used in this work are presented in Fig. 4. Analyzing the SEM images, a porous structure due to crystallites agglomeration can be observed. This structure equalizes with a large number of pores inside of ceramic electrode. Large pores amount lead to a higher specific surface with channels which favour oxygen adsorption / desorption process and lead to a high concentration of superficial active ions.

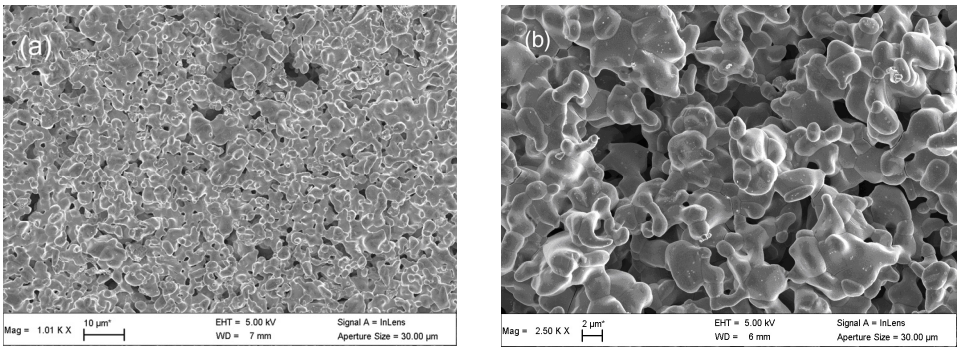

Figure 4. SEM images of the $YBaCo_4O_7$ electrode's surface before electrochemical oxidation/reduction at 1000x(a) and 5000x(b) magnification

Based on all information presented above we are presenting a mechanism for Co (II) to Co (III) global oxidation process in neutral aqueous solution in Fig. 5.

This way the oxygen activity in the superficial layer becomes more pronounced than oxygen activity in the bulk of mixed oxide. This activity gradient determines to the oxygen diffusion from the surface of Y-114 compound into the mass of mixed oxide. Oxygen diffusion rate is much lower in comparison with charge transfer or hydroxyl ions diffusion from the electrolyte solution to the electrode surface.

Therefore, the electrochemical oxidation of Co (II) to Co (III) actually consists in oxygen insertion into the crystalline structure of $YBaCo_4O_7$. Consequently, during oxidation the crystalline network of Y-114 mixed oxide becomes more compact (dense), so that oxygen diffusion is slower. Furthermore, the oxidation process of Co (II) to Co(III) is not complete.

The constriction of the mixed oxide layer induces a slight irreversible character to the oxidation of Co (II) ions, which leads to the disappearance of the oxidation plateau (3) and also to the attenuation of the reduction peak (6) in comparison with the oxidation peak (Fig. 1).

According with the presented mechanism, at anodic polarization, after the OCP, the oxidation process is controlled by the charge transfer step; this is supported by the electrochemical impedance spectra.

The electrochemical impedance spectra recorded for the $YBaCo_4O_7$ electrode during oxidation at E = 0.3 V in neutral solution are given in Fig.6.

The experimental complex plane plots show distinct features depending on the frequency range. Thus, the final part of an incomplete semicircle can be observed at high frequencies, between 100 kHz and 30.9 kHz, which is related to a charge transfer process. A slightly curved line related to a Gerischer element appears at intermediate frequencies, between 30.9 kHz and 141 Hz. Finally, a large semicircle is observed at low frequencies, between 141 Hz and 1 mHz.

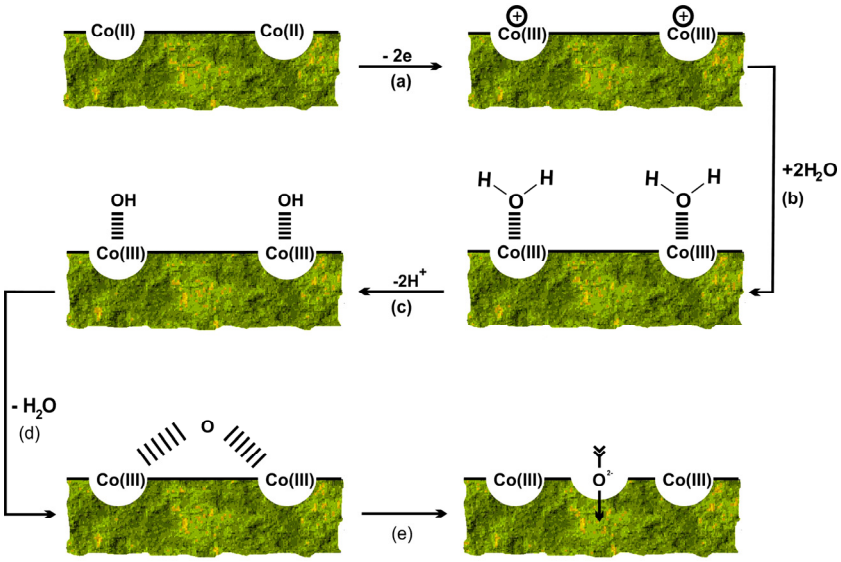

Figure 5. Proposed mechanism for the electrochemical oxidation of $YBaCo_4O_7$ in neutral solutions:

a) oxidation of Co^{2+} ions at electrode interface;
b) addition of water molecules at newly formed Co^{3+} cations;
c) elimination of H^+ ions;
d) elimination of H_2O and structural rearrangement of $YBaCo_4O_7$;
e) diffusion of oxygen ions; *lines*- preponderant ionic interaction.

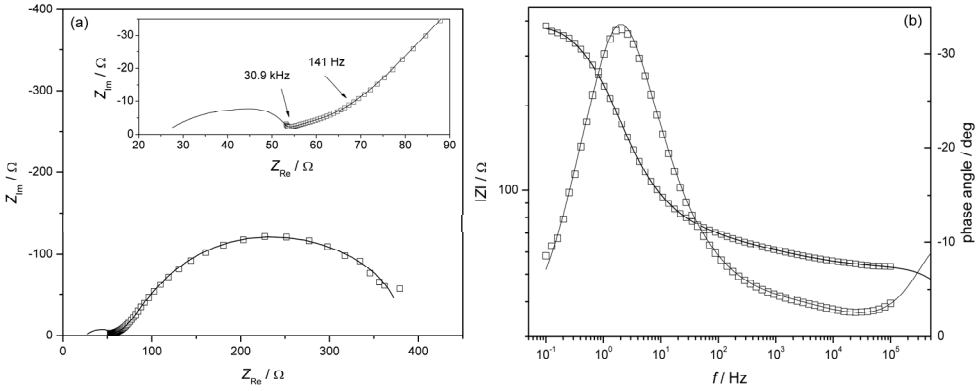

Figure 6. Experimental Nyquist (a) and Bode (b) plots for $YBaCo_4O_7$ at E = 0.3 V in 0.5 mol L^{-1} Na_2SO_4. Inset: enlargement of the medium to high frequency domain. Open symbols are experimental points and continuous lines are simulated by the CNLS fitting according to the equivalent circuit.

The experimental impedance data were modelled using the equivalent circuit given in Fig. 7. It consists of an ohmic resistance R_{Ohm} in series with a parallel connection of a constant phase element (CPE) and the charge transfer resistance R_{ct} followed by a Gerischer element (GE) and a parallel connection of a Warburg element (W) and a resistance (R) in series with a capacitor (C).

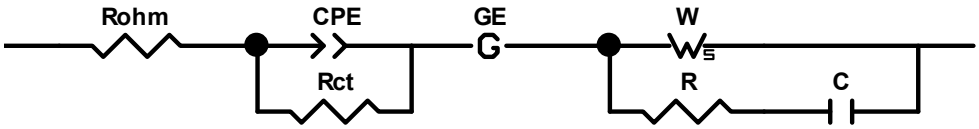

Figure 7. Equivalent electric circuit for modelling oxygen insertion into the $YBaCo_4O_7$ electrode in neutral solution.

The ohmic resistance includes the uncompensated solution resistance and a contribution from the resistance of the $YBaCo_4O_7$ electrode. The constant phase element replaces the double layer capacitance since it has been observed that it describes more accurately the behaviour of real electrochemical systems. The Gerischer element [13] is a diffusion element, similar to the Warburg impedance, which has been proposed to describe the alternating current response of an electrochemical system where a chemical reaction is preceding or following the electrochemical reaction. In its most simple form the impedance of a Gerischer element is given by:

$$Z_{GE} = Z_0 / (k + j\omega)^{1/2}$$

where Z_0 is the magnitude of the impedance at $\omega = 1$ rad s^{-1} and k is a rate constant parameter.

The experimental impedance data were fitted to the equivalent circuit using a complex non-linear least squares procedure. The results of the fitting are shown as continuous lines in Fig. 6 and the corresponding values of the circuit elements, together with their standard errors are given in Table 2.

The high frequency part of the impedance spectra could be fitted only if the ohmic resistance was imposed to a fixed value. However, if the proposed model is used to simulate the response at high frequencies up to 10^8 Hz the whole semicircle is visible as a continuous line in the inset of Fig. 6a. The constant phase angle parameter n has a value of 0.52 and is considered to be related to surface inhomogeneities and porosity of the electrode. Values around 0.9 are common for metal electrodes, while lower values of 0.6 have been reported for porous electrodes [14].

Table 2. Experimental values of the circuit elements during oxidation of $YBaCo_4O_7$ in neutral solution

Parameter	Value
R_{Ohm} [Ω]	25 (fixed)
T [F s^{n-1}]	$7.04 \times 10^{-4} \pm 2.54 \times 10^{-4}$
n	0.52 ± 0.04
R_{ct} [Ω]	10.07 ± 0.89
Z_0 [Ω $s^{1/2}$]	$0.00344 \pm 6.2 \times 10^{-5}$
k [s^{-1}]	1.72 ± 0.03
R_W [Ω]	126.0 ± 2.2
τ_D [s]	$1.855 \times 10^{-6} \pm 0.185 \times 10^{-6}$
ϕ	0.5 (fixed)
R [Ω]	34.57 ± 0.71
C [F]	$9.06 \times 10^{-4} \pm 0.17 \times 10^{-4}$

CONCLUSIONS

Results obtained by cyclic voltammetry in neutral aqueous solution showed that the $YBaCo_4O_7$ mixed oxide is sensitive to anodic or cathodic polarization. Based on the experimental data we can conclude that the electrochemical oxidation of Co(II) ions consist in oxygen insertion in the mixed oxide structure. Because of that during oxidation the Y-114 crystalline network becomes denser, so that oxygen diffusion rate is lowered.

The compaction of Y-114 during oxidation imposes a partial irreversible character of this process, and as a consequence the oxidation leads to disappearance of the oxidation plateau and also to the attenuation of the reduction peak.

Based on the EIS spectra and the presented mechanism, the oxidation process is controlled by the charge transfer step. Thus, a complete structural characterization of the fully oxidized phase will be discussed in a forthcoming paper.

EXPERIMENTAL SECTION

The $YBaCo_4O_7$ compound was obtained using a solid state reaction, by mixing the precursor Y_2O_3, $BaCO_3$ and $CoO_{4/3}$ according to the stoichiometric cation ratio. After decarbonisation at 1000°C the powder was pressed in bars (2x2x10 mm). The bars were fired in air for 48h at 1200°C and then removed rapidly from furnace and set to ambient temperature. [1,3,4,6,12].

The electrochemical measurements were carried out using an Autolab PGSTAT 302N equipped with electrochemical impedance spectroscopy (EIS) module. The electrochemical cell was a conventional one-compartment, three-electrode glass cell with a volume of 50 mL. Two graphite counter electrodes were placed symmetrically next to the working electrode made of $YBaCo_4O_7$ pressed bar and a Ag/AgCl(sat) electrode was used as reference. All potentials in this work are given versus the reference electrode. All electrochemical measurements were performed in 0.5 mol L^{-1} Na_2SO_4 electrolyte solution. Electrochemical impedance spectroscopy measurements were carried out using the FRA module of Autolab 302N, in the frequency range from 0.1 Hz to 100 kHz and AC voltage amplitude of 10 mV. For each spectrum 60 points were collected, with a logarithmic distribution of 10 points per decade. The experimental electrochemical impedance data were fitted to the electrical equivalent circuit by a complex non-linear least squares (CNLS) Levenberg – Marquardt procedure using ZView – Scribner Associates Inc. software.

The surface area was determined according to the Brunauer-Emmet-Teller (BET) method using a ASAP 2020 M (Micromeritics Instrument Corporation USA).

REFERENCES

1. E.V. Tsipis, D.D. Khalyavin, S.V. Shiryaev, K.S. Redkina, P. Núñez, *Materials Chemistry and Physics*, **2005**, *92*, 33.
2. H. Hao, J. Cui, C. Chen, L. Pan, J. Hu, X. Hu, *Solid State Ionics,* **2006**, *177*, 631.
3. H. Haoshan, Z. Limin, H Jie, H. Xing, H Hongwei, *Journal of Rare Earths*, **2009**, *27*, 815.
4. E.V. Tsipis, V.V. Kharton, J.R. Frade, P. Núñez, *Journal of Solid State Electrochemistry*, **2005**, *9*, 547.
5. K. Zhang, Z. Zhu, R. Ran, Z Shao, V.V. Jin, S. Liu, *Journal of Alloys and Compounds*, **2010**, *492*, 552.
6. M. Valldor, M. Andersson, *Solid State Science*, **2002**, *4*, 923.
7. M. Valldor, *Solid State Science*, **2004**, *6*, 251.
8. M. Dan, V. Pralong, N. Vaszilcsin, A. Kellenberger, N. Duteanu, *Journal of Solid State Electrochemistry*, published online, DOI 10.1007/s10008-010-1189-3.
9. J.C. Grenier, A. Wattiaux, J.P. Doumerc, P. Dordor, L. Fournes, J.P. Chaminade, M. Pouchard, *Journal of Solid State Chemistry*, **1992**, *96*, 20.
10. J.C. Grenier, J.M. Bassat, J. P. Doumerc, J. Etourneau, Z. Fang, L Fournes, S. Petit, M. Pouchard, A. Wattiaux, *Journal of Materials Chemistry*, **1999**, *9*, 25.
11. K.M. Ismail, W.A. Badawy, *Journal of Applied Electrochemistry*, **2000**, *30*, 1303.
12. M.D. Levi, H. Gizbar, E. Lancry, Y. Gofer, E Levi, D. Aurbach, *Journal of Electroanalytical Chemistry*, **2004**, *569*, 211.
13. H. Gerischer, *Zeitschrift für Physikalische Chemie*, **1951**, *198*, 216.
14. A. Kellenberger, N. Vaszilcsin, W. Brandl, *Journal of Solid State Electrochemistry*, **2007**, *11*, 84.

EQUILIBRIUM AND KINETIC STUDIES OF IRON (II) REMOVAL FROM 34% CALCIUM CHLORIDE SOLUTIONS BY CHELATING RESIN PUROLITE S930

CAMELIA POPA[a], PETRU BULAI[a], MATEI MACOVEANU[a]

ABSTRACT. This work presents equilibrium, thermodynamic and kinetic studies of iron removal from 34% $CaCl_2$ solution (that was obtained from electrolysis sludges) using chelating resin Purolite S930 with iminodiacetic acid functional groups.

Batch sorption experiments were performed using both forms of the resin (S930-Na and S930-H) by varying the initial conditions such as initial solution pH (2.0-5.0), initial concentration of iron (20-400mg/L), solution temperature (22-40^{0}C) and contact time (10 minutes up to 24 hours). The practical capacity of the resin increases with initial solution pH, temperature and the initial concentration of iron(II). Freundlich constants (n) had values bigger than 1 for the whole range of temperature that was studied, so, the sorbtion of iron on Purolite S930-Na form resin is a favourable one. The values of correlation coefficients (R^2) higher than 0,99 show that on the studied concentration (200-400mg Fe(II)/L) and temperature (295-313 K) range the data were more suitable to the Langmuirl model. The values obtained for the Langmuir (R_L) constant ($0 < R_L < 1$) show a favourable isotherme for the whole range of temperature that was studied (295-313 K). The maximum sorption capacity (q_{max}) was 238 mg Fe(II)/g for pH5. The values of calculated thermodynamic parameters (ΔG^0, ΔH^0 and ΔS^0) indicate that the sorption of iron onto Purolite S930 resin is an endothermic and spontaneous process. The kinetic data show that, initially, sorption increases rapidly, but after that, the rate becomes slower; the equilibrium can be considered attained after 24 hours. Kinetic studies reveal that the sorption of iron from 34% $CaCl_2$ solution onto chelating resin follows a pseudo-second order model.

Keywords: *Iron (II) removal, Purolite S 930, Sorption isotherm, Thermodynamics, Kinetics*

INTRODUCTION

From chemical industry results important quantities of sludges. The most part of these sludges contain useful compounds that can be reused to obtain other chemical products. Depending on the method used to recover this compounds, the new chemical products may contain also heavy metals.

[a] *"Gh. Asachi" Technical University of Iasi, Faculty of Chemical Engineering & Environmental Protection, Department of Environmental Engineering & Management, 71 A, D. Mangeron Blvd., 700050 Iasi, Romania*

The presence of the heavy metals in the environment is a major problem, so to find another purification technique than chemical precipitation is very important in environmental protection.

Ion exhange methodes are profitable and ecological as purification methodes and may be used for organic and inorganic compounds. Some advantages of these methodes are: good percent of removal, safe operation, easy to use, no sludges and recovery of the sorbed. Ion exhangers have also great exchange capacity, long operating life and big number of operating cycles[1, 2].

The aim of this work is to extend the application of Purolite S930 chelating resin for the purification of 34% $CaCl_2$ solution obtained from electrolysis sludges [3].

The sorption characteristics of iron ions onto iminodiacetic resin Purolite S930 was studied in various operating conditions like: initial pH, initial iron concentration, contact time, temperature, ionic form of the resin and resin dose.

RESULTS AND DISCUSSIONS

Sorption isotherms. The relationship between the amount of Fe(II) sorbed onto Purolite S930 and equilibrium concentration in 34% $CaCl_2$ solution is described by the sorption isotherms. The analysis of equilibrium data was used to verify the sorption models and also to determine the values of real sorption capacity.

The sorption of Fe(II) by Purolite S930 resin was quantitatively evaluated by percent of Fe(II) removal *R* (%) and by amount of Fe(II) retained on resin, *q* (mg/g), according to Eqs.1 and 2:

$$R = \frac{C_0 - C_e}{C_0} 100 ; \quad (1)$$

$$q = \frac{(C_0 - C_e)V}{m} ; \quad (2)$$

where C_0 and C_e are the initial and the equilibrium concentration of Fe(II) in the solution (mg/L), *V* is the volume of solution (L) and *m* is the amount of the resin (g).

Figure 1 shows the sorption isotherms of iron (II) from 34% $CaCl_2$ solution onto sodium form of Purolite S930 resin, for different values of solution pH. The influence of the initial iron concentration on loading capacity of the resin is presented in Figure 2.

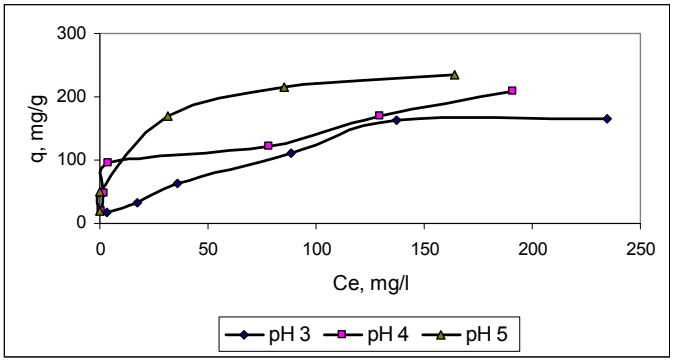

Figure 1. Isotherm plot for Fe (II) sorption onto Purolite S930-Na resin; T=22^{0}C, resin dose=1g/L, contact time=24h;

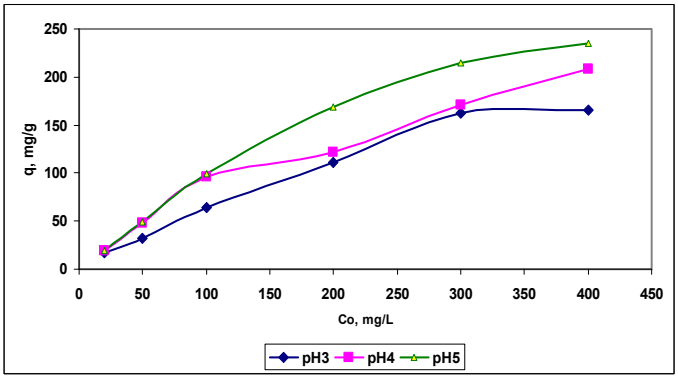

Figure 2. The influence of the initial iron concentration on loading capacity; T=22^{0}C, resin dose=1g/L, contact time=24h;

The equilibrium data obtained from sorption experiments were fitted using Freundlich, Langmuir and Dubinin models. The equation parameters of these models provide important information about the sorption mechanism, the surface properties and the affinity of the sorbent [6].

Freundlich model

The *Freundlich* equation is an empirical relationship established upon sorption onto a heterogeneous surface supposing that different site involve different sorption enegies.

$$q = K_F C^{1/n} \quad (3)$$

where K_F (mg/g) and n are Freundlich constants witch incorporate all factors affecting the sorption process such as sorption capacity and intensity of sorption. These constants are determined from the intercept and slope of linear plot of log q_e versus log C_e [7].

$$\lg q = \lg K_F + \frac{1}{n} \lg C_e \tag{4}$$

To determine the values of Freundlich parameters (K_F and n) the experimental data where plotted as *log q* versus *log* C_e, as shown in Figure 3.

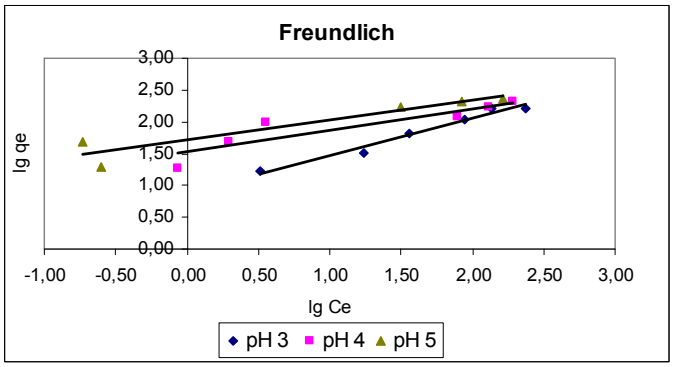

Figure 3. Freundlich isotherm plots for the sorption of iron (II) from 34%$CaCl_2$ solution onto Purolite S930-Na resin; T=22^{0}C, resin dose=1g/L, contact time=24h

Langmuir model

Langmuir sorption isotherm shows the maximum sorption capacity supposing monolayer sorption on a surface with a finite number of identical sites.

$$\frac{C_e}{q} = \frac{1}{q_{\max}} C_e + \frac{1}{K_L q_{\max}} \tag{5a}$$

$$\frac{1}{q} = \left(\frac{1}{K_L q_{\max}} \right) \frac{1}{C_e} + \frac{1}{q_{\max}} \tag{5b}$$

where q_{max} and K_L are Langmuir isotherm constants. Thus, q_{max} show the maximum sorption capacity (mg/g) while K_L is the equilibrium constant relating adsorption capacity (L/mg). Langmuir constants are evaluated from the slope and intercept of the C_e/q_e versus C_e. The dimensionless parameter of the equilibrium R_L was calculated using eq. 6.

$$R_L = \frac{1}{1 + K_L \cdot C_0} \tag{6}$$

where C_0 (mg/L) is the initial metal ion concentration. This parameter may have four values: $R_L = 0$ for an irreversible sorption isotherm, $0 < R_L < 1$ for a favourable sorption isotherm, $R_L = 1$ for a sorption linear isotherm and $R_L > 1$ for an unfavourable sorption [7].

The equilibrium data were also fitted to linear Langmuir I and Langmuir II equations (5a, 5b). The Langmuir parameters (q_{max} and K_L) were determined by plotting Ce/q_e versus C_e (Fig. 3.4.) and $1/q_e$ versus $1/C_e$ respectively (Figure 4 and Figure 5).

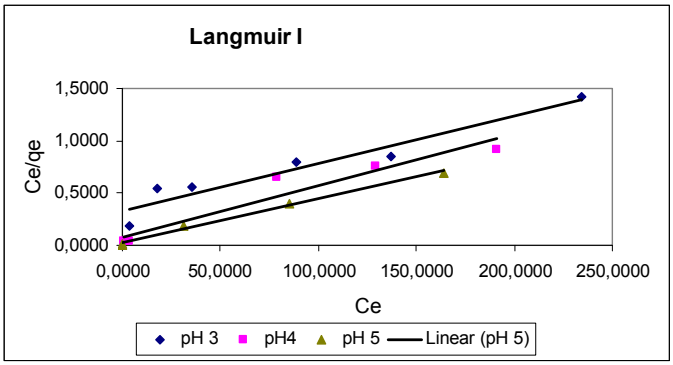

Figure 4. Langmuir I isotherm plots for the sorption of iron(II) from 34%$CaCl_2$ solution onto Purolite S930-Na resin; T=22^{0}C, resin dose=1g/L, contact time=24h;

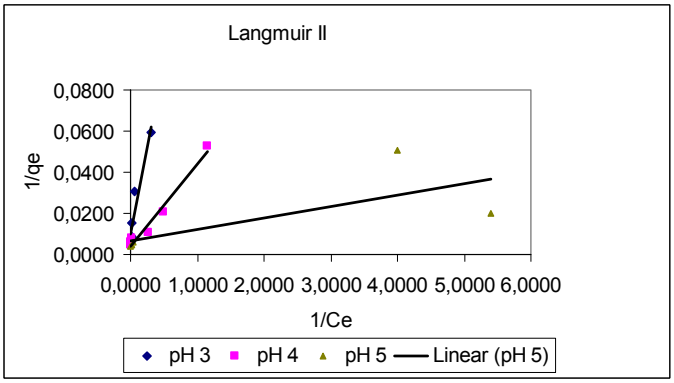

Figure 5. Langmuir II isotherm plots for the sorption of iron(II) from 34%$CaCl_2$ solution onto Purolite S930-Na resin; T=22^{0}C, resin dose=1g/L, contact time=24h;

For defining the model wich describes in the best way possible the experimental data, there were used linear regression analysis.

The values of isotherm parameters for different initial pH are presented in Table 1.

The high coefficient of determination (R^2 = 0.994) of the plot shows that the linear Langmuir equation gives the best fit to the sorption isotherm for the sorption of Fe(II) onto Purolite S930 resin at 295 K. For an initial pH = 5 and a temperature of 295 K, the Langmuir maximum sorption capacity q_{max} was 238 mg Fe (II)/L and the Langmuir equilibrium constant K_L, had a value of 0.178 L/g.

Table 1. pH dependence of the isotherm parameters for iron(II) sorption onto Purolite S930 resin from 34% $CaCl_2$ solutions at T = 295 K

	pH=3	**pH=4**	**pH=5**
Freundlich	y=0.583x+0.887 R^2=0.974 n=1.71 K_F =7.72	y=0.342x+1.526 R^2=0.823 n=2.92 K_F =33.59	y=0.202x+0.888 R^2=0.567 n=4.92 K_F =77.57
Langmuir I	y=0.004x+0.336 **R^2=0.928** q_{max} =222.2mg/g K_L=0.107L/mg = 6000 L/mol ΔG= - 21337.27 kJ/mol	y=0.005x+0.072 **R^2=0.937** q_{max} =200 mg/g K_L=0.069 L/mg = 3872.75 L/mol ΔG= - 20263.5 kJ/mol	y=0.004x+0.023 **R^2=0.994** q_{max} =238.1 mg/g K_L=0.178 L/mg = 9974.04L/mol ΔG= - 22441.56 kJ/mol
Langmuir II	y=0.168x+0.0095 R^2=0.915	y=0.039x+0.0041 R^2=0.966	y=0.005x+0.0068 R^2=0.518
Dubinin	y=-0.0053x+7,30 β=0.006mo l^2/J^2 q_{max}=793.14 mg/g R^2=0.936 *E*=9.12 kJ/mol	y=-0.0027x+6,25 β=0.004mo l^2/J^2 q_{max}=384.9 mg/g R^2=0.992 *E*=11.18 kJ/mol	y=-0.0041x+5,95 β=0.002mo l^2/J^2 q_{max}=519.57 mg/g R^2=0.797 *E*=15.81kJ/mol

Each ,,R^{2}" value, was calculated for 6 points of concentration: 20, 50, 100, 200, 300, 400 mg Fe(II)/L.

Figure 6 shows the variation of sorption intensity (R_L) with initial metal concentration in the 34% $CaCl_2$ solution, for the range of pH (3-5) and temperature 295 K.

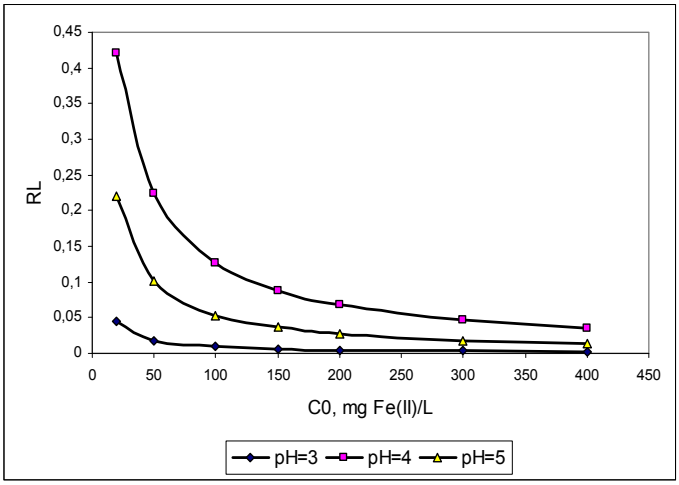

Figure 6. Variation of sorption intensity (R_L) with initial metal concentration; 34%$CaCl_2$ solution, 1 g/L S930 - Na, contact time 24 h, pH = 3-5, temperature: 295 K

The values for sorption capacity q_{max}=200-238 mg/g are comparable with literature data that are described in Table 2 [4].

The Dubinin–Radushkevich isotherm is expressed in linear form as follows [8,9].

$$\ln q = \ln q_{\max} - \beta\varepsilon^2 \tag{7}$$

where q_{max} is the maximum sorption capacity (mg/g), β, the activity coefficient related to mean sorption energy (mol^2/J^2) and ε is the Polanyi potential (J/mol) equal to:

$$\varepsilon = RT \ln(1 + \frac{1}{C_e}) \tag{8}$$

where R is the gas constant and T is the temperature. The mean free energy of sorption, E (kJ/mol), can be estimated using the following equation:

$$E = \frac{1}{\sqrt{-2\beta}} \tag{9}$$

Table 2. Sorption capacity for Fe(III) on different kinds of resins

Metal	Resin	Loading capacity, mg/g
Fe(III)	Amberlite IRC-50	200
Fe(III)	Amberlite IRC-76	235,2
Fe(III)	Dowex MAC-3	182,9
Fe(III)	Duolite C-433	231,5
Fe(III)	Duolite C-436	216,5
Fe(III)	Amberlite IRC-86	225,9

The mean free energy of sorption E, gives information about the type of the sorption mechanism as chemical, ion-exchange or physical sorption.

If ,,*E"* value is between 8 and 16 kJ/mol, the sorption process follows a chemical ion-exchange; if ,,E" value is less than 8 kJ/mol, the sorption is physical [7].

To determine the nature of sorption process (physical or chemical), the experimental data were fitted to the *Dubinin isotherm mode*l based on the heterogeneous surface of the sorbate (Figure 7).

The isotherm parameters were computed from the graphical representation of *ln q* = f(ε^2) equation. (Table 1). The value of the mean free energy of sorption E calculated with Eq. (9) was 11.62 KJ/mol indicating that the sorption process follow a chemical ion-exchange mechanism.

The validity of Freundlich and Langmuir models within the range of 295-313 K. The isotherms for this range of temperature are presented in Figure 8 and the results are shown in Table 3.

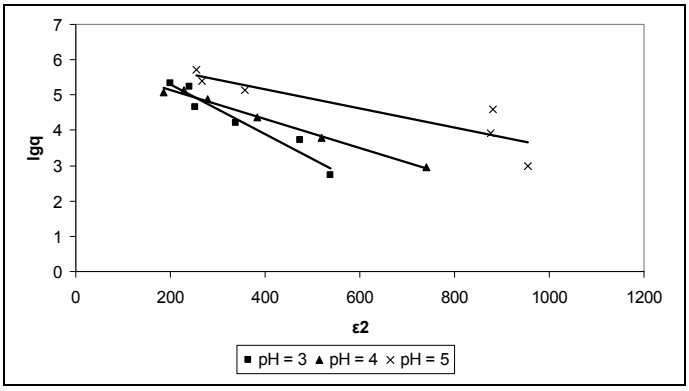

Figure 7: D-R isotherm plots for the sorption of Fe (II) from $CaCl_2$ 34% solution, onto S930 – Na resin;1 g/L S930-Na, contact time 24 h, temperature: 22 ºC

The high coefficient of determination (R^2) of the plot shows that the linear Langmuir equation gives the best fit to the sorption isotherm for the sorption of Fe(II) onto Purolite S930 resin in the whole range of temperature that was studied.

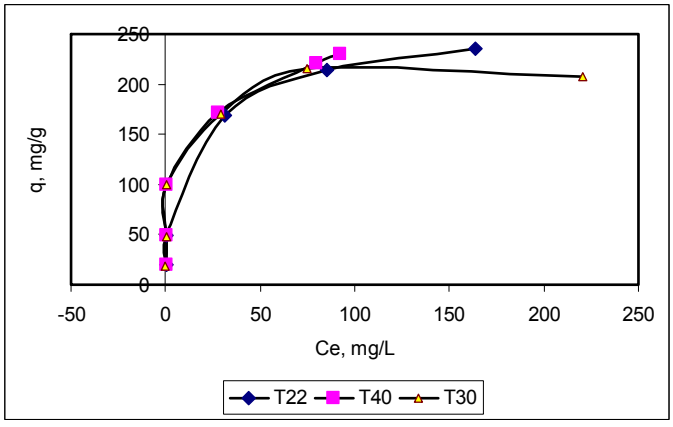

Figure 8. Sorption isotherms from iron(II) onto Purolite S930-Na form resin, different temperatures, 34% $CaCl_2$ solution

Table 3. Temperature dependence of the isotherm parameters for iron(II) sorption onto Purolite S930-Na form resin from 34% $CaCl_2$ solutions at pH=5

	T=295K	T=303K	T=313K
Freundlich	y=0.202x+0.888 R^2=0.56 n=4.92 K_F =77.5711	y=0.271x+1.802 R^2=0.82 n=3.68 K_F =63.44	y=0.309+1.820 R^2=0.78 n=3.24 K_F =66.17

	T=295K	T=303K	T=313K
Langmuir I	y=0.004x+0.023 **R^2=0.994** q_{max} =238.1mg/g K_L=0.178 L/mg = 9974.04L/mol ΔG = - 22441.5 J/mol	y=0.004x+0.005 **R^2=0.939** q_{max} =267.8 mg/g K_L=0.183 L/mg = 10265.62L/mol ΔG = - 23279.7 J/mol	y=0.003x+0.016 **R^2=0.937** q_{max} =272.3 mg/g K_L=0.206 L/mg = 11540.46L/mol ΔG = - 24352.4 J/mol
Langmuir II	y=0.005x+0.006 R^2=0.519	y=0.004x+0.004 R^2=0.990	y=0.007x+0.002 R^2=0,77

The values for sorption intensity (0 < *RL* < 1) describes a favourable isotherm for the whole range of temperature (295-313 K), Figure 9.

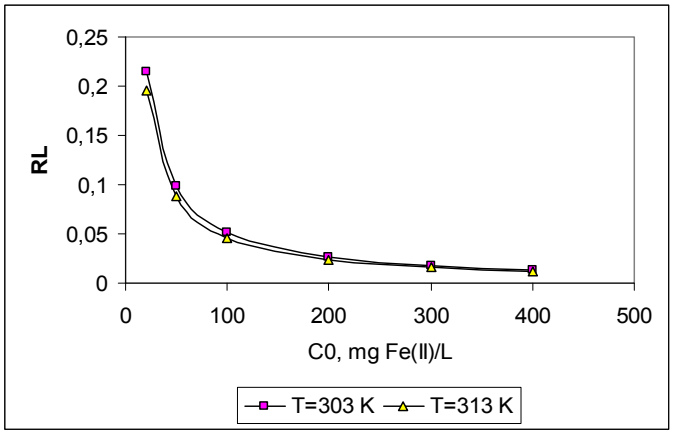

Figure 9. The variation of sorption intensity (R_L) with initial metal concentration for different temperatures; 1 g/L S930 – Na form, contact time 24 h, pH = 5.

Thermodynamic studies

The thermodynamic parameters for sorption of iron (II) on Purolite S930 chelating resin were evaluated using the Langmuir equilibrium constant, K_L, which depends on temperature. The free energy (ΔG^o), was evaluated using equation [10].

$$\Delta G^{O} = -RT \ln K_L \tag{10}$$

where *R* is the gas constant (j/mol*K) and *T* is the temperature (^{0}K). The standard enthalpy (ΔH^o) and standard entropy (ΔS^o) associated to the sorption process were calculated by Eq**.** (8) [7].

$$\ln K_L = \frac{\Delta S^{O}}{R} - \frac{\Delta H^{O}}{RT} \tag{11}$$

The Gibbs free energy change of sorption (ΔGº) values calculated using Eq.(7) for different temperatures are presented in Table 4.

Table 4. Thermodynamic parameters for iron(II) sorption onto Purolite S930-Na form resin

T, K	ΔG^0, kJ/mol	ΔH^0, kJ/mol	ΔS^0, J/mol.K
295.15	-22.59	6.31	97.84
303.15	-23.28		
313.15	-24.35		

The negative value of free energy *ΔGº* indicated us that sorption of Fe (II) onto Purolite S930-Na form resin is spontaneous from thermodynamical point of view. In addition, the decrease in *ΔGº* values with increase in temperature shows that the sorption was favourable at higher temperatures. The enthalpy change (ΔHº) and the entropy change(*ΔSº*) for the sorption process were obtained from the *ln K* versus *1/T* plot (Figure 10). The enthalpy change (ΔHº) was 6.31 kJ/mol. The positive value indicates the endothermic nature of the sorption process. The positive value of the entropy change (ΔSº=97.84 j/mol K) proves the affinity for iron(II) sorption onto Purolite S930 chelatic resin.

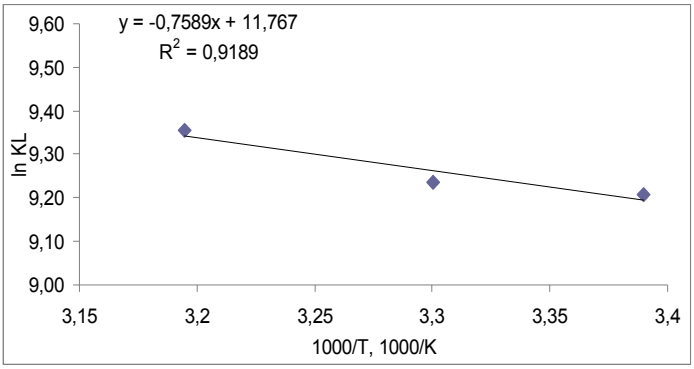

Figure 10. Dependence of *ln* K_L vs. *1/T* for Fe(II) sorption onto Purolite S930-Na

Sorption kinetics

The effect of the phases contact time on Fe (II) sorption onto sodium ionic form of the resin Purolite S930 is presented in Figure 11. The experiments were conducted using solutions of 200 mg Fe (II) /L at temperature 295 K and the initial pH = 5.

The equilibrium was considered attained after 24 hours; a further increase in contact time has a negligible effect on the percent of removal.

The sorption of Fe (II) onto Purolite S930-Na form resin was investigated in terms of the kinetics of the sorption mechanism by using two models: Lagergren and Ho.

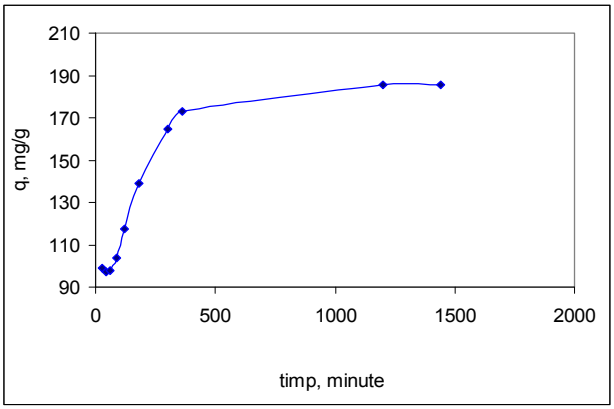

Figure 11. Effect of contact time on the Fe (II) removal on S930-Na form resin: C_0 = 200 mg Fe(II)/L, pH = 5, T = 295 K, resin dose = 1g/L

Pseudo-first-order model (Lagergren)

The pseudo-first-order rate expression is presented in Eq. (12)

$$\log(q_e - q_t) = \log q_e - \frac{k_1}{2{,}303} t \tag{12}$$

where, q_e is the amount of Fe (II) sorbed at equilibrium (mg/g), q is the amount of Fe (II) sorbed at time t (mg/g) and k_1 is the rate constant of first order sorption (min^{-1}).

The values of pseudo-first-order model parameters (k_1 and q_e) were determined by plotting $ln\ (q_e - q_t)$ versus t, and the values of pseudo-second-order model parameters (k_1 and q_e) were determined by plotting t/q_t versus t (Figure 12 and Figure 13). The values of parameters calculated for various initial concentrations and various temperatures are presented in Table 5.

Pseudo-second-order model (Ho)

The pseudo-second-order rate expression is presented in Eq. (13)

$$\frac{t}{q_t} = \frac{1}{k_2 q_e^{\,2}} + \frac{1}{q_e} t \tag{13}$$

where k_2 (g/mg min) is the rate constant of the second-order equation; q_t (mg/g), the amount of sorption time t (min) and q_e is the amount of adsorption equilibrium (mg/g).

The initial sorption rate, h (mg/ g. min), at t = 0 is defined as:

$$h = k_2 q_e^2 \quad (14)$$

where q_e and h values were determined from the slope and intercept of the plots of t/q against t.

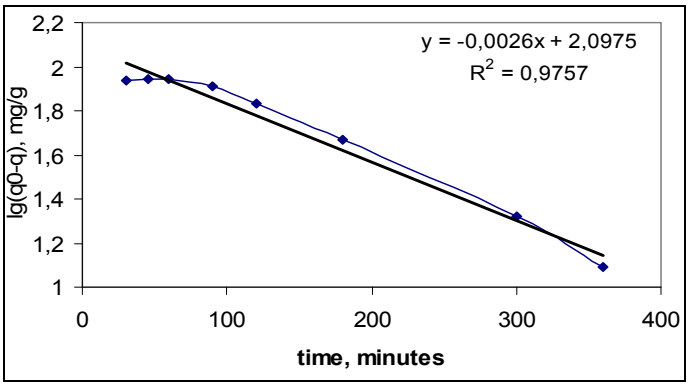

Figure 12. Lagergren-first-order model, Fe(II) sorption onto Purolite S930-Na form resin, C_0=200 mg Fe(II)/L, T=295 K

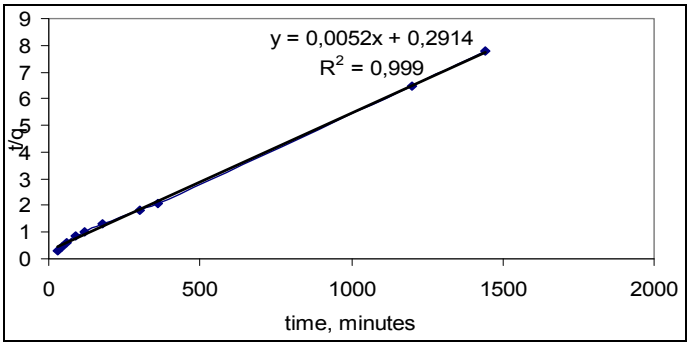

Figure 13. Ho pseudo-second-order model, Fe(II) sorbtion onto Purolite S930-Na resin, C_0=200 mg Fe(II)/L, T=295 K

Table 5. Pseudo first-order and pseudo-second-order parameters for the sorption of Cu (II) onto Purolite S930 at various temperatures and various initial concentrations

T (^{0}K)	Pseudo first-order model			Pseudo second-order model			
	k_1, min^{-1}	q_{max}, mg/g	R^2	k_2, g/mg min	q_{max}, mg/g	h, mg/ g. min	R^2
C_0 = 200 mg Fe(II)/L							
295	$5.98 \cdot 10^{-3}$	125.7	0.9757	$7.87 \cdot 10^{-6}$	192.3	3.43	**0.9999**

The results presented Table 5 reveal that the pseudo-second-order kinetics is expected to be followed in the sorption of Fe(II) onto Purolite S930 resin since the values of R^2 (0.9999*)* are higher than values obtained for pseudo first-order. Also, the value for sorption capacity (q_{max}) for this model is close to experimental sorption capacity values.

EXPERIMENTAL

Materials. The chelating resin used in the experiments was S930 obtained from Purolite International Limited (Hounslow, UK). The main physical and chemical properties of the resin are presented in Table 6. The resin was dried in an oven at 65 ºC.

Table 6. Proprietes of chelating resin *

Polymer matrix structure	Macro porous styrene divinylbenzene
Functional groups	Iminodiacetic acid
Ionic Form (as shipped)	Na^+
pH range (operating): H^+ form, Na^+ form	2 - 6; 6 - 11
Maximum operating temperature	70ºC
Particle size range	+ 1.0mm <10%, -0.3mm <1%
Total exchange capacity	≥ 1.9 meq /mL

* Manufacturer supplied.

The stock solution of iron (2000 mg Fe (II)/L) was prepared from analytical-reagent grade iron sulphate ($FeSO_4.7H_2O$) in distilled water and hydrochloric acid, analytical-reagent grade.

The work solutions were prepared from stock solution using different aliquot parts for the range of concentration 20-400 mg Fe (II)/L, respective: 1mL; 2.5mL; 5mL; 15mL; 20mL; 25 mL of stock solution. Required pH adjustments of the solutions were performed with hydrochloric acid or calcium hydroxide solution.

The calcium chloride 34 % solution was prepared using calcium chloride pro analysi and distilled water.

Sorption experiments. Sorption of Fe(II) ions on Purolite S930 in sodium (S930-Na) and hydrogen (S930-H) forms was carried out in batch experiments using amounts of 100 mL of $CaCl_2$ 34% solution with different initial concentrations in Fe(II) (20–400 mg Fe (II)/L) that where added to Erlenmeyer flasks already containing the required quantity of 0.1g dried resin. The initial pH of the solutions was adjusted using diluted solutions of HCl or $Ca(OH)_2$ solution. The flasks where mechanically shacked at several fixed temperatures and at the rate of 120 cycles min^{-1} using Orbital Shaking Incubator GFL3031. After equilibrium (24 hours), the resin and solution were separated by filtration. The iron content of the solution and also the final pH of solution (pH_e) were measured.

For kinetic experiments the samples were analyzed after a specified period of time. For thermodynamic studies the experiments were repeated in the same conditions but for different temperatures. The concentration of Fe(II) in solutions was measured using a spectrophotometric method with 1,10-phenantroline and hydroxilaminochlorohidrat (λ=510nm) using Hach DR/2000 spectrophotometer [5]. Because in the presence of O_2 from air a part of Fe(II) becomes Fe(III),all experiments measured the concentration of total iron as Fe(II).

CONCLUSIONS

The *equilibrium data* were analysed using Freundlich, Langmuir and Dubinin sorption isotherm models; sorption was best fitted by the Langmuir 1 model. The values of sorption intensity ($0 < RL < 1$) indicate that iron(II) sorption onto Purolite S930-Na form resin has a favourable sorption isotherm and the resin is a good sorbent for the sorption of iron(II) from 34% $CaCl_2$ solution.

Thermodynamic studies reveal the big affinity of the sorbent for Fe(II) ions from 34% $CaCl_2$ solution and the endothermic nature of sorption process. The negative value of free energy ΔG^o indicated us that sorption of Fe (II) onto Purolite S930-Na form resin is spontaneous from thermodynamical point of view. The positive value of enthalpy change (ΔH^o = 6.31 kJ/mol) indicates the endothermic nature of the sorption process. The process is favourable at higher temperatures; the growth of temperature is favourable for the velocity constant (k). The positive values for ΔS^0 reveal the increasing disorder of the system.

The *kinetic studies* show that the sorption process of Fe(II) from 34% $CaCl_2$ solution onto Purolite S930-Na form resin follows a pseudo-second-order model.

REFERENCES

1. M. Macoveanu, D. Bîlba, N. Bîlba, M. Gavrilescu, G. Şoreanu, "Ion Exchange Processes in Environment Protection", Matrix Rom Press, Bucharest, Romania, **2002**, chapter 1.
2. T.D. Ionescu, "Ion exhangers," Technical Press, Bucharest, Romania, **1964**.
3. C. Scripcariu**,** S. Mironeasa, P. Bulai, M. Macoveanu, *Annals of the Suceava University – Food Engineering*, **2009**, *VIII*, 30.
4. P.A. Riveros, *Hydrometallurgy*, **2004**, *72*, 279.
5. G. Popa, S. Moldoveanu, "Quantitative Chemical Analysis Using Organic Reagents", Technical Press, Bucharest, Romania, **1969**.

6. V.C. Srivastava, M.M. Swamy, I.D. Mall, B. Prasad, I.M. Mishra, *Colloids and Surfaces A: Physicochemical and Engineering Aspects*, **2006**, *272*, 89.
7. A. Sari, M. Tuzen, D. Citak, M. Soylak, *Journal of Hazardous Materials*, **2007**, *149*, 283.
8. L. Bulgariu, C. Cojocaru, B. Robu, M. Macoveanu, *Journal of Environmental Engineering and Management*, **2007**, *6*, 425.
9. V.B.H. Dang, H.D. Doan, T. Dang-Vu, A. Lohi, *Bioresource Technology*, **2009**, *100*, 211.
10. Y. Zhang, J. Chen, X. Yan, Q. Feng, *Journal of Chemical Thermodynamics*, **2007**, *39*, 862.

STUDIA UBB CHEMIA, LVI, 1, 2011

AMS RADIOCARBON DATING OF THE VERY LARGE PEDUNCULATE OAK OF CAJVANA

ADRIAN PATRUT[a,*], KARL F. VON REDEN[b], VASILE SAVU[c], DANIEL A. LOWY[d], RALUCA MITEA[a], IOANA BARBUL[a]

ABSTRACT. Using a new approach of dating live angiosperm trees, three wood samples collected from the inner cavity of the very large pedunculate oak (*Quercus robur* L.) of Cajvana, Romania, were processed and radiocarbon dated by AMS for determining the age of the tree. The radiocarbon date of the oldest sample was found to be 736 ± 23 BP, which corresponds to a calibrated calendar age of 735 ± 10 years. By considering the original position of this sample in the hollow trunk, one can estimate that the age of the oak is around 810 years.

Keywords**:** *radiocarbon dating, accelerator mass spectrometry, dendrochronology, pedunculate oak, tree growth.*

INTRODUCTION

The pedunculate oak (*Quercus robur* L.), which belongs to the family Fagaceae, is considered to be one of the most longlived native European tree. The age limit of the pedunculate oak, based mainly on age estimates of the largest specimens, remains controversial. Modern tree researchers consider that the upper limit of its age could be close to 1,000 years [1, 2].

The age determination of large oaks is a very difficult task. A complete ring counting on remaining stumps of old dead specimens is usually not possible, due to the existence of large cavities in their trunks. The use of the size/diametre-age relation for oaks is very questionable and may generate large errors. Age estimates based mainly on ring counting or cross-dating of increment cores collected from the exterior of the trunk were done on several big live individuals. The obtained age values were extrapolated to the theoretical pith, which is assimilated to the geometric midpoint, according to different formulas which consider growth rate values based on research done on stumps and especially on younger live trees growing in somewhat similar conditions [3, 4]. Other estimates are based on growth rates determined by

[a] *Babes-Bolyai University, Faculty of Chemistry and Chemical Engineering, 11 Arany Janos, RO-400028, Cluj-Napoca, Romania*
** Email: apatrut@gmail.com*
[b] *NOSAMS Facility, Department of Geology & Geophysics, Woods Hole Oceanographic Institution, 360 Woods Hole Rd., Mailstop 8, Woods Hole, MA 02543, U.S.A.*
[c] *Cajvana School Group, RO-727100 Cajvana, Romania*
[d] *FlexEl, LLC, College Park, MD 20742, U.S.A.*

successive girth measurements of large individuals, performed over longer periods of time [1]. Even in such cases, the age estimate error, which remains unknown, can be important.

The radiocarbon investigation of wood samples represents the most accurate method for dating trees without a continuous sequence of growth rings in the trunk [5, 6]. Ages of the oldest radiocarbon dated samples are significantly greater than the relatively short tree-ring sequences of the increment cores collected from the exterior of the trunk; therefore, the necessary age extrapolation to the pith is less demanding in radiocarbon dating. Previously we determined the age of the dead historic pedunculate oak of Țebea, Romania, by radiocarbon dating of wood samples originating from the upper part of its trunk, which was removed [7]. Traditionally, radiocarbon investigation was limited to dating wood samples from the remains of dead or severely damaged trees. Recently, we extended considerably the possibility of ageing large angiosperm trees, by introducing a methodology which allows to date by radiocarbon standing and live specimens. This new approach is based on radiocarbon dating of wood samples collected from the inner cavities of live hollow trees [8].

Here we present and discuss the AMS (accelerator mass spectrometry) radiocarbon dating results of three wood samples collected from the cavity of the largest Romanian pedunculate oak, located in Cajvana.

RESULTS AND DISCUSSION

The pedunculate oak of Cajvana and its location

The Cajvana oak has a long history, handed down from one generation to the other. It is stated that in 1476 the prominent Prince of Moldavia, Stephen the Great (1457-1504), accompanied by his soldiers, stopped underneath the tree. However, the history of the oak is claimed to be much older. Residents of the area believe that the oak originates from time of the Tartar invasion of 1241. In this year, the entire male population of the settlement perished in the battle and was buried in a huge common grave. An oak was planted for marking the site; this would be the today's giant oak. In 1942, the Romanian Academy nominated the Cajvana oak as a Monument of Nature.

The city of Cajvana is situated in the NE part of Romania, in the centre of Suceava county, on the county road 178 D, at 36 km NW from Suceava. The city is crossed by the river Cajvana, which is a branch of the Soloneț river. The mean annual temperature in the area is 7.6 ºC and the mean annual rainfall is 579 mm (Suceava station). The large pedunculate oak (Figure 1) is located on a hill just in the centre of the city, at a distance of ca. 120 m from the Cajvana river. Its GPS coordinates are 47º42.117' N, 025º58.072' E; the altitude is 399 m. The tree has a height of 20.1 m and a circumference at breast height (cbh; 1.30 m above ground level) of 11.01 m, which corresponds to a formal diametre (dbh) of 3.50 m.

The large trunk, which has an almost cylindrical shape, divides at the height of 3.45 m into two heavy branches with basal diametres of 1.85 and 1.75 m (Figures 2 and 3), which rises quasi-vertically and divide further forming a large canopy. The maximum dimensions of the canopy are of 22.4 m (in NE-SW direction) and 18.8 m (ca. 25 m before 2006, when a large secondary branch was cut; in NW-SE direction). A volume estimate indicates a total wood volume of around 85 m^3, out of which 35 m^3 for the trunk, 39 m^3 for the two large primary branches and 11 m^3 for the smaller branches. The volume was over 90 m^3 in 2006, when a long secondary branch, which extended just over the county road and was partially damaged during a storm, was cut for security reasons.

Figure 1. General view of the large oak of Cajvana taken from the south, during summer time.

In present, the tree is in a stage of decline, which started over a century ago. An investigation across the trunk revealed that three primary and several large secondary branches are missing; they broke off during storms and heavy winters or were cut by the local people. Around 1870, the tree was hit by lightning, it burst into flames and a part of the canopy broke off; a large vertical mark along the biggest primary branch testifies to this event. According to local sources, over the first half of the 20th century the canopy was still twice larger than it is today and it was also significantly taller.

Figure 2. View of the oak of Cajvana taken from the east, showing its trunk and branches at the end of autumn.

Consequently, we estimate that the overall wood volume of the Cajvana oak was once around 140 m^3; this value is close to the volume of the oak of Ivenack, Germany, which is considered to be the largest in Europe [1, 3]. According to the above values, the tree of Cajvana is one of the biggest European oaks and the largest pedunculate oak in south-eastern Europe.

Figure 3. The image taken from the west shows the trunk and the two remaining primary branches of the Cajvana oak.

As of today, the percentage of dead and dry branches in the remaining canopy is of over 15 %. The county road, located at only 10 m distance from the oak, is getting the busier and busier; the upgrading of the road around 1985 required cutting a large root. In addition, no speed limit is enforced and no weight limit is imposed on truck trailers in the proximity of the old tree. All these factors likely sped up the decline of the oak.

The trunk has a large bell-shaped cavity, which extends vertically up to the second largest branch, reaching the height of 3.81 m. The cavity base at ground level is quasi-ellipsoidal, with the length of the two axis of 2.24 and 1.82 m. Somewhat surprisingly, the big cavity has a small opening/ entrance toward east, with a width of only 0.23 m and a height of 0.50 m; however, these dimensions of the entrance are sufficient for allowing a skinny person to access the inside of the cavity (Figure 4) wood at the surface of the cavity walls is partially rotten, showing that the cavitation process is still in progress.

Figure 4. The image shows the trunk of the Cajvana oak, with the small entrance to the cavity

Three small wood samples collected from the cavity were pretreated and investigated by AMS radiocarbon analysis.

AMS results and calibrated ages

Fraction modern values and radiocarbon dates of the three samples are presented in Table 1. Radiocarbon dates and errors were rounded to the nearest year. Calibrated (cal) ages, which were derived directly from fraction modern values, are also listed in Table 1. The 1-σ probability distribution was selected to calculate calibrated age ranges. For sample 2, the 1-σ distribution corresponds only to one range. For sample 1 and 3, the 1-σ distribution

corresponds to several ranges of calendar years. In this case, the confidence interval of one range (marked in bold) is much greater than of the others; therefore, it was selected as the most probable cal AD range of the respective sample, for the purpose of this discussion.

For obtaining single calendar age values of samples, we derived a mean calendar age of each sample from the 1-σ range with the highest probability. Calendar ages of samples represent the difference between AD 2010 and the mean value of the selected 1-σ range, with the corresponding error. Calendar ages of samples and errors were rounded to the nearest 5 years.

Table 1. AMS dating results and calibrated calendar ages

Sample code	Height[1] [m]	Diametre[2] [m]	Fraction modern [error]	Radiocarbon date [error] (^{14}C yr BP)	Cal AD range(s) 1-σ [confidence interval]	Sample age [error] (cal yr)
1	1.20	3.30	0.9621 [± 0.0033]	310 [± 26]	**1521-1577 [45.8%]** 1582-1591 [6.1%] 1621-1642 [16.3%]	460 [± 30]
2	0.90	3.58	0.9125 [± 0.0029]	736 [± 23]	**1263-1284 [68.2%]**	735 [± 10]
3	0.30	3.68	0.9822 [± 0.0030]	144 [± 24]	1678-1696 [10.3%] **1726-1765 [22.2%]** 1772-1776 [2.0%] 1800-1814 [8.1%] 1837-1844 [2.9%] 1852-1876 [9.2%] 1918-1940 [13.7%]	265 [± 25]

[1] Height of sample above ground level.
[2] Diametre of the trunk at sampling height.

Dating results of samples

The three samples were collected from the cavity at different heights above ground, according to the cavity shape and to the profile of walls. Even if the trunk is quasi-cylindrical from ground level up to breast height, there are some diametre differences, according to height and direction. The maximum and minimum diametre values at 1 m above ground are of 3.78 and 3.22 m. The diametre at sampling height was considered to be the diametre of the trunk which passes by the geometric/symmetry centre of the trunk at this height and the sampling point. The sample heights and the diametres at sampling height are shown in Table 1. The cross-section of the trunk at 1 m above ground, showing also the inner cavity and the sampling positions is displayed in Figure 5.

The black bark has a thickness of 4-10 cm, with a mean value of ca. 6 cm. We used this value for calculating the three trunk diametres inside bark at sampling height, which are 3.18, 3.46 and 3.56 m. Mention should be made that the dated segment of each sample originates from a distance of 3 cm (for sample 1 and 2) and 5 cm (for sample 3) inside wood from the sampling point.

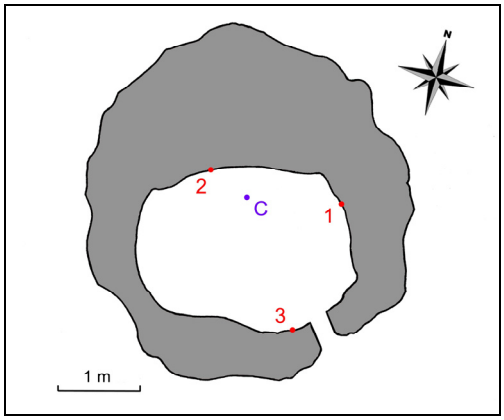

Figure 5. Schematic cross-section of the Cajvana oak's trunk (at 1 m above ground; bark included), showing the inner cavity, the positions of the sampling points (labeled 1, 2 and 3) and the geometric/ symmetry centre of the trunk (noticed by C). As a reference, the entrance to the cavity is also shown, even if it has a height of only 0.50 m.

The radiocarbon dates of the three samples were found to be of 310 ± 26, 736 ± 23 and 144 ± 24 BP (radiocarbon years before present, i.e. before AD 1950). These values correspond to calibrated calendar ages of 460 ± 30, 735 ± 10 and 265 ± 25 years.

Growth rates

For each sample, we calculated the distances from the dated segment to the bark and to the geometric centre of the trunk, respectively. For calculating and comparing growth rate values of the trunk, measured by the increase in radius, we converted all these values for a mean diametre of the trunk at breast height dbh = 3.50 m, which corresponds to a dbh value inside bark of 3.38 m and to a radius inside bark of 1.69 m.

In this case, the distances from the dated segments of the three samples to the bark are of 0.68, 1.30 and 0.32 m, while the distances to the geometric centre are 1.01, 0.39 and 1.37 m. By considering also the ages of the three samples, one can state that the radial increase of the trunk of Cajvana oak was of 0.32 m over the past ca. 265 years, 0.68 m over the past ca. 460 years and 1.30 m over the past ca. 735 years.

Age of the tree

For determining the age of the investigated oak one should extrapolate the age of the oldest sample, i.e. sample 2, to the geometric centre of the trunk at the respective height. As mentioned above, the converted distance from the dated segment of sample 2 to the geometric centre is 0.39 m. Therefore, for calculating the age of the tree, one should add to the age of sample 2 (735 ± 10 years) the time needed by the trunk for growing from 0 to a radius of 0.39 m, i.e. a diametre dbh = 0.78 m.

Since it started growing, the oak of Cajvana has probably been a solitary tree, without competition in its close proximity. According to research done in Europe at comparable latitudes on solitary pedunculate oaks, growing in open conditions [9] and also to our research in Romania done on several stumps of isolated oaks and on live oaks of known age, we estimate that the time needed to the oak of Cajvana to reach a dbh of 0.78 m was 75 ± 15 years. One can also add a maximum additional error of ± 50 years, due to assigning the geometric centre of the trunk to the pith. Consequently, the final age value for the oak of Cajvana becomes 810 ± 75 years. One can state that the tree started growing around AD 1200, more precisely in the time frame 1125 – 1275.

Therefore, the dating results do not exclude the claim of the area's residents that the oak was planted in 1241, for marking the cruel Tartar invasion. On the other hand, the obtained dating results suggests that the oak of Cajvana could be even older than this historic date.

CONCLUSIONS

Using our new approach of dating live angiosperm trees, three samples were collected from the cavity of the large pedunculate oak of Cajvana, Romania, and investigated by AMS radiocarbon dating. According to the age of the oldest dated sample, i.e. 735 ± 10 years, the tree of Cajvana becomes one of the oldest pedunculate oaks with accurate dating results. By considering the position of the oldest sample in the trunk, the calculated tree age is 810 ± 75 years. This value is practically similar to that we determined for the historic pedunculate oak of Țebea, which died in 2005 [7]. The obtained results confirm that Romanian oaks can live to ages exceeding 800 years.

Given that the majority of old oaks develop open hollows in their trunks [10], this approach can be used on the large scale for getting accurate age estimates of big live specimens.

EXPERIMENTAL SECTION

Measurements. The external measurements of the tree and the measurements inside the cavity were performed by using a Bosch DLE 70 Professional laser rangefinder and graduated tapes.

Sample preparation. The standard acid-base-acid pretreatment method [11] was used to remove soluble and mobile organic components. The resulted cellulose samples were combusted to CO_2, by using the closed tube combustion method [12]. Then, CO_2 was reduced to graphite on iron catalyst, under hydrogen atmosphere [13]. Eventually, the graphite samples were analyzed by AMS.

AMS measurements. Radiocarbon measurements were carried out at the National Ocean Sciences AMS Facility of the Woods Hole Oceanographic Institution, with the Pelletron ® Tandem 500 kV AMS. The surface of the graphite samples was sputtered with cesium ions and the secondary negative ions were extracted and accelerated in the AMS system. ^{12}C and ^{13}C ions were measured in Faraday cups, where a ratio of their currents was recorded. Simultaneously, ^{14}C ions were recorded in a solid state detector, so that instantaneous ratios of ^{14}C to ^{12}C were also recorded. The raw signals were compared to ratios obtained with a known standard material (Oxalic Acid I, NIST-SRM-4990) and converted to a fraction modern value. Fraction modern values, corrected for isotopic fractionation with the normalized $\delta^{13}C$ value of -25 $^{0}/_{00}$, were converted to radiocarbon dates, expressed in years BP [14].

Calibration. Fraction modern values were calibrated and converted into calendar ages with the OxCal v4.1.5 for Windows [15], by using the IntCal09 atmospheric data set [16].

ACKNOWLEDGEMENTS

This research was fully funded by CNCSIS-UEFISCDI under grant PN II – IDEI 2354, Nr. 1092. AMS radiocarbon dating at the NOSAMS Facility is supported by the U.S. National Science Foundation under Cooperative Agreement OCE-0753487. We would like to thank Gheorghe Pițu for offering interesting information about the history of the city of Cajvana and its historic oak.

REFERENCES

1. J. Pater, “Monumentale bomen in Europa”, Lannoo, **2006**.
2. A. le Hardÿ de Beaulieu, T. Lamant, “Le guide illustré des chênes”, Vol. 1-2, Huitième, Paris, **2007**.
3. Ullrich, U. Kühn, S. Kühn, “Unsere 500 ältesten Bäume“, BLV, München, **2009**.
4. S. Kühn, B. Ullrich, U. Kühn, “Deutschlands alte Bäume“, BLV, München, **2007**.
5. A. Patrut, K.F. von Reden, D.A. Lowy, A.H. Alberts, J.W. Pohlman, R. Wittmann, D. Gerlach, L. Xu, C.S. Mitchell, *Tree Physiol*., **2007**, *27*, 1569.
6. A. Patrut, K.F. von Reden, D.A. Lowy, D.H. Mayne, K.E. Elder, M.L. Roberts, A.P. McNichol, *Nuclear Instr. and Meth. B*, **2010**, *268*, 910.
7. A. Patrut, K.F. von Reden, D.A. Lowy, S. Pasca, L. Kekedy-Nagy, I. Sovago, *Studia UBB Chemia*, **2010**, *55*, 113.

8. A. Patrut, K.F.von Reden, D.H. Mayne, D.A. Lowy, R. Van Pelt, A.P. McNichol, M.L. Roberts, D. Margineanu, *Radiocarbon*, **2010**, *52*, 717.
9. E. Uhl, H-G. Metzger, T. Seifert, *18 Jahrestagung DVFFA*, **2006**, 46.
10. T. Ranius, M. Niklasson, N. Berg, *For. Ecol. Manage.*, **2009**, *257*, 303.
11. I.U. Olsson, in B. Berglund (ed.), "Handbook of Holocene palaeoecolgy and palaeohydrology", Wiley, Chichester, **1986**, p. 273.
12. Z. Sofer, *Anal. Chem.*, **1980**, *52*, 1389.
13. J.S. Vogel, J.R. Southon, D.E. Nelson, T.A. Brown, *Nuclear Instr. and Meth. B,* **1984**, *5*, 289.
14. A. Patrut, K. von Reden, D.A. Lowy, P. Lindeque, A.H. Alberts, R. Wittmann, E. Forizs, D. Margineanu, J. Pohlman, L. Xu, D. Gerlach, C.S. Mitchell, *Studia UBB Chemia*, **2006**, *51*, 71.
15. C. Bronk Ramsey, *OxCal Program, v4.1.5*, **2010**, http://www.rlaha.ox.ac.uk/oxcal/oxcal.html.
16. P.J. Reimer, M.G.L. Baillie, E. Bard, A. Bayliss, J.W. Beck, P.G. Blackwell, C. Bronk Ramsey, C.E. Buck, G.S. Burr, R.L. Edwards, M. Friedrich, P.M. Grootes, T.P. Guilderson, I. Hajdas, T.J. Heaton, A.G. Hogg, K.A. Hughen, K.F. Kaiser, B. Kromer, F.G. McCormac, S.W. Manning, R.W. Reimer, D.A. Richards, J.R. Southon, S. Talamo, C.S.M. Turney, J. van der Plicht, C.E. Weyhenmeyer, *Radiocarbon*, **2009**, *51*, 1111.

STUDIA UBB CHEMIA, LVI, 1, 2011

DEPENDENCE BETWEEN DETERMINATION COEFFICIENT AND NUMBER OF REGRESSORS: A CASE STUDY ON RETENTION TIMES OF MYCOTOXINS

SORANA D. BOBLOACĂ[a,*], LORENTZ JÄNTSCHI[b,c], RADU E. SESTRAŞ[c,*]

ABSTRACT. In the present work, a dependence analysis of the determination coefficient and the number of regressors was carried out on a set of 65 mycotoxins. The simple and multiple regression techniques were used to identify the linear relationship between retention times and molecular descriptors calculated with HyperChem from the optimized 3D structures. The highest number of regressors to be used in investigating the retention times as function of mycotoxins investigated properties must be equal to 5. As far as the dependence between number of regressors and determination coefficient was concerned, the analysis revealed that the best relationship is linear if the cutoff is set at 4 or 5 regressors while exponential for more than 5 regressors. The results must be verified on other classes of compounds and other dependent or independent variables in order to be extrapolated.

Keywords: *mycotoxins; retention time; regression analysis.*

INTRODUCTION

Mycotoxin, a secondary metabolite produced by a fungus [1,2], is produced according to the intrinsic and extrinsic environmental conditions [3,4]. Aflatoxins, discovered in later 1950's and early 1960's [5], produced by species of Aspergillus (*Aspergillus flavus*, *Aspergillus parasiticus*), are known to act at the DNA level (e.g. gene point mutations, deletions and insertions, recombination, rearrangements and amplifications) as carcinogenetic substances [6,7]. Trichothecenes, produced by species as *Fusarium*, *Myrothecium*, *Trichoderma*, *Trichothecium*, *Cephalosporium*, *Verticimonosporium*, and *Stachybotrys*, proved to be detrimental to the neurological system [8,9]. Roquefortin, produced by fungi from Penicillium genus [10,11], proved to be toxic for animals [12,13]. Ochratoxin, mycotoxins produced by some *Aspergillus* (e.g. *Aspergillus*

[a] *„Iuliu Haţieganu" University of Medicine and Pharmacy Cluj-Napoca, 13 Emil Isac, RO-400023 Cluj-Napoca, sbolboaca@umfcluj.ro*
[b] *Technical University of Cluj-Napoca, 28 Memorandumului, RO-400114 Cluj-Napoca, Romania, lori@academicdirect.org*
[c] *University of Agricultural Sciences and Veterinary Medicine Cluj-Napoca, 3-5 Mănăştur Street, RO-400372 Cluj-Napoca, rsentras@usamvcluj.ro*

ochraceus) and *Penicillium* species (e.g. *Penicillium viridicatum*) is accumulated in the meat of animals and is known to be a human carcinogen [14,15,16]. Thus, mycotoxins proved to have important effects on animal and human health [17,18,19,20]. Moreover, a series of researches have been conducted to assess the cost and efficacy of public health interventions carried out in order to reduce the mycotoxin-induce human diseases [21,22,23].

The present research was aimed to obtain the dependence of determination coefficient of retention times as function of the number of independent variables, as properties obtained from the structure of a sample of mycotoxin. Starting with these results, the best dependence between determination coefficients and the number of regressors was investigated.

RESULTS AND DISUSSIONS

The search of the maximum determination between retention times and some properties of the studied mycotoxins revealed the following:

The distribution of the steps where an increase in determination coefficient value was observed, is: 5 (1 independent variable) - 3 (2 independent variables) - 7 (3 independent variables) - 4 (4 independent variables) - 10 (5 independent variables) - 5 (6 independent variables) - 3 (7 independent variables) - 2 (8 independent variables) - 6 (9 independent variables) - 9 (10 independent variables).

The descending classification of the range (defined as the difference between maximum and minimum value) of the determination coefficient according to the same number of independent variable was as follow: ▪ 0.3909 (1 variable); ▪ 0.0977 (5 variables); ▪ 0.0647 (2 variables); ▪ 0.0605 (3 variables); ▪ 0.0517 (4 variables); ▪ 0.0239 (6 variables); ▪ 0.0132 (9 variables); ▪ 0.0108 (8 variables); ▪ 0.0102 (7 variables); and ▪ 0.0083 (10 variables). Note that all models were statistically significant at a significance level of 5%.

The summary of the results obtained in the best regression when the dependence between retention times and properties of the studied mycotoxins was investigated is presented in Table 1.

The matrix of properties used as independent variables in the regressions models when the highest value of the determination coefficient was obtained is shown in Table 2.

The dependence between the number of regressors (independent variables) and determination coefficient was as follows:

- Case $x \leq 4$, linear (Figure 1): $\hat{y} = 6.797 \cdot 10^{-2} * x + 0.3270$

$$(r^2 = 0.9991,\ r^2_{adjusted} = 0.9987;\ F = 2299) \qquad \text{Eq(1)}$$

where x = number of independent variables; $\hat{y}$ = estimated determination coefficient.

- Case $4 < x \leq 10$, exponential (Figure 2): $\hat{y} = 0.8173 - 0.7972*\exp(-x/2.6772)$ ($r^2 = 0.9998$; $r^2_{adjusted} = 0.99965$; $F = 7044$) Eq(2)

Table 1. Summary of linear regressions: mycotoxins dataset

x	r^2	t	p
1	0.3935	6.39	$1.13 \cdot 10^{-8}$
2	0.4635	7.32	$3.02 \cdot 10^{-10}$
3	0.5343	8.37	$5.17 \cdot 10^{-12}$
4	0.5964	9.42	$9.88 \cdot 10^{-14}$
5	0.6943	11.58	$4.04 \cdot 10^{-17}$
6	0.7318	12.58	$1.61 \cdot 10^{-18}$
7	0.7599	13.43	$1.32 \cdot 10^{-19}$
8	0.7766	13.95	$3.57 \cdot 10^{-20}$
9	0.7898	14.38	$1.41 \cdot 10^{-20}$
10	0.7982	14.61	$1.03 \cdot 10^{-20}$

x = number of independent variable; r^2 = determination coefficient;
t = t-value associated to r^2; p = p-value associated to t-value

Table 2. Matrix of mycotoxins properties used in the models with highest determination coefficients

x	LogP	InvHydE	LnPol	LnRefr	Vol	SAG	LnMW	negte	dm	negsae	sce	Invnegte	Invnegsae	Invnegsbe	Lnnegsae	Lnnegsbe	Lnsce	Lnnegsee	**Total**
1	0	0	**1**	0	0	0	0	0	0	0	0	0	0	0	0	0	0	0	**1**
2	0	0	**1**	0	**1**	0	0	0	0	0	0	0	0	0	0	0	0	0	**2**
3	0	0	0	0	0	0	**1**	0	0	0	**1**	0	**1**	0	0	0	0	0	**3**
4	0	**1**	**1**	0	**1**	**1**	0	0	0	0	0	0	0	0	0	0	0	0	**4**
5	0	**1**	**1**	0	**1**	0	0	**1**	0	0	0	0	0	0	0	0	0	**1**	**5**
6	0	**1**	**1**	0	**1**	0	0	0	0	**1**	0	0	0	0	0	**1**	**1**	0	**6**
7	0	**1**	**1**	0	**1**	0	0	0	**1**	**1**	0	0	0	0	0	**1**	**1**	0	**7**
8	**1**	**1**	**1**	0	**1**	0	0	**1**	**1**	0	0	0	0	**1**	0	0	**1**	0	**8**
9	**1**	**1**	**1**	**1**	**1**	0	0	**1**	**1**	0	0	0	0	**1**	0	0	**1**	0	**9**
10	**1**	**1**	**1**	**1**	**1**	0	0	0	**1**	0	0	**1**	0	0	**1**	**1**	0	**1**	**10**
Total	**3**	**7**	**9**	**2**	**8**	**1**	**1**	**3**	**4**	**2**	**1**	**1**	**1**	**2**	**1**	**3**	**4**	**2**	**55**

LogP = octanol-water partition coefficient (log scale);
HydE = hydration energy; Pol = polarizability; Refr = refractivity;
Vol = volume; SAG = surface area grid; MW = molecular weight;
te = total-energy; dm = dipole moment; sae = scf-atom-energy;
sce = scf-core-energy; sbe = scf-binding-energy;
see = scf-electronic-energy; ln = natural logarithm; inv = inverse value

The regression between retention times and five mycotoxin properties also provided a linear dependence between determination coefficient and the number of regressors but the performance of the model decreased with 0.005 in terms of determination coefficient of the overall model:

- $r^2 = 0.9941$, $r^2_{adjusted} = 0.9921$; $F = 504$ Eq(3)

The correlation between determination coefficients and the number of regressors, presented in terms of correlation coefficient, t-value associated to correlation coefficient and its p-value, are shown in Table 3.

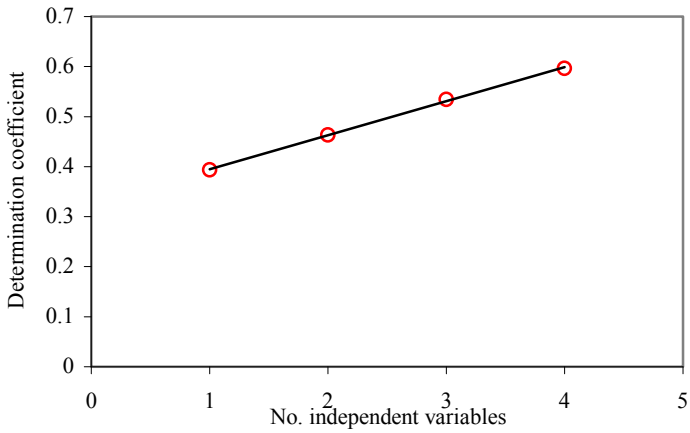

Figure 1. The dependence between r^2 and the number of independent variables for *1 ≤ x ≤ 4*

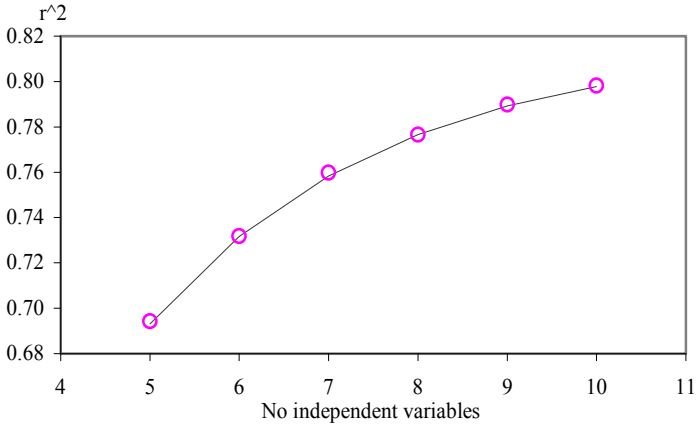

Figure 2. The dependence between r^2 and the number of independent variables for *4 < x ≤ 10*

Table 3. Summary of linear relation between determination coefficient and the number of independent variables

x	r	t-value	p-value
3	> 0.9999	282.72	$1.13 \cdot 10^{-3}$
4	0.9996	47.95	$2.17 \cdot 10^{-4}$
5	0.9970	22.45	$9.68 \cdot 10^{-5}$
6	0.9964	23.54	$9.66 \cdot 10^{-6}$
7	0.9907	16.31	$7.90 \cdot 10^{-6}$
8	0.9808	12.31	$8.75 \cdot 10^{-6}$
9	0.9690	10.38	$8.37 \cdot 10^{-6}$
10	0.9557	9.19	$7.96 \cdot 10^{-6}$

x = number of regressors; r = correlation coefficient;
t-value = Student statistics associated to r;
p-value = significance associated to Student statistics

The present study was aimed to answer to the following questions: "How many regressors (independent variables) are needed to obtain a certain determination of retention times as a function of mycotoxins properties?" and "Which is the type of relation between the determination coefficient and the number of regressors able to estimate the mycotoxins retention times?". The answers are as follows.

All linear regression models, able to explain the retention times as function of investigated mycotoxins properties, where selected such as to accomplish the Hawkins principles [24]: highest correlation coefficient, highest Fisher parameter, lowest standard error of the estimate, and smallest possible number of significant parameters ($n = 5 \cdot v$, where n = sample size, v = number of variables in the model).

As expected, the highest determination coefficient was obtained by a linear regression model with 10 independent variables. The number of acceptable models, identified for a given number of independent variables, varied, for the studied mycotoxins, from 2 to 9 (e.g., for v=8; 2 models while for v=10; 9 models). Naturally, the number of regressions increases with the number of independent variables as well as the possible combinations of variables; in the present experiment, we limited the investigation at 10 independent variables. Within such limits, no linear dependence between the number of independent variables and the number of significant models could be identified on linking the retention times with mycotoxin selected properties.

The results are as follows:

- The most important increase in determination coefficient is observed when one independent variable is used, followed by the case when 5 and respectively 2 independent variables were used.

- The highest difference is observed when the best 4-regressors model was compared to the best 5-regressors model. The observed difference in determination coefficient was of 0.0978. This observation suggest that the highest number of regressors to be used in investigation of the retention times as function of mycotoxin properties must not exceed 5. The use of more than 6 regressors is useless and will not bring a significant increasing of the determination coefficient in explaining the retention times as function of mycotoxin properties.
- The most frequent mycotoxin property able to explain the retention times proved to be the polarizability (it appears in all models with one exception, the model with 3 independent variables), closely followed by the molecular volume (it appears in all models with two exceptions, the model with one independent variable and the model with three independent variables) and the inverse of hydration energy (it appears in all model with more than three variables) (Table 2).

The relationship between retention times and structural properties of mycotoxins has previously been studied. A set of 15 toxins with the trichothecene nucleus was investigated by applying a ComMFA ($r^2 = 0.921$) [25]. Khosrokhavar et al. [26] had identified, on a set of 67 mycotoxins, a multiple linear regression model with a determination of 0.931 that included the following descriptors: the octanol/water partition coefficient, electronic energy, dipole length, and the LUMO energy. It is no doubt that the models reported in literature are better than models presented in this paper, in terms of determination coefficient. However, the identification of the linear relationship between the retention times and the investigated properties was performed in order to answer to the research questions.

As far as dependence between the number of regressors and determination coefficient was concerned, the performed analysis revealed the following:

- The identified linear model (presented in Eq(1)) as well as the exponential model (presented in Eq(2)) proved to be statistically significant ($F > 2200$).
- The linear relationship was identified if the applied cutoff was set at 4 regressors. For this regression, 99.91% of the variation of determination coefficient proved to be explained by a linear relationship with the number of regressors (Eq(1)). The cutoff set to 5 regressors also led to a statistically significant linear regression between the number of regressors and determination coefficient. In this case, 99.41% of variation in determination coefficient could be explained (Eq(3)). Although the models presented in Eq(1) and Eq(3) are statistically significant, the F-statistics is almost 5 times smaller if the cutoff is set at 5 regressors compared to a cutoff set at 4 descriptors.

- The best relationship between the determination coefficient and regressors proved to be of exponential type. Almost 100% from variation of determination coefficient could be explained, with a number of regressors between $4 < x \leq 10$ (Eq(2)).

As far as the results presented in Table 3 are concerned, the minimum value of the significance was obtained for $1 \leq x \leq 7$ ($p = 7.90 \cdot 10^{-6}$). This means that the maximum number of regressors able to explain the relationship between retention times and investigated mycotoxin properties must not exceed 7.

The present study was aimed to provide answers to two main research questions: "How many regressors (independent variables) are needed to obtain a certain determination of retention times as a function of mycotoxin properties?" and "Which is the type of relation between the determination coefficient and the number of regressors in case of linear regressions?". Valid answers were identified and the aim of the research was reached. However, a new questions arise: "Is the cutoff maintained as far as the number of regressors is concerned dependent by the sample size?", "The exponential relationship between the determination coefficient and the number of regressors is valid only for the investigated set of structures or it is obeyed to any sets of compounds?" Current research in our laboratory is aimed to answer to these new questions.

CONCLUSIONS

In the present study, the dependence of maximum value of determination coefficient of the number of regressors, as well as the type of this relationship were investigated on a set of 65 mycotoxin properties. The most frequent mycotoxin properties able to explain the retention times proved to be the polarizability, closely followed by the molecular volume and inverse of hydration energy. The highest number of regressors to be used in investigation of the retention times as function of mycotoxin properties needed do not exceed 5. As far as the dependence between number of regressors and determination coefficient was concerned linear, the cutoff was set at 4, or > 4 for an exponential dependence. The obtained results must be verified on other classes of compounds and other dependent or independent variables in order to be extrapolated.

EXPERIMENTAL SECTION

A sample of 65 mycotoxins was included in the present study. The structures of the mycotoxins were downloaded from PubChem. The name of the investigated mycotoxins and the PubChem compound identifier (CID) is listed in Table 4.

A home made *.php program was used to transform the *.sdf files in *.hin files. Another *.php program was used to prepare the structures for modeling. This program used the HyperChem, release 8, software to prepare the mycotoxins for modeling. A three-step protocol was implemented in this respect: ▪ obtain the 3D structure of mycotoxins (1st step); define the molecular mechanics model (AMBER) and optimize the molecular structure (AM1 method [27], Polak-Ribiere algorithm [28]) (2nd step); ▪ minimize the energy (3rd step).

Table 4. Mycotoxins and treir retention times

	Compound	CID	t_R (min)
Aflatoxins and their precursors			
1	Aflatoxicol I	104744	12.45
2	Aflatoxin B_1	14403	11.50
3	Aflatoxin B_2	2724360	10.33
4	Aflatoxin B_2 α	23648	6.60
5	Aflatoxin G_1	14421	10.16
6	Aflatoxin G_2	2724362	8.97
7	Aflatoxin G_2α	105095	5.00
8	Aflatoxin M_1	23236	7.21
9	Austocystin A	115307	21.57
10	Averufin	131171	25.65
11	5-Methoxysterigmatocystin	5379210	18.02
12	Demethyl-diacetyl-sterigmatocystin	151544	17.70
13	Methoxysterigmatocystin	5351257	15.03
14	Sterigmatocystin	5280389	18.91
15	Norsolorinic acid	25102	31.08
16	Parasiticol	90905	10.73
Trichothecenes			
1	Nivalenol	31829	1.27
2	Fusarenone X	31763	2.35
3	Deoxynivalenol	430147	1.54
4	3-Acetyldeoxynivalenol	104759	5.21
5	15-*O*-Acetyl-4-deoxynivalenol	16218854	5.10
6	Scirpentriol	73495	1.82
7	15-Acetoxyscirpenol	105023	7.40
8	Diacetoxyscirpenol	422111	11.28
9	3α-Acetyldiacetoxyscirpenol	11969469	15.56
10	Neosolaniol	72650	3.19
11	HT-2 Toxin	73050	13.69
12	T-2 Toxin	44575871	17.06
13	Acetyl-T-2 toxin	3034766	21.12
14	Trichodermin	20806	16.13
15	Trichodermol	114680	9.69
16	7-α-Hydroxytrichodermol	127380	2.59
17	Verrucarol	5660	2.89
18	4,15-Diacetylverrucarol	6451372	14.15
19	Trichothecin	260779	16.29
20	Trichothecolone	107974	3.63
21	Trichoverrol A	6440574	10.16

	Compound	CID	t_R(min)
Roquefortines			
1	Agroclavine-1	73484	17.00
2	Auranthine	130919	10.51
3	Aurantiamine	375594	10.49
4	Chanoclavine-I	5281381	8.59
5	Costaclavine	160462	17.00
6	Cyclopenin	73525	11.60
7	Cyclopenol	101201	6.20
8	Cyclopeptin	n.a.	12.05
9	Dihydroergotamine	10531	18.60
10	Elymoclavine	11051	5.34
11	Epoxyagroclavine-1	133945	10.00
12	Ergocristine	31116	25.10
13	Ergotamine	3251	19.60
14	Fumigaclavine C	173878	21.40
15	Marcfortine A	433181	19.59
16	Marcfortine B	n.a.	17.39
17	Meleagrin	6437857	18.90
18	Oxaline	6438440	21.60
19	Pyroclavine	3083578	14.81
20	Roquefortine C	21608802	20.50
21	Roquefortine D	n.a.	6.09
22	Rugulovasine A and B	115153	8.43
23	Secoclavine	n.a.	20.40
24	α-Ergocryptin	134551	19.20
Ochratoxins			
1	Ochratoxin α	107911	5.60
2	Ochratoxin B-methyl ester	609664	20.00
3	Ochratoxin B-ethyl ester	609665	19.41
4	Ochratoxin α-methyl ester	n.a.	16.16

n.a. = not available in PubChem (these mycotoxins were drawn with HyperChem v. 8.0).

The following properties were evaluated by HyperChem to be the regressors for modeling the retention times (experimental values were taken from ref. [29]) of the investigated mycotoxins: negative value of the total-energy (abbreviated as *negte*), dipole moment (*dm*), negative value of the scf-atom-energy (*negsae*), negative value of the scf-binding-energy (*negsbe*), scf-core-energy (*sce*), negative value of the scf-electronic-energy (*negsee*), heat-of-formation (*hf*), molecular weight (*MW*), surface area (*SA*), surface area grid (*SAG*), volume (*Vol*), hydration energy (HydE), octanol-water partition coefficient (*LogP*), refractivity (*Refr*) and polarizability (*Pol*). The corresponding abbreviations are listed at the bottom of Table 2.

Since the expression of dependence of the retention times vs. one ore more mycotoxin properties could be inversed or logarithmical, the search was extended by including the following regressors: LogP, InvlogP, HydE, InvHydE, Invhf, Pol, LnPol, LnRefr, Vol, InvVol, LnVol, SAG, MW, InvMW, LnMW, negte, dm, negsae, negsbe, sce, negsee, Invnegte, Invdm, Invnegsae, Invnegsbe, Invsce, Invnegsee, Lnnegte, Lndm, Lnnegsae, Lnnegsbe, Lnsce, and Lnnegsee (where `ln` is for natural logarithm and `inv` for inverse value).

A home made *.php program was developed in order to identify the best regression (the main criterion used was r^2 = max, where r^2 is determination coefficient) for every number of regressors (abbreviated as *x*, $1 \leq x \leq 10$). Other objective of the current research was to find the model of the dependence between the determination coefficient and the number of regressors. The SlideWrite software was used in order to identify non-linear relationships (a significance level of 5% was used).

ACKNOWLEDGEMENTS

This paper is dedicated to Prof. Simion GOCAN on the occasion of his 80th birthday.

REFERENCES

1. N.W. Turner, S. Subrahmanyam, S.A. Piletsky, *Anal. Chim. Acta,* **2009**, *632(2)*, 168.
2. J.L. Richard, *Int. J. Food Microbiol.,* **2007**, *119(1-2)*, 3.
3. H.S. Hussein, J. M. Brasel, *Toxicology,* **2001**, *167(2)*, 101.
4. M. Reverberi, A. Ricelli, S. Zjalic, A.A. Fabbri, C. Fanelli, *Applied Microbiology and Biotechnology,* **2010**, *87(3)*, 899.
5. W.P. Blount, *Journal of the British Turkey Federation,* **1961**, *9*, 55.
6. M.C. Lancaster, F.P. Jenkins, J.M. Philp, *Nature,* **1961**, *192*, 1095.
7. F.G. Peers, C.A. Linsell, *Ann. Nutr. Aliment.,* **1977**, *31*, 1005.
8. E. Karunasena, M.D. Larrañaga, J.S. Simoni, D.R. Douglas, D.C. Straus, *Mycopathologia,* **2010**, *170(6)*, 377.
9. B.B. Jarvis, J.D. Miller, *Appl. Microbiol. Biotechnol.,* **2005**, *66(4)*, 367.

10. A.A. El-Banna, J.I. Pitt, L. Leistner, *Systematic and Applied Microbiology,* **1987**, *10(1)*, 42.
11. M. Kokkonen, M. Jestoi, A. Rizzo, *International Journal of Food Microbiology,* **2005**, *99(2)*, 207.
12. D.L. Arnold, P.M. Scott, P.F. McGuire, *Food and Cosmetics Toxicology,* **1978**, *16(4)*, 369.
13. I.M.L.D. Storm, J.L. Sørensen, R.R. Rasmussen, K.F. Nielsen, U. Thrane, *Stewart Postharvest Review,* **2008**, *4(6)*, 1.
14. O.O.M. Iheshiulor, B.O. Esonu, O.K. Chuwuka, A.A. Omede, I.C. Okoli, I.P. Ogbuewu, *Asian Journal of Animal Sciences,* **2011**, *5(1)*, 19.
15. R.R. Paterson, N. Lima, *EXS,* **2010**, *100*, 31.
16. A. Pfohl-Leszkowicz, *Arhiv za Higijenu Rada i Toksikologiju,* **2009**, *60(4)*, 465.
17. A.K. Bingham, T.D. Phillips, J.E. Bauer, *J. Am. Vet. Med. Assoc.,* **2003**, *222(5)*, 591.
18. R. Krska, *Analytical and Bioanalytical Chemistry,* **2009**, *395(5)*, 1203.
19. G.H. Degen, *Journal of Veterinary Pharmacology and Therapeutics,* **2009**, *32 (SUPPL. 1)*, pp. 28.
20. C. Raghavender, B. Reddy, *World Mycotoxin Journal,* **2009**, *2(1)*, 23.
21. P. Khlangwiset, F. Wu, *Food Addit. Contam. Part A Chem. Anal. Control Expo. Risk Assess.,* **2010**, *27(7)*, 998.
22. F. Wu, P. Khlangwiset, *Food Addit. Contam. Part A Chem. Anal. Control Expo. Risk Assess.,* **2010**, *27(5)*, 658.
23. D.L. Park, T.C. Troxell, *Adv. Exp. Med. Biol.,* **2002**, *504*, 277.
24. D.M. Hawkins, *J. Chem. Inf. Comput. Sci.,* **2004**, *44(1)*, 1.
25. W.E. Steinmetz, C.B. Rodarte, A. Lin, *European Journal of Medicinal Chemistry,* **2009**, *44(11)*, 4485.
26. R. Khosrokhavar, J.B. Ghasemi, F. Shiri, *International Journal of Molecular Sciences,* **2010**, *11(9)*, 3052.
27. M.J.S. Dewar, E.G. Zoebisch, E.F. Healy, J.J.P. Stewart, *J. Am. Chem. Soc.,* **1985**, *107*, 3902.
28. B. Polak, G. Ribiere, *Rev. Fr. Imform. Rech. Oper.,* **1969**, *16*, 35.
29. K.F. Nielsen, J. Smedsgaard, *J. Chromatog. A,* **2003**, *1002*, 111.

STUDIA UBB CHEMIA, LVI, 1, 2011

EVALUATION OF A RURAL SETTLEMENT WELL WATERS BASED ON THE QUANTIFICATION OF SOME PHYSICAL AND CHEMICAL PARAMETERS. A CASE STUDY

LADISLAU KÉKEDY-NAGY[a] AND GYÖNGYI PETŐ[a]

ABSTRACT. Water samples from 30 wells from Remetea Oaşului village (Satu Mare county, Romania) have been characterized by the determination of 2 physical parameters (temperature and electrical conductivity) and of 19 chemicals (the Na, K, Li, Rb, Ca, Mg, Zn, Cu, Fe, Pb, Cd, Cl^-, NO_3^-, NH_4^+, SO_4^{2-} content, pH, total hardness (D,°G), alkalinity (Alk.) and chemical oxygen demand (COD). The chemical composition of the waters shows their suitability for household and agriculture purposes. Among the determined constituents only the Cd, Cu and NO_3^- content exceed the concentration limits for drinking water, being inappropriate for human and animal consumption. The hierarchical cluster analysis shows that the water samples are classified best based on the Pb, Cd, Zn, Cu, COD content, the well waters are grouped in 5 clusters. The waters can be only partially classified; wells from different zones are not separated. Considering the most eight significant variables, they are grouped in two factors, which cover 90.78 % of the total variance.

Keywords: *well water, chemical composition, pollution, cluster analysis, factor analysis*

INTRODUCTION

The freshwater plays a vital role in our life and in the everyday (industrial, agronomical and household) activity. In our days, the water consumption exhibits an increasing trend worldwide; being obtained from surface and underground sources. For rural and remote settlements the driven or sunken wells assure the water for everyday use, including for human and animal consumption. The quality and the quantity of the available drinking water from healthcare point of view are considered as one of the measure of the wellbeing and civilization [1]. From this point of view the drinking water must fulfill the most restrictive conditions, including the physical, chemical and biological parameters. The United Nations World Health Organization (WHO), the European Union's as well as the Romanian legislations set exactly the quality of the drinking water, the nature and the quantity of different substances that could be contained [2]. The characteristics of well waters are diverse,

[a] *Universitatea Babeş-Bolyai, Facultatea de Chimie şi Inginerie Chimică, Str. Kogălniceanu, Nr. 1, RO- 400084 Cluj-Napoca, Romania, lkekedy@chem.ubbcluj.ro*

depending on many factors, such as: geological structure of the rocks and their chemical composition, the position of the aquifer layer, the environmental temperature, the geochemical reactions, meteorological conditions and on the mode of water extraction, human activity, etc. Usually, the water brought to the surface is used for different purposes without any further treatment, despite of its physical, chemical and biological characteristics. For the unequivocal characterization of the waters a series of standardized determinations must be carried out [3-5]. From the data one can predict the utility of the water, the effect on the health, the chemical composition of the rocks, including the aquifers, the origin of the water source, etc.

In order to reveal of the hidden relationships among the data statistical and chemometrical methods are employed efficiently in large scale [6]. The cluster-, factor- and principal component analysis, as well as the linear discriminant analysis allow the classification of the waters based on the physical and chemical data; to establish the similarity among the water sources; to get the main parameters on which the classification is performed; to identify the aquifer layers, the pollutants, etc. [7-13].

The aim of this work is to evaluate the well water quality of a rural settlement, to identify the most frequent inorganic pollutants by the quantification of the inorganic components and to estimate the structure of the aquifer layers. In order to reveal the hidden relationships the chemometric approach of the data has been proposed.

RESULTS AND DISCUSSION

The results of the quantification data are summarized in the Tables 1-3.

Water samples exhibit medium hardness and salinity, with low organic matter content. The NH_4^+-ion is present only in 4 samples (noted 9, 11, 26 and 27) probably due to infiltration of manure liquor. The NO_3^--ion is present in all samples, exceeding many times the maximum allowable quantity of 44.2 mg/L sets by WHO for drinking water. The infiltration of the long term used ammonium nitrate as fertilizer could be responsible for this fact. The Cd content of the waters is also too high for drinking water, exceeding with about two orders of magnitude the WHO set value (0.003 mg/L). The abnormal high Cd-content is the consequence of the corrosion of the galvanized iron pipes and buckets used for water outtake. Taking into account the high Cd and NO_3^--ion content it is not recommended to use these waters for human and animal consumption.

In order to reveal the hidden relationships among the parameters, and to classify the wells, first the cluster analyses have been performed. Three of the parameters were excluded from the calculations (T, Rb and NH_4^+ content), being irrelevant. The tree diagram (the Euclidean distance as similarity measure and complete linkage) is presented in the Figure 1.

Table 1. The physical data of the well water samples

Sample	Zone	T (°C)	pH	D (°G)	TDS	Alk.	COD
					(mg / L)		
1	**A1**	1	7.24	13.0	188	4.04	1.62
2	**A1**	3	6.94	5.8	68	2.10	1.75
3	**A1**	1	7.10	12.7	160	3.90	3.24
4	**A1**	1	7.12	27.3	402	6.20	3.16
5	**A1**	0	7.03	8.4	150	2.74	3.00
6	**B**	4	6.97	18.4	206	5.16	0
7	**B**	5	6.36	6.47	82	1.50	1.22
8	**B**	1	6.54	22.3	355	3.70	1.00
9	**B**	1	6.71	9.3	142	1.88	4.05
10	**B**	1	6.74	28.0	355	5.13	1.62
11	**B**	4	7.01	26.3	316	6.65	1.75
12	**B**	5	7.03	14.4	159	4.33	1.38
13	**B**	3	6.62	13.0	211	2.03	1.75
14	**C1**	1	6.81	11.5	203	2.91	1.46
15	**C1**	3	6.90	13.0	308	4.14	3.73
16	**C2**	0	5.90	1.9	23	0.34	2.19
17	**C2**	2	7.10	14.8	164	4.68	1.21
18	**C2**	1	6.53	18.0	329	1.80	2.03
19	**C2**	2	6.90	23.2	340	4.97	3.80
20	**C2**	2	6.47	13.0	247	3.13	2.43
21	**C2**	2	7.26	22.5	297	5.55	2.84
22	**C2**	1	7.26	9.6	157	2.86	2.35
23	**A2**	3	6.72	15.8	281	4.00	2.02
24	**A2**	1	6.83	11.0	149	2.89	4.05
25	**A2**	5	6.90	17.8	267	3.46	1.05
26	**A2**	3	7.05	8.6	115	1.20	3.80
27	**A2**	2	7.37	26.3	363	3.12	3.32
28	**A2**	1	7.41	31.3	490	7.24	4.21
29	**A2**	3	7.44	14.3	148	3.84	2.68
30	**A2**	3	6.44	35.0	491	2.64	2.84

Table 2. The metal content of the well water samples

Sample	Zone	Concentration (mg / L)					
		Na	K	Rb	Mg	Ca	Cu
1	**A1**	29	3.1	0	26.2	27.4	1.4
2	**A1**	7.4	2.5	0	4.5	7.9	1.4
3	**A1**	15.8	6.8	0	26.2	43.3	1.5
4	**A1**	90.3	4.3	0	36.2	66.5	1.4
5	**A1**	38.5	14.6	0	12.7	27.0	1.4
6	**B**	20.0	1.4	0	28.4	57.0	1.5
7	**B**	12.0	0.8	0	8.5	16.0	1.4
8	**B**	72.5	0.7	0	26.8	62.4	1.5
9	**B**	19.8	6.0	0	12.4	34.7	1.6

Sample	Zone	Concentration (mg / L)					
		Na	K	Rb	Mg	Ca	Cu
10	**B**	34.2	4.8	0	38.8	67.4	1.5
11	**B**	44.6	2.7	0	40.9	59.7	1.5
12	**B**	14.2	0.5	0	18.8	48.8	1.6
13	**B**	39.1	17.9	0	15.4	16.0	1.6
14	**C1**	31.1	49.5	0.1	15.4	19.7	1.5
15	**C1**	45.3	113	0.1	21.3	19.2	1.6
16	**C2**	2.5	2.2	0	4.6	3.8	1.5
17	**C2**	20.4	24.8	0	25.4	37.0	1.5
18	**C2**	80.5	13.6	0	21.2	14.7	1.6
19	**C2**	48.5	22.2	0	30.5	42.9	1.6
20	**C2**	29.2	67.7	0.1	18.5	14.7	1.7
21	**C2**	43.2	36.9	0	33.0	43.3	1.7
22	**C2**	28.7	32.2	0	13.0	16.0	1.7
23	**A2**	52.3	57.6	0.1	19.5	30.6	1.6
24	**A2**	31.5	15.7	0	14.3	9.2	1.7
25	**A2**	31.2	31.1	0	27.0	34.7	1.7
26	**A2**	5.6	6.3	0	11.6	33.8	1.8
27	**A2**	46.8	14.2	0	40.5	65.1	1.7
28	**A2**	84.6	3.3	0.1	56.5	72.9	1.8
29	**A2**	16.2	2.0	0	24.3	42.9	1.9
30	**A2**	73.2	1.6	0	55.1	78.3	1.7

Table 3. The metal and the anion content of the well water samples (cont.)

Sample	Zone	Concentration (mg / L)						
		Zn	Pb	Cd	NH_4^+	Cl^-	SO_4^{2-}	NO_3^-
1	**A1**	0.48	0.0001	0.42	0	33.0	20.0	119.3
2	**A1**	0.52	0.0002	0.04	0	2.2	0.0	25.7
3	**A1**	0.52	0.0002	0.04	0	12.7	17.7	64.8
4	**A1**	0.52	0.0002	0.39	0	128.8	27.6	445.2
5	**A1**	3.41	0.0002	0.45	0	27.7	10.0	172.7
6	**B**	0.65	0.0002	0.39	0	12.5	0.0	209.1
7	**B**	0.45	0.0001	0.55	0	6.8	8.8	106.1
8	**B**	0.45	0.0002	0.36	0	146	10.0	589.2
9	**B**	0.45	0.0002	0.33	0.1	35.5	14.6	201.6
10	**B**	0.45	0.0002	0.42	0	111.0	29.7	342.5
11	**B**	0.45	0.0001	0.80	0.1	47.7	27.4	57.0
12	**B**	0.68	0.0002	0.17	0	6.0	0.0	48.7
13	**B**	0.45	0.0002	0.33	0	62.0	14.1	973.4
14	**C1**	0.62	0.0003	0.61	0	38.5	18.2	524.2
15	**C1**	0.68	0.0002	0.77	0	73.2	29.4	682.8
16	**C2**	0.62	0.0003	0.77	0	2.1	16.7	114.5
17	**C2**	0.62	0.0002	1.27	0	3.6	0.0	212.6
18	**C2**	0.68	0.0019	0.61	0	154.0	29.2	831.7
19	**C2**	0.68	0.0003	0.30	0	73.4	29.4	837.3
20	**C2**	0.65	0.0001	0.30	0	62.0	25.2	640.8

Sample	Zone	Concentration (mg / L)						
		Zn	Pb	Cd	NH_4^+	Cl^-	SO_4^{2-}	NO_3^-
21	**C2**	0.68	0.0001	1.14	0	71.8	20.9	44.3
22	**C2**	0.75	0.0002	0.52	0	24.6	0.0	328.5
23	**A2**	0.91	0.0002	0.64	0	80.2	9.4	690.0
24	**A2**	0.75	0.0002	0.83	0	35.6	0.0	108.6
25	**A2**	1.34	0.0002	0.42	0	77.6	2.7	643.5
26	**A2**	1.11	0.0002	0.04	0.2	47.0	1.2	368.3
27	**A2**	0.94	0.0002	0.39	0.1	182.4	29.3	290.8
28	**A2**	0.81	0.0003	0.39	0	192.4	20.9	235.7
29	**A2**	0.75	0.0000	0.23	0	7.7	0.0	481.7
30	**A2**	1.27	0.0002	0.26	0	260	30.1	1060

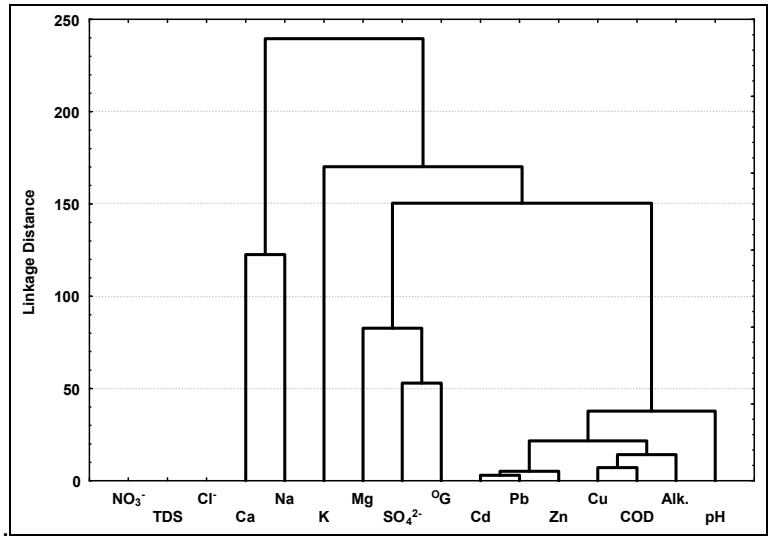

Figure 1. The tree diagram for the 16 variables considered

The variables are grouped in 5 groups, according to linkage distances, the greatest distances being for NO_3^-, TDS and Cl^- (in descending order), variables, less proper for classification. The most suitable variables for this purpose are Cd, Pb, Zn, Cu and COD content of the water samples. Significant correlation exists between the variables Na and Cl^--ion content (r = 0.83) and Mg and Ca content (r = 0.87), respectively. Using all the 16 variables the classification of the wells (cases) is represented in the Figure 2.

The diagram shows that the wells have close similar chemical composition, being grouped in 4 main groups. Wells from different zones, some of them situated at 200-300 m distance to each other, take part close, in the same subgroup. This suggests that the wells are feed by the same

aquifer layers, they communicate between each other (an important feature of public health aspect). The differences seem to appear mainly due to the distinct mode of exploitation by the owners, such as the distinct frequency and water withdrawal quantity from the well.

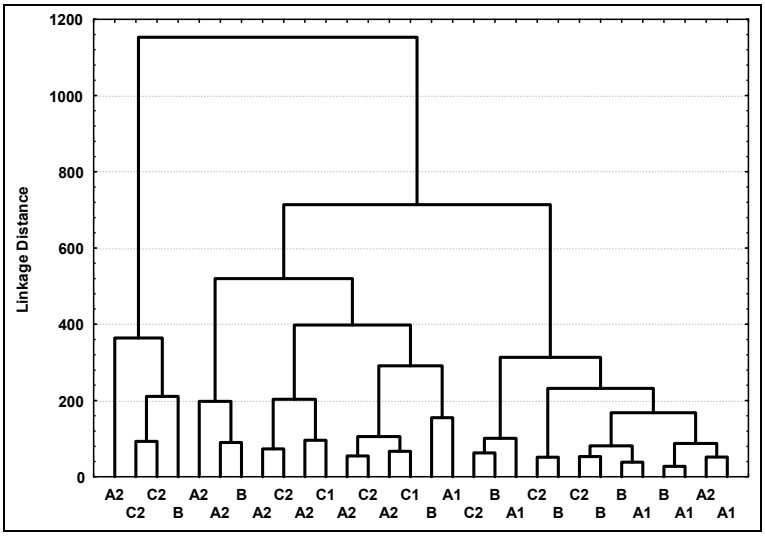

Figure 2. The tree diagram for the 30 well water samples

In the next step the factor analysis was carried out. Based on the scree plot data, 5 factors were retained, also the first three factors cover 95.77 % of the variance. The factor loadings for each variable are synthesized in the Table 4.

Table 4. Factor Loadings (Varimax normalized)

	Factor 1	Factor 2	Factor 3	Factor 4	Factor 5
pH	0.207563	**0.770780**	0.236369	0.008961	0.215662
Alk.	**0.667291**	0.598495	-0.112624	0.233278	-0.110554
COD	0.129281	0.072931	0.638477	0.075670	0.412815
^{O}G	**0.971984**	0.103140	0.060046	-0.081636	-0.079986
TDS	**0.967382**	-0.101480	0.175258	0.079374	-0.009263
Na	**0.851140**	-0.277206	0.051300	0.138125	0.179426
K	-0.083540	-0.149300	0.398450	**0.790085**	-0.068063
Mg	**0.933271**	0.231893	0.086673	-0.073718	-0.042683
Ca	**0.816476**	0.351372	-0.022124	-0.344708	-0.048337
Cu	0.106008	0.113988	**0.859824**	-0.067920	-0.055023
Zn	-0.045120	-0.004045	0.063097	-0.053661	**0.882874**

	Factor 1	Factor 2	Factor 3	Factor 4	Factor 5
Pb	-0.163514	0.647606	0.126985	-0.072130	-0.196369
Cd	0.043922	0.085520	-0.274024	**0.798977**	0.005318
Cl^-	**0.842973**	-0.339580	0.244909	-0.119279	0.098616
SO_4^{2-}	0.659487	-0.349934	0.023661	0.244843	0.002926
NO_3^-	-0.346795	0.651629	-0.433585	-0.044882	0.139131

highlighted loadings > 0.700

The first factor (covering 62.08 %, includes the variables Alk., D(^{O}G), TDS, Na, Mg, Ca and Cl^-, the main components of the waters; the second one includes only the pH (covering 28.68 % of total variance), the followings each includes only one variable: Cu, Cd, and Zn, respectively.

CONCLUSIONS

The well waters take part of medium mineralized and hardness waters, being suitable for household and agriculture purposes. The high Cd and NO_3^--ion content make the waters unsuitable for human and animal consumption. The well waters have similar chemical composition, the wells being fed by the same aquifer layers. The hierarchical cluster analysis shows that the waters could be classified best based on the Pb, Cd, Zn, Cu, COD content; the wells being grouped in 5 clusters. They can be only partially classified; wells from different zones could not be separated. 8 variables could be grouped in two factors, which cover 90.78 % of the total variance.

EXPERIMENTAL SECTION

Selection of the settlement

In order to get representative results, the followings were taken into account in the selection of the sampling site: to have a population greater than 500 inhabitants, the freshwater water supply realized by wells, constant everyday water consumption. All these conditions were fulfilled by Remetea Oaşului village (Satu Mare county), located in the north-western part of Romania with the following geographic coordinates: Latitude - 47° 52' 60 N, Longitude - 23° 19' 0 E, altitude: 200 m above the sea level. The village lies in the Tur-stream valley, surrounded by 50-100 m high hills, with about 600 habitants. The people deal with animal breeding, plant cultivation; the well waters are used for agricultural, stock-raising, household purposes, including human and animal consumption. The wells are placed usually in the farmyards, and are covered with lids; the water is brought to the surface using metal buckets or immersion pumps.

Sampling and sample handling

Waters of 30 private wells from village were sampled. Three different zones of the settlement were selected, situated evenly along the main- and the neighboring side roads plots. There were collected 13 samples from the southern zone (labeled A), 8 samples from the northern zone (labeled B) and 9 samples from the central zone (labeled C) of the village. The samples were collected during November 2007 period in according to the EPA prescriptions: collected in 500 mL PET bottles, conserved on the spot with 1 mL of conc. HNO_3 and kept at 4 °C.

Instrumentation

The quantification of the metals was carried out with a Perkin Elmer 373 (Waltham, MA, USA) flame atomic absorption spectrophotometer. The original burner head for C_2H_2 – air flame was replaced with a home made one for CH_4 – air flame [14]. The instrumental parameters for each element were optimal, set as indicated in the manufacturer's prospect. The chloride-ion content, the alkalinity (Alk.) and the total hardness (D) were determined by potentiometric titration (670 Titroprocessor, Mettler, Herisau, Swiss). The electric conductivity was quantified by using an OK – 102/1 (Radelkis, Budapest, Hungary) conductometer. The total dissolved salts (TDS) values were calculated by converting the conductivity data. The chemical oxygen demand (COD) has been determined by using the Kubelka method. The quantification of the SO_4^{2-}, NO_3^- and NH_4^+ ions were performed in molecular absorption mode, at λ = 490 nm, 210 nm and 401 nm respectively, using a double beam UV-Vis spectrophotometer (T80+, PG Instruments Ltd., UK) [3, 4].

Chemicals

All stock standard solutions were of 1000 mg/L, prepared from RbCl, CsCl, Li_2CO_3 (Merck, Darmstadt, Germany), NaCl, KCl, KNO_3, NH_4Cl (Reactivul, Bucuresti, Romania), $CaCO_3$, Cd, Fe, Cu, Zn and Mg (Specpure, Johnson Matthey Chemicals Limited, England), HCl, H_2SO_4, HNO_3 (analytical grade, Merck, Darmstadt, Germany)), respectively. The calibration solutions were obtained by diluting a given volume of stock solution with double distilled water. The diluted solutions were prepared just before measurements. $KMnO_4$, $C_2H_2O_4.2H_2O$, $AgNO_3$ and EDTA 0.1 N solutions are all manufacturer-made volumetric solutions and were used as received (Reactivul, Bucharest, Romania).

Procedure

The temperature, electric conductivity and the pH values were determined in the field; the other parameters were quantified in the laboratory. For the flame AES, AAS and spectrophotometric quantifications the standard calibration method was used in all cases. The titrations were carried out in the

dynamic automatic titration mode, using appropriate potentiometric sensors. Three parallel measurements were made, the mean, and the SD were calculated. The statistical and chemometrical processing of the data was carried out by using the Statistica software program, version 6, (StatSoft.Inc., OK, USA).

REFERENCES

1. C. Baird, *Environmental Chemistry* (2nd edition), W.H. Freeman & Company, New York, **1999**, chapter 2.
2. Ordin 161/16.02.2006, Normativ privind clasificarea calității apelor de suprafață în vederea stabilirii stării ecologice a corpurilor de apă.
3. L.S. Clesceri, A.E. Greenberg, R.R. Trussel (Eds.), *Standard Methods for examination of water and wastewater*, 17th Edition, APHA – AWWA – WPCF, **1989**, chapter 6.
4. W. Fresenius, K.E. Quentin, W. Schneider (Eds.), *Water Analysis*, Springer-Verlag, Berlin, Heidelberg, New York, London Paris Tokyo, **1987**, chapter 3.
5. United Nations Environment Programme, *Analytical Methods for Environmental Water Quality*, UNEP Global Environment Monitoring System (GEMS)/Water Program and International Atomic Energy Agency, New York, **2004**, chapter 4.
6. R.G. Brereton, *Applied Chemometrics for Scientists*, John Wiley & Sons Ltd, Chichester, **2007**, chapter 4.
7. M.L. Wu, Y.S. Wang, C.C. Sun, et al., *Oceanologia*, **2009**, *51*, 217.
8. H. Juahir, T.M. Ekhwan, S.M. Zain, et al., *American-Eurasian J. Agric. & Environ. Sci.,* **2008**, *4*, 258.
9. A.R. Kumar, P. Riyazuddin, *Current Sci.,* **2008**, *94*, 1012.
10. E. Vončina, D.B. Vončina, N. Mirkovič, et al., *Acta Chim. Slov.,* **2007**, *54,* 119.
11. R. Bro, *Anal. Chim. Acta*, **2003**, *500*, 185.
12. T. Jerič, A.M.L. Marechal, D. Kavšek, A.D.B. Vončina, *Nova Biotech*., **2009**, *9*, 155.
13. A.R. Kumar, P. Riyazuddin, Curr. Sci., **2008**, *94*, 1012.
14. E.A. Cordoş, L. Kékedy-Nagy*, Studia UBB Chemia*, **1992**, *37*, 61.

STUDIA UBB CHEMIA, LVI, 1, 2011

STRUCTURAL INVESTIGATIONS OF AG_2O-B_2O_3-CAO-P_2O_5 GLASS AND GLASS-CERAMIC SYSTEM

RĂZVAN ŞTEFAN*[a], IOAN BRATU[b], GHEORGHE BORODI[b], NICOLAE LEOPOLD[c], VIORICA SIMON[c]

ABSTRACT. The paper investigated the $1.5Ag_2O \cdot 98.5[0.47B_2O_3(0.53\text{-}x)\ CaOxP_2O_5]$ system prepared in vitreous state using the rapid melt quenching method. In order to obtain glass-ceramic samples, the glass was heat treated to 650ºC during 6 hours. The structural units BO_3 and BO_4 which build the vitreous network and the modifications occurred following partial crystallization were clearly highlighted by Raman and IR spectroscopy. The analysis by X-ray diffraction showed the vitreous features of the samples before the heat treatment and reveals that the crystalline phase developed into the vitreous matrix is $Ca_{10}\ (PO_4)_6\ (OH)_2$. The structural changes before and after the heat treatment have been investigated considering the B_2O_3/P_2O_5 ratio.

Keywords: *glass, glassceramic, phosphorous oxide, silver*

INTRODUCTION

The boron oxide was generally studied [1-4] due to its capacity to build vitreous network. The main structural units in glass were identified and has been demonstrated that the boron may be tetra- and three coordinated. The oxide matrix on B_2O_3 are used in tissue engineering as structural scaffold for cell growth that are to be implanted into the body, having direct clinical implications in cartilage, skin and vascular system restoration [4].

The oxide glass containing silver oxide are used in the infections treatment, due to their bacteriostatic and bactericide properties [5], but also in implantology, these two aforesaid properties are also beneficial in this last mentioned medical field. Due to the silver properties, these materials are considered as a separate class of oxide materials, being difficult to obtain, because metallic silver separates in drops on the surface of the new formed glass, during cooling process. The glass doped with Ag^+ can be prepared using the surface ionic exchange method, sol-gel method [6] and using rapid melt quenching method [7].

[a] *University of Agricultural Science and Veterinary Medicine, Biophysics Department, Calea Manastur 3-5, Cluj-Napoca, Romania, Tel. +40 264 596 384, Int. 207, Fax +40 264 593 792, rstefan@usamvcluj.ro*

[b] *National Institute for Research and Development of Isotopic and Molecular Technologies, Donath 65-103, Cluj-Napoca, Romania*

[c] *Babes-Bolyai University, Faculty of Physics, Kogalniceanu 1, Cluj-Napoca, Romania*

The vitreous materials based on phosphorus are widely used [1, 8] for growth stimulation of bone tissues, leading to the formation of hidroxyapatite (HA) layer between the organic tissue and inorganic material. The presence of vitreous network modifiers as CaO in the vitreous material structure helps the formation of bioactive glass which can be used in implants [9] without "non-self" rejection or in stimulation of bone tissue regenerations. The bond between inorganic and organic component is stronger than the bone itself.

The Raman and IR spectroscopy are extremely sensitive techniques for the structural analysis and for the modifications occurring after the heat treatment, allowing the identification of structural units [10] in vitreous structure and for detecting of (HA) formation on the surface of material tested "in vitro" conditions.

The aim of this paper was to obtain a vitreous oxide material based on B_2O_3 which to homogenous include silver ions in a molar content as large as possible and its structural characterization using Raman and IR spectroscopy in order to identify the structural units which are formed in the new materials. The paper is an investigation of vitreous network structure changes occurred following the modification of the molar ratio of two classical forming compounds of vitreous network B_2O_3 and P_2O_5. Also the possibility that their structural units participate together to the formation of vitreous network has been studied. The research aims to obtain a new system, useful in medical area to deliver sufficient ions content for having bactericide and bacteriostatic effect and to build (HA) layer in contact with bone tissue.

RESULTS AND DISCUSSION

X-ray powder diffraction patterns for the thermally untreated samples are shown in Figure 1. One can see that the all investigated samples are in amorphous state. The samples with x = 0 and 0.02 are characterized by two halos which are specific to amorphous samples, the most intense maximum being located at 29.6º (2θ). The relation between the most frequently occurring interatomic distance R and the position of the strongest observable maximum is given by the relationship [11]: $R = \frac{5\lambda}{8\sin(\theta)}$, where λ is the wavelength of X-ray beam and θ is the diffraction angle. From this relation R= 3.76Å for samples x = 0 and x = 0.02.

For samples with $x \geq 0.05$ a new halo appears for 2θ ~21.7º value. The frequently corresponding interatomic distances for this maximum is R = 5.11Å. The appearance of an additional maximum at a smaller angle suggests a supplementary order between atoms corresponding to some larger distances.

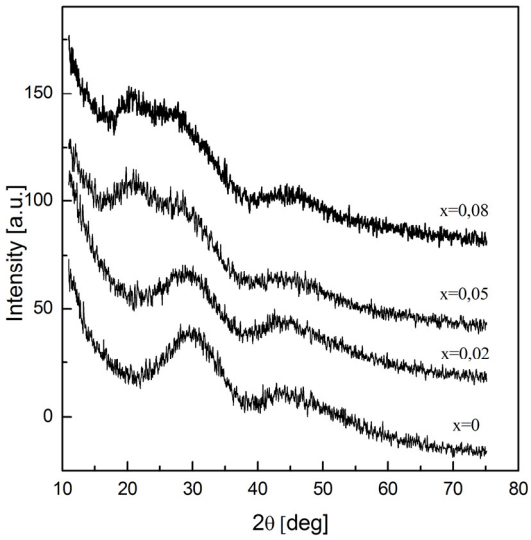

Figure 1. X-ray powder diffraction patterns for the thermally untreated samples of 1.5%Ag_2O 98.5%[0.47B_2O_3(0.53-x)CaOxP_2O_5] system

The X-ray powder diffraction patterns for heat treated samples are presented in Figure 2. The samples with x = 0 and x = 0.02 contain only amorphous phase, while samples x = 0.05 and x = 0.08 contain both crystalline and vitreous phase. The crystalline phase was identified as being $Ca_{10}(PO_4)_6O$, as listed in PDF 89-6495, which crystallizes in hexagonal system having the following [12] lattice parameters: a = 9.432 Å and c = 6.881 Å. One can remark that for the samples which have an additional halo at 21.7º (2θ) before heat treatment, after heat treatment they contain both crystalline and amorphous phase. CaO reacts with B_2O_3 and P_2O_5 the two classical vitreous network formers depending on their optical basicity [13], thus it is natural that the crystalline state containing PO_4 to be formed.

The IR spectra of vitreous samples (Figure 3) from the oxide system 1.5Ag_2O98.5[0.47B_2O_3(0.53-x)CaOxP_2O_5] with $0 \leq x \leq 0.08$ mol% content in glass matrix, present absorption bands in the spectral domain 1600-400 cm^{-1}. The wide bands structure points to the structural disorder within the system itself, i.e., for each molar ratio among its components.

As shown [14] the glass exclusively based on B_2O_3 is composed of boroxol rings which form a vitreous network [15], with local order and of BO_3 triangles. The vitreous structure based on boroxol rings is maintained also depending on the quantity and type of the network modifier oxide introduced in the starting matrix up to 25% molar content.

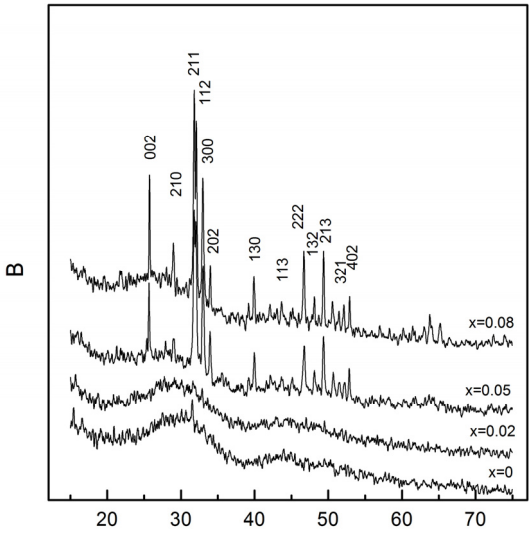

Figure 2. X-ray powder diffraction patterns for the thermally treated samples of 1.5%Ag_2O98.5%[0.47B_2O_3(0.53-x)CaOxP_2O_5] system

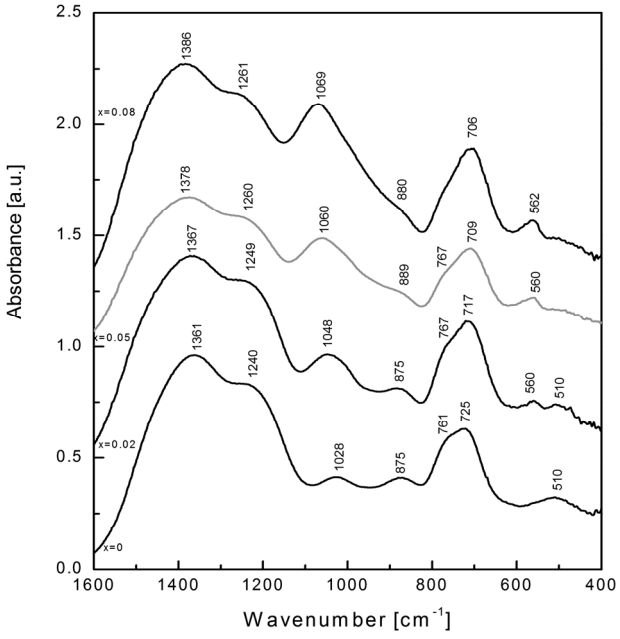

Figure 3. IR spectra of 1.5%Ag_2O 98.5% [0.47B_2O_3(0.53-x)CaO xP_2O_5] vitreous system

In the investigated vitreous system $1.5\%Ag_2O98.5\%[0.47B_2O_3$ $(0.53\text{-}x)CaOxP_2O_5]$, one expects the occurrence of the bands characteristic to other borate units, resulting for the fragmentation of the network, together with the modification of the oxides ratio. These are as follow diborate ($B_4O_7^{2-}$), tetraborate ($B_8O_{13}^{2-}$), pentaborate ($B_5O_8^-$) etc. and the boron atoms will exist in both three- and four-coordinated states.

The samples with $x \leq 0.02$ reveal identical absorption bands in the entire spectral range with the exception with the small wave numbers range 400-600 cm^{-1}. Thus, if in $x = 0$ and $x = 0.02$ spectra, there is a wide IR band at ~510 cm^{-1}, in $x = 0.02$ sample a new band at ~560 cm^{-1} appears, in the same spectral domain. The band at ~510 cm^{-1} was assigned to the B-O-B bending vibration [16], this vibration type being more possible when there are no boroxol rings B_3O_6 in glass structure.

While the P_2O_5 content increases in the B_2O_3-CaO-P_2O_5 matrix, the intensity of the band at ~560 cm^{-1} increases without modifying its spectral position and the broad band at 510 cm^{-1} become invisible in spectra. The band at ~560 cm^{-1} was assigned to the characteristic bands of bending vibration of P-O-P linkage in basic units of phosphate glasses [17-19].

Around 700 cm^{-1} it is the domain of B-O-B bending vibrations in borate networks [20] and the IR band at ~706 cm^{-1} was assigned to B-O-B linkage in borate networks [13], this vibration may be assigned to a certain linkage between two trigonal boron atoms [21]. The intensity and width of this band depend on the matrix composition and its position shifts towards smaller wave numbers with the increase of P_2O_5 in the oxide matrix, which demonstrate that the borate network has a limited vibrational freedom in the presence of phosphate groups.

The band has a shoulder at 761 cm^{-1} ($x = 0$) that decreases in intensity, being included in the line assigned to B-O-B vibration (~700 cm^{-1}), was attributed to the O_3B-O-BO_4 linkage bending vibrations [22, 23], while to the B-O bond stretching vibration in BO_4^- units, was associated with the band at ~870 cm^{-1} [17].

The wide band at ~1028 cm^{-1} becomes more clearly defined and more intense as the P_2O_5 molar content increases into the oxide matrix and move towards larger wave numbers. This is the characteristic of BO_4 units, specifically to the stretching vibration of B-O bond in BO_4 tetrahedron [24]. Once with the further addition of the P_2O_5 content (the number of BO_4 units increases) the band moves towards larger wave numbers, for $x = 0.08$ reaching to ~1080 cm^{-1}, last frequency is also assigned to $(PO_3)_{as}$ vibrations [25]. This band movement assigned to boron towards larger wave numbers shows that the borate network is more fragmented and has a larger freedom of motion.

The binary glass based on boron contains triangular BO_3 units besides BO_4 tetrahedron units. These can be comprised in BO_3^- orthoborate dimmer units and the band at ~1240 cm^{-1} is assigned for them [26]. This band intensity decreases once with the reduction of molar ratio B/P into the matrix, but for $x > 0.02$ has the same intensity with the BO_4 units typical band.

For larger wave numbers there is a wide band at ~1366 cm^{-1}. The band line width remains unchanged in the whole composition domain researched and was attributed to asymmetric stretching mode of borate triangles BO_3 occurring in complex units [26].

The modification of CaO/P_2O_5 ratio into the oxide matrix leads to modification of the ratio between three coordinate boron (1240 cm^{-1}) and tetracoordinate boron (1080 cm^{-1}) and isomerisation occurs in boron based species.

Due to the formation of Ag-O covalent bond in the glass, the absorption band appears at ~620 cm^{-1} [16]. This peak is absent here, thus we cannot establish that these bonds are forming, or their number is very small and have no influence upon the glass network vibration.

The influence of heat treatment (t = 650°C) upon vitreous samples from $1.5\%Ag_2O98.5\%[0.47B_2O_3(0.53\text{-}x)CaOxP_2O_5]$ system cannot be observed in all spectra of the investigated samples. Thus for $x \leq 0.02$ the samples IR spectra are identical with those of the samples of vitreous system (Figure 4).

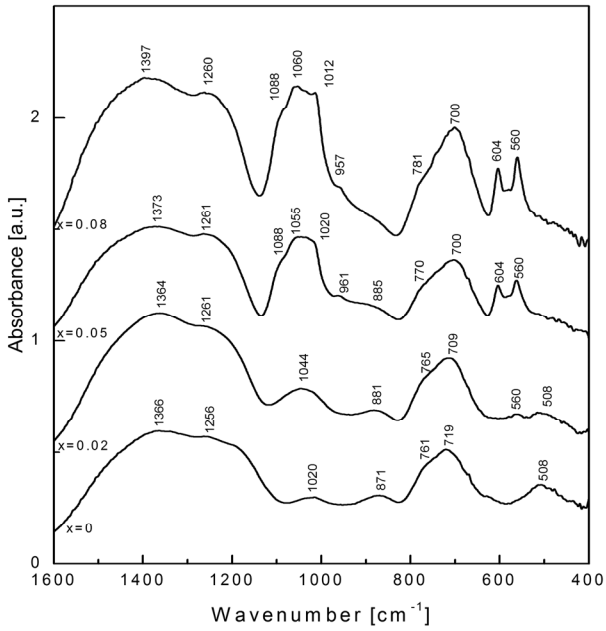

Figure 4. IR spectra of $1.5\%Ag_2O98.5\%[0.47B_2O_3(0.53\text{-}x)CaOxP_2O_5]$ heat treated system

For x ≥ 0.05 the heat treatment effect is obvious in IR spectra, due to the occurrence of a new band at ~604 cm^{-1} near the band at ~560 cm^{-1} and disappearance of the band at 508 cm^{-1}. The band at ~560 cm^{-1} and at ~604 cm^{-1} was assigned to the bending vibrations of the P-O-P phosphate structural units occurring in oxide glass [17]. In this compositional domain the band at ~560 cm^{-1} is more intense and narrow than the one appearing at the same wave number in the vitreous structures and the band at ~604 cm^{-1} is localized. The shape of the two bands reveals the appearance of the structural order at distance and of the crystalline phases containing P_2O_5 as shown by the X-rays.

Following the thermal treatment, the spectral domain $\nu \in$ [850-1100] cm^{-1}, assigned to the B-O bond bending vibrations from BO_4 units, is restructured through the occurrence of a significant number of bands into the samples sensitive to thermal treatment.

The IR band at ~961 cm^{-1} is due to the groups containing BO_4 units [21] especially in diborate groups.

Thus, starting from the same concentration of P_2O_5 in the vitreous matrix, in the spectral range, three IR bands are revealed: at ~1020 cm^{-1}, ~1055 cm^{-1} and ~1088 cm^{-1}, which replace the wide band at ~1020 cm^{-1} (x = 0). According to Gaafar [17] this spectral domain is associated with the B-O bond stretching vibrations of BO_4^- tetrahedral (830-1120 cm^{-1}).

In the IR spectra we are expecting the occurrence of the bands due to the isolated tetrahedral ionic PO_4^{3-} (Q^0) units or PO_4^{2-} (Q^1) for any molar content of P_2O_5 in glass, reason for which we assigned the band at 1088 cm^{-1} to the Q^1 units [27].

Bands restructuring in the spectral domain 1000-1080 cm^{-1} and the occurrence of a narrow bands at ~560 cm^{-1} and ~604 cm^{-1}, lead to conclusion that the structural local order is established by the occurrence of crystalline volume domains and the formation of glass-ceramic structures.

The spectral domain specific to the BO_3 structural units stretching vibrations remains unchanged, the groups containing trigonal boron are unaffected by thermal treatment.

The Raman spectra (Figure 5) of the samples of $1.5\%Ag_2O{\cdot}98.5\%[0.47B_2O_3(0.53\text{-}x)CaOxP_2O_5]$ vitreous system are dominated in intensity by two bands located into the 900-1100 cm^{-1} spectral interval. Thus, if the sample x = 0 has a wide band centered around the ~960 cm^{-1} value, more intense than any other spectrum band, the sample with x = 0.02 reveals two bands in this spectral range at ~992 cm^{-1} respectively at ~960 cm^{-1}. The Raman band at ~960 cm^{-1} was associated to the borate groups [28, 29], and the separation occurs due to the vibrations caused by the groups containing phosphorus.

The band at 992 cm^{-1} was assigned to symmetric stretching vibrations of the final units PO_3^{2-} (Q^1 species) connected to a borate ring, through B-O-P linkage and/or to the orthophosphate ions PO_4^{3-} (Q^o species) [20, 23]. Because the band at ~992 cm^{-1} becomes the most intense and narrow line in the spectra, with the increase of x, one may say that the number of B-O-P linkages increases in the vitreous network with the increase of the available phosphorus quantity into the glass composition.

Isolated ions PO_4^{3-} are responsible for the band at ~952 cm^{-1} [20] this one being assigned to $P\text{-}O^-$ bond vibrations in Q^o species.

These two aforesaid bands are well defined and narrow comparing with the other bands occurring in Raman spectra which reveals the existence of several well defined P_2O_5 structural units.

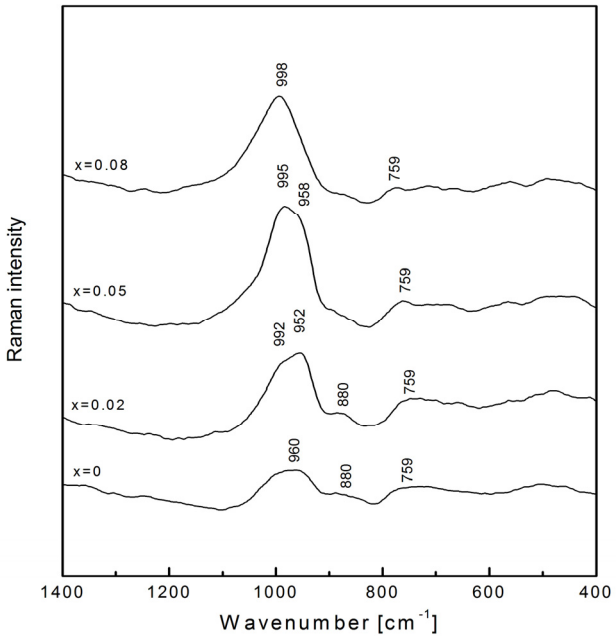

Figure 5. Raman spectra of 1.5%Ag_2O 98.5%[0.47B_2O_3(0.53-x)CaOxP_2O_5] vitreous system

The absence of Raman band at 806 cm^{-1} indicate the absence of boroxol rings in the glass structure [15], this band is usually assigned to the breathing vibrations of this ring and the result is in good agreement with IR spectral data.

In the spectral range 765-785 cm^{-1} a relative wide band may be observed for all the investigated samples, which was assigned [11] to symmetrical vibrations B-O-B which involves the displacement of oxygen atoms in boroxol

ring only, where one or two BO_3 triangles were replaced by BO_4 tetrahedral units or as shown [13] the band at 780 cm^{-1} has to be correlated with the BO_4 units vibrations.

The wide Raman band centered at ~470 cm^{-1} (x=0) was assigned to diborate groups and BO_4 groups lost by the network [22].

After heat treatment of investigated oxide system significant changes of Raman spectra can be observed (Figure 6).

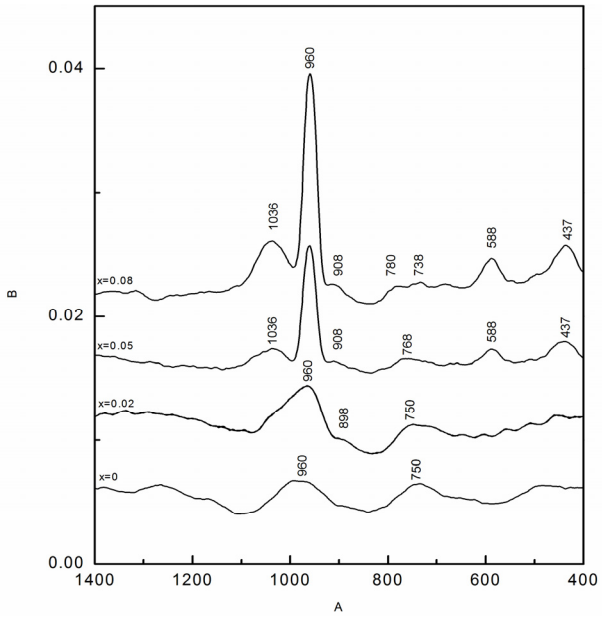

Figure 6. Raman spectra of 1.5%Ag_2O 98.5%[0.47B_2O_3(0.53-x)CaOxP_2O_5] heat treated system

At x = 0 in the spectral range $\upsilon \in$ [900-1100] cm^{-1} a wide band assigned to orthoborate units [30] appears, although it is characteristic for pure borate glass, its origin could not be precisely determined [23]. The band at ~960 cm^{-1} becomes more intense and sharp with the increase of P_2O_5 molar content and the simultaneous presence of Raman bands at ~429 cm^{-1}, ~587 cm^{-1} reveals that the PO_4^{3-} ions vibrations appear into the glass [31] starting with x = 0.02.

The gradual sharpening of Raman band ~959 cm^{-1} assigned to (Q^o species) and its increase in intensity represents a spectroscopic confirmation that the system crystalline domains are due to the structural units that involves P_2O_5 and also that the crystalline units number increases as well as the glass structure changes in glass-ceramics.

The PO_4^{3-} may react with the calcium oxide and form individual groups. The Raman band at 587 cm^{-1} was assigned to the symmetric stretching vibrations of $P\text{-}O^-$ [13] bonds and appears just once in vitroceramic samples.

In the whole investigated concentration range $0 \leq x \leq 0.08$, the structural units building the borate glass network, orthoborate at ~900 cm^{-1} and dipentaborate [21] at ~759 cm^{-1}, maintain their position and intensities which proves that the heat treatment affect only phosphate units.

After the heat treatment a new band at ~1035 cm^{-1} appears in the Raman spectra, being assigned to the stretching mode of PO_3 symmetric vibrations (chained end groups) [20, 32]. The band becomes narrow at further addition of P_2O_5 into the matrix and has an increased intensity.

In the Raman spectra of heated samples, starting with x = 0.05, on these frequencies the bands become narrower and the boron ones, diminish for investigates Ca/P ratio.

The structural modifications highlighted by the Raman spectra following the heat treatment support the results obtained by means of IR spectroscopy, meaning that the tendency of the vitreous system for crystallization increases as much as the P_2O_5 concentration increases, starting with x = 0.05.

CONCLUSIONS

The X-rays diffractogram revealed that the researched system samples are non-crystalline (vitreous) in the whole composition system researched. The heat treatment at 650°C for 6 h determined the appearance of crystalline islands with the following composition: $Ca_{10}(PO_4)_6(OH)_2$.

Glasses from $1.5\%Ag_2O$ $98.5\%[0.47B_2O_3(0.53\text{-}x)CaOxP_2O_5]$ system were prepared with high modifier glass oxide content. The IR spectra reveal the existence of BO_3 and BO_4 groups in different structural units for all the investigated glasses and glass-ceramics. Raman spectra showed the crystallization of isolated PO_4^{3-} units as well as the formation of B-O-P linkages. Structural changes for $x \geq 0.04\%$ induced by heat treatment are revealed by both spectroscopic techniques.

EXPERIMENTAL

The oxide glass of the $1.5\%Ag_2O$ $98.5\%[0.47B_2O_3(0.53\text{-}x)CaO\ xP_2O_5]$ system with $0 \leq x \leq 0.08$ mol% have been prepared using start materials: Ag_2O, $CaCO_3$, P_2O_5, H_3BO_3 of reagent grade purity. The mixtures were melted in air at 1250°C, in sintered corundum crucibles, and kept for 15 min. at this temperature. The oxide glasses were partially crystallized by heat treatment of the samples at 650°C in a single step.

X-ray powder diffraction data were obtained with Bruker D8 Advanced Diffractometer equipped with Si monochromator for incident beam in order to obtain only Cu Kα radiation.

The obtained materials were grinded as powder and mixed with KBr in order to obtain 0.3 mm thick discs using the tablet forming technique. The FTIR spectra characteristic for the vitreous samples and the heat samples were recorded using a JASCO 6100 spectrometer in the spectral domain 4000-400 cm^{-1} with a resolution of 4 cm^{-1}.

The FT-Raman spectra were recorded in backscattering geometry with a FRA 106/S (Bruker) Raman accessory equipped with nitrogen cooled Ge detector. The 1064 nm Nd:YAG laser was used as excitation source, and the laser power was set at 300 mW. The FT-Raman spectra were recorded with a resolution of ~4 cm^{-1}.

ACKNOWLEDGMENTS

This work was supported by CNCSIS–UEFISCDI, project number 1117 PNII – IDEI code 2528/2008.

REFERENCES

1. R.K. Brow, *J. Non-Cryst. Solids*, **1996**, *194,* 267.
2. C. Dem, I. Ardelean, D. Maniu, T. Iliescu, *Asian Chemistry Letters,* **1999**, *3,* 275.
3. E. Culea, Al. Nicula, I. Bratu, *Phys. Status Solidi A,* **1984**, *K15,* 83.
4. W. Liang, Y. Tu, H. Zhou, C. Liu, C. Rüssel, *J. Non-Cryst. Solids*, **2011**, *357*, 958.
5. I. Ahmed, D. Ready, M. Wilson, J. C. Knowles, *J. Biomed. Mater. Res.–A,* **2006**, *79*, 618.
6. M. Kawashita, S. Tsuneyama, F. Miyaji, T. Kokubo, H. Kozuba, K. Yamamoto, *Biomaterials*, **2000**, *21*, 393.
7. Y. Xu, J. Cheng, W. Zheng, D. Gao, *J. Non-Cryst. Solids*, **2008**, *354*, 1341.
8. Y.B. Peng, D.E. Day, *Glass Technol.-Eur. J. Glass Sci. Technol. Part A*, **1991**, *32,* 166.
9. L.L. Hench, *J. Mater. Sci.-Mater. M.,* **2006**, *17,* 967.
10. L. Baia, R. Stefan, J. Popp, S. Simon, W. Kiefer, *J. Non-Cryst. Solids,* **2003**, *324,* 109.
11. H.P. Klug, L.E. Alexander, "X –ray diffraction procedure for polycrystalline and amorphous materials", John Wiley, New York, London, **1974**.
12. P.A. Henning et al., *Acta Crystallogr. B,* **1999**, *55,* 170.
13. S. Agathopoulos, D.U. Tulyaganov, J.M.G. Ventura, S. Kannan, A. Saranti, M.A. Karakassides, J. M. F. Ferreira, *J. Non-Cryst. Solids,* **2006**, *352,* 322.

14. J. Krogh-Moe, *Phys. Chem. Glasses,* **1962**, *3,* 101.
15. S.P. Yawale, S.V. Pakade, C.S. Adgaonkar, *Indian J. Pure Ap. Phy.,* **1995**, *33,* 34.
16. R. C. Lucacel, C. Marcus, V. Timar, I. Ardelean, *Solid State Sci.,* **2007**, *9,* 850.
17. M.S. Gaafar, H.A. Afifi, M.M. Mekaway, *Physica B*, **2009**, *404,* 1668.
18. L. Koudelka, P. Mośner, *Mater. Lett.,* **2000**, *42,* 194.
19. S. Rani, S. Sanghi, A. Agarwal, N. Ahlawat, *J. Alloy. Compd.,* **2009**, *477,* 504.
20. A. Saranti, I. Koutselas, M.A. Karakassides, *J. Non-Cryst. Solids*, **2006**, *352,* 390.
21. E.I. Kamitsos, M.A. Karakassides, G.D. Chryssikos, *J. Phys. Chem. A*, **1987**, *91,* 1073.
22. R.C. Lucacel, I. Ardelean, *J. Non-Cryst. Solids*, **2007**, *353,* 2020.
23. J.F. Ducel, J.J. Videau, M. Couzi, *Phys. Chem. Glasses-B*, **1993**, *34,* 212.
24. L. Baia, R. Stefan, W. Kiefer, S. Simon, *J. Raman Spectrosc.*, **2005**, *36,* 262.
25. A. Chahine, M. Et-Tabirou, M. Elbenaissi, M. Haddad, J.L. Pascal, *Mater. Chem. Phys.,* **2004**, *84,* 341.
26. Y. Dimitriev, A. Bachvarova-Nedelcheva, R. Iordanova, *Mater. Res. Bull.,* **2008**, *43,* 1905.
27. A.M. Efimov, *J. Non-Cryst. Solids*, **1997**, *209,* 209.
28. H. Li, H. Lin, W. Chen, L. Luo, *J. Non-Cryst. Solids*, **2006**, *352,* 3069.
29. K. Knoblochova, H. Ticha, J. Schwarz, L. Tichy, *Opt. Mater.*, **2009**, *31,* 895.
30. T. Iliescu, S. Simon, D. Calugar, *J. Mol. Struct.,* **1992**, *267,* 231.
31. L. Koudelka, P. Mošner, J. Pospisil, L. Montagne, G. Palavit, *J. Solid State Chem.,* **2005**, *178,* 1837.
32. A. Moguš-Milanković, A. Santić, S.T. Reis, K. Furić, D.E. Day, *J. Non-Cryst. Solids*, **2005**, *351,* 3246.

STUDIA UBB CHEMIA, LVI, 1, 2011

STRUCTURAL INVESTIGATION OF $xFE_2O_3\cdot(70-x)B_2O_3\cdot15ZNO\cdot15CAO$ GLASSES BY INFRARED SPECTROSCOPY AND DFT CALCULATIONS

RĂZVAN ŞTEFAN*[a], EMIL VINȚELER*[b], ALEXANDRU MARCU[b], GEORGETA TARALUNGA[a], SILVANA POPESCU[a], IOAN BRATU[c]

ABSTRACT. The vitreous system $xFe_2O_3\cdot(70-x)B_2O_3\cdot15ZnO\cdot15CaO$ with $0 \le x \le 25$ mol% was prepared using the rapid melt quenching method. The effect of Fe_2O_3 on the borate glass structure was investigated by IR spectroscopy and illustrated by Density Functional Theory (DFT) method. The boron atoms are situated in trigonal $[BO_3]$ and tetragonal $[BO_4]$ groups and their ratio depends on Fe_2O_3 content. Two structural models were built, using DFT method, in agreement with IR experimental data, one for base glass $70B_2O_3\cdot15ZnO\cdot15CaO$ (x = 0 mol%) and another for the highest iron content in sample $25Fe_2O_3\cdot45B_2O_3\cdot15ZnO\cdot15CaO$ (x = 25 mol%). Calculations with DFT method show that the addition of iron determines the breaking of B-O bonds in borate network and increases the number of $[BO_3]$ groups.

Keywords: *glass, chemical synthesis, infrared spectroscopy*

INTRODUCTION

Boron glass network has been investigated and the main structural units highlighted by different techniques, one of the most important being the infrared spectroscopy [1]. The borate glass network is built from trigonal $[BO_3]$ units, where every boron atom is situated at the centre of a triangle of oxygen atoms, and boroxol rings $(B_3O_3Ø_3)^0$, which are six-membered planar and regular B_3O_3 rings, connected by three bridging oxygens Ø atoms [1,2].

The addition of oxides (CaO, ZnO or Fe_2O_3) in the borate glass network determines the formation of new structural units such as pentaborate $(B_5O_6Ø_4)^-$, diborate $(B_4O_5Ø_4)^{2-}$, triborate $(B_3O_4Ø_4)^-$ and ditriborate $(B_3O_5Ø_4)^{2-}$ units. These new structural units, containing four-coordinated boron $[BO_4]$ sites, can be revealed by nuclear magnetic resonance [2].

[a] *University of Agricultural Science and Veterinary Medicine, Biophysics Department, Calea Mănăştur 3-5, RO-400372 Cluj-Napoca, Romania, Tel. +40 264 596 384, Int. 207, Fax +40 264 593 792, rstefan@usamvcluj.ro*

[b] *Babeş-Bolyai University, Faculty of Physics, Str. M. Kogălniceanu 1, RO-400084 Cluj-Napoca, Romania, evinteler@phys.ubbcluj.ro*

[c] *National Institute for R&D of Isotopic and Molecular Technology, P.O. Box 700, RO-400293 Cluj-Napoca, Romania*

One can obtain in the binary (100-x)Fe_2O_3·xB_2O_3 system [3], various crystalline phases such as: $FeBO_3$, $FeBO_3$-Fe_3BO_6, α-Fe_2O_3-Fe_3BO_6, depending on preparation condition and compounds ratio. This item of information, about crystalline phases is rather important as it is used in Density Functional Theory (DFT) simulations.

Fe_2O_3 is not a glass network former and this feature makes relatively difficult to prepare glasses containing a high iron oxide content, but for low concentration it acts like a network modifier [4], when it is introduced within borate glass. The glass-forming region of the ternary Fe_2O_3–Bi_2O_3–B_2O_3 system [5] shows that the glass structure can be obtained, in the binary Fe_2O_3–B_2O_3 system, only for molar content of Fe_2O_3 lower than 5%. The addition of zinc, barium and calcium oxides enlarges the glass formation domain in Fe_2O_3–B_2O_3 system up to 25 mol% Fe_2O_3 [6-8].

In the present work, glasses with the molar composition xFe_2O_3·(70-x)B_2O_3·15ZnO·15CaO, with 0 ≤ x ≤ 25 mol%, were prepared. The structure and the effects of Fe_2O_3 on the glass network were investigated by IR spectroscopy. For x = 0 mol% and 25 mol%, two models were built by using DFT method.

RESULTS AND DISCUSSION

IR Spectra of vitreous xFe_2O_3·(70-x)B_2O_3·15ZnO·15CaO system

Figure 1 shows the FT-IR spectra of the xFe_2O_3·(70-x)B_2O_3·15ZnO· 15CaO with 0 ≤ x ≤ 25 mol%. The borate glasses FT-IR spectra within range of 400-1600 cm^{-1} were divided in three main regions [1, 9] associated with: bending of B-O-B linkages in the borate network between 400–790 cm^{-1}; B-O bond stretching in tetrahedral [BO_4] units between 790–1140 cm^{-1} and asymmetric B-O stretching vibration in triangular [BO_3] units in the spectral range 1140–1600 cm^{-1}.

Usually in glass IR spectra appear as overlapping bands belonging to various borate units and this feature makes difficult to detect a separate and clear vibrations by IR analysis.

In the above mentioned spectral range, the shapes of bands (Fig. 1) are dependent on Fe_2O_3 molar content, being more narrow for base glass 70B_2O_3·15ZnO·15CaO, while for high iron concentration broad bands appear in the same spectral range.

Thus the shoulder at 1212 cm^{-1}, attributed to B-O bond vibrations in metaborate chains, increases in relative intensity when comparing with band at 1405 cm^{-1}, attributed to B-O bond vibration in [BO_3] units, with the increase of Fe_2O_3 content [10-13]. This denotes the increase in metaborate chains $(B_3O_5Ø_2)^{3-}$ number.

The decrease in relative intensity of the broad band at ~958 cm^{-1}, when comparing with bands at ~849 cm^{-1} and ~1091 $cm^{-}1$, indicates the decrease of diborate units number, with the increase of Fe_2O_3. The absorption band at 683 cm^{-1}, attributed to B-O-B linkage bending vibration [10] become higher than the envelope that contain $[BO_4]$ specific vibration, i.e., 790-1140 cm^{-1}, during the replacement of B_2O_3 by Fe_2O_3 in the glass composition [9].

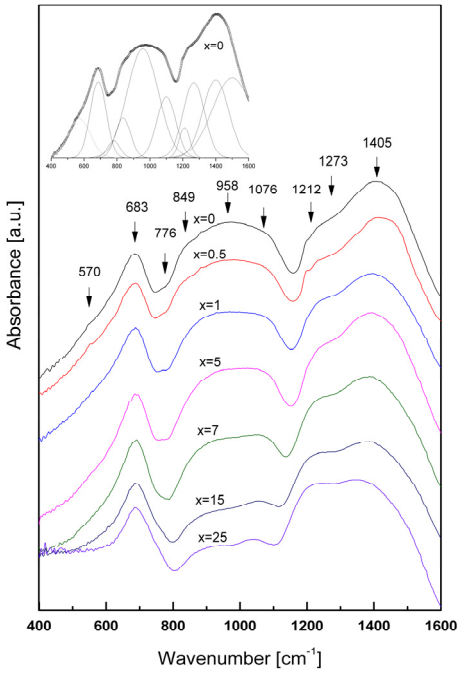

Figure 1. The FT-IR absorption spectra of $xFe_2O_3·(70-x)B_2O_3·15ZnO·15CaO$ glasses with $0 \le x \le 25$ mol%. In the inset picture the deconvolution bands of FT-IR spectrum for x = 0 mol% is presented

The structural changes associated with the Fe_2O_3 addition have been analyzed on the basis of the ratio $Ar = A_4/A_3$, A_4 and A_3 being calculated as the integral of the absorption signal in the 790-1140 cm^{-1} (A_4) and 1140-1600 cm^{-1} (A_3) spectral ranges [14]. The quantities A_4 and A_3 reflect the relative content of tetrahedral $[BO_4]$ and triangular $[BO_3]$ borate species, respectively. The Ar ratio versus Fe_2O_3 content is given in Figure 2.

For all the investigated glasses, the Ar values are lower than 1, showing the prevalence of $[BO_3]$ units in these glass structures. The presence of $[BO_4]$ units, for x = 0 mol%, in the absence of iron in the glass bulk and the continuous decrease of the Ar ratio demonstrates that the $[BO_4]$ units are replaced by $[BO_3]$ units when the Fe_2O_3 content increases in the glass composition as well as the network modifying role played by Fe cations [6].

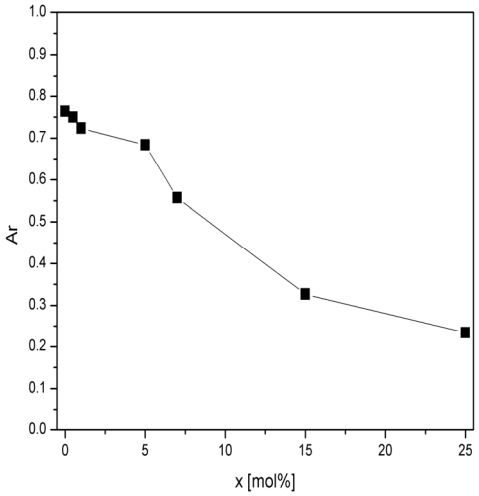

Figure 2. Values of the Ar ratio versus x in $xFe_2O_3 \cdot (70\text{-}x)\ B_2O_3 \cdot 15ZnO \cdot 15CaO$

A more in-depth study of the FT-IR spectra, presenting large bands, characteristic for glasses, needs spectra deconvolution. In the inset of Figure 1 is presented the deconvolution of FT-IR spectrum in the region 400-1600 cm^{-1} for x = 0 mol%. Thus in the region 400-1600 cm^{-1} deconvolution reveals the appearance of 10 bands (for x = 0 mol%) at ~570 cm^{-1}, ~691 cm^{-1}, ~776 cm^{-1}, ~836 cm^{-1}, ~958 cm^{-1}, ~1103 cm^{-1}, ~1212 cm^{-1}, ~1273 cm^{-1}, ~1394 cm^{-1} and ~1503 cm^{-1}, respectively. The deconvoluted spectra for all investigated samples, with characteristic full widths at half maximum (FWHM) and relative areas, are presented in Table 1. The relative area is the component band area divided by the area of the full spectrum in the region 400-1600 cm^{-1}.

The wavenumber bands in spectral range 400-790 cm^{-1}, assigned to borate network bending vibrations, maintain the same spectral position within the investigated compositional range.

The band at ~1212 cm^{-1} (Table 1) shifts to 1181 cm^{-1}, attributed to B-O bond vibrations in pyro- $(B_2O_5)^{4-}$ and orthoborates $(BO_3)^3$, indicating the gradual transformation of metaborate chains into pyro- and orthoborates units.

The band at ~1273 cm^{-1}, attributed to B-O bond vibrations in tri- $(B_3O_4Ø_4)^-$, tetra- $(B_8O_{10}Ø_6)^-$ and pentaborate $(B_5O_6Ø_4)^-$ groups [9, 10, 11], shifts to 1297 cm^{-1}, attributed to B-O bond vibrations [11-13] in pyro- and orthoborates, indicating the transformation of previous mentioned groups into pyro- and orthoborates.

The shift to lower wanumber values of the band at around 1103 cm^{-1} (Table 1) attributed to B-O vibration in $[BO_3]$ units, demonstrates the strong influence of Fe_2O_3 on borate network.

Table 1. Deconvolution parameters of the experimental infrared spectra of $xFe_2O_3\cdot(70-x)B_2O_3\cdot15ZnO\cdot15CaO$ glasses (C is the component band centre (cm^{-1}), W is the band full width at half maximum (cm^{-1}) and A is the relative area (%) of the component band).

x=0	C	**570**	**691**	**776**	**836**	**958**	**1103**	**1212**	**1273**	**1394**	**1503**
	W	158	121	97	109	230	133	73	145	194	230
	A	6	9	2	4	24	8	3	12	14	18
x=0.5	C	**570**	**691**	**776**	**836**	**958**	**1103**	**1212**	**1261**	**1406**	**1503**
	W	158	121	85	109	219	145	73	145	170	230
	A	6	9	2	4	23	9	2	11	15	19
x=1	C	**570**	**691**	**776**	**848**	**958**	**1091**	**1212**	**1261**	**1394**	**1503**
	W	158	109	73	97	218	145	84	158	194	230
	A	7	9	1	4	22	9	3	12	13	20
x=5	C	**570**	**691**	**-**	**836**	**958**	**1091**	**1212**	**1261**	**1394**	**1503**
	W	158	109	-	121	218	133	85	170	218	230
	A	5	9	-	5	22	8	3	13	18	17
x=7	C	**570**	**688**	**-**	**843**	**963**	**1087**	**1204**	**1268**	**1344**	**1469**
	W	158	109	-	121	218	133	85	170	218	230
	A	4	10	-	5	19	7	5	12	9	29
x=15	C	**570**	**690**	**-**	**868**	**989**	**1076**	**1189**	**1299**	**1403**	**1500**
	W	136	113	-	110	183	92	112	188	116	133
	A	3	12	-	4	14	4	9	29	10	15
x= 25	C	**570**	**694**	**-**	**889**	**993**	**1066**	**1181**	**1297**	**1410**	**1500**
	W	141	100	-	98	130	88	114	185	121	102
	A	4	10	-	4	8	4	11	34	15	10

The introduced iron ions break the B-O bond in the vitreous structure and the $[BO_3]$ number increase as well as the nonbridging oxygen atoms O . The more disordered glass structure is illustrated by broadening of the IR absorption lines (Fig. 1) in spectral range 1140-1600 cm^{-1}.

Density Functional Theory Calculations

The spectroscopic results reveal a complex network of iron borate glasses with zinc and calcium formed from di- $(B_4O_5Ø_4)^{2-}$, meta- chain $(B_3O_5Ø_2)^{3-}$, pyro- $(B_2O_5)^{4-}$ and orthoborate $(BO_3)^{3-}$ groups.

For the construction of the models the crystallographic data were utilized for iron borate crystals: vonsenite Fe_3BO_5, Fe_3BO_6 isostructural with nobergite, and $FeBO_3$, isostructural with calcite [16-18]. Thus in the crystal Fe_3BO_6, the iron atoms are six-coordinated by oxygen atoms and are disposed in distorted octahedra and the boron atom is exclusively tetrahedral-coordinated by oxygen atoms. In $FeBO_3$ and Fe_3BO_5 crystals, the boron atom is trigonal-coordinated by oxygen atoms.

Two fully optimized structural models were constructed and are shown in Figures 3a and 3b. The first and the second model simulates the structure of random network of $5B_2O_3 \cdot 1ZnO \cdot 1CaO$ glass (model I in Fig. 3a with 71.43%B_2O_3, 14.285%ZnO and 14.285% CaO) and $2Fe_2O_3 \cdot 3B_2O_3 \cdot 1ZnO \cdot 1CaO$ glass (model II in Fig. 3b with 28.57% Fe_2O_3, 42.86% B_2O_3, 14.285% ZnO and 14.285% CaO), respectively.

The utilized simulation method is able to provide a realistic description of the iron borate glass with zinc and calcium $xFe_2O_3 \cdot (70\text{-}x)B_2O_3 \cdot 15ZnO \cdot 15CaO$ for x = 0 mol% and x = 25 mol%.

For each proposed model we performed direct optimization of the geometry with the help of B3LYP/LanL2DZ [19-26] method and using Gaussian 09 program [27].

Frequency analysis followed all optimizations in order to establish the nature of the stationary points found, so that all the reported structures in this study are genuine minima on the potential energy surface, without any imaginary frequencies. For the proposed models we calculated vibrational frequencies with IR absorption intensities using the same method and basis set.

The simulated vibrational frequencies are listed in Table 2 and compared with the values obtained from the deconvolution of experimental spectra for x = 0 and x = 25 mol% (x = moles number of Fe_2O_3 content in glass). A scaling factor of 0.961 was applied to the infrared simulated frequencies.

The bands assignment is in agreement with previous IR studies on borate glasses [9-15].

The two investigated models, describing the random network in the $xFe_2O_3 \cdot (70\text{-}x)B_2O_3 \cdot 15ZnO \cdot 15CaO$ glass with x=0 and x=25 mol% are highly possible. The probability to find the simulated structure in vitreous state is higher for a more stable structure with a lower energy per atom. We obtained for, model I without iron, and for model II with iron, the Hartree-Fock energy value per atom E = -50.968 au/atom and E = -65.662 au/atom, respectively.

Table 2. Infrared vibrational properties of $xFe_2O_3 \cdot (70\text{-}x)\ B_2O_3 \cdot 15ZnO \cdot 15CaO$ glasses for x = 0 mol% and x = 25 mol% inferred from Gaussian deconvolution of the experimental results and quantum-chemical calculations.

Experimental Frequency [cm^{-1}]		Theoretical Frequency [cm^{-1}]		IR assignment
x = 0	x = 25	x = 0	x = 25	
570	570	591	568	O-B-O bond bending vibrations
691	694	679	710	B-O-B bond bending vibrations between two [BO_3] units
776	-	777	774	B-O-B bond bending vibrations between [BO_3] and [BO_4] units
836		839		B-O symmetric stretching vibrations in [BO_4] units in borate rings

Experimental Frequency [cm^{-1}]		Theoretical Frequency [cm^{-1}]		IR assignment
x = 0	x = 25	x = 0	x = 25	
	889		872	B-O symmetric stretching vibrations in [BO_4] units from tri-, tetra- and pentaborate groups
958		928 960 992		B-O bond vibrations in diborate groups
	993		933 972	B-O symmetric stretching vibrations in pyro- and orthoborates shifted by Fe cations
	1066		1067 1102	B-O asymmetric stretching vibrations in pyro- and orthoborates shifted by Fe cations
1103		1105 1121		B-O asymmetric stretching vibrations in [BO_4] units in tri-, tetra- and pentaborate groups
1212		1173		B-O bond vibrations in metaborate chains
	1181		1210	B-O bond vibrations in pyro- and orthoborates
1273		1234 1256 1274		B-O asymmetric stretching vibrations in [BO_3] units in tri-, tetra- and pentaborate groups
	1297		1256 1307 1346	B-O asymmetric stretching vibrations in [BO_3] units in pyro- and orthoborates
1394		1383 1399 1428		B-O asymmetric stretching in [BO_3] units in various borate rings
	1410		1413 1428	B-O asymmetric stretching vibrations in [BO_3] units in ortho-borates
1503	1500	1468 1538		$B\text{-}O^-$ bond vibrations

The borate network of model I is build from (Fig. 3a):

i) one diborate unit $(B_4O_5Ø_4)^{2-}$ formed from two trigonal boron atoms B1 and B4 and two tetrahedral boron atoms B2 and B3 linked by a common oxygen atom,

ii) one borate ring unit $(B_4O_4Ø_5)^-$ formed from three trigonal boron atoms B4, B5 and B6 and one tetrahedral boron atom B2,

iii) one metaborate chain unit $(B_3O_5Ø_2)^{3-}$ formed from four trigonal boron atoms B
7, B8, B9 and B10,

iv) one zinc cation (two-coordinated) and one calcium cation (four-coordinated).

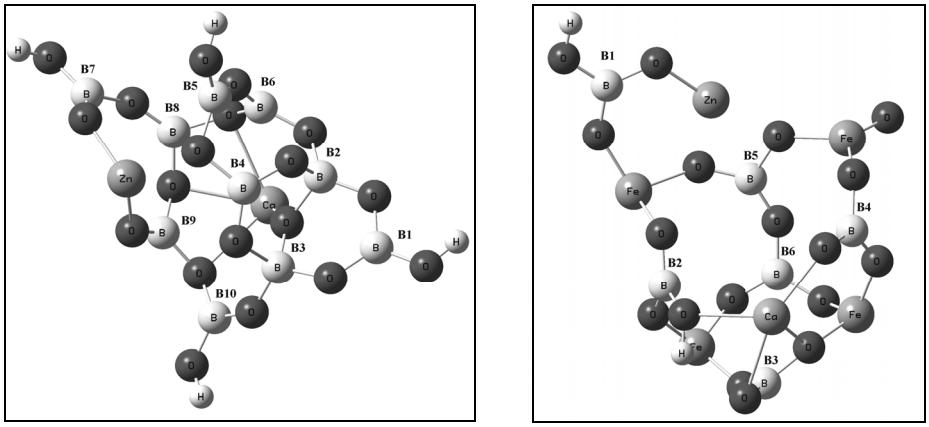

Figure 3. The optimized structures of two possible models obtained by DFT computations: a) $5B_2O_3 \cdot 1ZnO \cdot 1CaO$ glass (model I); b) $2Fe_2O_3 \cdot 3B_2O_3 \cdot 1ZnO \cdot 1CaO$ glass (model II).

The borate network of model II is build from (see Fig. 3b):

i) four orthoborate units $(BO_3)^{3-}$ containing the trigonal boron atoms B1, B2, B3 and B4,

ii) one pyroborate unit $(B_2O_5)^{4-}$ containing the trigonal boron atoms B5 and B6,

iii) four iron cations (three-coordinated), one zinc cation (two-coordinated) and one calcium cation (four-coordinated).

CONCLUSIONS

The addition of iron oxide ($0 \leq x \leq 25$ mol%) to borate $70B_2O_3 \cdot 15ZnO \cdot 15CaO$ glasses, with a high content of B_2O_3, determines important changes in the boron network at intermediate-distance order. By using the infrared spectroscopy the main structural units $[BO_4]$ and $[BO_3]$ of the glass network have been studied and also the gradual conversion of tetrahedral boron units in trigonal ones.

DFT calculations show that the conversion of structural groups as well as creation of new groups at intermediate distance, is due to the insertion of iron cations and the break-up of B-O bonds in borate network as well. DFT calculations are in good agreement with IR experimental spectra of $xFe_2O_3 \cdot (70-x)B_2O_3 \cdot 15ZnO \cdot 15CaO$ vitreous system for x = 0 mol% and x = 25 mol%.

EXPERIMENTAL SECTION

Samples from $xFe_2O_3 \cdot (70-x)B_2O_3 \cdot 15ZnO \cdot 15CaO$ vitreous system with $0 \leq x \leq 25$ mol% were prepared using pure reagent-grade compounds, i.e., H_3BO_3, Fe_2O_3, ZnO and CaO, in appropriate ratios. The mixtures corresponding to the desired compositions were melted in air, in sintered corundum crucibles, in an electric furnace at 1200ºC, t = 15 min. The melts were quickly cooled to room temperature by pouring onto stainless-steel plates.

The structure of the samples was examined by means of X-ray diffraction using a standard Bruker X D8 Advance diffractometer with a Si monochromator for incident beam in order to obtain only CuKa radiation (λ = 1.5406 Å). The diffractograms have been measured in the range of 2θ = 0-90º. The analysis was made on powdered samples to satisfy the diffraction condition of Bragg. The amorphous nature of the glass under investigation was confirmed by the absence of any sharp peaks in X-ray diffraction patterns.

The Fourier-Transform infrared (FT-IR) absorption spectra were recorded with a JASCO 6100 spectrophotometer, at room temperature, in the range 400-4000 cm^{-1}, with a resolution of 4 cm^{-1}, using the KBr pellet technique.

For each proposed model of $xFe_2O_3 \cdot (70-x)B_2O_3 \cdot 15ZnO \cdot 15CaO$ with x=0 mol% and x=25 mol% we performed direct optimization of the geometry with the help of B3LYP/LanL2DZ method and using Gaussian 09 program [27]. Dangling bonds of outer atoms of the models were saturated with hydrogen atoms. After attaining the equilibrium configuration of the models, we calculated vibrational frequencies with IR absorption intensities using the same method and basis set.

ACKNOWLEDGMENTS

This work was supported by CNCSIS–UEFISCSU, project number 1117 PNII – IDEI code 2528/2008.

REFERENCES

1. Y.D. Yiannopoulos, G.D. Chryssikos, E.I. Kamitsos, *Phys. Chem. Glass*, **2001**, *42*, 164.
2. P.J. Bray, *Inorg. Chim. Acta*, **1999**, *289,* 158.
3. H. Makram, L. Touren, J. Loners, *J. Cryst. Growth*, **1972**, *585,* 13.
4. L. Baia, R. Stefan, J. Popp, S. Simon, W. Kiefer, *J. Non-Cryst. Solids*, **2003**, *324,* 109.
5. H.H. Qiu, T. Ito, H. Sakata, *Mater. Chem. Phys.*, **1999**, *58,* 243.
6. I. Ardelean, P. Pascuta, *Mater. Lett.,* **2004,** *58,* 3499.
7. M. Toderaş, S. Filip, I. Ardelean, *J. Optoelectron. Adv. M.*, **2006**, *8(3),* 1121.

8. S. Hiroshi, *J. Jpn. I. Met.*, **2004**, *68(2),* 152.
9. C.P. Varsamis, E.I. Kamitsos, G.D. Chryssikos, *Solid State Ionics*, **2000**, *136,* 1031.
10. E.I. Kamitsos, M.A. Karakassides, G.D. Chryssikos, *Phys. Chem. Glass*., **1986**, *90,* 4528.
11. S.G. Motke, S.P. Yawale, S.S. Yawale, *Bull. Mater. Sci*., **2002**, *25,* 75.
12. J.F. Ducel, J.J. Videau, M. Couzi, *Phys. Chem. Glasses,* **1993**, *34*, 212.
13. S.P. Yawale, S.V. Pakade, C.S. Adgaonka, *Indian J. Pure Ap. Phy.,* **1995**, *33*, 34.
14. M.S. Gaafar, H.A. Afifi, M.M. Mekaway, *Physica B*, **2009**, *404,* 1668.
15. E.I. Kamitsos, M.A. Karakassides, G.D. Chryssikos, *J. Phys. Chem.*, **1987**, *91,* 1073.
16. J.S. Swinnea, H. Steinfink, *Am. Mineral.*, **1983**, *68,* 827.
17. J.G. White, A. Miller, R.E. Nielsen, *Acta Crystallogr.,* **1965**, *19,* 1060.
18. R. Diehl, *Solid State Commun.*, **1975**, *17(6),* 74.
19. A.D. Becke, *J. Chem. Phys*., **1993**, *98*, 1372.
20. A.D. Becke, *Phys. Rev. A*, **1988**, *38 (6)*, 3098.
21. Chengteh Lee, Weitao Yang and Robert G. Parr, *Phys. Rev. B,* **1988**, *37*, 785.
22. S.H. Vosko, L. Wilk and M. Nusair, *Can. J. Phys.,* **1980**, *58*, 1200.
23. T.H. Dunning Jr., P.J. Hay, In: Modern Theoretical Chemistry, H. F. Schaefer III, Vol. 3 Plenum, New York, **1976**, 1.
24. P.J. Hay and W.R. Wadt, *J. Chem. Phys.*, **1985**, *82*, 270.
25. P.J. Hay and W.R. Wadt, *J. Chem. Phys.*, **1985**, *82*, 299.
26. W.R. Wadt and P.J. Hay, *J. Chem. Phys.*, **1985**, *82,* 284.
27. M.J. Frisch, G.W. Trucks, H.B. Schlegel, G.E. Scuseria, M.A. Robb, J.R. Cheeseman, G. Scalmani, V. Barone, B. Mennucci, G.A. Petersson, H. Nakatsuji, M. Caricato, X. Li, H.P. Hratchian, A.F. Izmaylov, J. Bloino, G. Zheng, J.L. Sonnenberg, M. Hada, M. Ehara, K. Toyota, R. Fukuda, J. Hasegawa, M. Ishida, T. Nakajima, Y. Honda, O. Kitao, H. Nakai, T. Vreven, J. A. Montgomery, Jr., J.E. Peralta, F. Ogliaro, M. Bearpark, J.J. Heyd, E. Brothers, K.N. Kudin, V.N. Staroverov, R. Kobayashi, J. Normand, K. Raghavachari, A. Rendell, J.C. Burant, S.S. Iyengar, J. Tomasi, M. Cossi, N. Rega, J.M. Millam, M. Klene, J.E. Knox, J.B. Cross, V. Bakken, C. Adamo, J. Jaramillo, R. Gomperts, R.E. Stratmann, O. Yazyev, A.J. Austin, R. Cammi, C. Pomelli, J.W. Ochterski, R.L. Martin, K. Morokuma, V.G. Zakrzewski, G.A. Voth, P. Salvador, J.J. Dannenberg, S. Dapprich, A.D. Daniels, Ö. Farkas, J.B. Foresman, J.V. Ortiz, J. Cioslowski, D.J. Fox, Gaussian 09, Revision A.1, Gaussian, Inc., Wallingford CT, **2009**.

STUDIA UBB CHEMIA, LVI, 1, 2011

STRUCTURE AND VIBRATIONAL SPECTRUM OF L-LEUCINE: A DFT-PCM INVESTIGATION

CAMELIA BERGHIAN GROŞAN*[a], VALER ALMĂŞAN[a]

ABSTRACT. The structure of L-Leucine in solution was examined using Density Functional Theory coupled with the Polarized Continuum Model (DFT-PCM). The geometry of L-Leucine zwitterion was studied with the B3LYP/6-311++G(d,p)-PCM method and the results were compared with those previously reported in the literature for X-ray diffraction of L-Leucine. The vibrational frequencies calculated on the most stable zwitterionic conformer of L-Leucine at B3LYP/6-311++G(d,p) were unscaled and in good agreement with the experimental data.

Keywords: *L-Leucine, zwitterions, DFT-PCM, vibrational spectroscopy*

INTRODUCTION

L-Leucine ((2*S*)-2-Amino-4-methylpentanoic acid) is an essential Branched-Chain Amino Acid (BCAA) like L-Isoleucine and L-Valine.

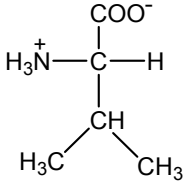

L-Valine

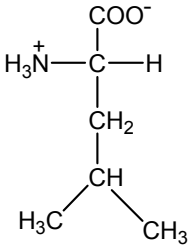

L-Leucine

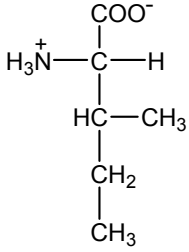

L-Isoleucine

Scheme 1.

It is a non-polar and hydrophobic amino acid occurring in proteins about 9.1 % [1]. It is synthesized in living systems being involved in regulations of blood sugar levels and muscular tissue repairing process. Leucine also has a significant contribution in the binding of hydrophobic ligands (lipids) playing an important role in the substrate recognition [2].

[a] *National Institute for Research and Development of Isotopic and Molecular Technologies 65-103 Donath Str., RO-400293 Cluj-Napoca, Romania, *camelia.grosan@itim-cj.ro*

According to [1, 3] in solution at neutral pH, L-Leucine has a predominant zwitterionic form when the amino group is protonated ($-NH_3^+$) and the carboxyl group is deprotonated ($-COO^-$) while the occurance of the nonionic form with amine ($-NH_2$) and carboxyl (-COOH) groups is insignificant.

On the other hand, it is know that vibrational spectroscopy is able as well to provide information on the general aspects of proteins i.e. structure and dynamics [4]. Thus, due to the protein sensitivity to infrared irradiation (*e.g.* vibrational spectroscopic measurements are responsive to pH, phase, solvent polarity and temperature), the use of a model substrate, such as an amino acid, is essential. In addition, a theoretical study is usually required in order to facilitate the interpretation of infrared spectra.

To the best of our knowledge, but a few theoretical (conformational and vibrational) studies focused on L-Leucine were published [2, 5-7].

Recently, Rai *et al.* [2] proposed for L-Leucine fifteen stable conformers in the gas phase, obtained by geometry optimization at the B3LYP/6-311++G(d,p) level. Thus, they analyzed the predicted vibrational infrared spectra of various nonionic L-Leucine conformers. Next, they realized a systematic search on the existence of zwitterionic form of L-Leucine in gas phase and found that the zwitterionic structures revert spontaneously into the canonical form on optimization.

Linder *et al.* [5] investigated, by experimental and theoretical methods, the gas-phase IR spectra of some natural amino acid including L-Leucine. Since they used high temperature (570 K), their study considered limited conformational states and non-hydrogen bonded structures to assume that different conformations would have similar spectra.

In 2010, Dokmaisrijan *et al.* [7] proposed the eight minimum energy conformers of L-Leucine obtained at MP2/6-311++G(2d,2p) level in the gas phase. Their results, relative stability order and some conformational properties of the most stable conformer, were significantly different from the above ones of Rai *et al.* [2]. They also analyzed the effects of intermolecular H-bond and side-chain orientations on the relative stability of L-Leucine.

It is worth to emphasize that these studies [2, 5, 7] considered but the gas-phase state of L-Leucine. This approach may be insufficient as inadequate for the complete description of biological molecules in their natural medium, aqueous solution.

In order to accomplish such a theoretical simulation, it is possible to take into account the solvent effect in two ways i) a certain number of solvent molecules are placed around the solute and ii) the solvent is considered as a continuum medium (with specific physical properties) and the solute molecule is placed in a cavity within the solvent [8].

Vibrational analysis of L-Leucine in hydrated media was previously reported by Derbel *et al.* [6]. They found that if the amino acid was surrounded by twelve water molecules, a good correlation between theoretical calculation at B3LYP/6-31++G(d) level of theory and experimental data occurred.

Hence, in order to study the stability of L-Leucine zwitterions in aqueous solution, for the present exploration we applied a density functional method (DFT/B3LYP) in conjunction with a continuum solvation model, Polarized Continuum Model (PCM). This model uses a cavity of overlapping spheres centered on the solute atoms and apparent surface charges that depend on the dielectric constant ε of the solvent.

We also reporte herein the calculated I.R. spectrum of L-Leucine zwitterion at the B3LYP/6-311++G(d,p) level together with a tentative assignment of its vibrational modes. Thus, all our calculations were carried out using Gaussian03 Package [9]. To display the molecular structure and the simulated I.R. spectra, the Program we used for visualization was Gabedit 2.3.0 [10]. The Avogadro 1.0.1 Program provided information on vibrational modes [11].

RESULTS AND DISCUSSION

1. Molecular geometry

The atom numbering and the most stable zwitterionic conformer of L-Leucine optimized at B3LYP/6-311++G(d,p) in aqueous solution employing PCM model (DFT-PCM) are shown in Figure 1.

The calculations were realized on two geometries i) the X-ray zwitterionic L-Leucine from leucin01 [12] and ii) the zwitterionic structure obtained by transferring the proton from the carboxyl group to the amino group in the lowest-energy gas-phase conformer reported by Rai *et al* [2].

Starting from structures i) and ii), two optimized geometries were obtained. For these geometries, we performed frequency calculations in order to assess which one represents the global minima. The results revealed that the geometry of X-ray zwitterionic L-Leucine optimized using PCM, to include the effect of water, at the B3LYP/6-311+G(d,p) level is not a global minimum because we found three imaginary frequencies.

Next, no imaginary frequency was found for the second zwitterionic structure optimized at the DFT-PCM (water) level; that is, the geometry depicted in Figure 1 is a true minimum on the Potential Energy Surface (PES).

Table 1 lists the selected optimized geometrical parameters of the structure studied in aqueous solution by DFT-PCM. Our results are compared with the DFT data previously reported for L-leucine + $12H_2O$ (*DFT in hydrated media*) [6] and the corresponding experimental X-ray values [12].

The *intramolecular N-H...O interaction* is a characteristic feature for several α-amino acids both in crystal state and in solution. The two or three-center *intermolecular N-H...O hydrogen bonds* are met in crystal structures of non-polar amino acids (L-Leucine crystallizes as hydrogen-bonded dimmers) [13]. In solution, our theoretical study revealed a value of 1.87 Å for the

intramolecular hydrogen bond between one ammonium hydrogen and one carboxylic oxygen atom (H-9-O-2, Figure 1). Following this intramolecular hydrogen bond interaction, in our model, the atoms N-6, C-4, C-1, O-2 were close to planarity, with a N-6-C-4-C-1-O-2 dihedral angle of -9.3 degree meanwhile in the X-ray structure the N-6-C-4-C-1-O-2 dihedral angle is about -31.7 degree.

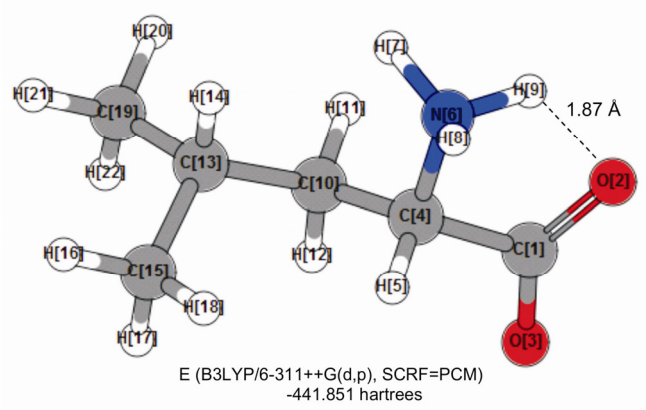

Figure 1. Optimized molecular structure of L-Leucine using PCM (water) model at B3LYP/6-311++G(d,p) level of theory.

In our PCM model, the optimized values for the N-H bond lengths were shorter than the corresponding ones issued from the DFT calculation in hydrated media or from experimental X-ray data, see Table 1. However, the N-H bond lengths values obtained by us were in good agreement with those obtained by [6], the difference being less than 2.28%.

In our model, the N-6-H-9 bond length value (1.044 Å) was longer than the other two N-H bonds (Table 1) and we supposed that happened because the hydrogen atom, H-9, is involved in the intramolecular hydrogen-bonding H-9-O-2 (Figure 1).

As shown in Table 1, the bond length N-6-C-4 (1.515 Å) obtained using our model was longer than the standard C-N bonds (1.47 Å) [14], this situation being characteristic for the C-NH_3^+ bond from amino acids [15]. In the two theoretical models, our DFT-PCM model and the DFT in hydrated media model, the C-N bond lengths (1.515 Å and 1.508 Å) were longer than the experimental value (1.497 Å), but the theoretical and experimental values were in a good agreement.

The COO^- bond lengths are stretched, but our theoretical values were more closer to the experimental ones than the values reported by [6] for DFT in hydrated media model.

Table 1. Selected parameters of zwitterionic L-Leucine. Comparison between our results obtained with DFT-PCM model and the results reported by [6] and [12].

Energies	Zwitterionic structure		
	L-Leucine B3LYP/ 6-311++G(d,p) PCM	Leucine+12H_2O B3LYP/ 6-31++G(d) [6]	L-Leucine Experimental X-ray [12]
E_e (Hartrees)	-441.851	-1359.009	-
Bond Lengths (Å)			
N-6-H-7	1.029	1.040	1.080
N-6-H-8	1.029	1.053	1.081
N-6-H-9	1.044	1.046	1.080
N-6-C-4	1.515	1.508	1.497
C-4-H-5	1.092	1.094	1.080
C-4-C-1	1.561	1.560	1.539
C-1-O-2	1.261	1.270	1.254
C-1-O-3	1.247	1.254	1.237
C-4-C-10	1.531	1.528	1.550
C-10-C13	1.543	1.546	1.508
C-13-C-15	1.535	1.538	1.539
C-13-C-19	1.536	1.538	1.481
Valence Angles (°)			
H-7-N-6-H-8	107.7	105.6	109.4
H-7-N-6-H-9	109.9	106.97	109.4
H-8-N-6-H-9	108.3	105.9	109.4
H-7-N-6-C-4	114.1	116.4	119.4
H-8-N-6-C-4	112.4	111.8	107.1
H-9-N-6-C-4	104.2	109.6	101.5
N-6-C-4-H-5	107.2	106.3	111.5
N-6-C-4-C-1	106.5	105.0	109.9
H-5-C-4-C-1	108.3	107.3	107.5
C-4-C-1-O-2	115.7	114.5	115.7
C-4-C-1-O-3	116.0	119.96	116.5
O-2-C-1-O-3	128.3	125.5	127.7
C-4-C-10-C-13	116.2	116.1	114.9
C-10-C-13-C-15	112.2	112.4	113.7
C-10-C-13-C-19	109.6	109.5	108.4
Torsion Angles (°)			
N-6-C-4-C-1-O-2	-9.3	-	-31.7
N-6-C-4-C-1-O-3	171.2	-	148.8
O-2-C-1-C-4-C-10	112.2	-	85.7
O-3-C-1-C-4-C-10	-67.4	-	-93.7

The C-4-C-1 bond was stretched whereas the C-4-C-10 was shortened compared to the experimental values (Table 1); this situation was encountered in the model reported by Derbel too [6], but our values were more closer to the experimental data. The other bond lengths and angles computed by us showed satisfactory agreement with experiment.

2. *Vibrational data*

The Leucine contains 22 atoms and according to the 3*N*-6 rule (*N*-the number of atoms), it exhibits 60 normal modes of vibration.

In Figure 2, the theoretical vibrational spectrum at B3LYP/6-311++G(d,p) level for zwitterionic L-Leucine previously optimized at PCM (water)-B3LYP/6-311++G(d,p) is presented. The I.R. spectrum was simulated on the region 0-4000 cm^{-1}.

Vibrational proposed spectral assignments for zwitterionic L-Leucine are presented in Table 2, together with its computed unscaled frequencies at B3LYP/6-311++G(d,p) level of theory and the experimental I.R. spectrum. The vibrational assignments were achieved by combining i) the motions observed using Avogadro Program, ii) the infrared band intensities with iii) L-Leucine experimental I.R spectra [16, 17] and iv) previously tentative assignments [6, 16, 17]. Thus, for the experimental values, we were interested only in L-Leucine I.R. spectra measured in aqueous solution (500-1800 cm^{-1}) [16] or film sample obtained from aqueous solutions at different pH (0-700 cm^{-1}) [17].

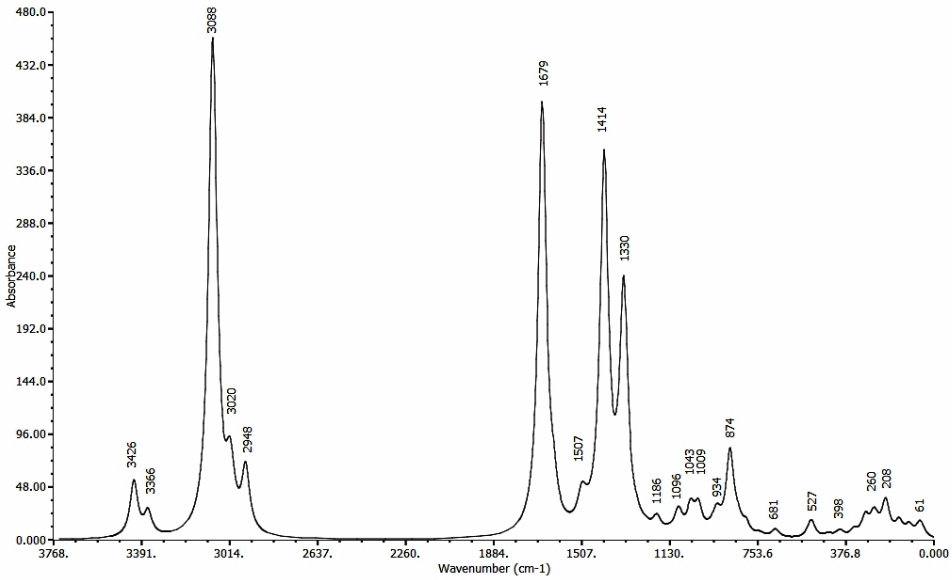

Figure 2. Simulated infrared spectrum of zwitterionic L-Leucine at B3LYP/6-311++G(d,p) level.

The I.R. spectra of the amino acid are characterized by the absorption due to the carbonyl asymmetric and symmetric vibration (ν COO^-) and the stretches and bends of ammonium group (NH_3^+).

Carbonyl (COO^-) vibrations

Wolpert *et al.* [16] assigned for the group COO^- of the amino acids the following arbitrary positions (cm^{-1}): 1530 (antisymmetric stretching, ν_{as}), 1410 (symmetric stretching, ν_s) for most significant modes and ~ 800 (β COO^- scissoring), ~ 650 (w COO^- wagging) and ~ 650-600 (r COO^- rocking) for other modes.

In our exploration, by B3LYP/6-311++G(d,p) level of theory, the three bending vibrations of COO^- group were predicted at 681 (δ COO^-, w COO^-), 527 (δ COO^-, w COO^-) and 398 (r COO^-) cm^{-1}. These values were in good agreement with the experimental frequencies (670, 535, 343 cm^{-1}). We did not find the other deformation modes (629, 586, 579, 364 cm^{-1}) assigned in the literature [16, 17] for the COO^-group (Table 2). For asymmetric COO^- stretch (ν_{as}) we found the absorption at 1679 cm^{-1} while the symmetric COO^-stretches (ν_s) occur at 1414 (strong), 1401 (weak), 1376 (weak), and 1354 (weak) cm^{-1}. These bands are in agreement with the values reported in the literature for the strong COO^- stretching (near 1600 cm^{-1} for asymmetric and near 1400 cm^{-1} for symmetric vibration [18]) and with the values reported by Wolpert for L-Leucine in aqueous solution at pH= 3 (Table 2) [16].

Ammonium (NH_3^+) vibrations

The amino acids exhibit NH_3^+ stretching and deformation vibrations that appear in the region 3200-3000 cm^{-1} (asymmetric stretch), near 2700 and 2100 cm^{-1} (symmetric stretch, these bands are not always present), 1660-1590 cm^{-1} (asymmetric deformation, δ_{as}), 1550-1485 cm^{-1} (symmetric deformation, δ_{as}) and 1295-1090 cm^{-1} (rocking vibration, r), [19].

In our study, the NH_3^+ asymmetric stretching vibrations appeared in the range 3426-3078 cm^{-1}, while for the symmetric stretching we did not find any band. The bands due to the NH_3^+ asymmetric deformation were observed at 1679, 1660 and 1632 cm^{-1} as the NH_3^+ symmetric deformations occur at 1428 and 1414 cm^{-1}. In the region 1238-1009 cm^{-1}, rocking vibrations of NH_3^+ group were observed. These frequencies are in agreement with the previous literature data [19] and the infrared spectra reported for L-Leucine in aqueous solution (Table 2) [16].

C-N, C-C, C-H vibrations

The C-N stretching absorptions of L-Leucine at B3LYP/6-311++G(d,p) occur at 874, 842, 746 cm^{-1}. These vibrations were coupled with CH or COO^- deformations or C-C stretching vibrations (Table 2).

Tabel 2. Vibrational wave numbers obtained at B3LYP/6-311++G(d,p) level, experimental FTIR Spectra for zwitterionic L-Leucine and vibrational assignments

Vibrational mode number obtained from DFT simulation	Unscaled wavenumbers (cm^{-1}) B3LYP/6-311++G(d,p)	Experimental (cm^{-1}) [16, 17]	Vibrational assignments
1	55	53	τ NH_3, τ CH_3, δ CH
2	61	73	τ NH_3, τ CH_3, τ COO^-
3	108	107	τ NH_3, τ CH_3, τCH_2, τ COO^-
-	-	122	τ COO^-, τ CC, rotational
4	151	138	τ COO^-, τ CC
-	-	170	τ COO^-
5	208	203	r NH_3, δ CCN, τ CH_3
6	232	223	δ CH_2, w CH_3
7	254	-	δ $CH(CH_3)_2$
8	260	-	r CH_3, w CH_3, w NH_3, δ CH_2
9	295	-	w NH_3, δ CCC
-	-	330	δ CCN, δ CCC
10	344	-	δ CH, δ CCN
11	398	343	r COO^-, δ CCN, δ CCC
-	-	364	r COO^-, δ CCN
-	-	402	δ CCC
12	411	442	δ CCC
13	454	456	δ $CH(CH_3)_2$
14	527	535	δ COO^-, w COO^-, δ CCN
-	-	579	γ OCO^-
-	-	586	δ COO^-
-	-	629	w COO^-
15	681	670	δ COO^-, w COO^-, δ CCN
-	-	716	-
16	746	736	δ CH, ν CN
17	806	834	ν CC, r CH_2, w NH_3
18	842	848	δ COO^-, ν CC, ν CN
19	874	-	δ CH, ν CC, ν CN
20	924	907	r CH_3, ν CC
21	934	943	ν CCN, ν CC
22	953	-	δ CH
23	969	973	ν CC, r CH_3
24	1009	1003	r NH_3, r CH_3, ν CC
-	-	1031	ν CN

Vibrational mode number obtained from DFT simulation	Unscaled wavenumbers (cm^{-1}) B3LYP/6-311++G(d,p)	Experimental (cm^{-1}) [16, 17]	Vibrational assignments
25	1043	-	δ CH, r NH_3
26	1096	-	δ CCN, r NH_3, ν CC
27	1137	1135	r CH_3, ν CC, δ CCN
28	1186	1174	r NH_3^+, δ CH
29	1198	1185	r NH_3^+, r CH_3, ν CC
30	1238	1239	r NH_3^+, t CH_2, r CH_3, ν C-COO^-
-	-	1295	t CH_2
31	1279	1316	δ CH
32	1322	-	ν CC, t CH_2
33	1330	1340	ν CC, t CH_2
34	1354	1353	ν_s COO^-, δ CH
35	1376	1372	ν_s COO^-, δ_s CH_3
36	1401	1392	ν_s COO^-, ν CC, δ COO^-
37	1406	-	δ $CH(CH_3)_2$
-	-	1412	ν_s COO^-
38	1414	-	ν_s COO^-, δ_s NH_3^+
39	1428	-	δ_s NH_3^+, δ CH_2, δ_{as} CH_3
-	-	1440	δ CH_2
-	-	1455	-
-	-	1471	δ_{as} CH_3
40	1480	-	δ CH, δ CH_2, δ_{as} CH_3
41	1488		δ CH (C-4), δ CH_2, δ_{as} CH_3
42	1496	-	δ CH (C-4), δ CH_2, δ_{as} CH_3
43	1507	-	δ CH_2, δ_{as} CH_3
44	1512	-	δ CH_2, δ_{as} CH_3
-	-	1520	-
-	-	1538	δ_{as} NH_3^+
5	1632	1625	δ_{as} NH_3^+
46	1660	-	δ_{as} NH_3^++ δ CH
47	1679	1598	ν_{as} COO^-, δ_{as} NH_3^+
48	2948	-	ν CH_3
49	3007	-	ν CH
50	3016	-	ν CH_3, ν CH2
51	3020	-	ν CH_3, ν CH2
52	3075	-	ν CH
53	3078	-	ν NH_3^+/ ν CH
54	3082	-	ν NH_3^+/ ν CH

Vibrational mode number obtained from DFT simulation	Unscaled wavenumbers (cm^{-1}) B3LYP/6-311++G(d,p)	Experimental (cm^{-1}) [16, 17]	Vibrational assignments
55	3084	-	ν CH
56	3087		ν NH_3^+/ ν CH
57	3088		ν NH_3^+/ ν CH
58	3094		ν NH_3^+/ ν CH
59	3366		ν NH_3^+
60	3426		ν NH_3^+

ν: streching, δ: deformation, γ: out of plane deformation, τ: torsion, w: wagging, r: rocking, t: twisting; a: antisymmetric, s: symmetric.

According to Barth [20], the aliphatic side chain of amino acids gives several characteristic absorbance bands of medium to weak intensity. In solid phase, the characteristic vibrations δ_{as} CH_3, δ CH_2, δ_s CH_3 appear near 1465, 1450, 1475 cm^{-1} and are not coupled to other vibrational modes while the δ CH and γ CH_2 are often coupled to other modes. In solution, Wolpert [16] assigned the δ_{as} CH_3, δ CH_2, δ_s CH_3 vibrations at 1471, 1440, 1372 cm^{-1} respectively; the latter is coupled with ν COO^-. Our finding consists of the δ_{as} CH_3 to be coupled with δ CH_2, δ CH vibrations and appeared in the range 1512-1428 cm^{-1} while δ_s CH_3 appeared at 1376 cm^{-1} together with ν_s COO^- vibration. Our theoretical I.R. spectrum revealed bands in the region 3094-2948 cm^{-1} for the CH stretching (ν CH) that it is in good agreement with the experimental data (3000-2850 cm^{-1}) [19].

The band below 500 cm^{-1} was mainly assigned to the CCN and CCC skeletal deformation and torsional vibrations.

CONCLUSIONS

The present work described a theoretical study of the structure and I.R. spectrum of zwitterionic L-Leucine. In order to obtain reasonable information about this amino acid at physiological conditions, we optimized the zwitterionic structure of L-Leucine using a density functional method [DFT/B3LYP/6-311++G(d,p)] in conjunction with a continuum solvation model, Polarized Continuum Model (PCM). The comparison between our theoretical results and experimental structural parameters indicates that our data are in good agreement with the experimental values.

Vibrational frequencies, calculated by B3LYP/6-311++G(d,p), agree very well with the I.R. spectra of L-Leucine in aqueous solution. Thus, tentative assignments of this zwitterionic amino acid normal modes of vibrations were performed.

Our study demonstrates the performance of DFT-PCM methods in calculating molecular structure and frequencies of L-Leucine in aqueous solution.

EXPERIMENTAL SECTION

The calculations were carried out using Gaussian03 package [9]. The programs used for visualization were: Gabedit 2.3.0 to display molecular structure and simulated infrared spectra [10] and Avogadro 1.0.1 to obtain information on vibrational modes [11].

The zwitterionic L-Leucine was optimized using a density functional method (DFT/B3LYP/6-311++G(d,p)) in conjunction with a continuum solvation model, Polarized Continuum Model (PCM).

Vibrational frequencies were simulated at B3LYP/6-311++G(d,p) level of theory. An approximate assignment of vibrational frequencies was realized by analysis of normal modes motion using Avogadro program. Our results were compared with the previously tentative assignments for L-Leucine [6, 16, 17].

ACKNOWLEDGMENTS

We are thankful to the financial support of CNCSIS (the National University Research Council) through Human Resources-Postdoctoral Program (PD_585/2010).

We gratefully acknowledge to Data Center of NIRDIMT (National Institute for Research and Development of Isotopic and Molecular Technologies) Cluj-Napoca for providing computer facilities.

The authors would like to express their very sincerely thanks to the reviewer for his valuable many comments and suggestions.

REFERENCES

1. D.L. Nelson, M.M. Cox, “Lehninger Principles of Biochemistry”, Fourth Edition, W. H. Freeman and Co., New York, **2004**, chapter 3.
2. A.K. Rai, C. Song, Z. Lin, *Spectrochimica Acta Part A*, **2009**, *73*, 865.
3. J.M. Berg, J.L. Tymoczko, L. Stryer “Biochemistry”, Sixth Edition, W. H. Freeman and Co., New York, **2007**, chapter 2.
4. F. Siebert, P. Hildebrandt, “Vibrational Spectroscopy in Life Science”, Wiley-VCH, Weinheim, **2008**, chapter 5.
5. R. Linder, M. Nispel, T. Haber, K. Kleinermanns, *Chemical Physics Letters*, **2005**, *409*, 260.
6. N. Derbel, B. Hernandez, F. Pfluger, J. Liquier, F. Geinguenaud, N. Jaidane, Z.B. Lakhdar, M. Ghomi, *J. Phys. Chem. B*, **2007**, *111*, 1470.

7. S. Dokmaisrijan, V.S. Lee, P. Nimmanpipug, *Journal of Molecular Structure: THEOCHEM*, **2010**, *953*, 28.
8. S. Tiwari, P.C. Mishra, *Spectrochimica Acta Part A*, **2009**, *73*, 719.
9. Gaussian 03, Revision C.02. M.J. Frisch, G.W. Trucks, H.B. Schlegel, G.E. Scuseria, M.A. Robb, J.R. Cheeseman, J.A. Montgomery, Jr., T. Vreven, K.N. Kudin, J.C. Burant, J.M. Millam, S.S. Iyengar, J. Tomasi, V. Barone, B. Mennucci, M. Cossi, G. Scalmani, N. Rega, G.A. Petersson, H. Nakatsuji, M. Hada, M. Ehara, K. Toyota, R. Fukuda, J. Hasegawa, M. Ishida, T. Nakajima, Y. Honda, O. Kitao, H. Nakai, M. Klene, X. Li, J.E. Knox, H.P. Hratchian, J.B. Cross, C. Adamo, J. Jaramillo, R. Gomperts, R.E. Stratmann, O. Yazyev, A.J. Austin, R. Cammi, C. Pomelli, J.W. Ochterski, P.Y. Ayala, K. Morokuma, G.A. Voth, P. Salvador, J.J. Dannenberg, V.G. Zakrzewski, S. Dapprich, A.D. Daniels, M.C. Strain, O. Farkas, D.K. Malick, A.D. Rabuck, K. Raghavachari, J.B. Foresman, J.V. Ortiz, Q. Cui, A.G. Baboul, S. Clifford, J. Cioslowski, B.B. Stefanov, G. Liu, A. Liashenko, P. Piskorz, I. Komaromi, R.L. Martin, D.J. Fox, T. Keith, M.A. Al-Laham, C.Y. Peng, A. Nanayakkara, M. Challacombe, P.M.W. Gill, B. Johnson, W. Chen, M.W. Wong, C. Gonzalez, and J.A. Pople, Gaussian, Inc., Wallingford CT, **2004**.
10. A.R. Allouche, *Journal of Computational Chemistry*, **2011**, *32*, 174.
11. Avogadro: an open-source molecular builder and visualization tool. Version 1.0.1, http://avogadro.openmolecules.net/
12. M. Coll, X. Solans, M. Font-Altaba, J.A. Subirana, *Acta Crystallographica Section C*, **1986**, *42*, 599.
13. H.B. Burgi, J.D. Dunitz, "Structure Correlation", VCH, Weinheim, **1994**, chapter 11.
14. G.W. Gokel, "Dean's Handbook of Organic Chemistry", McGraw-Hill, New York, **2004**, chapter 3.
15. T. Hahn, *Zeitschrift für Kristallographie*, **1957**, *109*, 438.
16. M. Wolpert, P. Hellwig, *Spectrochimica Acta Part A*, **2006**, *64*, 987.
17. A. Trivella, T. Gaillard, R.H. Stote, P. Hellwig, *J. Chem. Phys.*, **2010**, *132*, 115105.
18. D.L. Pavia, G.M. Lampman, G.S. Kriz, J.R. Vyvyan, "Introduction to Spectroscopy", Fourth Edition, Brooks/Cole, **2009**, chapter 2.
19. G. Socrates, "Infrared and Raman Characteristic Group Frequencies: Tables and Charts", Third Edition, John Wiley & Sons, **2004**, chapter 23.
20. A. Barth, *Progress in Biophysics & Molecular Biology*, **2000**, *74*, 141.

STUDIA UBB CHEMIA, LVI, 1, 2011

SEM CHARACTERIZATION OF STARCH GRANULES

OSSI HOROVITZ[a,*], NICOLAE CIOICA[b], NICOLAE JUMATE[c], MARIA POJAR-FENEŞAN[d], ANA BALEA[d], VICTOR LITEANU[a], AURORA MOCANU[a], MARIA TOMOAIA-COTIŞEL[a]

ABSTRACT. Maize and potato starch samples were investigated by three scanning electron microscopy techniques (secondary electron imaging, Everhart Thornley secondary electron detection, backscattered electron imaging) at different magnifications. The starch granules were visualized and their shapes, surface morphology and size were revealed. From the SEM images the size distribution of the granules was inferred and compared for the different samples. These investigations will contribute to the characterization of native starches as raw materials for the production of biodegradable plastics.

Keywords: *potato starch; maize starch; SEM; granulometry*

INTRODUCTION

In the current search for "green" alternatives to petrochemical based plastic products, starch remains in the top of the options. This biopolymer presents numerous advantages, such as its abundance, low cost and biodegradability [1]. Excepting its use as filler in starch-filled polymer blends [2], in the production of biodegradable plastics, native granular starch has to be modified (destructured), giving thermoplastic starch or foamed starch [3-5]. It is also used in various blends with synthetic polymers, both non-biodegradable (such as polyethylene) and biodegradable (polylactic acid, PLA, polycaprolactone, PCL etc.).

Starch is a polysaccharide, consisting of D-glucose units, linked together into two different macromolecules: amylose and amylopectin. Amylose contains linear or sparsely branched chains based on α-1,4 glucosidic bonds and has a molecular mass of 10^5-10^6; the chains configuration is that of single or double helixes. Amylopectin, on the other hand, is based on both α-1,4 bonds and α-1,6 linkages, the latter giving the branch points of the chain, at every 20-25 glucose units The molecular mass of this multiple branched polymer [6-8] is as high as 10^7-10^9, and it is present in the semi-crystalline structure of the starch granule, amylose being amorphous [9].

[a] *Babeş-Bolyai University, Faculty ofChemistry and Chemical Engineering,11, Arany J. Str., RO-400028 Cluj-Napoca, Romania, * ossihor@yahoo.com*
[b] *INMA, 59 Al. Vaida-Voievod Str., 400436 Cluj-Napoca, Romania*
[c] *Technical University of Cluj-Napoca, Faculty of Material Science and Engineering, 103, Muncii Bd., 400641, Cluj-Napoca, Romania*
[d] *Raluca Ripan Institute of Chemistry, 30 Fantanele Str., 400294 Cluj-Napoca, Romania*

Starch is known to be the main storage substance in plants (cereals, legumes and tubers). Main sources for separation of starch granules are potato, maize, wheat, rice, pea, cassava (manioc) etc. The amylose/amylopectin ratio in starch granules varies according the resource, the starch from most cereals containing 20-30% amylose. In waxy maize (*Zea mais cerata*) and waxy rice, starch contains almost only amylopectin (98%), while high amylose maize starch and some species of peas contain 60-80% amylase [10]. Native starch granules from different plants have dimensions between 0.5 and 175 μm and various shapes: spherical, oval, disk, polygonal, rods [11, 12]. Within the starch granule, amylose and amylopectin molecules seem to be interdispersed [9], while amylose is concentrated at the periphery of the granule, where a tightly associated amylose and amylopectin network is formed [13, 14].

The surface morphology, size and shape of starch granules are therefore important topics to be known for the different practical applications of starch. Scanning electron microscopy (SEM) proved itself to be a valuable method in the study of the granulate microstructure and surface characteristics of starch and for the investigation of the enzymes effect on starch granules [15-23]. This technique allows for an observation of the sample characteristics at nanometric scale, as compared with the 0.2 μm resolution available in the optical microscope. Previously, we reported on the surface characteristics of starch granules using atomic force microscopy (AFM) investigations [24].

The goal of the present work is to reveal, by SEM observations, the size, shape and surface morphology of starch granules from native maize and potato starches, which are used for the production of biodegradable plastics.

RESULTS AND DISCUSSION

Some of the SEM images of the starch granules from potatoes in the thin film examined by the secondary electron imaging (SEI) technique are given in Figure 1 for different magnifications. The analogous pictures of starch granules from maize are given in Figure 2.

From the sizes of a great number of particles (some hundreds), measured on the SEM images, the average size (equivalent diameter of the granules) and the standard deviation (SDEV) were calculated and are given in Table 1, together with the extreme values of the granule sizes. The histograms providing the size distribution of starch granules, obtained from SEM pictures, are given in Figure 3. The size distribution is similar in the two samples, i.e. there are no significant differences between the potato (Fig. 3a) and maize (Fig. 3b) starch granules.

From these histograms, the granulometry of the starch samples was derived and given in Table 2, both for number of particles and particles weight. While in the potato starch powder the fraction with granule diameters between

10 and 12 μm are predominant both in number (Fig. 3a) and in weight (Table 2), for the maize starch the granules with diameters between 8 and 10 μm are the most numerous (Fig. 3b), but the major contribution to the weight is given by the larger particles, with diameters in the 12...14 μm range.

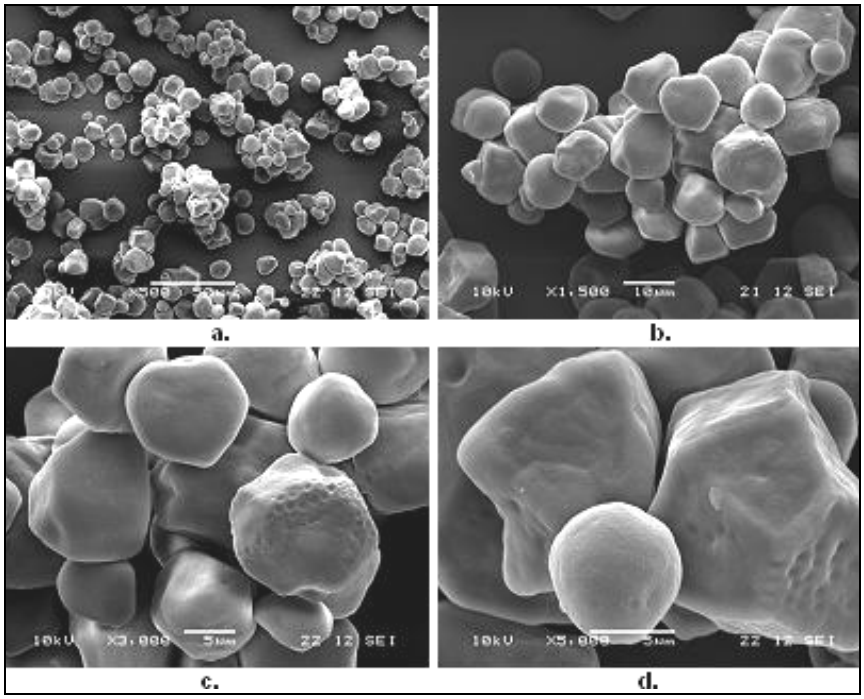

Figure 1. Potato starch granules (sample 1) visualized by SEM (SEI technique), the bar lengths are respectively: 50 μm (a); 10 μm (b); 5 μm (c); 5 μm (d).

Table 1. SEM characterization of starch granules

Sample	Average size of granules [μm]	SDEV [μm]	Extreme values [μm]
Potato starch, sample 1, thin film	10.3	2.7	3.8 ... 16.2
Maize starch, sample 2, thin film	9.3	2.9	3,7 ... 16.0
Potato starch, sample 1, compact tablet	9.5	3.5	2.2 ... 23.7
Maize starch, sample 2, compact tablet	9.3	3.3	2.2 ... 22.8
Potato starch, sample 1, from BSE	8.6	3.4	2.3 …19.1
Maize starch, sample 2, from BSE	9.2	3.9	3.2 …21.8
Maize purified starch, sample 3	11.1	6.6	2.3 …37.3

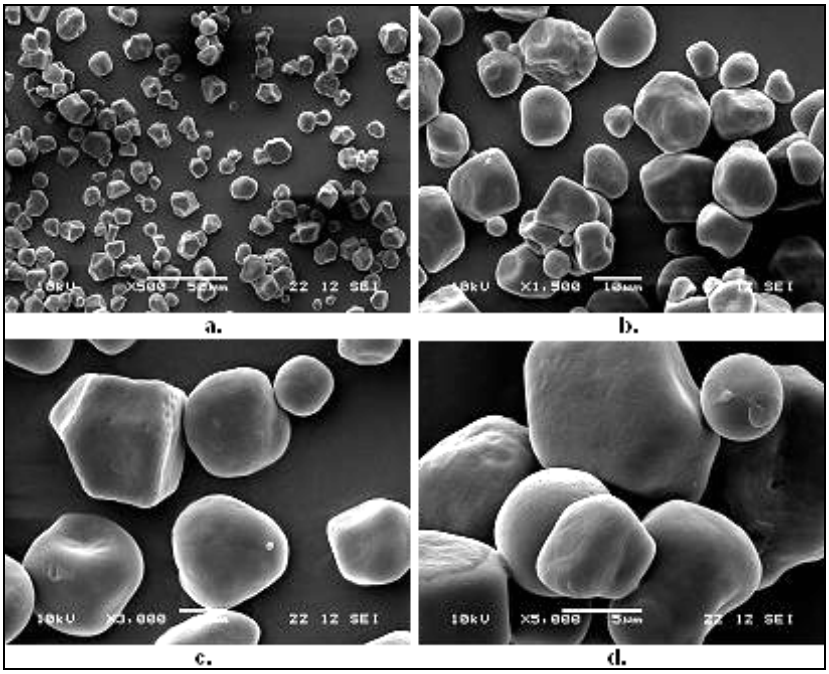

Figure 2. Maize starch granules (sample 2) visualized by SEM (SEI technique), the bar lengths are respectively: 50 μm (a); 10 μm (b); 5 μm (c); 5 μm (d).

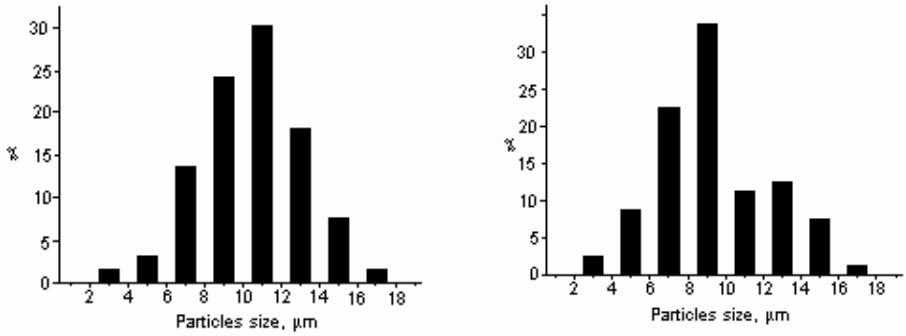

a. **b.**

Figure 3. Histograms of size distribution of granules in the potato starch sample 1 (a) and the maize starch – sample 2 (b) thin films

Some of the SEM images at different magnification ratios, obtained with the SEM-ETD technique on compact starch tablets, are given in Figure 4 for the potato starch (sample 1) and in Figure 5 for the maize starch (sample 2). The sizes of the granules, measured from the SEM images, are given in Table 1 and the histograms for the size distribution are presented in Figure 6.

Table 2. Granulometry (size distribution) of potato and maize starch samples in thin films

Diameter (μm)	% particles number		% particles weight	
	Potato starch (sample 1)	Maize starch (sample 2)	Potato starch (sample 1)	Maize starch (sample 2)
2-4	1.8	2.4	0.0	0.1
4-6	3.2	8.6	0.3	1.0
6-8	13.6	22.4	3.4	7.1
8-10	23.9	33.6	12.8	22.6
10-12	30.1	11.3	29.4	13.8
12-14	18.1	12.6	29.2	25.5
14-16	7.7	7.6	19.1	23.6
16-18	1.6	1.4	5.8	6.3

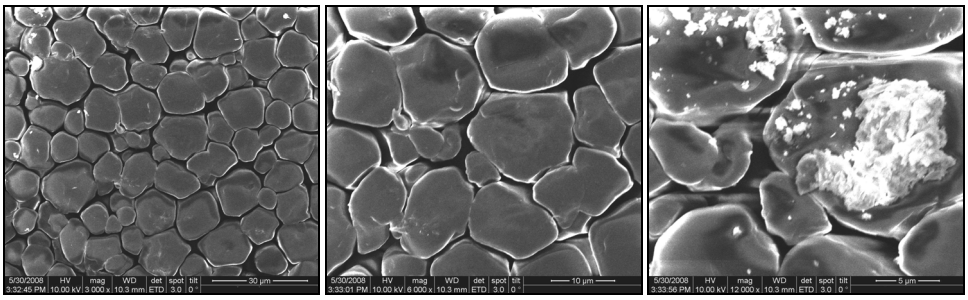

a. **b.** **c.**

Figure 4. Potato starch granules (sample 1) visualized by SEM with ETD technique in compacted tablet; bar lengths: 30 μm (a); 10 μm (b); 5 μm. (c).

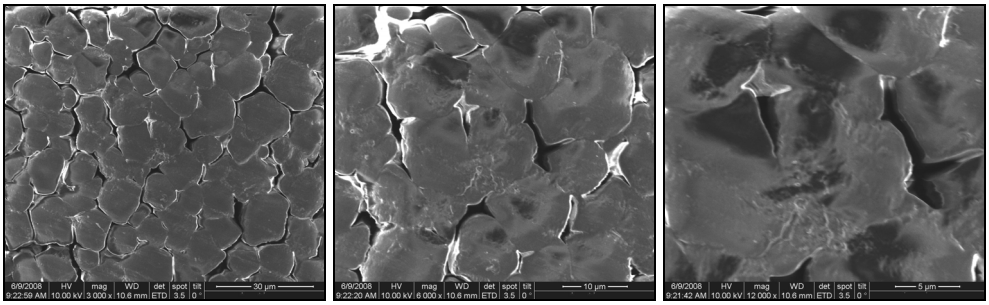

a. **b.** **c.**

Figure 5. Maize starch granules (sample 2) visualized by SEM with ETD technique in compacted tablet; bar lengths: 30 μm (a); 10 μm (b); 5 μm. (c).

Some of the starch granules visualized in the SEM images (Figs. 1, 2, 4, 5) present smooth surfaces, for other the surface roughness is rather pronounced. A variety of particle shapes can be observed on the images, from spherical and oval to irregular polygonal shape. These shapes are more or

less conserved in the compact tablets (Figs. 4, 5), but some of the particles are fragmented or present cracks (see for instance Fig. 4 c, d). These observations are consistent with the results of AFM investigations on similar starch samples [24]. AFM allows for a more detailed visualization of the ultrastructure of the granules surface. While the average size of the granules is little affected by compression, particularly for the maize starch, the distribution of the diameters is enlarged in the tablets (as seen from the standard deviation and the extreme values in Table 1). Smaller particles are present as result of the fragmentation of granules, but also larger particles result by the aggregation of granules.

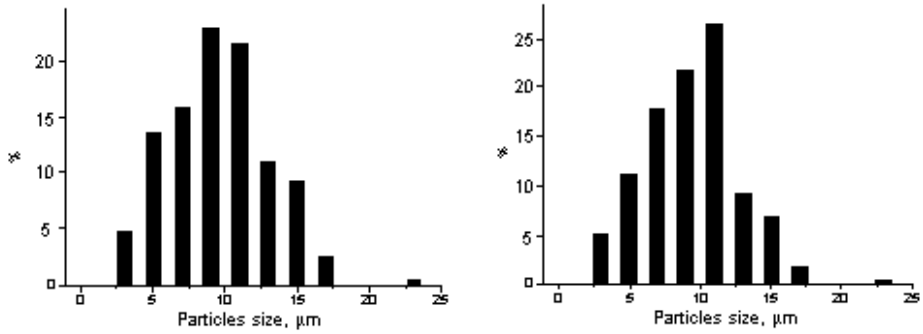

a. **b.**

Figure 6. Histograms of size distribution of granules in the potato starch – sample 1 (a) and the maize starch – sample 2 (b) tablets

The SEM images obtained with the BSE technique for the same two starch samples (1 and 2) give also a clear visualization of the starch granules, as seen from the examples given in Figure 7. The size distribution is similar to that seen from the other SEM imaging techniques.

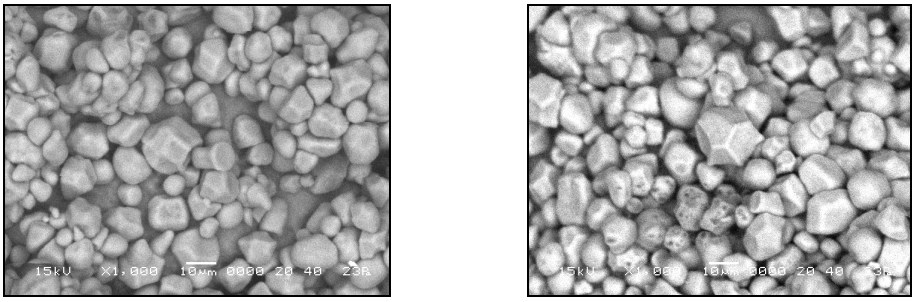

a. **b**.

Figure 7. Potato starch – sample 1 (a) and maize starch – sample 2 (b) granules visualized by SEM - BSE technique; the bar length in the images is 10 µm.

The purified maize starch (sample 3) was also investigated by the BSE technique; a typical image is given in Figure 8, along with the histogram of the particles distribution. The size distribution of the granules in particles numbers and in particles weights is given in Table 3.

As compared with sample 2, there are more small granules, but there are also a few very large granules, so that the distribution is larger (from 2 to 37 μm, standard deviation 6.6 μm) and the average size is somewhat higher (11.1 μm).

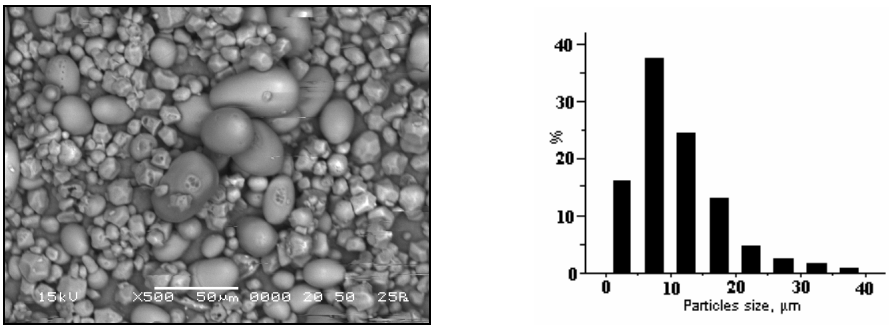

a. **b.**

Figure 8. Maize starch granules (sample 3) visualized by SEM - BSE technique; the bar length is 10 μm (a), and histogram of size distribution of granules (b)

Table 3. Granulometry of maize purified starch (sample 3) from SEM-BSE imaging

Diameter (μm)	% granules number	% granules weight
2-5	16.8	0.1
5-10	36.6	4.7
10-15	24.4	14.6
15-20	13.0	21.3
20-25	4.6	16.0
25-30	2.3	14.6
30-35	1.5	15.7
35-37	0.8	12.9

CONCLUSIONS

Knowing the granulate microstructure of starch is imperative for the correct specification of the processing conditions in the production process of biodegradable materials, based on thermoplastic starch.

The investigation by three SEM techniques, viz. secondary electron imaging (SEI) technique on gold sputtered samples, the use of the Everhart Thornley secondary electron detector (ETD) on starch tablets and backscattered-electron (BSE) imaging technique has enabled us to characterize commercial native starch samples from two different sources, potato and maize, as well as purified maize starch. SEM allows for a good visualization of the starch granules,

revealing their shapes, their surfaces morphology and sizes. Thus, some Romanian starches were investigated for the first time and their granulometry was established from histograms based on the measurement of granules sizes by SEM images. We could also follow the effect of compression on the morphology of starch granules.

The present SEM studies complete our AFM observations on the same type of starches, which helped to better understanding of the ultrastructure of the granule surfaces. These techniques will be applied in our laboratories to characterize the thermoplastic starch products obtained from the investigated native starch samples.

EXPERIMENTAL SECTION

The investigations were made on commercial native potato (sample 1) and maize (sample 2) starches, and on purified maize starch (sample 3). The moisture of the starch samples was about 12%.

The granulate microstructure of the samples was analyzed by scanning electron microscopy (SEM), with three imaging techniques, namely scanning electron microscope, JEOL JSM 5510 LV, Japan, using the secondary electron imaging technique (SEI); scanning electron microscope, FEI Company, Netherlands, with the Everhart Thornley Seconday Electron Detector (ETD) [25]; scanning electron microscope, JEOL JSM 5600 LV, Japan, using the backscattered-electron (BSE) imaging technique.

For the SEI imaging, the starch powder was deposited in thin layer on an adhesive metallic support and then was gold sputtered in the AGAR, Auto Sputter Coater. The thin gold coating (thickness 10 nm) was sputtered in 3 sputtering cycles taking about 10 s each. These metallized samples were examined on the SEM, with accelerating voltage of 10 kV, working distance between 10.3 and 10.7 mm and a spot size of 3 to 3.5 μm, at magnification ratios from 100 to 10,000 times.

With the Everhart Thornley Secondary Electron Detector (ETD), compact starch tablets can be used, without metallization. The starch tablets were prepared as follows: the starch powder (around 1g) is crushed in a hydraulic press in vacuum, without any binding agent. The accelerating voltage was also 10 kV, the working distance 21-22 mm and the spot size 12 μm. Images were obtained with magnification ratios between 800 and 12,000 times.

For the BSE imaging, the samples were deposited as an uniform layer on the adhesive graphitized tape and were examined in low vacuum (20 – 25 Pa), with an accelerating voltage of 15 kV, a working distance of 20 mm, an electron spot size of 40 or 50 μm, at magnification ratios from 500 to 1,000 times.

ACKNOWLEDGMENTS

This research was financially supported by the project 31-039 from the 2nd National Program.

REFERENCES

1. M. Thunwall, A. Boldizar, M. Rigdahl, *Carbohydrate Polymers*, **2006**, *11*, 419.
2. G.L. Griffin, *Advances in Chemical Research*, **1973**, *134*, 159.
3. H.F. Zobel, *Starch/Stärke*, **1988**, *40*, 1.
4. K. Poutanen, P. Forssell, *Trends in Polymer Science - TRIP,* **1966**, *4*(4), 128.
5. R. van Tuil, J. van Heemst, G. Schennink, In „Biorelated polymers. Sustainable polymer science and technology", E.Chiellini et al. Edts., Kluwer Academic/ Plenum Publ., New York, **2001**, pp.3-17.
6. H.F. Zobel, *Starch/Stärke,* **1988**, *40*(2), 44.
7. D.J.Gallant, B. Bouchet, A. Buleon, S. Perez, *European Journal of Clinical Nutrition*, **1992**, *46,* 316.
8. S. You, J. Jane, *Carbohydrate Polymers*, **2001**, *49*, 307.
9. J. Jane, *J. Appl. Glycosci.*, **2006**, *53*, 205.
10. N. Singh, J. Singh, L. Kaur, N. Singh Sodhi, B. Singh Gill, *Food Chemistry,* **2003**, *81*, 219.
11. D. French, In "Starch: chemistry and technology", Whistler, R.L, Bemiller, J.N., Paschall, E.F., Eds.; Academic Press: London, **1984**, pp. 183-247.
12. J. Jane, T. Kasemsuwan, S. Leas, H. Zobel, J.F. Robyt, *Starch/Stärke*, **1994**, *46*, 121.
13. J. Jane, J.J. Shen, *Carbohydrate Research*, **1993**, *247*, 279.
14. D.D. Pan, J. Jane, *Biomacromolecules*, **2000**, *1*, 126.
15. J.M.V. Blanshard, In "Starch: Properties and Potential", T. Galliard, Edit., J. Wiley and Sons: Brisbane, **1987**, pp. 16-54.
16. H. Fuwa, Y. Sugimoto, T. Takaya, Z. Nikuni, *Carbohydrate Research*, **1979**, *70*, 233.
17. M.R. Sandhya Rani, K.R. Bhattachrya, *Starch/Stärke*, **1995**, *47*, 334.
18. R.S. Policegoudra, S.M. Aradhya, *Food Hydrocolloids*, **2008**, *22*, 513.
19. S. Wang, J.L. Yu, O. Zhu, J. Yu, F. Jin, *Food Hydrocolloids*, **2009**, *23*, 426.
20. J. Szymonska, M. Targosz-Korecka, F. Ktok, *Journal of Physics: Conference Series*, **2009**, *146*, 012027.
21. M. Sujka, J. Jamroz, *LWT – Food Science and Technology*, **2009**, *42*, 1219.
22. F.H. Cisneros, R. Zevillanos, L. Cisneros-Zevillanos, *Journal of Agricultural and Food Chemistry*, **2009**, *57*, 7363.
23. H.Yan, G.U. Zhengbiao, *Food Research International*, **2010**, *43*, 767.
24. M. Tomoaia-Cotisel, N. Cioica, C. Cota, Cs. Racz, I. Petean, L.D. Bobos, A. Mocanu, O. Horovitz, *Studia UBB Chemia*, **2010**, *55* (2), 313.
25. T.E. Everhart, R.F.M. Thornley, *Journal of Scientific Instruments,* **1960**, *37* (7), 246.

STUDIA UBB CHEMIA, LVI, 1, 2011

DETERMINATION OF THE ABSOLUTE CONFIGURATION OF 3-AMINO-3-(TETRAHYDROFURAN) CARBOXYLIC ACID BY VIBRATIONAL CIRCULAR DICHROISM AND DFT CALCULATION

SHENGLI MA[a], SHERRY SHEN[a], ZHENGXU HAN[a], YIBO XU[a], HEEWON LEE[a], DHILEEPKUMAR KRISHNAMURTHY[a], CHRIS SENANAYAKE[a], NELU GRINBERG[a,*]

ABSTRACT. The absolute configuration of 3-amino-3-(tetrahydrofuran) carboxylic acid was determined using vibrational circular dichroism and DFT calculation. The conformation of 3-amino-3-(tetrahydrofuran) carboxylic acid in gas phase and aqueous solution was calculated, along with the vibrational circular dichroism (VCD) and infrared (IR) spectra. In addition, experimental VCD and IR spectra were collected in aqueous solution. Each calculated IR and VCD spectra was compared to the experimental spectra. The band assignment was unambiguously determined from the DFT calculation. Based on the calculation and the experimental data it was determined that the absolute configuration of the compound was (S)-enantiomer.

Keywords: *VCD, absolute configuration, THF amino acid, DFT*

INTRODUCTION

Amino acids are essential building blocks for proteins. In addition they have been extensively used as intermediates in the synthesis of many chiral molecules.[1-9] Heterocyclic amino acids are of particular interest, as exemplified by 3-amino-3-(tetrahydrofuran) carboxylic acid (THF amino acid 1), which possesses diverse physiological activities and has been utilized as a building block for a large number of chiral drug molecules.[1,10-15] As such, the absolute configuration of amino acid is critical; yet very few methods can be applied for such determination. Single crystal X-ray is the straightforward way; however, sometimes it is very difficult, if not impossible, to get single crystals. Another method for the determination of absolute configuration is NMR; however, the technique requires chiral reagents for the formation of diastereomeric species, and the reagents are often not readily available.

Recently we have synthesized a tetrahydrofuran (THF) amino acid **1** and used it as a building block in the synthesis of a series of chiral drug candidates.[11,12] In order to pursue the synthesis in the subsequent steps it

a *Chemical Development Department, Boehringer Ingerheim Pharmaceuticals Inc., Ridgefield, CT USA 06877, *nelu.grinberg@boehringer-ingelheim.com*

was important to determine the absolute configuration of the starting material. The polar nature of the compound rendered it solubile only in water. Using such solvent, the generation of a single crystal amenable to X-ray analysis was not possible.

Vibrational circular dichroism (VCD) is a spectroscopic method that was developed in the 1970s. VCD is a chiroptical technique which measures the difference in absorbance of a chiral molecule upon interacting with a left versus right circularly polarized light in the infrared part of the spectrum. As such the technique is very sensitive not only to structural changes in biomacromolecules and small molecules, but also to the mutual orientation of different chemical groups within it. VCD is also very sensitive to changes in the bond strength, bond distortion during the catalytic reaction, etc.[16] As a result, VCD provides a wealth of information about the structure and absolute configuration of chiral compounds.[17,18]

The theories of IR and VCD were first developed decades ago and significant progress has been made since then. Although the theoretical predication of VCD of large molecules such as proteins is still a difficult task, the *ab initio* quantum chemical calculations applied to small to medium size molecules have become fast and reliable even on PC computers.[19-21] Such advancements have greatly enhanced the application of VCD as a tool to elucidate the structure, and especially the absolute configuration (AC), of chiral molecules.

The calculation of VCD intensity for a chiral molecule becomes routine with the availability of commercial software such as Gaussian 98/03.[22] The density functional theory (DFT) method provides electron correlation by including an exchange correlation that is a function of the electron density, thus implicitly accounting for electron correlation. Numerous studies have shown that density functional theory (DFT) with a hybrid functional such as B3LYP and a basis set of 6-31G(d) provides the best combination of spectral accuracy and calculation expense. The commercial software Gaussian 03 computes VCD spectra along with performing the geometry optimization, which is achieved at the same level as the calculation of the VCD spectrum, generating the molecular geometry at a stationary point on the potential energy surface. Once the optimized geometry is obtained, corresponding dipole strengths, rotational strengths and vibrational frequencies are calculated based on the magnetic field perturbation (MFP) theory. [23,24]

In this paper, we present the determination of the absolute configuration and conformation of amino acid **1** by VCD, along with DFT calculation. Since amino acid **1** is only soluble in water, experimental VCD was performed in aqueous solution. The DFT calculation was first carried out on zwitterionic form, in gas phase. The comparison between the calculated and experimental results were not in agreement. We further extended the DFT calculation with the polarizable continuum model and added explicit water molecules surrounding the amino acid **1**. It is demonstrated that this model provides dramatically more

accurate results, allowing for a better correlation between the experimental and calculated results and consequently for the determination of absolute configuration and solution conformation.

RESULTS AND DISCUSSION

To study the absolute configuration of amino acid **1**, we first performed the DFT calculations in gas phase with the assumption that the compound is not self-interacting and is in the neutral state. Indeed, the DFT calculation of the zwitterionic species led to a neutral structure, indicating that the stable form in gas phase is not the zwitterionic specie, but a neutral specie in which the carboxy group is a carboxyl and the amine is in the form of NH_2 (Fig. 1). The calculated VCD spectra and its comparison with the experimental results is presented in Fig. 2. All major VCD bands were labeled with numbers for clarity. The spectral region between 1700-1600 cm^{-1}, presents in the experimental spectra a (+,-,+) feature (band # 1, 1' and 2) (1674 cm^{-1}, 1662 cm^{-1} and 1627cm^{-1}, respectively).

The calculation, however, showed only two negative peaks in the same spectral region (band #1 and # 2) (1674 and 1627 cm^{-1}), corresponding to C=O stretching and $–NH_2$ bending modes, respectively. In the spectral region between 1600-1400 cm^{-1}, only band #3 was observed in both the experimental and calculated spectra. This band corresponds to the methylene vibration from the THF ring. Large discrepancies between the calculated and experimental spectra were observed in the region of 1400-1200 cm^{-1}. In particular, the bands # 4' and 4 display intense negative peaks in the calculated spectra, while the experimental spectra show very weak bands in this region. These two bands correspond to the vibrations of carboxylic –OH and $–NH_2$ respectively, coupled with THF ring.

In the region between 1200-1000 cm^{-1}, calculated VCD shows three positive peaks (bands #5, #6 and #7), with relative intensities quite different from the experimental spectra. For example, band #7 (corresponding to $-NH_2$ bending coupled with ring vibration) shows intense intensity in the calculated spectra, while in the experimental spectra, only broad bands are observed. Similar disagreements were observed when comparing experimental and calculated IR spectra. Under these circumstances, the absolute configuration of amino acid **1** cannot be accurately determined due to the discrepancies between the experimental and calculated spectra.

The broadening of the bands observed in the experimental spectra can be attributed to the interaction of water with the functional groups of the amino acid. As a consequence, the DFT simulation was performed introducing molecules of water in the calculation in this case. The method involves the use of a self-consistent reaction field (SCRF). Molecules of water were placed in an environment that had the same dielectric constant as the desired solvent. There are several types of SCRF which range in complexity from a single dielectric sphere around the whole molecule, to individual spheres around each atom of the molecule, which can each be polarized independently.

Gaussian 03 provides the functions for VCD calculation using the polarizable continuum model (PCM). [25-27] We used PCM to simulate the water solvent environment. In addition, three water molecules were placed at sites in which hydrogen bonding occurred (NH_2, COOH and ether oxygen).[28,29] It is preferable to use the minimum number of water molecules that can still produce agreement with the experimental data, because calculation times increase dramatically with the number of atoms in the molecule. Thus, water molecules were placed according to Fig. 3, and the calculation was pursued. Under these parameters the calculation approximates the experimental spectrum very well, in peak frequency as well as both relative and absolute intensity (Fig. 4). This calculation also showed a reduction of the VCD intensities of bands #4, #4' and #7, previously observed without water molecules docked to the amino acid. The addition of these three molecules of water, hydrogen bonded to the carboxyl, amino and ether oxygen, accounted for a better correlation between the experimental and the calculated spectrum.

In addition to the VCD results, the model with three explicit water molecules offers a significant improvement in the calculated IR spectra. This formation of the water bridges also affected the low intensity of these groups in the experimental VCD spectrum. From the close agreement between the experimental and calculated VCD spectra, the absolute configuration of amino acid **1** can be unambiguously assigned as (***S)-enantiomer***.

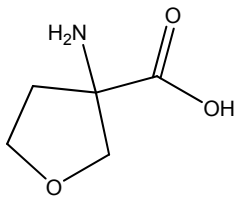

Scheme 1

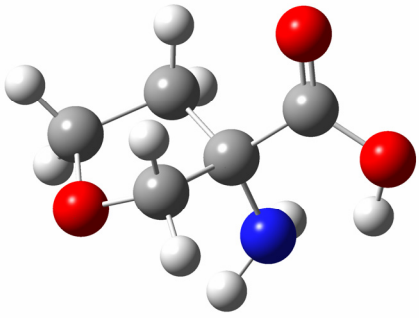

Figure 1. Structure of neutral form of amino acid 1

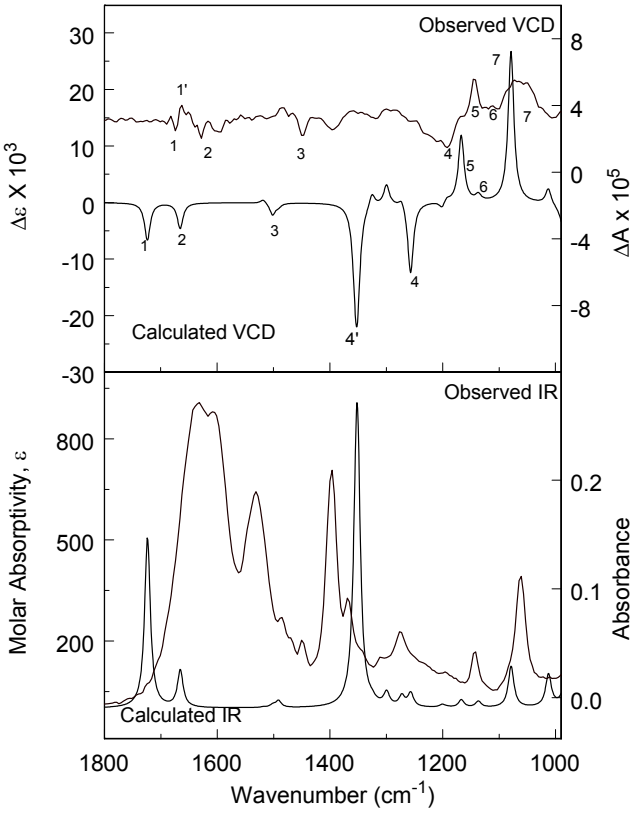

Figure 2. Comparison of calculated and experimental VCD and IR spectra of amino acid 1: calculation on neutral form.

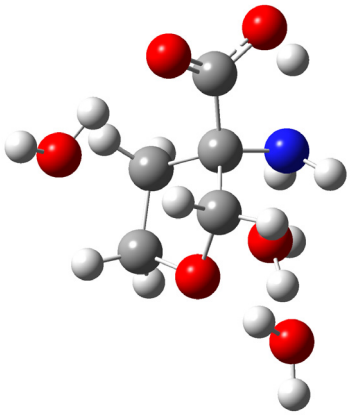

Figure 3. Structure of amino acid 1 with three explicit water molecules

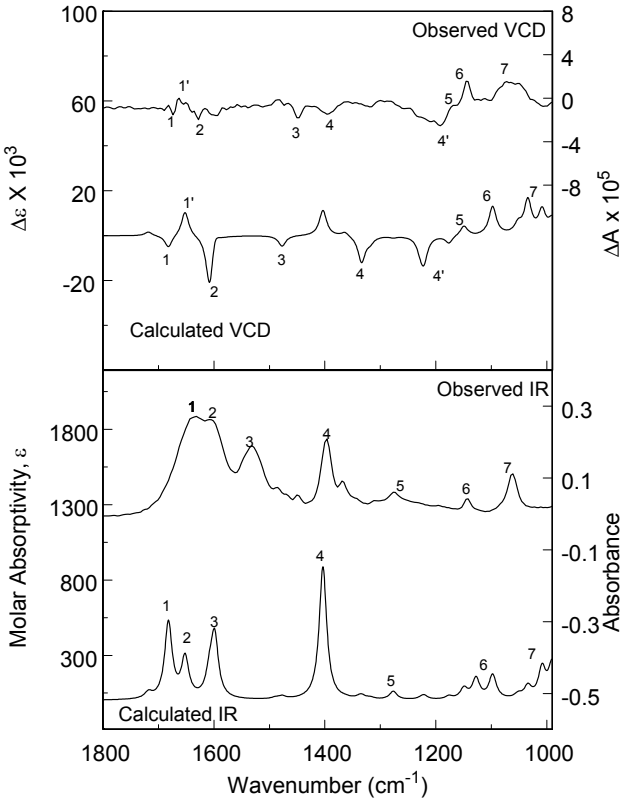

Figure 4. Comparison of calculated and experimental VCD and IR spectra of amino acid 1: calculation on PCM with three explicit water molecules surrounding amino acid 1.

CONCLUSIONS

The experimental and calculated VCD spectra of amino acid 1 are reported and the absolute configuration is determined. The PCM model with the addition of specific water molecules produces accurate VCD and IR calculated spectra for the amino acid. The model can be extended to other molecules such as peptides. This protocol presents a promising approach for the determination of the absolute configuration of amino acids in aqueous solution.

EXPERIMENTAL SECTION

The chiral amino acid was prepared from its butyl ester by hydrolysis in MeOH with NaOH, followed by purification on the column.[11,13]

To compute the structure of the amino acid, we used Hyperchem software (Hypercube, Inc., Gainesville, FL). All structural and spectroscopic calculations were performed using Gaussian 03. Structural optimizations were conducted under the polarizable continuum model (PCM) self-consistent reaction field (SCRF). Once a standard optimization was performed with PCM, the molecule was considered to be fully optimized. The VCD spectrum of the molecule was calculated in PCM, and this calculation was extended to find the VCD spectra of 1. Calculations were repeated for systems with zero or three explicit water molecules using B3LYP/6-31G(d) basis sets and functionals. Spectra were analyzed and compared. Mode assignments are based on the animation of vibrations in Gaussview 3.1.

All VCD measurements were performed on a ChiralIR spectrometer (BioTools, FL, USA). The amino acid was dissolved in H_2O solution at the concentration of 1.3 M. Spectra were collected for 4 hours in a 9 μm path length cell. The final VCD spectra were corrected by subtracting the corresponding solvent spectra (water) measured in the same conditions.

REFERENCES

1. R. Pfau, H. Priepke, K. Gerlach, W. Wienen, A. Schuler-Metz, H. Nar, S. Handschuh, in, (Boehringer Ingelheim International G.m.b.H., Germany; Boehringer Ingelheim Pharma G.m.b.H. & Co. K.-G.). Application: WO, **2005**, 268 pp.
2. T. Ziegler, D. Roseling, L.R. Subramanian, *Tetrahedron: Asymmetry,* **2002**, *13*, 911.
3. S.J. Zuend, M.P. Coughlin, M.P. Lalonde, E.N. Jacobsen, *Nature (London, U. K.)* **2009**, *461*, 968.
4. T.K. Chakraborty, S. Ghosh, S. Jayaprakash, *Curr. Med. Chem.,* **2002**, *9*, 421.
5. S. Kotha, *Acc. Chem. Res.,* **2003**, *36*, 342.
6. M.G. Natchus, X. Tian, *Org. Synth.: Theory Appl.,* **2001**, *5*, 89.
7. K. Plankensteiner, H. Reiner, B.M. Rode, *Curr. Org. Chem.,* **2005**, *9*, 1107.
8. F. Schweizer, *Angew. Chem., Int. Ed.,* **2002**, *41*, 230.
9. J. Yoneda, A. Andou, K. Takehana, *Curr. Rheumatol. Rev.,* **2009**, *5*, 252.
10. A. Grauer, A. Spaeth, D. Ma, B. Koenig, *Chem.--Asian J.,* **2009**, *4*, 1134.
11. Z. Han, K. Gerlach, D. Krishnamurthy, B. Matthes, H. Nar, H. Priepke, A. Schuler-Metz, C.H. Senanayake, P. Sieger, W. Tang, W. Wienen, Y. Xu, N.K. Yee, in, (Boehringer Ingelheim International G.m.b.H., Germany; Boehringer Ingelheim Pharma Gmbh & Co. K.-G.; Pfau, Roland), **2008**, WO 2008080891.
12. N. Hauel, A. Ceci, H. Doods, I. Konetzki, J. Mack, H. Priepke, A. Schuler-Metz, R. Walter, D. Wiedenmayer, in, (Boehringer Ingelheim International GmbH, Germany). 2010097372.
13. K. Lavrador, D. Guillerm, G. Guillerm, *Bioorg. Med. Chem. Lett.,* **1998**, *8*, 1629.

14. D.D. Long, M.D. Smith, A. Martin, J.R. Wheatley, D.G. Watkin, M. Mueller, G.W.J. Fleet, *J. Chem. Soc., Perkin Trans.,* **2002**, *1,* 1982.
15. D.M. Walker, E.W. Logusch, *Tetrahedron Lett.,* **1989**, *30*, 1181.
16. S. Ma, C.A. Busacca, K.R. Fandrick, T. Bartholomeyzik, N. Haddad, S. Shen, H. Lee, A. Saha, N. Yee, C. Senanayake, N. Grinberg, *Org. Lett.,* **2010**, *12*, 2782.
17. T.B. Freedman, X. Cao, R.K. Dukor, L.A. Nafie, *Chirality,* **2003**, *15*, 743.
18. P.J. Stephens, F.J. Devlin, J.-J. Pan, *Chirality,* **2008**, *20*, 643.
19. C.S. Ashvar, F.J. Devlin, K.L. Bak, P.R. Taylor, P.J. Stephens, *J. Phys. Chem.,* **1996**, *100*, 9262.
20. J.R. Cheeseman, M.J. Frisch, F.J. Devlin, P.J. Stephens, *Chem. Phys. Lett.,* **1996**, *252*, 211.
21. P.J. Stephens, C.S. Ashvar, F.J. Devlin, J.R. Cheeseman, M.J. Frisch, *Mol. Phys.,* **1996**, *89*, 579.
22. M. Frisch, in Gaussian 03, Revision B. 03, **2003**.
23. P.J. Stephens, *J. Phys. Chem.,* **1985**, *89*, 784.
24. P.J. Stephens, *J. Phys. Chem.,* **1987**, *91*, 1712.
25. F. Floris, M. Persico, A. Tani, J. Tomasi, *Chem. Phys. Lett.,* **1992**, *199*, 518.
26. S. Miertus, V. Frecer, M. Majekova, *J. Mol. Struct.: THEOCHEM,* **1988**, *48*, 353.
27. A.J. Duben, S. Miertus, *Chem. Phys. Lett.,* **1982**, *88*, 395.
28. E. Deplazes, W. van Bronswijk, F. Zhu, L.D. Barron, S. Ma, L.A. Nafie, K.J. Jalkanen, *Theor. Chem. Acc.,* **2008**, *119*, 155.
29. K.J. Jalkanen, I.M. Degtyarenko, R.M. Nieminen, X. Cao, L.A. Nafie, F. Zhu, L.D. Barron, *Theor. Chem. Acc.,* **2008**, *119*, 191.

STUDIA UBB CHEMIA, LVI, 1, 2011

INVESTIGATION OF INITIAL PEROXIDE INDEX VALUE INFLUENCE ON AFB1, AFB2, AFG2 AND T-2 MYCOTOXINS DECOMPOSITION IN SUNFLOWER OIL

PAUL ŞERBAN AGACHI[a], GOMBOS SÁNDOR[b]

ABSTRACT. In this paper, experiments were conducted to investigate mycotoxins homogenous photodegradation using various peroxide index (IP, caused by peroxides and hydroperoxides) in order to assess the efficiency of sunflower oil decontamination by ultravilolet light irradiation. Was studied the UV assisted peroxides activation, their contribution to decompose mycotoxins, to decrease their concentration. Was proposed a mathematical model of the process, model parameters were identified and adjusted with software environment. The photodegradation process efficiency increased differentiated using sunflower oil with higher peroxide indexes; there exist optimal values of peroxide index for each investigated mycotoxin. This way, the observed rate constants can be increased and the residual mycocotoxin concentration can be decreased. Using favorable peroxide index value in decontamination process provides an effective technology for the removal of mycotoxins from contaminated sunflower oil. The rapid degradation is related to the inherently contented peroxides transformation in reactive free radicals, this radicals reacting with mycotoxins. With the elaborated model is possible to predict the concentrations of residual mycotoxins in different operating conditions depending on initial peroxide index values.

Keywords: *Mycotoxins, Aflatoxin B1, Aflatoxin B2, Aflatoxin G2, T-2 toxin, photochemical degradation, ultraviolet light, sunflower oil, peroxide index, HPLC.*

INTRODUCTION

The term "mycotoxin" is usually reserved for toxic chemicals produced by fungi which commonly colonize crops [1]. Most plant parasitic fungi use oxygen and are found almost everywhere in small quantities, as a result of dispersion of spores. They metabolize organic substances, they develops where humidity and temperature are favorable. Species of fungi can produce different mycotoxins, and/or a mycotoxin may be produced by several species [2]. In 1971, Turner systematized 500 species of fungi and 1200 secondary metabolites. Hawksworth (1991) identified 69000 species of fungi, representing only 5% of all species, said the availability of the 1,5 million secondary metabolites.

[a] *Babeş-Bolyai University, Faculty of Chemistry and Chemical Engineering, 11. Arany Janos, RO-400028 Cluj-Napoca, Romania, sagachi@staff.ubbcluj.ro*
[b] *Sapientia University Cluj-Napoca, Faculty of Sciences Miercurea Ciuc, 1. Piata Libertatii, RO-530104 Miercurea Ciuc, Romania, gombossandor@sapientia.siculorum.ro*

Other assessments have evaluated approximately 100000 secondary metabolites. Mycotoxins can appear in the food chain as a result of fungal infection of crops, that are consumed by humans or used as animal feeds. Even at extreme temperatures of processing, such as by boiling or roasting in the preparation process of foods (100-200 °C), mycotoxins decompose very slowly. International Commission seeks to achieve regulatory universal limit standards for mycotoxins concentrations in foods. Currently over 100 countries have adopted regulations for mycotoxins, special attention are accorded to food industry, in which 13 groups of mycotoxins are reason of concern [3]. Based on chemical structure, mycotoxins can be classified in coumarin derivatives, malonates, mevalonates, acetates and unsaturated lactones [4].

Figure 1 shows the molecular formulas of the most important representatives of the family of mycotoxins.

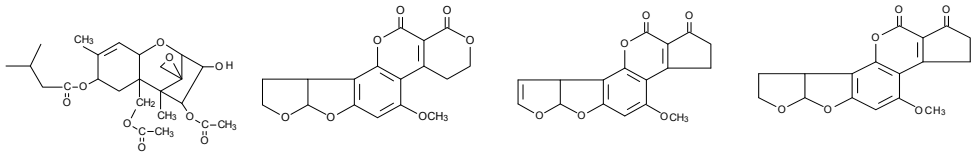

T-2 Toxin | Aflatoxin G2 | Aflatoxin B1 | Aflatoxin B2

Figure 1. Chemical structure of studied mycotoxins

Table 1 shows the molecular formulas, molar masses and melting temperatures of the investigated mycotoxins.

Table 1. Molecular formulas, molar masses and melting temperatures of the investigated mycotoxins

Mycotoxin	Molecular formula	Molar mass, g/mol	Melting temperature, (ºC)
AFB1	$C_{17}H_{12}O_6$	312	268-269
AFB2	$C_{17}H_{14}O_6$	314	286-289
AFG2	$C_{17}H_{14}O_7$	330	237-240
T-2	$C_{24}H_{34}O_9$	466	282

Mathematical model

The inactivation of mycotoxins by ultraviolet light involves two stages. In the first stage, the mycotoxins have to difuse to the radiation exposed area. If the mycotoxin molecule reaches a sufficiently small distance (λ) of surface irradiance, the photons are absorbed mainly by mycotoxins and peroxides, peroxide molecules generates free radicals, free radicals reacts with excited state mycotoxins, this way mycotoxins are inactivated. Distance λ is the penetration depth of radiation, where the photon flux is 10% of the initial flow at the surface radiation I_0.

Under UV decontamination process, unsaturated fatty acids specific autoxidation reactions not take place due to lack of contact with atmospheric oxygen and dissolved oxygen in sunflower oil, preliminary was removed the dissolved oxygen by vacuum degassing. Instead, must cosider hydroperoxides and peroxides which are inherently present in sunflower oil due to storage and manufacturing process steps and the peroxides and hydroperoxides possible decomposition reactions by the action of UV radiation.

Parameters and refining stages can decisively influence the effectiveness of UV treatment (UV absorbance, peroxide index). The peroxide index is usually expressed in meq/kg, also the peroxide index can be expressed in SI units as milimoles per kilogram. The value expressed in milimoles/kg is half of that expressed in meq/kg. The method is based on the properties of peroxides and hydroperoxides to free molecular iodine in the acidic environment from potassium iodide. Released iodine is very reactive and can be linked by double bonds of unsaturated fatty acids, which will lead to an error in determining the peroxide index. To block this reaction is carried out in chloroform and glacial acetic acid (2:1). High acidity environment determinine virtually blocking of the double bonds of unsaturated fatty acids. According to Daneshvar et al. studies [5], high concentrations of peroxides can lead reactions between peroxides and generated free radicals, decreasing the decontamination capacity. Therefore, high concentrations of peroxides and hydroperoxides does not offer benefits, on the other hand are not even allowed in the finished product (CMA 3.0 mEq/kg). 253,7 nm wavelength is most effective in terms of excitation of mycotoxins, since photons are efficiently absorbed by mycotoxins at this specific wavelength. UV light with wavelengths below 230 nm is most effective for the dissociation of peroxides and hydroperoxides [6].

In limited area of concentrations of investigated mycotoxins can be performed the degradation kinetics linearization, especially if it seeks to minimize changes of essential fatty acids, which logically require a relatively short irradiation times. We can write the equation:

$$-\frac{d[MT]}{dt} = k_{apMT}[MT] \tag{1}$$

For each mycotoxin, $[MT]$ represent the actual concentration of mycotoxin, k_{apMT} is the pseudo-first order transformation constant, *t* is the time of irradiation [7]. According to the analytical determinations carried out, peroxides and hydroperoxides (which concentrations are expressed by peroxide index) decomposes under the action of UV radiation, their decomposition generating free radicals that contribute to the degradation of mycotoxins. The relation between k_{apMT} and peroxide index (*IP*) can be modeled by linear regression. The model can be defined by considering ineffective the inhibitory

reactions caused by the direct irradiation of the mycotoxins. This account is very plausible, because in an inert environment, even if mycotoxins are irradiated, they decomposing just very slowly. In conclusion, k_{apMT} can be expressed as:

$$k_{apMT} = \frac{a\left[IP\right]_0 / \left[MT\right]_0}{1 + b(\left[IP\right]_0 / \left[MT\right]_0) + c(\left[IP\right]_0 / \left[MT\right]_0)^2} \quad (2)$$

where k_{apMT} is the dependent variable, *a*, *b* and *c* are model parameters, and $\left[IP\right]_0$ is the initial peroxide index value is the reaction mass. The calculated values of Reynolds criteria for the flow regimes clearly indicate the laminar flow in the UV reactor. Therefore, it might be considered as operating with an ideal tubular reactor [8]. For a PFR (tubular) reactor, the equation that describes the operation can be described as follows:

$$-\frac{d\left[MT\right]}{dV} = -\frac{r_{MT}}{\nu_0}, \quad (3)$$

$$\text{where } V = \frac{\pi}{4}\left(d_0^2 - d_i^2\right)l \text{, and } -r_{AMT} = -\frac{d\left[MT\right]}{dt} \quad (4)$$

In previous relations *V*, ν_0 ,d_0, d_i and *l* are the volume, volume flow, inner diameter, outer diameter and the length of photochemical reactor [9].

From the last two equations we get:

$$-\frac{d\left[MT\right]}{dl} = \frac{\pi / 4\left(d_0^2 - d_i^2\right)}{\nu_0}\left(-\frac{d\left[MT\right]}{dt}\right) \quad (5)$$

With the additional use of previous equations, the obtained model is:

$$-\frac{d\left[MT\right]}{dl} = \frac{\pi / 4\left(d_0^2 - d_i^2\right)}{\nu_0}\left(\frac{a\left[IP\right]_0 / \left[MT\right]_0}{1 + b(\left[IP\right]_0 / \left[MT\right]_0) + c(\left[IP\right]_0 / \left[MT\right]_0)^2}\right)\left[MT\right] \quad (6)$$

EXPERIMENTAL SECTION

Materials

AFB1, AFB2, AFG2 and T-2 toxin standards were purchased from Makor Chemicals Ltd. (Jerusalem, Israel), sunflower oil was purchased from SC Expur SA, methanol (HPLC grade) was purchased from Sigma-Aldrich (Redox Lab Supplies Com SRL), and carbon dioxide was purchased from Linde Gaz România SRL.

Reactor system

The degradation experiments were conducted in reactor system, 100 ml plug-flow photoreactor was serial connected with a jacketed vessel, used for temperature control and stirring. The scheme of the used experimental treatment system is presented in figure 2.

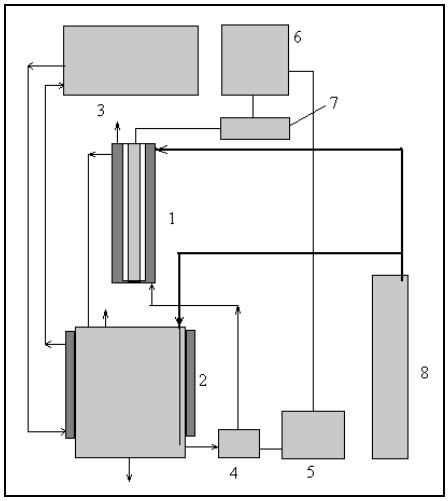

Figure 2. The used experimental system

1- PFR photoreactor;
2- storage vessel;
3- ultrathermostat;
4- adjustable flow pump;
5- pump control unit;
6- stabilized power supply;
7- UV power source control unit;
8- CO_2 cylinder.

In the UV activation experiment, a 20 W Philips-LPMHO (Low Pressure Mercury High Output) was used as the light source. UV source measured emission power was 29,8 mW/cm^2 at 5 cm distance, volume flow was 185 ml/min, system temperature was 20 °C. All experiments were carried out in same conditions. Carbon dioxide gas adding was used to remove of atmospheric oxygen.

Analysis

The degradation of mycotoxins was monitored by HPLC. The reaction mass samples were processed using Hettich Micro 20 centrifuge (13000 rot/min, 5 minutes), was split the higher density oil phase, which was pipetted into

an extraction bottle, it was determined the mass, after this was performed methanol extraction of mycotoxins in 8 steps, obtained mixtures were separated with Hettich Universal 32 centrifuge (3400rot./min, 5 minutes), alcoholic liquid phases were pipetted and unified. Since resulted alcoholic mixtures were cloudy, a new set of centrifugations were carried out to realise the perfect separation. Obtained methanolic extracts were subjected to evaporation, and portions of extracts was injected in Varian Pro Star HPLC, using fluorescent and UV detector, Supelcosil LC 18 column, flow rate was 0,9 ml/min, without derivatization. HPLC equipment was controlled with Varian Star Chromatography Workstation Version 6.00 software. The eluent was water-methanol-acetonitrile mixture, with 130:70:40 ratio. Fluorescence detector was set for excitation at 365 nm, and the emission at 435 nm. Based on HPLC chromatograms provided by the HPLC, we can evaluate the concentration of MT in the samples, which is proportional to the area under the signal curve offered by that component.On the basis of changes in decreasing concentrations of mycotoxins, taking into account the fact that the concentration of mycotoxins is much smaller than the concentration of peroxidies who are sensitive to UV irradiation, as previously we found a 12-27% reduction in the amount of IP in the time of UV treatment, we assumed that the determining factor of decomposition speed may be the initial peroxide (IP_0) of sunflower oil under photochemical decontamination.

Because IP_0 have determinant influence on the kinetics of photo-degradation process, we performed a series of experimental determinations with contaminated sunflower oil, starting with different initial concentrations of peroxides, peroxide index, respectively. Initial, the sunflower oil IP value was IP_0 = 0,89 and for the next experimental determinations became necessary preparation of sunflower oil with higher IP values. To this, in sunflower oil was introduced dry air until was reached a higher peroxide index, after that was applied preparation of mixtures between the original sunflower oil and artificially increased IP oil [10], were prepared samples with required peroxide indexes (1-10) for further determinations.

RESULTS AND DISCUSSION

Variations of mycotoxins HPLC areas (A_{MT}) by the starting IP (IP_0) are shown in table 2, mycotoxins concentrations variation (dc_{AFB1}, dc_{AFB2}) and apparent photodegradation constant variation (k_{apAFB1}, k_{apAFB2}) according on ratio between initial peroxide index value (IP_0) and initial mycotoxin concentration ($[MT]_0$) are shown in table 3 and 4.

Variations in concentrations ($c/c_{0\ MT}$) of the studied mycotoxins by the starting IP (IP_0) of the reaction mass (with equal times of irradiation) are shown in figure 3.

Table 2. Variations of mycotoxins HPLC areas (A_{MT}) according on initial peroxide index (IP_0) of sunflower oil

IP_0	A_{AFB1}	A_{AFB2}	A_{AFG2}	A_{T2}
1	147994	96304	98251	132562.00
2	146805	95859	97528	131734.00
3	145794	95347	96734	130763.00
4	144758	94985	96045	130095.00
5	142894	94438	95264	129264.00
6	141634	93985	94467	128321.00
7	140421	93589	93793	127563.00
8	139452	93245	93049	126635.00
9	138253	92675	92330	125865.00
10	137045	92236	91524	125058.00

Table 3. AFB1, AFB2 concentrations variation (c_{AFB1}, c_{AFB2}) according on ratio between initial peroxide index value (IP_0) and initial mycotoxin concentration ($[MT]_0$)

c_{AFB1}	c_{AFB2}	$IP_0/[MT]_0$
2.00000	2.00000	0.5
1.98393	1.99076	1.0
1.97027	1.98013	1.5
1.95627	1.97261	2.0
1.93108	1.96125	2.5
1.91405	1.95184	3.0
1.89766	1.94362	3.5
1.88456	1.93647	4.0
1.86836	1.92463	4.5
1.85203	1.91552	5.0

Table 4. AFG2, T-2 concentrations variation (c_{AFB1}, c_{AFB2}) according on ratio between initial peroxide index value (IP_0) and initial mycotoxin concentration ($[MT]_0$)

c_{AFG2}	c_{T2}	$IP_0/[MT]_0$
2.00000	2.00000	0.5
1.98528	1.98751	1.0
1.96912	1.97286	1.5
1.95509	1.96278	2.0
1.93920	1.95024	2.5
1.92297	1.93601	3.0
1.90925	1.92458	3.5
1.89411	1.91058	4.0
1.87947	1.89896	4.5
1.86307	1.88679	5.0

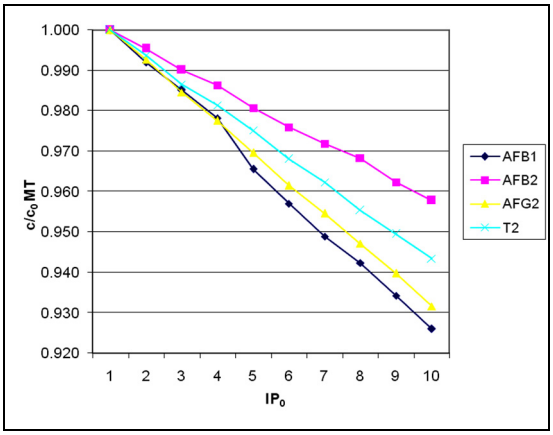

Figure 3. Variations of relative concentrations of MT (c/c_{0MT}) depending on the initial IP value of reaction mass (IP_0)

Variations of the mycotoxins (AFB1, AFB2, AFG2 and T-2) concentrations (dc_{MT}) depending on the ratio between initial peroxide index and initial mycotoxin concentration ($IP_0/[MT]_0$) are presented in figure 4.

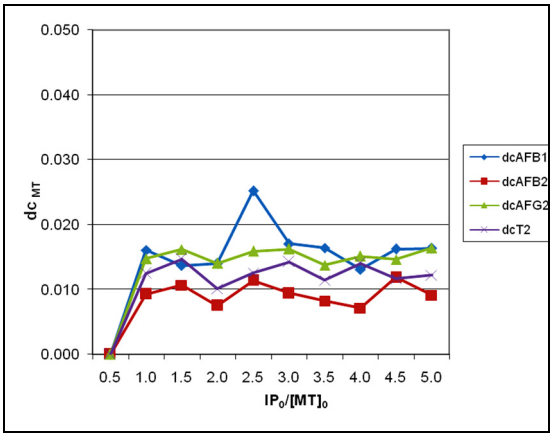

Figure 4. Variations of AFB1, AFB2, AFG2 and T-2 concentrations (dc_{MT}) depending on the ratio between initial peroxide index and initial mycotoxin concentration ($IP_0/[MT]_0$)

Variations of the studied MT photodegradation apparent coefficients (k_{apAFB1}, k_{apAFB2}, k_{apAFG2} and k_{apT2}) depending on the initial peroxide index of the reaction mass (IP_0) are presented in figure 5.

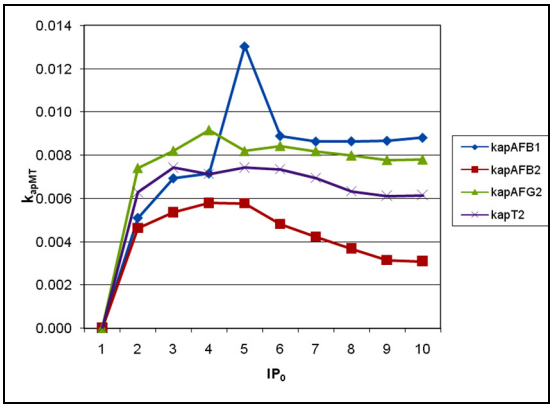

Figure 5. Variations of the studied MT photodegradation apparent coefficients (k_{apAFB1}, k_{apAFB2}, k_{apAFG2} and k_{apT2}) depending on the initial peroxide index of the reaction mass (IP_0)

To obtain the individual kinetic parameters for MT, we adjusted the experimental data to the proposed model by Polymath software environment. Using the model equation, the parameters of individual models with 95% confidence level and using the sum of the squares error method (SSE) as a function of error were obtained by nonlinear regression; results are presented in Figures 6, 7, 8 and 9.

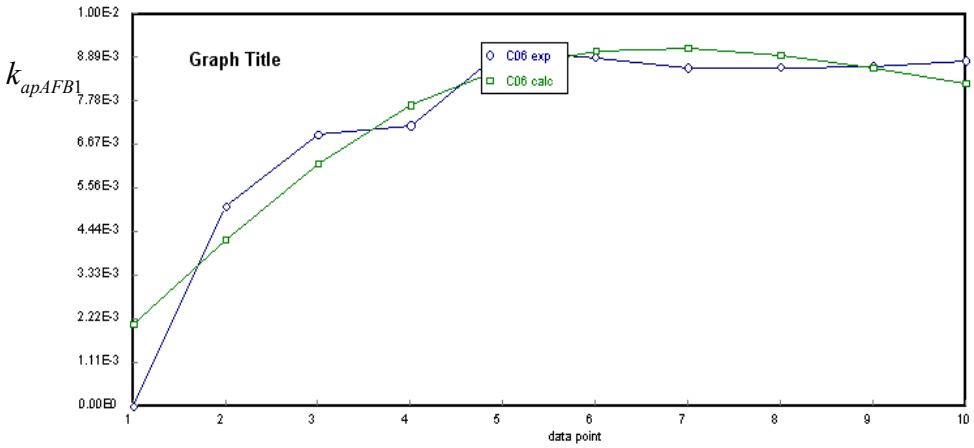

Figure 6. AFB1 experimental data adjustment

k_{apAFB2}

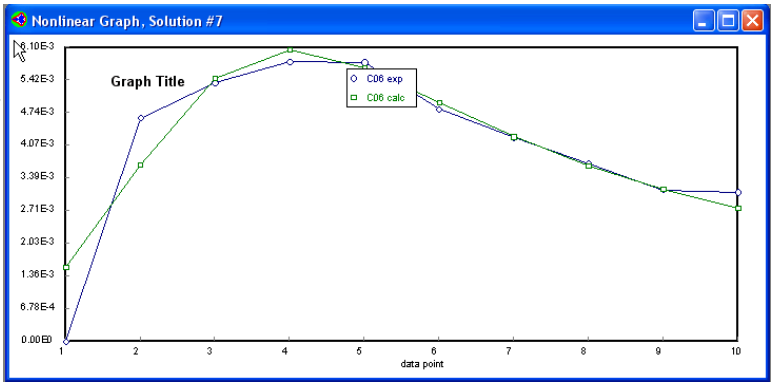

Figure 7. AFB2 experimental data adjustment

k_{apAFG2}

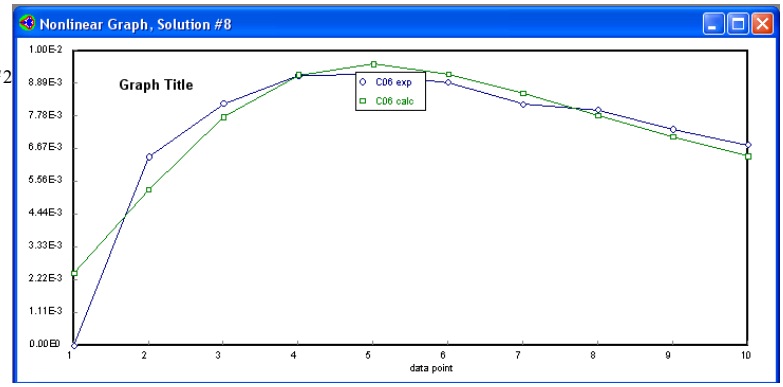

Figure 8. AFG2 experimental data adjustment

k_{apT-2}

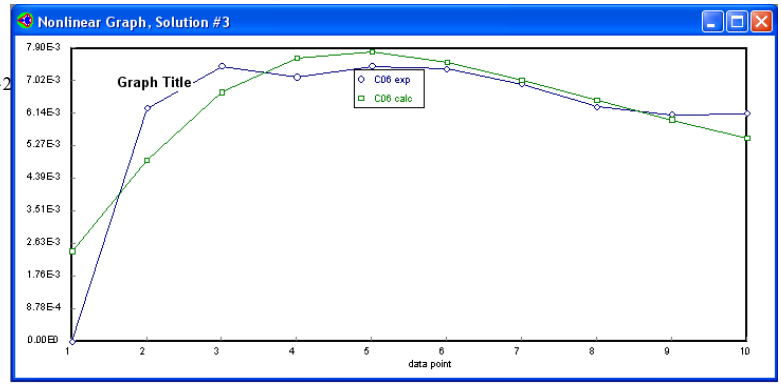

Figure 9. T-2 experimental data adjustment

Values obtained by regression of the parameters *a*, *b* and *c* is presented in Table 5.

Table 5. Values obtained by regression of the model parameters for the MT photodegradation

Parameter	AFB1	AFB2	AFG2	T-2
a	0,0029	0,0155	0,0028	0,0030
b	0,4489	0,2642	0,3454	0,4407
c	0,0498	0,0808	0,0562	0,0820

RESULTS AND DISCUSSION

On the basis of changes in decreasing concentrations of mycotoxins, taking into account the fact that the concentration of mycotoxins is much smaller than the concentration of peroxidies who are sensitive to UV irradiation, as previously we found a 12-27% reduction in the amount of IP in the time of UV treatment, we assumed that the determining factor of decomposition speed may be the initial peroxide (IP_0) of sunflower oil under photochemical decontamination. Because IP_0 have determinant influence on the kinetics of photodegradation process, we performed a series of experimental determinations with contaminated sunflower oil, starting with different initial concentrations of peroxides, peroxide index, respectively. Initial, the sunflower oil IP value was IP_0 = 0,89 and for the next experimental determinations became necessary preparation of sunflower oil with higher IP values. To this, in sunflower oil was introduced dry air until was reached a higher peroxide index, after that was applied preparation of mixtures between the original sunflower oil and artificially increased IP oil, were prepared samples with required peroxide indexes (1-10) for further determinations.

CONCLUSIONS

The proposed model for prediction of AFB1 photodegradation has a maximum for k_{apAFB1} at around 3,0 for the $[IP]_0 / [AFB1]_0$ ratio, which is in good agreement with experimental data obtained for AFB1, which resulted for k_{apAFB1} a 2,5 value of the ratio. The proposed model for prediction of AFB2 photodegradation has a maximum for k_{apAFB2} at around 2,5 for the $[IP]_0 / [AFB2]_0$ ratio, which is in good agreement with experimental data obtained for AFB2, which resulted for k_{apAFB2} a 2,0 value of the ratio. The proposed model for

prediction of AFG2 photodegradation has a maximum for k_{apAFG2} at around 2,5 for the $[IP]_0 / [AFG2]_0$ ratio, which is in good agreement with experimental data obtained for AFG2, where resulted for k_{apAFG2} a 2,0 value of the ratio. The proposed model for prediction of T-2 photodegradation has a maximum for k_{apT-2} at around 3,0 for the $[IP]_0 / [T-2]_0$ ratio, which is in good agreement with experimental data obtained for T-2, where resulted for k_{apT-2} a 2,5 value of the ratio.

The constructed models are useful to estimate the initial IP demand (IP_0) for the efficient photochemical degradation of mycotoxins in each case. On the other hand, it becomes obvious need for the sunflower oil refining such that when performing decontamination of mycotoxins, to achieve the photodegradation with low UV doses, must have IP_0 values between certain limits, depending on the nature of the present mycotoxins.

The necessary IP_0 values for decontamination at the same time require restrictions on storage conditions and storage period of sunflower seeds in silos.

After substituting the appropriate values of *a*, *b* and *c* for each mycotoxin, using d_0 and d_i, we can be obtain the mycotoxins concentrations at different lengths of the photoreactor, starting from initial concentrations of mycotoxins and from the initial value of IP, for different flow speeds through the fotoreactor. As we can see, it is possible to predict the concentrations of mycotoxins in different operating conditions depending on IP_0.

Based on obtained experimental data, on the four investigated molecular species of mycotoxins, under identical conditions, by comparing obtained data, we may notice some differences and similarities in the photochemical behavior of these mycotoxins. Highest sensitivity to the effect of peroxides and hydroperoxides decay occurs in case of AFB1, followed by T-2 toxin, AFB2, and finally, AFB1 showing the lowest sensitivity to peroxide index increase (at usual values), and at the same time it can be observed the existence for AFB1 of a favorable IP_0 for photodegradation process, which may be in correspondence with the behavior of other chemical species which are present in the matrix of sunflower oil.

ACKNOWLEDGMENTS

The authors are indebted to the referee for some critical suggestions leaded us to correct our main result. This work was partially supported by the Sapientia University Cluj-Napoca, Faculty of Sciences Miercurea Ciuc.

REFERENCES

1. N.W. Turner, S. Subrahmanyam, S.A. Piletsky, *Anal. Chim. Acta*, **2009**, *632-2*, 168-80.
2. C.A. Robbins, L.J. Swenson, M.L. Nealley, R.E. Gots, B.J. Kelman, *Applied Occupational and Environmental Hygiene*, **2000**, *15*, 773.
3. H.P. van Egmond, R.C. Schothorst, M.A. Jonker, *Anal Bioanal Chem*, **2007**, *389 (1)*, 147.
4. K. Gasztonyi, R. Lásztity, "Chimie alimentară", Ed. Mezőgazda, Budapesta, **1992**.
5. N. Daneshvar, M. Rabbani, N. Modirshahla, M.A. Behnajady, *J. Hazard. Mater.* **2005**, *118*, 155.
6. S. Clarke, W. Bettin, *Army Center for Health Promotion and Preventive Medicine*, **2006**, *31-006-0206*, 15, Aberdeen Proving Ground, MD.
7. S. Gombos, A. Szép, *15th International Conference of Chemistry*, **2009**, Tîrgu Mures, 21-22.
8. Z. Ye, "UV disinfection between concentric cylinders", **2007**, PhD Thesis, Georgia Institute of Technology.
9. J.R. Bolton, K.G. Linden, *J. Environ. Eng.*, **2003**, *129*, 209.

STUDIA UBB CHEMIA, LVI, 1, 2011

PRELIMINARY INVESTIGATIONS ON CLINOPTILOLITE USAGE AS SELECTIVE ADSORBENT FOR WASTEWATER ANALYSIS

CLAUDIA CIMPOIU[a,*], ANDRADA MĂICĂNEANU[a], ANAMARIA HOSU[a], HOREA BEDELEAN[b]

ABSTRACT. This work presents some preliminary studies regarding natural zeolite, namely clinoptilolite (from volcanic zeolitic tuff) as selective adsorbent. This material was used to separate organic isomers of industrial interest (dichlorobenzenes, dinitrobenzenes, chloronitrobenzenes). The quality of the separations achieved were sufficiently encouraging as to promote further investigations of its potential as selective adsorbent both for bulk liquid separations and in analytical applications. These preliminary results showed that good chromatographic resolutions were obtained - $R_{S,o,p\text{-}DCB}$=3.53; $R_{S,o,p\text{-}DNB}$=3.09 and $R_{S,o,p\text{-}CNB}$=4.25 and seem to be very promising in order to use this natural zeolite as selective adsorbent in different applications.

Keywords: *natural zeolite*, *clinoptilolite, selective adsorbent, dichlorobenzenes, dinitrobenzenes, chloronitrobenzene*

INTRODUCTION

Zeolites are a group of hydrated aluminosilicates of the alkali or alkaline earth metals (sodium, potassium, magnesium, calcium), with a three-dimensional crystalline framework. Zeolite structure has a special characteristic, the alumino-silicate framework, which is formed from $[SiO_4]^{4-}$ and $[AlO_4]^{5-}$ tetrahedra, where each of the oxygen atoms belong to two neighboring tetrahedral (bonding oxygens), with the exception of those situated in the exterior of the crystal. While each $[SiO_4]^{4-}$ tetrahedra is charged neutral, each $[AlO_4]^{5-}$ tetrahedra contain an extra negative charge. This excess charge is compensated by cations, such as Na^+, K^+, Ca^{2+}, Mg^{2+}, which will be placed in the framework gaps, coordinated by a defined number of water molecules. Silica and alumina tetrahedras are bonded in rings, therefore the zeolite structure will contain channel and pores with diameters between 3 and 10 Å. These channels (gaps) are filled with cations and water molecules with a higher or lower mobility, depending on the intensity of the bonds which are linked to the residual valence of the alumina tetrahedra.

[a] *Universitatea Babeş-Bolyai, Facultatea de Chimie şi Inginerie Chimică, Str. Kogălniceanu, Nr. 1, RO-400084 Cluj-Napoca,Romania, * ccimpoiu@chem.ubbcluj.ro*

[b] *Universitatea Babeş-Bolyai, Facultatea de Biologie şi Geologie, Str. Kogălniceanu, Nr. 1, RO-400084 Cluj-Napoca, Romania*

The main consequence of this structure type is represented by the reversibility of hydration and cation exchange processes that preserve the original network. These channels also allow easy movement (after removal of the zeolitic water) of different molecules depending on their size. Molecules with a diameter smaller that the channel diameter will be retained inside the zeolite framework, while higher molecules will remain in the exterior. Due to this type of selectivity towards the components of a mixture (molecule size, channel diameter), zeolites are also called molecular sieves. The existence of a negative charge in the alumina tetraedra, allows also the uses of zeolites as acid-basic catalysts. In hydrated conditions, on the surface of the zeolite Brönsted centers are formed due to the water adsorption on Al^{3+} site, while upon dehydration the same site became a Lewis center [1].

Natural zeolites are important aluminosilicates in sorption processes [2,3] because of their low cost and selectivity. In environmental applications, natural zeolites have been studied extensively to remove harmful substances from wastewater by adsorption and ion exchange processes [4,5].

The sedimentary zeolitic rocks from Romania are represented by volcanic tuffs of Neogene age. The main zeolite present in these rocks is clinoptilolite.

Clinoptilolite is a natural occurring zeolite, a hydrated aluminosillicate member of the heulandite group. Heulandite group zeolites, including mineral clinoptilolite and heulandite and their synthetic analogues, have the same framework topology (structure code HEU) characterized by infinite three-dimensional frameworks of aluminium, silicon and oxygen. The distinction between the clinoptilolite and the heulandite is based on the Si/Al ratio, i.e., clinoptilolite if Si/Al > 4 and heulandite if Si/Al < 4 [6]. The chemistry of these two species varies almost continuously between [7]:

$$(Na, K, Ca_{0,5})_{10}(Al_{10}Si_{26}O_{72})\cdot 24H_2O \quad \text{(heulandite, Si:Al=2,6)}$$

$$(Na, K, Ca_{0,5})_{5,4}(Al_{5,4}Si_{30,6}O_{72})\cdot 20H_2O \quad \text{(clinoptilolite, Si:Al=5,7)}$$

Clinoptilolite was used as adsorbent in many applications, namely: as solid-phase material for removal of some radionuclides from low-level radioactive liquid waste [8], as a novel drug carrier for the flavonoid aglycone constituents [9] and antibiotics [10], as adsorbent for low concentration of lindane and aldrin removal from wastewater [11], as cation exchanger [12], as catalyst in the estherification of glycerol with oleic acid [13] etc.

The aim of this paper was to investigate the potential of a natural zeolite, clinoptilolite (from volcanic zeolitic tuff) as selective adsorbent. A variety of aromatic isomeric structures found in wastewaters, such as dichlorobenzenes, dinitrobenzenes and chloronitrobenzene were chosen for this study.

RESULTS AND DISCUSSION

Prior chemical and mineralogical investigations realised on the zeolitic volcanic tuff samples collected from the same area, showed that: tuff samples contain high quantity of secondary and hydrated material (zeolite and probably smectitic clay minerals) as indicated by the high values of loss of ignition (L.O.I.) determined by bulk chemical analyses; tuff samples have a vitric and vitric crystal texture and are zeolitized and they consist of 60-70% of volcanic glass, 10-25% of crystals and lithic fragments in subordinate amounts (2-3%); the zeolites are present mainly as tabular clinoptilolite; the zeolite content reached values between 70% and 80% from the crystallized fractions of the tuff (semi-quantitative estimation from the X-ray diffraction patterns); FTIR spectra indicates presence of specific zeolite peaks; specific surface area (BET) is around 35 m^2/g [1,14].

Chromatographic separation

Dichlorobenzenes (DCBs), dinitrobenzenes (DNBs) and chloronitrobenzene (CNBs) are important organic intermediates which are extensively used in the production of dyes, pesticides, pharmaceuticals and rubber chemicals. In the viewpoint of clean technology, the recovery of valuable chemicals from the wastewaters is superior to the treatment of wastewater using degradation techniques. Based on high toxicity and stability of DCBs, DNBs and CNBs, they are resistant to biodegradation. The application of polymeric adsorbents in the recovery of DCBs, DNBs and CNBs from the wastewaters is limited because the recovered chemicals mainly consist of a mixture of isomers, and further purification by distillation or/and crystallization is necessary to obtain pure compounds. Therefore, the exploration and utilization of selective adsorbents is highly desirable to directly recover chemicals in high purity from wastewaters.

The optimum separation of *o- and p-DCB* was performed using heptane mixed with 0.1% ethanol as mobile phase (Figure 1a). The retention volumes were $V_{R,o\text{-DCB}}$ = 0.24 mL and $V_{R,p\text{-DCB}}$ = 0.59 mL. These results showed that the 1,4 isomer was more strongly adsorbed on stationary phase than 1,2 isomer. The order of elution was preliminary determined using standard solution of each isomer.

The *o- and p-DNB* were best separated by elution with heptane mixed with 1% ethanol (Figure 1b). In this case the retention parameters were: $V_{R,p\text{-DNB}}$ = 0.15 mL and $V_{R,o\text{-DNB}}$ = 0.57 mL. Introduction of the nitro-groups constituted an increase in polarity and it necessitated an increase in mobile phase polarity. The *o*-DNB was most preferred isomer, clinoptilolite having reverse order of elution, compared to DCBs and CNBs.

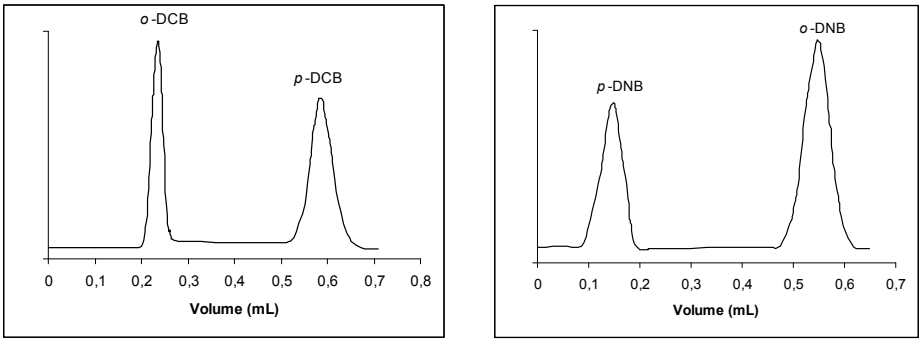

a b

Figure 1. Separation of: a) DCBs using 0.1% ethanol in heptane as eluent and b) DNBs using 1% ethanol in heptane as eluent.

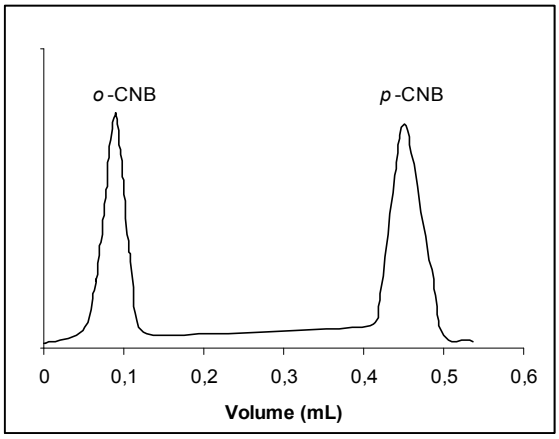

Figure 2. Separation of CNB isomers using heptane as eluent.

The following retention volumes were obtained for the o- and p-CNB using heptane as mobile phase: $V_{R,o\text{-CNB}}$ = 0.09 mL and $V_{R,p\text{-CNB}}$ = 0.48 mL. Elution order was the same as with DCBs compounds, *p*-isomer being the most strongly bounded (Figure 3).

From these preliminary experimental data it could be observed that good chromatographic resolutions were obtained: $R_{S,o,p\text{-DCB}}$=3.53; $R_{S,o,p\text{-DNB}}$=3.09 and $R_{S,o,p\text{-CNB}}$=4.25. These results seem to be very promising in order to use this adsorbent as stationary phase in liquid chromatography.

In order to completely establish the potential of natural zeolite as stationary phase in liquid chromatography further investigation such as: studies of the retention mechanism and the reproducibility of the retention parameters and comparison with other stationary phases are required.

CONCLUSIONS

The separations of DCBs, DNBs and CNBs previously observed on synthetic zeolites are confirmed here [15]. The purpose of the work reported here was to make a broadly based study of natural zeolite to assess its potential to perform bulk separations of important organic molecules. Liquid chromatography was chosen as a convenient approach, and also raised the possibility that the clinoptilolite could find use as stationary phases for this analytical technique.

The results will need further study if a detailed understanding of all the factors involved in the separations is to be attained. The zeolitic tuff presented mainly as tabular clinoptilolite, is a natural zeolite with a great potential for use as stationary phase in liquid chromatography. Moreover, the quality of the separations achieved were sufficiently encouraging as to promote further investigations of its potential as solid phases both for bulk liquid separations and in analytical applications.

In order to completely establish the potential of natural zeolite as stationary phase in liquid chromatography further investigation such as: studies of the retention mechanism and the reproducibility of the retention parameters and comparison with other stationary phases are required.

EXPERIMENTAL SECTION

The chromatographic separations were performed on a 20 cm glass column with internal diameter of 5 mm filled with clinoptilolite, laboratory made. The zeolitic volcanic tuff representative sample was collected from Măcicaş (M) quarry (Cluj County, Romania). In order to use this material as a stationary phase, the zeolitic volcanic tuff sample was subjected to a physical treatment (crushing, grinding, size separation) in order to obtain clinoptilolite samples with a grain diameter smaller than 0.2 mm.

Chromatographic analyses were optimised by using a series of mobile phases (heptane 100%, heptane mixed with 0.1% and 1% ethanol). The isomers used were from the purest materials available and injected first as individual standard, and then were injected simultaneously, as mixtures, onto the columns as 25 μL stock solution, using an automatic pipette. Standard stock solutions containing 0.1 mg/mL of *o*- and *p*-DCB, *o*- and *p*-DNB and *o*- and *p*-CNB were prepared in absolute ethanol. The compound separations were monitoring using TLC and UV detection at 254nm. For this purpose, equal fractions of the effluent were collected and then, spots from 0.03mL to 0.03mL were applied on the chromatographic plate and were examined under UV light. The intensity of the spots colour was examined and the spots area was determined using ImageJ software.

REFERENCES

1. A. Măicăneanu, H. Bedelean, M. Stanca, "Zeoliții naturali. Caracterizare şi aplicații în protecția mediului", Editura Presa Universitară Clujeană, Cluj-Napoca, **2008**, chapter 1-3.
2. V. Arambula-Villazana, M. Solache-Rios, M.T. Olguin, *Journal of Inclusion Phenomena and Macrocyclic Chemistry*, **2006**, *55*, 237.
3. M.R. El-Naggar, A.M. El-Kamash, M.I. El-Dessouky, A.K. Ghonaim, *Journal of Hazardous Materials*, **2008**, *154*, 963.
4. A. Abusafa, H. Yucel, *Journal of Separation and Purification Technology*, **2002**, *28*, 103.
5. P. Chutia, S. Kato, T. Kojima, S. Satokawa, *Journal of Hazardous Materials,* **2009**, *162*, 204.
6. D.S. Coombs, A. Alberti, T. Armbruster, G. Artioli, C. Colella, E. Galli, J.D. Grice, F. Liebau, J.A. Mandarino, H. Minato, E.H. Nickel, E. Passaglia, D.R. Peacor, S. Quartieri, R. Rinaldi, M. Ross, R.A. Sheppard, E. Tillmanns, G, Vezzalini, *Mineralogical Magazine*, **1998**, *35*, 1571.
7. D.L. Bish, J.M. Boak, "Clinoptilolite-Heulandite nomenclature", in: D.L. Bish, D.W. Ming (Eds.), Reviews in Mineralogy and Geochemistry, Natural Zeolites, Occurrence, Properties, Applications, **2001**, *45,* 207.
8. E.H. Borai, R. Harjula, L. Malinen, A. Paajanen, *Journal of Hazardous Materials*, **2009**, *172*, 416.
9. S. Göktaş, S. Ülkü, O. Bayraktar, *Applied Clay Science*, **2008**, *40*, 6.
10. G. Cerri, M. de Gennaro**,** M.C. Bonferoni, C. Caramella, *Applied Clay Science*, **2004**, *27*, 141.
11. M. Sprynskyy, T. Ligor, B. Buszewski**,** *Journal of Hazardous Materials*, **2008**, *151*, 570.
12. S. Hajialigol, M.A. Taher, A. Malekpour, *Adsorpion Science and Technology*, **2006**, *24*, 487.
13. M. Akgül, A. Karabakan, *Microporous and Mesoporous Materials*, **2010**, *131*, 238.
14. H. Bedelean, A. Măicăneanu, S. Burcă, M. Stanca, *Studia UBB Geologia*, **2010**, *55*, 9.
15. Z. Guo, S. Zheng, Z. Zheng, F. Jiang, W. Hu, L. Ni, *Water Research*, **2005**, *39,* 1174.

STUDIA UBB CHEMIA, LVI, 1, 2011

THE EFFECT OF BENTONITE ON AFB1, AFB2, AFG2 AND T-2 MYCOTOXINS DECOMPOSITION IN SUNFLOWER OIL UNDER THE IRRADIATION OF ULTRAVIOLET LIGHT

GOMBOS SÁNDOR[a], PAUL ŞERBAN AGACHI[b]

ABSTRACT. Bentonite was used as a photocatalyst in the degradation of mycotoxins in sunflower oil, under UV-illumination. The objective of this study was to investigate and evaluate the efficiency of bentonite adding to sunflower oil to decompose the solubilised B1, B2, G2 aflatoxins and T-2 toxin by UV light irradiating, as solution to increase vegetable oil quality. Identification of decontaminating process particularities consists in the formulation of mathematical model which describes the influence of process parameters on the decomposition of mycotoxins. In the present work, decontamination process was studied at laboratory scale using a plug-flow photoreactor, serial connected with a buffer vessel, at constant operating temperature and irradiating time. The kinetics of photocatalytic process was assumed to follow a pseudo-first-order rate law. The apparent photodegradation rate constant depend strongly on the present mycotoxin, the bentonite catalyst contribute to obtain much lower mycotoxin concentrations. The model predicted maximum values of apparent photodegradation constants were compared with the experimental data, the model was verified.

Keywords: *Mycotoxins, Aflatoxin B1, Aflatoxin B2, Aflatoxin G2, T-2 toxin, photochemical degradation, ultraviolet light, sunflower oil, kinetics, reaction mechanism, HPLC.*

INTRODUCTION

There is a growing negative reaction of the consumer public to added synthetic chemical compounds or existence of toxic chemicals in foods, such as for mycotoxins [1]. To approach the challenges and problems of the food industry, there are alternative possibilities of current food processing, these options usually are more sophisticated, often several ways of processing are investigated, and then the most appropriate is chosen [2]. As a method for decontaminating, the food irradiation with ultraviolet light (UV) can play an important role; there are large interests for this method. U.S. Food and Drug Administration (USFDA) and U.S. Department of Agriculture concluded that UV irradiation is safe [3, 4].

[a] *Babeş-Bolyai University, Faculty of Chemistry and Chemical Engineering, 11. Arany Janos, RO-400028 Cluj-Napoca, Romania, sagachi@staff.ubbcluj.ro*

[b] *Sapientia University Cluj-Napoca, Faculty of Sciences Miercurea Ciuc, 1. Piata Libertatii, RO-530104 Miercurea Ciuc, Romania, gombossandor@sapientia.siculorum.ro*

In 2000, the FDA approved the use of UV light treatment as an alternative to thermal pasteurization of fresh fruit juices. In addition, the USFDA issued 21CFR179.41 Code [5], which approved the use of UV light in the production, processing and handling of foods. Health Canada has conducted an assessment of UV treatment of apple juice and cider, and concluded that there is no reason for concern [6]. In Europe, UV irradiation is already used to disinfect water and air in the food industry. In addition, in 2004, the National Advisory Committee for Microbiological Criteria of Food (NACMCF) of USDA has reviewed the concept of "pasteurization" of foods. This term now includes any process of treatment, or a combination thereof, which is applied to foods, to reduce contamination levels [7, 8]. Many scientific publications are available on the UV treatment; we can see that there is a need for new methods of food treatment. However, in the literature insufficient data are available to integrate basic knowledge, for example, there is insufficient data about the interaction of UV light with foods, there are available performance evaluation systems of UV technologies, there are few recommendations for UV photoreactor practical design, there are few guidelines for selecting commercial UV sources, descriptions and application prospects for successful food handling are poor. Meesuk and Vorasith [10] showed that activated betonies can absorb efficiently the sunflower oil peroxides, starting from this premise it follows logically that can be adsorbed on the surface of betonies simultaneously micotoxins and peroxides, the free radicals formed by the photochemical decomposition of peroxides can react much easier with mycotoxins.

Process mechanism

The case of photochemical degradation of mycotoxins in presence of bentonite (B) is based on the following assumptions: mycotoxins (MT) are fully dissolved in the liquid phase (in the sunflower oil), the reaction mass is irradiated after being sufficiently mixed to form the adsorption equilibrium with bentonite on the active surface (Langmuir adsorption isotherm), where mycotoxin with bentonite forms an adsorption complex (MTB); there are no motive forces of the mycotoxins in the excited state which are dissolved or adsorbed on bentonite, photochemical reactions are not occurring if bentonite is not added to the sunflower oil. In fact, as it will be demonstrated later, photochemical reactions take place even without the presence of bentonite. Adsorption process can be described as follows:

$$MT + B \rightarrow MTB \qquad \text{described by} \qquad r = k_1[MT][B] \qquad (1)$$

The desorption process can be described as follows:

$$MTB \rightarrow MT + B \qquad \text{described by} \qquad r = k_{-1}[MTB] \qquad (2)$$

There is also an ineffective absorption of light, in a first step it occurs with absorption of light quanta:

$MT + h\nu \rightarrow MT^*$ described by I_{abs}^{MT} (3)

After this, relaxation can occur through the phenomenon of excited state fluorescence of MT:

$MT^* \rightarrow MT + \Delta$ described by $r = k_D[D^*]$ (4)

Formed complex may also to absorb a quantum of light:

$MTB + h\nu \rightarrow MTB^*$ described by I_{abs}^{MTB} (5)

After this, can occur the phenomenon of relaxation excited state fluorescence of MTB:

$MTB^* \rightarrow MTB + \Delta$ described by $r = k_D[MTB^*]$ (6)

The effectiveness photochemical processes are:

Photochemical excitation of bentonite:

$B + h\nu \rightarrow B^*$ described by $I_{abs}^{B^*}$ (7)

After this, may occur the relaxation of excited state of bentonite:

$B^* \rightarrow B + \Delta$ described by $r = k_B[B^*]$ (8)

Photochemical reaction of MT with bentonite located in the excited state:

$B^* + MT \rightarrow$ Products described by $r = k_R[B^*][MT]$ (9)

It may also take place an excitement of the adsorption complex:

$MTB + h\nu \rightarrow MTB^*$ described by I_{abs}^{MTB} (10)

Relaxation of excited complex adsorption state with decomposition:

$MTB^* \rightarrow$ Products described by $r = k_R[MTB^*]$ (11)

Real system is more complex, better accuracy should be taken into account the presence of peroxides and hydroperoxides who are inherently present in the sunflower oil [9]. For simplicity, subsequent experimental measurements were made from the sunflower oil with constant peroxide index.

Mathematical model

We consider that I_{abs}^{MT}, I_{abs}^{B} and I_{abs}^{MTB} represents the absorbed monochromatic light by the liquid phase components (moles of photons, $s^{-1} \cdot dm^{-3}$), [*MT*], [*B*] and [*MTB*] are the current concentrations of the MT, B and MTB components at *t* reaction time (mol/dm^3). Speed of photodegradation process can be described by the equation:

$$r = -\frac{d[MT]}{dt} = \frac{d[Products]}{dt} = \frac{k_R K_1 c_0^B [MT]}{k_B + k_B K_1 [MT] + k_R K_1 C_0^B [MT]} \cdot I_{abs}^B \quad (12)$$

Concentration of the adsorption complex which is formed:

$$[MTB] = \frac{K_1 c_0^B [MT]}{1 + K_1 [MT]} \quad (13)$$

where $K_1 = k_1/k_{-1}$, $c_0^B = [B] + [MTB]$, $c_0^{MT} = [MT] + [MTB]$, and the reaction speed at the beginning of irradiation is described by equation (φ_0 is the reaction constant):

$$r(0) = \varphi_0^\lambda \frac{S}{V} I_0 \left(1 - 10^{-A_{total}(0)}\right) \quad (14)$$

Monochromatic light is absorbed by the MTB complex (ε_{TD}), by the bentonite (ε_B) and by the present mycotoxins MT (ε_{MT}) in the reaction mass. Considering that L is the optical path through the system, the total absorbance is:

$$A_{total}(0) = (\varepsilon_{MTB}[MTB]_0 + \varepsilon_{MT}[MT]_0 + \varepsilon_B[B]_0)L \quad (15)$$

This relation expresses the total absorbed light, where I_0 is incident light intensity (moles of photons·s^{-1}·dm^{-2}). If S is the illumination area (dm^2), V is the active volume of the reactor (dm^3), then:

$$I_{abs}^{total}(0) = \frac{S}{V} I_0 \quad (16)$$

Usually, we can accept the assumption that light is absorbed in the reaction mass ($A_{total}(0)>2$) early entry into the reactor [11]. This simplification is valid for the use of bentonite, but could not be used for thin film reactor in the absence of bentonite.

The equation which describes the initial absorption of light by bentonite is:

$$I_{abs}^T(0) = \frac{S}{V} I_0 \frac{\varepsilon_T [B]_0}{\varepsilon_{MT}[MT]_0 + \varepsilon_B [B]_0 + \varepsilon_{MTB}[MTB]_0} \left(1 - 10^{-A_{total}(0)}\right) \quad (17)$$

Theoretically, the relation between $r(0)$ and $[MT]_0$ is predictable [12], where $r(0) = 0$ if $[MT]_0 = 0$:

$$r(0) = \frac{k_R K_1 c_0^T [MT]_0}{k_B + k_B K_1 [MT]_0 + k_R K_1 c_0^B [MT]_0} \cdot \frac{S}{V} \cdot \cdot I_0 \cdot \frac{\varepsilon_T [B]_0}{\varepsilon_{MT}[MT]_0 + \varepsilon_B [B]_0 + \varepsilon_{MTB}[MTB]_0} \cdot \left(1 - 10^{-A_{total}(0)}\right) \quad (18)$$

Simplified: $$r(0) = \varphi_0 \frac{S}{V} I_0 \left(1 - 10^{-A_{total}(0)}\right) \tag{19}$$

but $r(0) = 0$ if $[D]_0 \to \infty$ [13]. Function has a maximum (r_{max}, $[D]_0^{opt}$), which can be calculated from the following relation, where:

$$b = k_B K_1 + k_R K_1 c_0^B, \quad c = \varepsilon_{MT} - \varepsilon_{MTB}, \quad d = \varepsilon_B [B]_0 + \varepsilon_{MTB} c_0^{MT}$$

$$\frac{dr(0)}{d[MT]_0} = 0 \quad \text{hence} \quad [MT]_0^{opt} = \left(\frac{k_B d}{bc}\right)^{1/2} \tag{20}$$

Relations are valid for monochromatic light with a specific λ, and for polychromatic light may be used an integration [14], where we can define the initial integration constant (Φ_0) and the total initial rate of degradation of mycotoxins (R_0), resulting in the following equation:

$$\sum_{\lambda} rr_0^{\lambda} = RR_0 = \sum_{\lambda} \varphi_0^{\lambda} \frac{S}{V} I_0 \left(1 - 10^{-A_{total}(0)}\right) \tag{21}$$

The used light source was with mercury vapour, emission spectral bands are characteristic of mercury. Reaction rate equation at the beginning of irradiation (rr_0) and location of maximum (rr_0^{max}, $[MT]_0^{opt}$) depend on the wavelength and intensity of light emitted by the source. Knowing that MT had significant absorbance at the characteristic wavelength of the UV source, it became possible to carry out practically decontamination. The integral reaction speed RR_0 in response to polychromatic light source was obtained by summing rr_0^{λ} ($RR_0 = \sum rr_0^{\lambda}$). Function maximum ($RR_0^{max}$) at a concentration of dissolved MT, for known dissolved MT concentration can be predicted the $[MT]_0^{opt}$ if all experimental constants are known (s, V, I_0^{λ}), physical constants (ε_{MT}, ε_B, ε_{MTB}) and chemical constants (K_1, $k_{d,r}$). Kinetic model reveals that the rate of degradation of mycotoxins depends very much on the active surface affinity of bentonite. The ratio between the bentonite and mycotoxins must be adjusted according to need of process, but basically it cannot be used high doses of bentonite, there appear major difficulties of pumping. The scientific literature contains very few data on the optical properties of mycotoxins, suspensions of bentonite and bentonite-sunflower oil organogels. In limited area of concentrations of investigated mycotoxins can be performed the degradation kinetics linearization, especially if it seeks to minimize changes of essential fatty acids, which logically require a relatively short irradiation times. We can write the equation:

$$-\frac{d[MT]}{dt} = k_{apMT}[MT] \tag{22}$$

For each mycotoxin in part, $[MT]$ represent the actual concentration of mycotoxin, k_{apMT} is the pseudo-first order transformation constant, *t* is the time of irradiation.

For a PFR (tubular) reactor, the equation that describes the operation can be described as follows [15]:

$$-\frac{d[MT]}{dV} = -\frac{r_{MT}}{\nu_0}, \tag{23}$$

where $V = \frac{\pi}{4}\left(d_0^2 - d_i^2\right)l$, and $-r_{AMT} = -\frac{d[MT]}{dt}$. (24)

In previous relations *V*, ν_0, d_0, d_i and *l* are the volume, volume flow, inner diameter, outer diameter and the length of photochemical reactor. From the last two equations we get:

$$-\frac{d[MT]}{dl} = \frac{\pi/4\left(d_0^2 - d_i^2\right)}{\nu_0}\left(-\frac{d[MT]}{dt}\right) \tag{25}$$

The obtained model is:

$$-\frac{d[MT]}{dl} = \frac{\pi/4\left(d_0^2 - d_i^2\right)}{\nu_0}\left(\frac{a[B]_0/[MT]_0}{1+b([B]_0/[MT]_0)+c([B]_0/[MT]_0)^2}\right)[MT] \tag{26}$$

EXPERIMENTAL SECTION

In the reactor system [16], in the continuous mixing reactor which are previously cleaned, dried, was added 500 grams of Top Floris extra pure sunflower oil, which is a special product of SC Expur SA, and it was checked for lack of mycotoxins in the laboratory of Sapientia University Miercurea Ciuc. After dosing the sunflower oil, was started the carbon dioxide gas adding, so that in both reactors to reach a sufficient amount remove of atmospheric oxygen, gas dosing was continued until the end of experiments. Through a hole in the top of the batch reactor was added with a Hamilton microsyringe the amount of mycotoxin standard solution to achieve the initial concentration of mycotoxins. After setting the working parameters, after the start of pumping (50-1000 ml/minute), the UV source was ignited, which measured power output are 29,8 mW/cm^2 at a distance of 5 cm, and then at regular intervals were extracted samples in special vessels, which being filled, sealed and stored at -24 °C in the dark until analytical determinations were carried out. Samples were processed as follows: using centrifuge

Hettich Micro 20 (13000 rot./min, 5 minutes), bentonite was separated, we split (if necessary) the higher density oil phase, which was pipetted into an extraction bottle, it was determined the mass, after this was performed methanol extraction of mycotoxins in several steps, resulting mixtures were separated by centrifugation (Hettich Universal 32, 3400rot./min, 5 minutes), alcoholic liquid phases were pipetted and unified. Later, separated bentonite was extracted in several steps, for the extraction of adsorbed mycotoxin, and then unified. Since resulted alcoholic phases were sometimes cloudy, was needed a new set of centrifugations to perfect the separation. Alcoholic extracts thus obtained were subjected to evaporation, their mass was determined, and portions of alcoholic extracts was injected into an apparatus Varian Pro Star HPLC type, using fluorescent and UV detector, using Supelcosil LC 18 column, with flow rate of 0,9 ml/min, without derivatization, because previous derivatization tests did not provide the expected results. For accurate determinations using liquid chromatography (HPLC), it was necessary an adequate preparing of the apparatus, every time was given enough time for conditioning and stabilizing all components of the HPLC equipment. HPLC equipment was controlled by Varian Star Chromatography Workstation Version 6.00 software. The used eluent was a mixture of water, methanol and acetonitrile, mixture in the ratio of 130:70:40. Fluorescence detector was set for excitation at 365 nm, and the emission at 435 nm. Based on HPLC chromatograms provided by the HPLC, we can evaluate the concentration of MT in the samples, which is proportional to the area under the signal curve offered by that component.

RESULTS AND DISCUSSION

By using the bentonite as an additive to the reaction mass, after the experiments was carried out, extraction of MT from bentonite was necessary, with the unification of the extracts, followed by partly evaporation of methyl alcohol. The values of apparently degradation constants of MT depending on the mass ratio between bentonite (B) and MT (g B/μg MT) are indicated in figure 1.

We adjusted the experimental data to the proposed model, based on data from k_{ap} corresponding to bentonite additive use (B concentration expressed in g/l reported to the MT concentration expressed in μg/kg), the effects of the bentonite presence are differentiated: in case of AFB1 are obtained increase with 315% of the reaction speed, in case of AFB2 are obtained an increase with about 26%, in case of AFG2 are obtained an increase with about 44% and in case of T-2 are obtained an increase with about 65%. Parameters of individual models with 95% confidence level and using the sum of the squares error method (SSE) as a function of error were obtained by nonlinear regression using Polymath 5.0 software package.

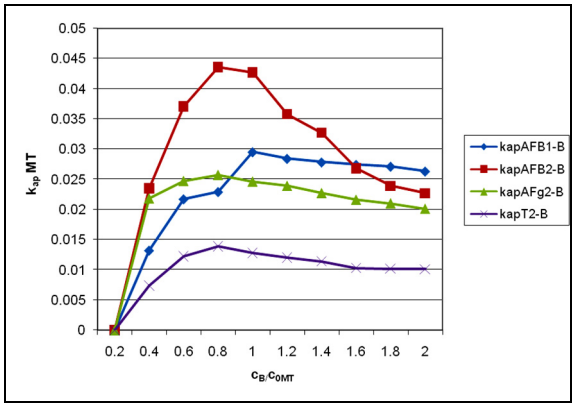

Figure 1. Values of apparently degradation constants of MT depending on the mass ratio between bentonite (B) and MT (g B/μg MT)

k_{apAFB1}

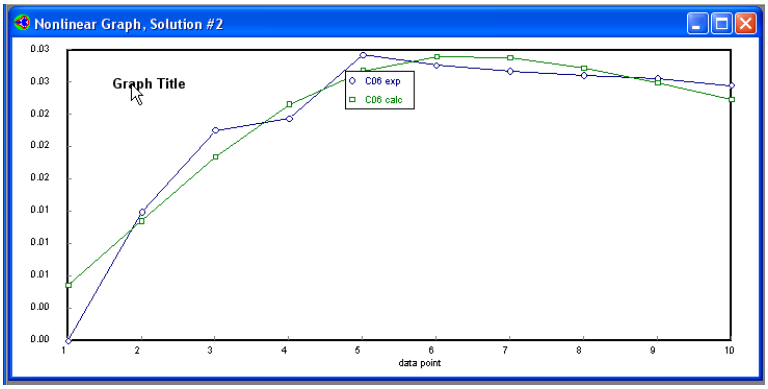

Figure 2. AFB1-B experimental data adjustment

k_{apAFB2}

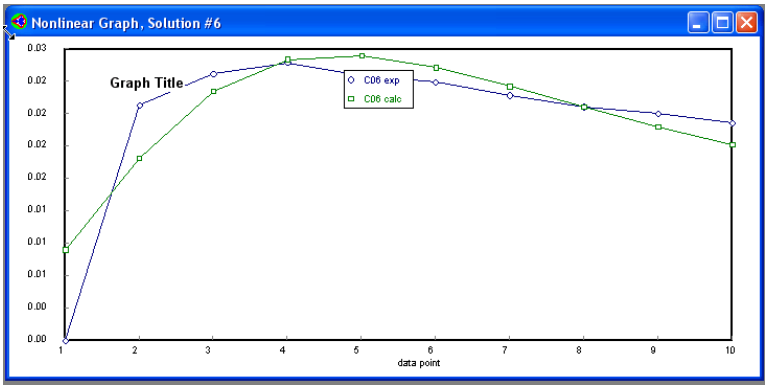

Figure 3. AFB2-B experimental data adjustment

We adjusted the experimental data from the proposed model; the results are shown in Figures 25, 26, 27 and 28, in order of AFB1, AFB2, AFG2 and T-2. The obtained values for the parameters *a*, *b* and *c* is presented in table 3.

k_{apAFG2}

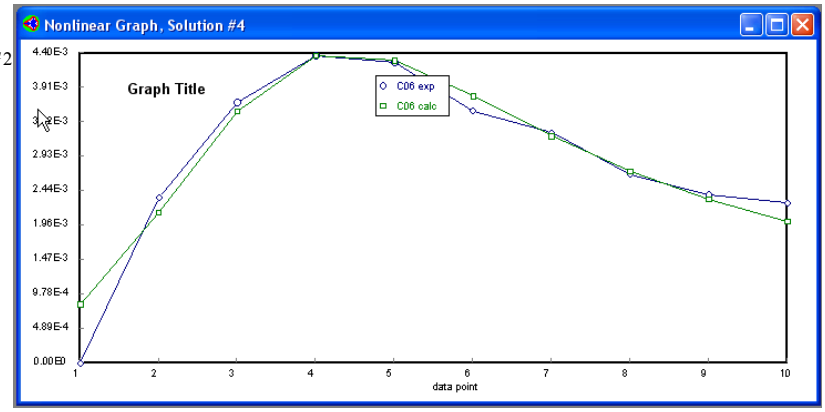

Figure 4. AFG2-B experimental data adjustment

k_{apT-2}

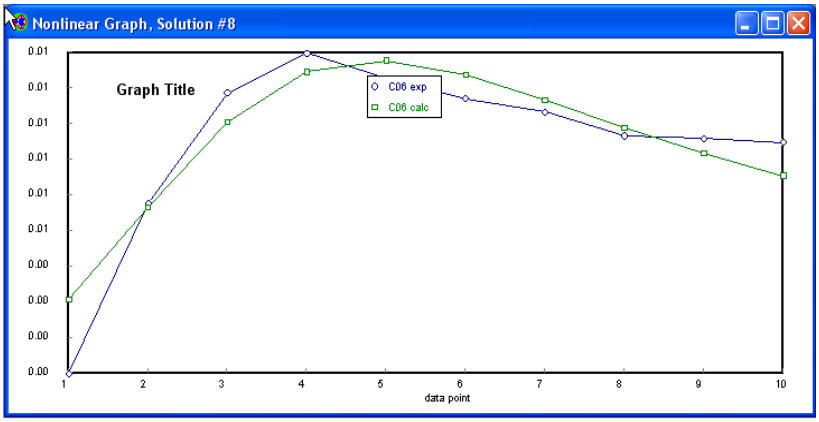

Figure 5. (T-2)-B experimental data adjustment

Table 1. Obtained values for the parameters *a*, *b* and *c* for MT photodegradation (AFB1, AFB2, AFG2, and T-2) in the presence of bentonite (B)

Parameter	AFB1	AFB2	AFG2	T-2
a	0,0153	0,0013	0,0360	0,0092
b	0,7131	0,3353	1,5101	0,7614
c	0,2177	0,2563	0,5732	0,3502

CONCLUSIONS

The proposed model for prediction of AFB1 photodegradation in the presence of bentonite has a maximum for k_{apAFB1} at around 1,3 for the $[B]_0/[AFB1]_0$ ratio, which is in good agreement with experimental data obtained for AFB1, which resulted for k_{apAFB1} a 1,0 value of the ratio. The proposed model for prediction of AFB2 photodegradation in the presence of bentonite has a maximum for k_{apAFB2} at around 1,2 for the $[B]_0/[AFB2]_0$ ratio, which is in good agreement with experimental data obtained for AFB2, which resulted for k_{apAFB2} a 1,0 value of the ratio. The proposed model for prediction of AFG2 photodegradation in the presence of bentonite has a maximum for k_{apAFG2} at around 0,8 for the $[B]_0/[AFG2]_0$ ratio, which is in very good agreement with experimental data obtained for AFG2, which resulted for k_{apAFG2} a 0,8 value of the ratio. The proposed model for prediction of T-2 photodegradation in the presence of bentonite has a maximum for k_{apT-2} at around 1,0 for the $[B]_0/[T-2]_0$ ratio, which is in good agreement with experimental data obtained for T-2, which resulted for k_{apT-2} a 0,8 value of the ratio. The constructed models may be used to estimate the B/MT concentrations ratio requirements for the photochemical degradation of mycotoxins in each hand. On the other hand, it becomes obvious need to be operated the sunflower oil refining such as decontamination of mycotoxins needs amounts of present bentonite ratios to be within certain limits, depending on the nature of mycotoxins. The value of B/MT ratio needed for decontamination at the same time requires restrictions on the choosing of circulation pumps.

ACKNOWLEDGMENTS

The authors are indebted to the referee for some critical suggestions leaded us to correct our main result. This work was partially supported by the Sapientia University Cluj-Napoca, Faculty of Sciences Miercurea Ciuc.

REFERENCES

1. N.W. Turner, S. Subrahmanyam, S.A. Piletsky, *Anal. Chim. Acta,* **2009**, *632-2*, 168.
2. L.J. Forney, J.A. Pierson, C.F. Goodridge, *Ann. Rep. for Food-PAC*, Atlanta, GA. **2002**.

3. U.S. FDA, "Irradiation in the production, processing and handling of food. Code of Federal Regulations". *U.S. Food and Drug Administration*, Washington, DC. **2000**, *21,* 179.
4. U.S. FDA, "Hazard analysis and critical control point (HACCP): Final rule". *U.S. Food and Drug Administration*, Federal Register 66 (13). Washington, DC. **2001**.
5. U.S. FDA, "Code of Federal Regulations 21CFR179.41". *Food and drugs*, **2005**, *21*, 179, Subpart B.
6. Health Canada, "Ultraviolet light treatment of apple juice/cider using the CiderSure 3500". *Novel Food Information*, **2004**.
7. U.S. FDA, "Kinetics of microbial inactivation for alternative food processing technologies". *J. Food Sci. Suppl.*, Institute of Food Technologists (http://vm.cfsan.fda.gov/~comm/ift-pref.html), **2000**.
8. U.S. FDA, "Kinetics of microbial inactivation for alternative food processing technologies", **2000**.
9. S. Gombos, A. Szép, *15th International Conference of Chemistry*. Tîrgu Mures, **2009**, 21-22.
10. L. Meesuk, N. Vorasith, *Journal of Environmental Science and Health*, **2006**, Part A, *41*, 1189.
11. Z. Ye, "UV disinfection between concentric cylinders", PhD Thesis, Georgia Institute of Technology, **2007**.
12. J.R. Bolton, K. G. Linden, *J. Environ. Eng.*, **2003**, *129*, 209.
13. J.R. Bolton, *Water Res.*, **2000**, *34*, 3315.
14. T. Koutchma, B. Parisi, S. Unluturk, *Chem. Eng. Commun.*, **2006**, *193*, 1.
15. G.F. Froment, K.B. Bischoff, *Chemical Reactor Analysis and Design*, John Wiley & Sons, New York. **1990**, chapter 3.
16. S. Gombos, “AFB1, AFB2, AFG2 and T-2 Mycotoxins degradation in sunflower oil under the action of UV radiation”, PhD Thesis, Universitatea Babeş-Bolyai of Cluj-Napoca, Faculty of Chemistry and Chemical Engineering, **2010**.

STUDIA UBB CHEMIA, LVI, 1, 2011

IMMOBILIZED POLYPHENOLOXIDASE FOR WASTEWATERS TRATEMENT

CORNELIA MAJDIK[a], GABRIEL KATONA[a], MIRCEA CHINTOANU[b], MARIUS ROMAN[b], EMIL LUCA[c], SIMONA MARIANA SIMON[d], TIBERIU RUSU[d], CECILIA ROMAN[b*]

ABSTRACT. A simple and efficient method for immobilization of crude polyphenol oxidase from potato by entrapment in calcium alginate was developed. The obtained enzyme preparate was tested for bioremediation of wastewaters in batch and packed bed reactor.

Keywords: *immobilized polyhenoloxidase, phenol removal, bioremediation, calcium alginate, batch reactor, packed bed reactor*

INTRODUCTION

The use of enzymes in the bioremediation processes is a protective methodology for the environment which can reduces the damages caused by industrial polluting effluents. The presence of phenolic compdunds in drinking and irrigation water represents a significant health and environmental hazard and, therefore, the development of methods for their removal and transformation have received increased attention in recent years. The most results dealing with the fundamental and applied aspects of free and immobilized polyphenoloxidases (PPO) for food industry wastewater processing was presented by Chiacchierini [1]. The enzyme was isolated from a large variety of plants and fungi [2], but the costs for obtaining pure enzyme preparation are still high. Many cheep available sources were tested. Recently, PPO was extracted from tomato fresh pulp and different trademarks of tomato puree sold in supermarkets by using sodium phosphate buffer at different pHs. The best pH values was 7.5 [3].

Polyphenol oxidase from mango (*Mangifera indica*) peel and green tea (*Camellia sinensis*) leaves were immobilized on various supports, e.g., polyacrylamide gel, DEAE-Sephadex, DEAE-cellulose, collagen, arylamine glass,

[a] *"Babeş-Bolyai" University, Faculty of Chemistry and Chemical Engineering, Arany Janos 11, RO-400028, Cluj-Napoca, Romania*
[b] *INCDO-INOE Research Institute for Analytical Chemistry-ICIA Donath-67, 400293 Cluj-Napoca, Romania * cici_roman@yahoo.com*
[c] *University of Agricultural Sciences and Veterinary Medicine Cluj Napoca Calea Mănăştur 3 400327Cluj-Napoca Romania*
[d] *Technical University of Cluj-Napoca, Bulevardul Muncii 103-105, Ro-400641, Cluj-Napoca, Romania*

and alkylamine glass and some important properties (optimum temperature, pH, Km, substrate specificity, thermal stability, storage stability and reusability) were studied and compared with those of native enzyme [4].

Gusarova and co. studied [5] the immobilization pf PPO from higher basidiomycetes (*Coriolus sp*.) on polyvinylalcohol fibers and the use of immobilized enzyme for purification of wastewater from hydrolysis-yeast industry.

The gel-entrapped tyrosinase and laccase prepared by immobilization of enzymes in gelatine [6] were capable of removing naturally occurring and xenobiotic aromatic compounds from aqueous suspensions and with different degrees of efficiency. A column packed with gel-immobilized tyrosinase was used to demonstrate that enzymes immobilized with this technique may be reused several times in the same reaction without loosing their efficiency. Moreover, this immobilization procedure enhanced the enzymes stability to thermal inactivation.

In this work, with the aim to improve the phenol removal from wastewaters, the immobilization of crude polyphenole oxidase from potato using a simple and efficient method, entrapement in calcium alginate, is presented. The immobilized enzyme was tested for phenol oxidation in batch and in packed bed reactors.

RESULTS AND DISCUSSION

Immobilization of crude PPO from potato, activity and stability of enzyme

Many methods are available for immobilization of enzymes and cells. Since the method greatly influence the properties of the resulting biocatalyst, the selection of the most suitable strategy determines the process specifications for the catalyst, such as overall catalytic activity, efficiency of the enzymatic process, deactivation and regeneration kinetics and cost.

In order to immobilize PPO in alginate beads, we used the entrapement of enzyme in calcium alginate. The immobilization procedure was studied with the aim to obtain the most performant biocatalyst for phenol removal from wastewaters. The quantity of included enzyme was determined from the protein content of enzyme solutions before and after immobilization, which was determined by Bradford method with Comassie Blue.

The enzymatic activity of each enzyme preparate was determined as previously described [7], with 4-aminoantipyrine (4-Amino-1,2-Dihydro-1,5-Dimethyl-2-Phenyl-3H-Pyrazol-3-One, AAP) in presence of potassium ferricyanide. As observed in Figure 1, the activity depends linear on the quantity of immobilized enzyme. In conclusion, the ability of alginate to include the entire crude enzyme corresponde our goal.

Next the stability of immobilized PPO in time was tested in comparison with those of the free enzyme. As observed in Figure 2, the most unstable is the free (soluble) enzyme. The immobilized enzyme preparates with < 0.5 g crude PPO are stable in time and retains more than 50% from their initial activity. The most suitable seems to be the calcium alginate beads obtained from 0.4 g enzyme.

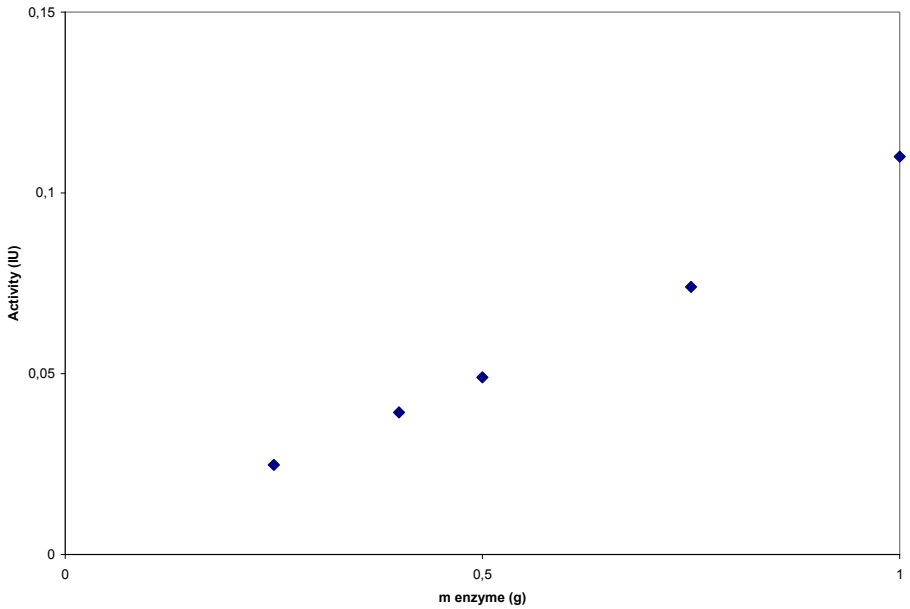

Figure 1. The influence of crude enzyme quantity on the enzymatic activity

Phenol removal with immobilized PPO in packed bed reactor

The bioremediation process was realized with the most efficient enzyme preparate (o.4 g crude PPO) and a solution of phenol (13 mM) in 0.2M phosfate buffer (pH 6.15). The phenolic solution was passed over the alginate beads which contain the calcium alginate beads included enzyme, until the concentration of phenol remain constant. After each step, the phenol concentartion was determined as described in section 1. As observed in Figure 3, in the first cycle the efficiency of process was approx. 25%. In the next cycles, the efficiency strongly decrease to 2-3%. In conclusion, due to the absence of stirring the diffusion of phenol through the alginate reduced the efficiency of bioremediation process.

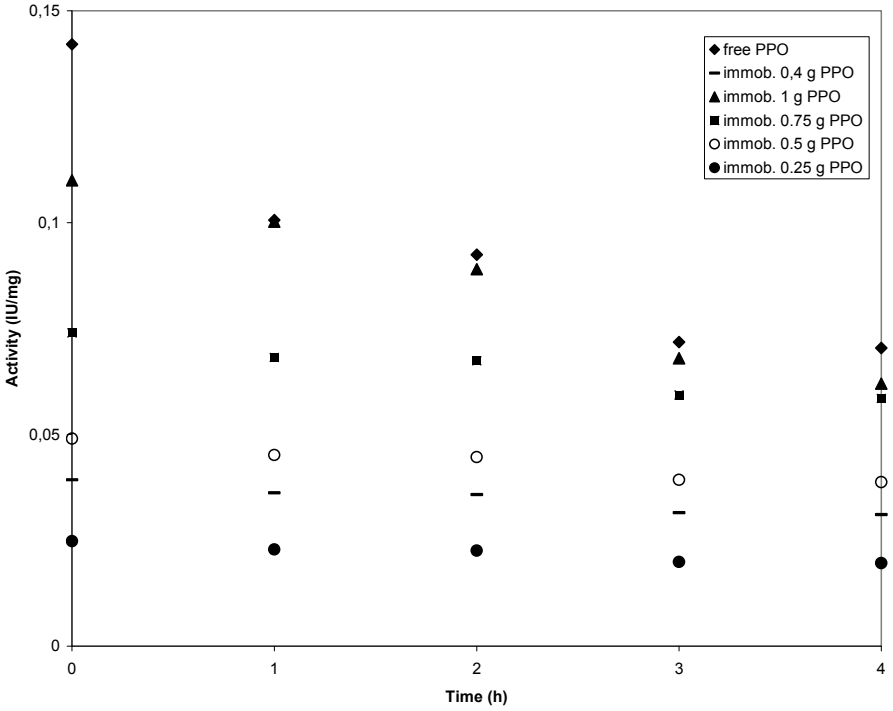

Figure 2. The stability of immobilized and free PPO in water

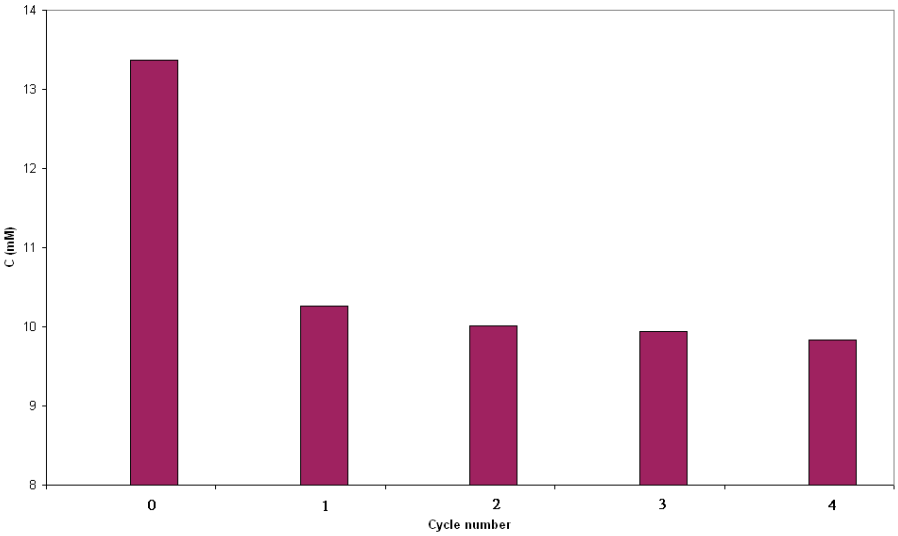

Figure 3. Phenol removal with immobilized PPO in packed bed reactor

Phenol removal with immobilized PPO in batch reactor

Next the process was realized in a batch reactor, under continously stirring, in the same conditions (initial phenol concentration, pH of buffer, quantity of immobilized PPO). Samples were tacken every hour and phenol concentration was determined colorimetrically. As ilustrated in Figure 4, after 5 hours 25% of phenol was removed and the process stopped.

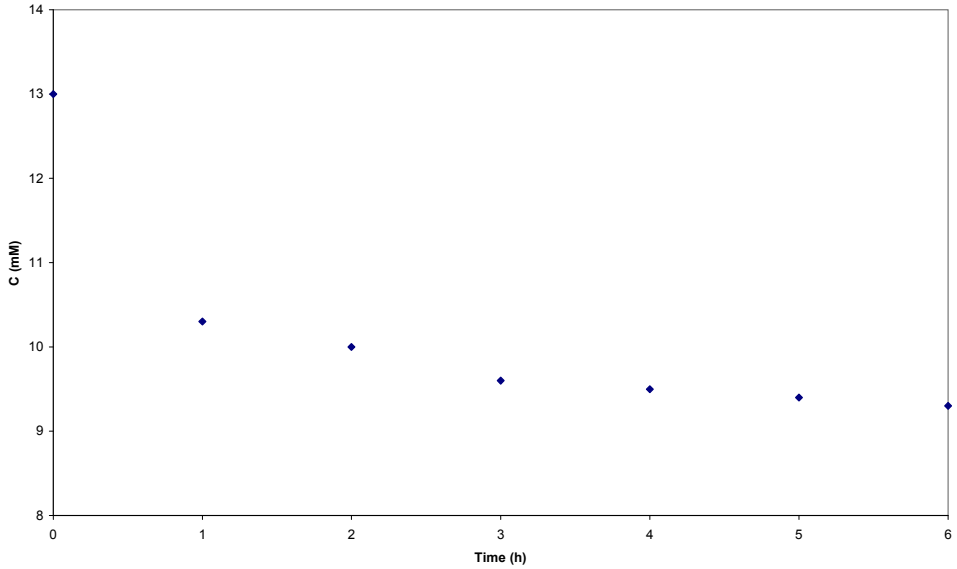

Figure 4. Phenol removal with immobilized PPO in stirred batch reactor

CONCLUSION

Polyphenol oxidase from potato with low purity immobilized by entrapement in calcium alginate showed a good potential for phenol removal from synthetic wastewaters. The entrapement in calcium alginate is a simple and cheep immobilization method which occurs with high yields (>90%). The enzyme preparates were tested for phenol removal from wastewaters in packed bed and batch reactors. In both cases, the phenol removal process occurs fast in the first period, with an approx. 25% yield. To increase the yield of phenol removal with this immobilized PPO, the use of packed bed reactor cascade can be an efficient solution.

EXPERIMENTAL PART

Materials and methods

Potato *(Solanum tuberosum*) tubers were obtained from commercial fields in Romania at 3- to 4-week intervals. All inorganic and organic reagents were products of Aldrich or Merck. The UV-VIS spectra were recorded on a Agilent 8453 spectrophotometer at room temperature. Crude PPO was prepared as earlier described by us [7]. Phenol concentration was measured using the colorimetric method with 4-aminoantipyrine (4-Amino-1,2-Dihydro-1,5-Dimethyl-2-Phenyl-3H-Pyrazol-3-One*,* AAP) in presence of potassium ferricyanide.

Immobilization of crude polyphenol oxidase in calcium alginate

A quantity of freshly obtained crude PPO from potato was dissolved in demineralized water (10 ml) and mixed with sodium alginate solution (2%) in 1:1 ratio. The mixture was added dropwise into calcium chloride (0.2 M) solution with continuous shaking. As soon as the drop of enzyme-alginate solution mixed with $CaCl_2$ solution, Na^+ ions of Na-alginate were replaced by the Ca^{+2} ions of $CaCl_2$ solution, which finally formed Ca-alginate beads. The beads thus formed were washed 3-4 times with deionized water and finally with 0.2 M phosphate (pH 6.15). These beads were used for further studies.

ACKNOWLEDGEMENTS

The financial support from the Romanian Ministry of Education and Research (PNCD II Project Nr. 31-016/2007, DEFENOL) is gratefully acknowledged.

REFERENCES

1. E. Chiacchierini, D. Restuccia, G. Vinci, *Food Sci. Technol. Int. l,* **2004**, *1,* 373-382.
2. Y.K. Cho, H.K. AHN, *J. Food Biochem.*, **1999**, *23*, 593.
3. E. Clemente, *Acta Scientiarum, Technology*, **2010**, *32(1)*, 91.
4. T.N. Prabha, M. Ramakrishna, M.V. Patwardhan, M.R. Rao, *Indian J. of Biochem. Biophysm*, **1981**, *18(6)*, 402.
5. L.A. Gusarova, V.P. Gavrilova, I.I. Shamolina, V. L. Komarov, *Biotekhnologiya*, **1989**, *5(5)*, 627.
6. C. Crecchio, P. Ruggiero, M.D.R. Pizzigallo, *Biotechnol.Bioeng.*, **1995**, *48(6)*, 585.
7. C. Majdik, C., G Katona, M. Chintoanu, M. Roman, E. Luca, S.M. Simon, T. Rusu, C. Roman, *Studia UBB Chemia*, **2011**, *in press*.

STUDIA UBB CHEMIA, LVI, 1, 2011

PHENOL REMOVAL FROM WASTEWATERS USING POLYPHENOLOXIDASE FROM POTATO

CORNELIA MAJDIK[a], GABRIEL KATONA[a], MIRCEA CHINTOANU[b], MARIUS ROMAN[b], EMIL LUCA[c], SIMONA MARIANA SIMON[d], TIBERIU RUSU[d], CECILIA ROMAN[b*]

ABSTRACT. An easy available enzyme preparation for bioremediation of phenol containing wastewaters was tested. The influence of most important parameters (pH, substrate-enzyme ratio) was studied.

Keywords: *Polyphenol oxidase, phenol removal, bioremediation*

INTRODUCTION

The rapid expansion and technological improvement in industrial fields increase the amount and complexity of toxic waste effluents. At the same time, regulatory authorities have been paying more attention to problems of contamination of the environment. There is a growing recognition that enzymes can be used in many industrial remediation processes to target specific pollutants for treatment [1]. The potential advantages of enzymatic treatment as compared with conventional treatments include: application to recalcitrant materials, operation at high and low contaminant concentrations over a wide pH, temperature and salinity range and the easy control of the process among others.

Among xenobiotic contaminants, aromatic compounds constitute one of the major classes of pollutants and are heavily regulated in many countries. This implies that the presence of phenols in industrial residues is an area of environmental concern, since toxic phenols enter the environment in wastewater streams, released by numerous industries, including pulp and paper mills, coal and steel works, wood preservation plants, and various chemical and petrochemical industries [2]. Moreover the presence of these compounds in drinking and irrigation water, or in cultivated land, also represents a significant

[a] *"Babeş-Bolyai" University, Faculty of Chemistry and Chemical Engineering, Arany Janos 11, 400028 Cluj-Napoca, Romania*
[b] *INCDO-INOE Research Institute for Analytical Chemistry-ICIA Donath-67, 400293 Cluj-Napoca, Romania * cici_roman@yahoo.com*
[c] *University of Agricultural Sciences and Veterinary Medicine Cluj Napoca Calea Mănăştur 3, 400327 Cluj-Napoca, Romania*
[d] *Technical University of Cluj-Napoca, Bulevardul Muncii 103-105, 400641 Cluj-Napoca, Romania*

health hazard and not only environmental: phenol concentrations greater than 50 ppb are toxic to some forms of aquatic life and ingestion of 1 g of phenol can be fatal in humans [3].

Conventional processes for removal of phenols and aromatic amines from industrial wastewaters include extraction, adsorption on activated carbon, steam distillation, bacterial and chemical oxidation, electrochemical techniques, irradiation, etc. All of these methods suffer from serious drawbacks as high costs, incompleteness of purification, formation of hazardous by-products, low efficiency and applicability to a limited concentration range [4]. Due to these drawbacks alternative methods may become important in a large scale in the near future. The treatment through enzymatic catalysis seems to have the potential to substitute conventional methods [5]. Bioremediation represents an important environmental remediation strategy because naturally occurring biological processes are used.

Polyphenole oxidase (PPO) from potato [6], a multi-copper-containing enzyme, belong to the classe of laccases (benzenediol: oxygen oxidoreductase, EC 1.10.3.2) which catalyze the oxidation of a wide range of phenolic and aniline compounds. In its reaction, substrates are oxidized by one electron to generate the corresponding phenoxy radicals, which are further oxidized to a quinone. This enzyme was isolated from a large variety of plants and fungi [7]. Due to the high price, its use in industrial wastewater treatment is still limited. Recently the presence laccases (LACs) and polyphenol oxidases (PPOs) in marine cyanobacteria was revealed [8]. These strains were efficient in decolourizing of synthetic aromatic dyes.

In this work the crude polyphenole oxidase from potato was investigated as an alternative catalyst for the phenol removal from aqueous solutions.

RESULTS AND DISCUSSION

Isolation of PPO from potato

Enzyme extracts were prepared by homogenizing diced peeled potato samples with L-ascorbic acid as antioxidant in cold 0.2 M sodium phosphate buffer (pH 6) and centrifugation. The collected solution was lyophilized for further use or storage. PPO activity of crude enzyme preparation was measured as the initial rate of oxygen uptake at 25°C in 50 mM sodium phosphate, pH 6.0. The reaction was measured using the colorimetric method with 4-aminoantipyrine (4-Amino-1,2-Dihydro-1,5-Dimethyl-2-Phenyl-3H-Pyrazol-3-One, AAP) in presence of potassium ferricyanide [9]. The analytic range covers phenol concentrations from 0.03 to 0.12 mM.

Enzyme stability

The activity of crude enzyme during the storage at -80 ºC was studied (Figure 1). After approximately 4 days, it decrease with 50 % and after 15 days only 2% from the initial activity (16.9 UI/mg) was retained. In conclusion, even

at low temperature, the polyphenol oxidase is an unstable biocatalyst and in order to improve its stability the immobilization could be a convenient method.

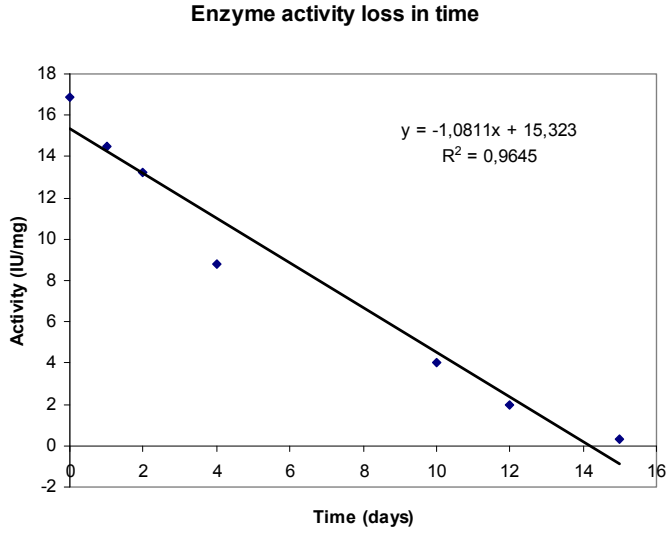

Figure 1. The stability of crude polyphenol oxidase at low temperature

The influence of pH on the bioremediation process

Several sets of samples are prepared, varying the pH of phenol solution, using acid solutions of sodium phosphate buffer 0.2 M. From the calibration curve determine the concentration of phenol in solution, before Adding to the enzyme preparation. Then add the same amount of enzyme, with same concentration (2 mg enzyme / ml sol.) and constant temperature (30°C) to phenolic solutions with different pH's. The solution will be put in to the shaker. The absorbance of each sample will be read, after certain intervals of time. For absorbance reading is used the same method as for determining the concentration of phenol from water.

The bioremediation experiments were realized for phenolic solutions having the same phenol concentration (13 mM) and different pH (using various phosphate buffer), with the same amount of enzyme. Best results were obtained pH 6.15, when after 5 days the removal of phenol was almost quantitative (Figure 2).

At the optimum pH the rate of biodegradation was much higher: after 1 day the yield was similar with those of bioremediation in alkaline conditions after 5 days.

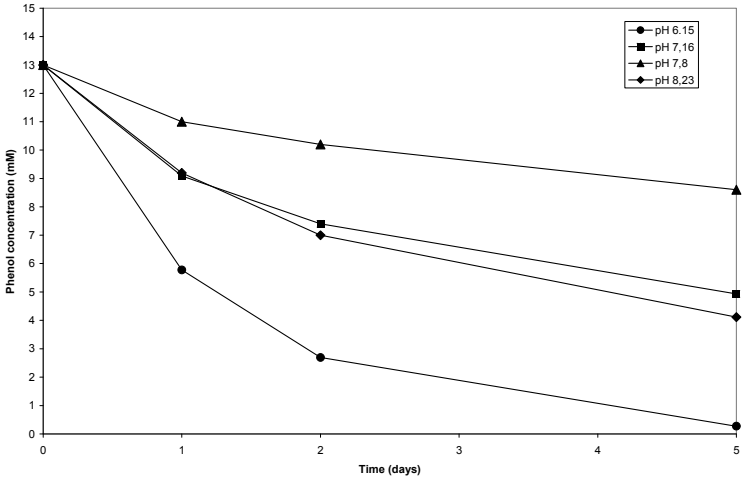

Figure 2. The inffluence of pH on phenol removal with soluble crude PPO

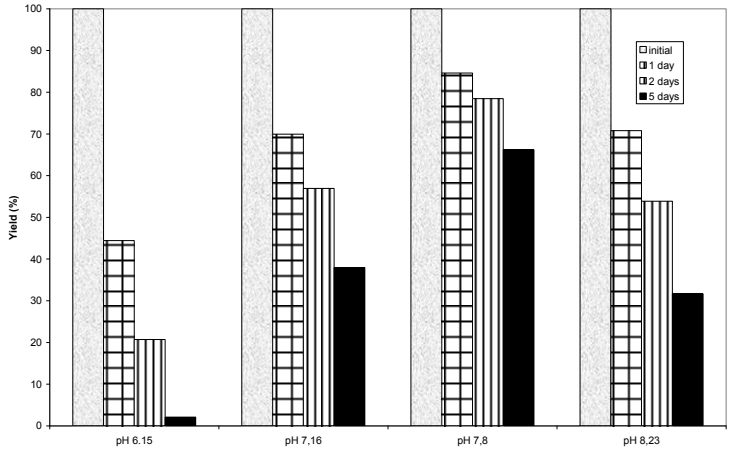

Figure 3. The efficiency of phenol removal with soluble crude PPO at different pH

The influence of enzyme-substrate ratio

Varying the amount of crude enzyme added to the solution having the optimum pH (6.15) and the same initial concentration (13 mM), using higher amounts of crude enzyme (2 mg enzyme/ml phenolic solution), the phenol was removed quantitatively in 6 days (Figure 4).

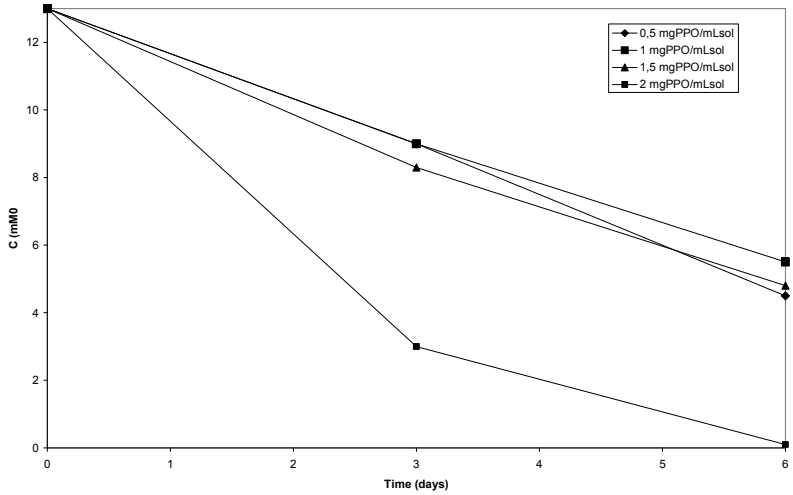

Figure 4. Influence of enzyme-subtrate ratio on phenol removal

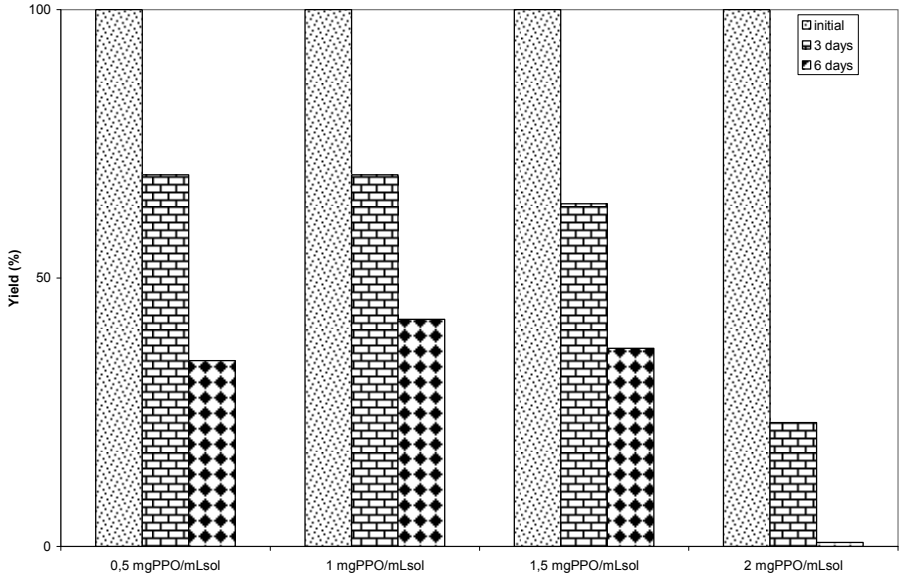

Figure 5. The efficiency of phenol removal with soluble crude PPO at different enzyme-substrate ratio

As expected, at lower enzyme concentrations the degree of bioremediation was in the field of 37-43 % after 6 days. The bioremediation process is also faster at higher enzyme concentration (Figure 5).

EXPERIMENTAL SECTION

Materials and methods

Potato *(Solanum tuberosum*) tubers were obtained from commercial fields in Romania at 3- to 4-week intervals. All inorganic and organic reagents were products of Aldrich or Merck. The UV-VIS spectra were recorded on a Agilent 8453 spectrophotometer at room temperature.

Preparation of potato extract (crude polyphenoloxidase)

Approximately 100 g of diced peeled potato sample were homogenized with L-ascorbic acid (0.3 g) and cold sodium phosphate buffer 0.2 M, pH 6 (100 ml). The mixture was centrifugated for 20 minutes at 10000 rpm. The collected supernatant (liquid phase) which contain the crude enzyme was lyophilized and stocked at –80°C.

Determination of phenol in water

Phenol concentration was measured using the colorimetric method with AAP in presence of potassium ferricyanide (Scheme 1). The analytic range covers phenol concentrations from 0.03 to 0.12 mM.

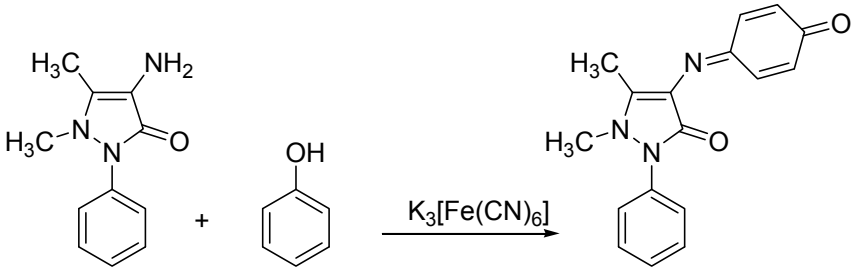

Scheme 1

Determination of Specific Activity

Enzyme activity in the stock enzyme solution was measured before use. 2 mL sample prepared from 1.9 mL phenol solution 0.2 M and 0.1 mL freshly preapared enzyme solution (100 mg crude enzyme in 25 mL phosphate buffer 0.2 M, pH 6) was mixed with 2 mL of 0.25 M sodium bicarbonate and 0.9 mL of 20.8 mM AAP. After vigorous mixing 0.9 mL of 83.4 mM potassium ferricyanide was added and mixed again. Samples absorbance was measured at 510 nm, 9 minutes after the ferricyanide addition and converted to concentration using the calibration curve. One international unit of activity represent the amount of enzyme which modify the absorbance with 0.001/min.

General experimental bioremediation procedure

Experiments were carried out in 200 mL beakers at 30º. Reaction medium was prepared by adding individually certain amounts of phenol and crude PPO into the corresponding phosphate buffer (0.2 M). The process was performed under continuously stirring at 200 rpm. Samples were taken at different intervals and the phenol concentration was determined colorimetric as described in section 2 of experimental part.

ACKNOWLEDGEMENTS

The financial support from the Romanian Ministry of Education and Research (PNCD II Project Nr. 31-016/2007, DEFENOL) is gratefully acknowledged.

REFERENCES

1. J. Karam, J.A. Nicell, *J. Chem. Technol. Biot.*, **1997***, 69*, 141.
2. E. Abadulla, T. Tzanov, S. Costa, K.H. Robra, A. Covaco-Paulo, G.M. Gubitz, *Appl. Environ. I Microb.*, **2000**, *66*, 3357; N. Durán, E. Esposito, *Appl. Catal. B: Environ.*, **2000**, *21(8)*, 83; A. M. Mayer, R.C. Staples, *Phytochemistry*, **2002**, *60*, 551; A.A. Dias, R.M. Bezerra, P.M. Lemos, A.N. Pereira, *World J. Microb. Biot.*, **2003**, *19*, 969.
3. C. Crecchio, P. Ruggiero, M.D.R. Pizzigallo, *Biotechnol. Bioeng.*, **1995**, *48*, 585.
4. A.M. Klibanov, B.N. Alberti, Morris E.D., Felshin L.M., *J. Appl. Biochem.*, **1980**, *2*, 414.
5. J. Karam, J.A. Nicell, *J. Chem. Technol. Biot.*, **1997**, *69*, 141.
6. W.P. Thygesen, I. B. Dry, S.P. Robinson, *Plant Physiol*., **1995**, *109*, 525; J.E. Lourenco, V.A. Neves, M.A. Da Silva, *J. Agric. Food Chem.*, **1992**, *40* (12), 2369.
7. Y.K. Cho, H.K. Ahn, *J. Food Biochem.*, **1999**, *23*, 593.
8. S. Palanisami, S.K. Saha, U. Lakshmanan, *World J. Microbiol. Biotechnol.*, **2010**, *26*, 63.
9. I.D. Buchanan, J.A. Nicell, M. Wagner, *J. Environ. Eng.*, **1998**, *124*, 794.

STUDIA UBB CHEMIA, LVI, 1, 2011

ASYMMETRIC Co(III)-COMPLEXES OF ETHYL-METHYL-DIOXIME

CSABA VÁRHELYI JR.[a], GYÖRGY POKOL[b], VLADISZLAV IZVEKOV[b], ÁGNES GÖMÖRY[c], CSABA VÁRHELYI[a], LÁSZLÓ KOCSIS[a]

ABSTRACT. There is abundant literature regarding the symmetric α-dioximes, R'–C(=NOH)–C(=NOH)–R", (R'=R") and their derivatives. However, this is not the case for asymmetric α-dioximes, and the goal of this research was to increase knowledge in this domain. The thermal stability of the asymmetric α-dioximes and their Co-complexes is lower than that of the similar symmetric derivatives. This difference has also been observed in spectroscopical analysis.

In this study, the synthesis of a series of Co-complexes of the type $[Co(Et\text{-}Me\text{-}DioxH)_2L_2]^+$, (L=amine) was described and characterized with thermoanalytical and spectroscopical methods.

Keywords: *α-dioxime, heterocyclic amines, Co-complexes, thermal decomposition, spectroscopic measurements*

INTRODUCTION

Coordination compounds of α-dioximes, R^1–C(=NOH)–C(=NOH)–R^2, (R^1=R^2, $R^1 \neq R^2$) along with mainly transition metals, were the subject of a great number of preparative, physico-chemical and analytical studies. Various physico-chemical properties (e. g., electrochemical relations, dipole-moments, polarizability, the variation of the energy level of these molecules) constitute the basis of the modern quantum-chemical examination.

The nature of the R^1 and R^2 groups influences the substitution reactions, spectral properties, and thermal stability of the above mentioned metal complexes. Among these derivatives the greatest stability have the symmetric compounds with $R^1 = R^2$ values.

There is scant research regarding the chemical properties of the asymmetric α-dioximes ($R^1 \neq R^2$, R^1, R^2 = H, alkyl-, aryl-, alicyclic-, heterocyclic groups). It was observed that the thermal stability of the asymmetric complexes is lower than that of the analogous symmetric ones, and their hydrolysis in solutions also takes place with higher rates [1–24].

[a] *Babeş-Bolyai University, Faculty of Chemistry, 400 028 – Cluj-Napoca Arany J. str. 11, Romania, vcaba@chem.ubbcluj.ro, varhelyi46@yahoo.com, donlaszlow@yahoo.com*

[b] *Department of Inorganic and Analytical Chemistry, Budapest University of Technology and Economics, H-1111 Budapest, Szt. Gellért tér 4, pokol@mail.bme.hu, izvekov@mail.bme.hu*

[c] *Hungarian Academy of Sciences, Chemical Research Center, H-1525 Budapest, Pf. 17, Pusztaszeri út 59–67, gomory@chemres.hu*

Some Co-dioximine complexes present antibacterial activity. The skeleton of the B_{12}-vitamine molecule, which is used in the treatment of pernicious anemia, is also a Co(III)-dioximine group. It is noteworthy that such substances can be useful in the field of medicine.

In this study a new synthesis of the ethyl-methyl-dioxime and some new Co(III)-complexes of this chelating agent were described and characterized by chemical and biochemical methods.

RESULTS AND DISCUSSION

Four Co(III)-complexes, type $[Co(DioxH)_2(amine)_2]X$ were obtained by oxidizing Co(II)-salts in water–alcohol solution, in the presence of dioximes, aromatic or heterocyclic amines with an oxidation reagent (O_2, H_2O_2).

$$2\ CoX_2 + 4\ DioxH_2 + 6\ Amine + ½\ O_2 = 2\ [Co(DioxH)_2(Amine)_2]^+X^- + H_2O + \\ + 2\ AmineH^+X^-,\ X^- = CH_3–CH_2–COO^-,\ NO_3^-,\ ClO_4^-$$

The used dioxime was ethyl-methyl-dioxime, also prepared. In the first step was prepared the Me-Et-dione-monoxime from methyl-n-propyl-ketone acidified with HCl, with isonitroso method, bubbling gaseous ethyl-nitrite, in a cooling mixture.

$$CH_3–CO–CH_2–CH_2–CH_3 + Et–ONO \rightarrow CH_3–CO–C(=NOH)–CH_2–CH_3 + EtOH$$

The intermediary product, methyl-ethyl-2,3-dion-monoxime, was transformed with hydroxyl-amine in the corresponding α-dioxime.

$$H_3C—\underset{\underset{O}{\|}}{C}—\underset{\underset{NOH}{\|}}{C}—CH_2—CH_3 + H_2N—OH \cdot HCl \xrightarrow[-\ H_2O,\ -\ KCl]{+\ KOH}$$

$$\xrightarrow{\eta = 70–80\%} H_3C—\underset{\underset{HON}{\|}}{C}—\underset{\underset{NOH}{\|}}{C}—CH_2—CH_3 + H_2O$$

The behaviour of the asymmetric α-dioximes, including Et-Me-dioxime, with transition metal ions is similar to behaviour of the symmetric α-dioximes. In some cases were obtained colored, water-insoluble products: $[Me\text{-}Et\text{-}(DioxH)_2M(II)]$ (M = Ni, Pd, Pt), and in other cases specific colored solutions. For example, orange-brown with Ni(II), Pd(II), Co(III), red with Fe(II), Re(IV), etc. [25].

Electronic spectra (UV–VIS)

The electronic-spectra were recorded for a few $[Co(Me\text{-}Et\text{-}DioxH)_2(amine)_2]X$ type complexes. Here we found the internal absorption bands for the oxime- and pyridine-derivative ligands. In the case of aromatic and heterocyclic amines, the observed band is shifted to higher wavelengths. The *d–d* very weak bands were also observed. We are planning to make more studies for the UV–VIS bands in the future.

IR-spectral measurements

We recorded the middle- and far-IR spectra for our compounds, and the most important results are summarized in the experimental part.

If we compare our IR-spectra with the spectrum of symmetric $[Co(DMG)_2(\beta\text{-picoline})_2]I$ compound, we can observe the following: The $\delta_{O-H\cdots O}$ weak, large band (1733–1750 cm^{-1}), which stabilizes the compound, appears in the same wave number region, in both cases, which indicates a very similar structure.

The bands $\nu_{C=N}$ appear close to each other in our studied compounds (1547–1551 cm^{-1}). Also we can observe a small difference between the ν_{NOH} and ν_{N-O} bands (1228–1230 cm^{-1} and 1104–1109 cm^{-1}). In the far IR the ν_{Co-N} band is just similar in the studied compounds (512–514 cm^{-1}).

In the range of 400–100 cm^{-1} several deformation vibrations appeared, mostly for the heterocyclic amines and for the N–Co–N groups (δ_{N-Co-N}: 379–383 cm^{-1}) [26].

Thermoanalytical study

The TG, DTG, DTA curves were recorded for the studied complexes. The thermal decomposition curves of $[Co(Me\text{-}Et\text{-}DioxH)_2(3,4\text{-lutidine})_2]Br$ are presented in Fig. 1, and the results for all studied complexes are included in Table 1.

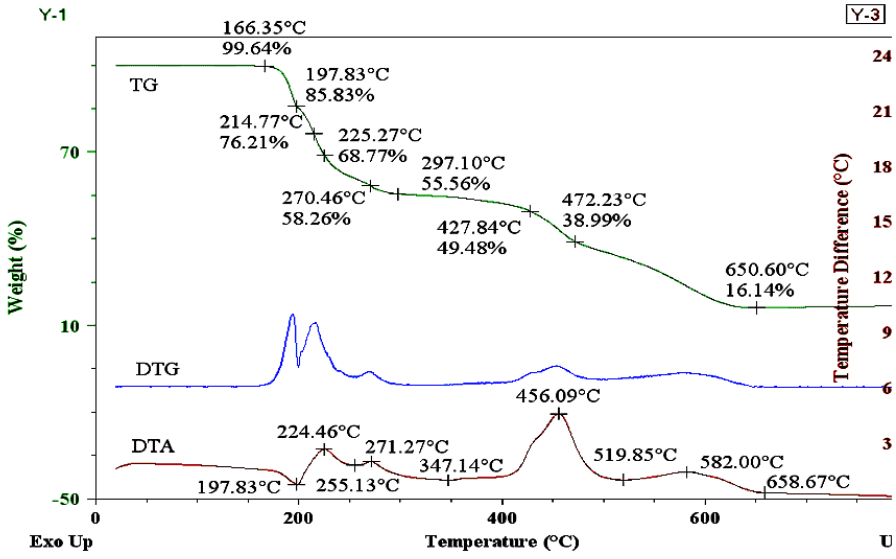

Figure 1. Thermal decomposition curves of *$[Co(Me\text{-}Et\text{-}DioxH)_2(3,4\text{-}lutidine)_2]Br$.*

Table 1. Thermoanalytical data of $[Co(Me\text{-}Et\text{-}DioxH)_2(amine)_2]X$-complexes

$[A(3,4\text{-}lut)_2]Br$		**$[A(3,4\text{-}lut)_2]I$**		**$[A(3\text{-}Me\text{-}Py)_2]Br$**		**$[A(3\text{-}Me\text{-}Py)_2]I$**	
t(°C)	**m; –Δm**	**t(°C)**	**m; –Δm**	**t(°C)**	**m; –Δm**	**t(°C)**	**m; –Δm**
166.35	99.64; 0.36	149.40	98.87; 1.13	102.59	98.71; 1.29	110.66	99.4; 0.6
197.83	85.83; 14.17	171.19	91.85; 8.15	113.08	91.06; 8.94	137.29	89.12; 10.8
214.77	76.21; 23.79	187.33	86.87; 13.13	138.91	84.53; 15.47	163.12	85.91; 14.09
225.27	68.77; 31.23	227.69	79.12; 20.88	192.18	82.11; 17.89	180.88	82.78; 17.22
270.46	58.26; 41.74	278.53	66.10; 33.90	209.13	76.03; 23.97	222.85	77.7; 22.3
297.10	55.56; 44.44	362.47	61.69; 38.31	234.14	64.22; 35.78	273.69	62.15; 37.85
427.84	49.48; 50.52	416.55	41.89; 58.11	264.81	59.17; 40.83	364.89	58.20; 41.80
650.60	16.14; 83.84	471.43	20.84; 79.16	410.90	51.05; 48.95	406.05	39.29; 60.71
				447.21	42.09; 57.91	463.36	12.25; 87.75
				690.95	15.55; 84.45		
$[A(3,4\text{-}lut)_2]Br$		**$[A(3,4\text{-}lut)_2]I$**		**$[A(3\text{-}Me\text{-}Py)_2]Br$**		**$[A(3\text{-}Me\text{-}Py)_2]I$**	
DTG	**DTA**	**DTG**	**DTA**	**DTG**	**DTA**	**DTG**	**DTA**
214, 225, 270, 456, 582	197.83 (endo), 224.46 (exo), 255.13 (endo), 271.27 (exo), 347.14 (endo), 456.09 (exo), 519.85 (endo), 582 (exo), 658.67 (endo)	171, 187, 228, 240, 270, 418	171.19 (endo), 241.41 (exo), 256.74 (endo), 310.82 (endo), 418.16 (exo), 484.3 (exo)	113, 192, 209, 265, 410, 690	113 (endo), 192.98 (endo), 222 (exo), 251.9 (endo), 268.85 (exo), 339.87 (endo), 423.3 (exo), 657 (exo)	163, 137, 238, 406	134.87 (endo), 238 (exo), 311 (endo), 405.25 (exo)

A = $Co(Me\text{-}Et\text{-}DioxH)_2$

The mechanism of the thermal decomposition of the $[Co(Me\text{-}Et\text{-}DioxH)_2(amine)_2]X$ type complexes was established from the TG steps. In the first step a redox process takes place:

$$Co^{3+} + e^- \rightarrow Co^{2+}$$

and the X^- anion is oxidized:

$$2\ Br^- - 2\ e^- \rightarrow Br_2$$
$$2\ I^- - 2\ e^- \rightarrow I_2$$

(For example, in the presented figure the Br^- elimination takes place until 198°C)

This is then followed by the amine and dioxime elimination:

$$[Co(Me\text{-}Et\text{-}DioxH)_2(amin)_2]^0 \rightarrow [Co(Me\text{-}Et\text{-}DioxH)_2(amin)]^0 \rightarrow$$
$$\rightarrow [Co(Me\text{-}Et\text{-}DioxH)_2]^0 \rightarrow [Co(Me\text{-}Et\text{-}DioxH)]^+ \rightarrow 1/3\ Co_3O_4$$

(In figure 1, the two amine elimination can be observed until 225°C, respectively 297°C. The two dioxime elimination takes place between 297 – 651°C)

Mass spectrometric measurements

In the mass spectra abundant positive ions corresponding to $[Co(Me\text{-}Et\text{-}DioxH)_2(amine)_2]$ species were observed (m/z 531 and 503 for lutidine and β-picoline containing compounds, respectively). Further fragment ions in the spectra correspond to loss of amine groups (table 2) [27].

Table 2. Electrospray mass spectrometric data for *[Co(Me-Et-DioxH)$_2$(amine)$_2$]X*

Nr.	Compound	Fragments (m/z)
1.	[Co(Me-Et-DioxH)$_2$ (3,4-lutidine)$_2$]Br	227 (2%) *[Co(Me-Et-furazane)$_2$]$^+$*, 317 (30%) *[Co(Me-Et-DioxH)$_2$]$^+$*, 424.2 (35%) *[Co(Me-Et-DioxH)$_2$(3,4-lutidine)]$^+$*, 531.2 (100%) *[Co(Me-Et-DioxH)$_2$(3,4-lutidine)$_2$]$^+$*
2.	[Co(Me-Et-DioxH)$_2$ (3,4-lutidine)$_2$]I	317 (25%) *[Co(Me-Et-DioxH)$_2$]$^+$*, 424.4 (40%) *[Co(Me-Et-DioxH)$_2$(3,4-lutidine)]$^+$*, 531.2 (100%) *[Co(Me-Et-DioxH)$_2$(3,4-lutidine)$_2$]$^+$*
3.	[Co(Me-Et-DioxH)$_2$ (β-picoline)$_2$]Br	317.2 (28%) *[Co(Me-Et-DioxH)$_2$]$^+$*, 410.2 (29%) *[Co(Me-Et-DioxH)$_2$(β-picoline)]$^+$*, 503.2 (100%) *[Co(Me-Et-DioxH)$_2$(β-picoline)$_2$]$^+$*
4.	[Co(Me-Et-DioxH)$_2$ (β-picoline)$_2$]I	317.0 (17%) *[Co(Me-Et-DioxH)$_2$]$^+$*, 410.2 (19%) *[Co(Me-Et-DioxH)$_2$(β-picoline)]$^+$*, 503.4 (100%) *[Co(Me-Et-DioxH)$_2$(β-picoline)$_2$]$^+$*

Biological probes

The antimicrobial effects of our complexes were studied for Gram-negative and Gram-positive germs. The Gram staining [28, 29] is an empirical solution for dividing the germs in two parts (Gram-negative and Gram-positive), in accordance with their physical and chemical properties of the cell-wall.

Our results are included in table 3. When the studied compound blocked the growing of germs, is marked with "+" [30–38].

Table 3. Antimicrobial studies

Nr.	Compound	Escherichia coli (Gram-negative)	B. Subtilis (Gram-positive)
1.	$[Co(Me\text{-}Et\text{-}DioxH)_2(3,4\text{-}lutidine)_2]Br$	–	+
2.	$[Co(Me\text{-}Et\text{-}DioxH)_2(3,4\text{-}lutidine)_2]I$	–	+
3.	$[Co(Me\text{-}Et\text{-}DioxH)_2(\beta\text{-}picoline)_2]Br$	–	+
4.	$[Co(Me\text{-}Et\text{-}DioxH)_2(\beta\text{-}picoline)_2]I$	–	–

CONCLUSIONS

The literature data and our XRD single crystal measurements for similar compounds [39] shows that the $[Co^{III}(DioxH)_2L_2]X$ type derivatives have octahedral structure. The equatorial plain of the octahedron is occupied by two dioxime ligands, and two O–H···O hydrogen-bridge stabilize the molecule. The two peak-points are occupied by two neutral or negative charged atomic groups, as shown in the figure 2.

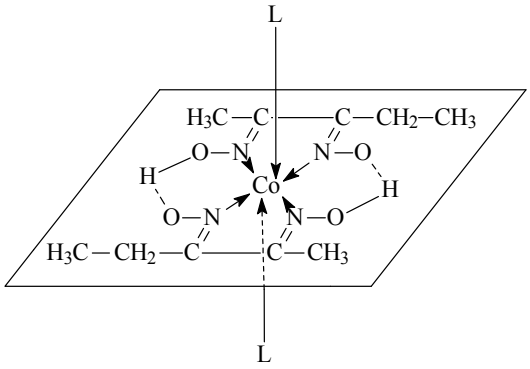

Figure 2. General structure of $[Co(Et\text{-}Me\text{-}DioxH)_2L_2]$ type complexes.

In our biological studies were used Gram positive and Gram negative germs. The results prove that the prepared complexes inhibit the growth of B. Subtilis germ.

EXPERIMENTAL SECTION

The electronic-spectra were recorded in ethyl-alcohol solution of 10^{-5} mol/l concentration with Jasco V-670 Spectrophotometer.

The IR spectra of the complexes were obtained in KBr and polyethylene pellets in the mid-IR (4000–450 cm^{-1}) and far-IR (650–150 cm^{-1}) range, respectively, on a Perkin–Elmer System 2000 FTIR spectrometer, operating with a resolution of 4 cm^{-1}.

Thermal measurements were performed with a 951 TG and 910 DSC calorimeter (DuPont Instruments), in air atmosphere, at a heating rate of 10 $K \cdot min^{-1}$ (sample mass 4–10 mg).

Mass spectrometric (MS) measurements were carried out by a PE Sciex API 2000 triple quadruple mass spectrometer, using electrospray ionization (ESI) in the 200–1200 m/z region. By ESI-MS, ionization takes place at milder conditions as compared with classical mass spectrometry, therefore it is more sensible for the detection of single and associated dimmer molecule ions and their fragment ions.

Synthesis of ethyl-methyl-dioxime

Me-Et-dione-monoxime was prepared with isonitroso method: in 0.5 mol methyl-n-propyl-ketone acidified with 2.5 ml HCl was bubbled gaseous ethyl-nitrite, in a cooling mixture (ice + NaCl + H_2O), ($-5 \div 5°C$) for 80–90 minutes.

The intermediary product, methyl-ethyl-2,3-dion-monoxime, was transformed with hydroxyl-amine (0.6 mol $NH_2OH \bullet HCl$ by neutralization with 0.6 mol NaOH at 60–70°C, solved in EtOH) in the corresponding α-dioxime.

The white Me-Et-dioxime crystallized after standing.

The crude product was re-crystallized from ethyl alcohol. Yield: 70–80%.

The preparation of Co(III)-complexes

If are oxidize Co(II)-salts (CoX_2, where X = acetate, NO_3, ClO_4) in water–alcohol solution, in the presence of ethyl-methyl-dioxime, aromatic or heterocyclic amines (mol-rate: 1:2:3) with an oxidation reagent (O_2, H_2O_2), it results in binary complex salts.

Table 4. Preparation data for $[Co(DioxH)_2(amine)_2]X$ type derivatives

Nr.	Starting materials (g; mol)				Product	Yield (g; %)
	$Co(Ac)_2$	Me-Et-$DioxH_2$	Amine	KX		
1.	10.65; 0.05	13.2; 0.1	3,4-lutidine 16; 0.15	KBr 10; 0.08	$[Co(Me\text{-}Et\text{-}DioxH)_2(3,4\text{-lutidine})_2]Br$	19; 62
2.	10.65; 0.05	13.2; 0.1	3,4-lutidine 16; 0.15	KI 10; 0.06	$[Co(Me\text{-}Et\text{-}DioxH)_2(3,4\text{-lutidine})_2]I$	20.7;63
3.	10.65; 0.05	13.2; 0.1	β-picoline 14; 0.15	KBr 10; 0.08	$[Co(Me\text{-}Et\text{-}DioxH)_2(\beta\text{-picoline})_2]Br$	18.3; 68
4.	10.65; 0.05	13.2; 0.1	β-picoline 14; 0.15	KI 10; 0.06	$[Co(Me\text{-}Et\text{-}DioxH)_2(\beta\text{-picoline})_2]I$	22.3; 70.8

It was bubbled 2–3 hours air through the solution of 0.05 mol $Co(acetate)_2 \cdot 2\ H_2O$, 0.10 mol Me-Et-$DioxH_2$ in 200 ml 50 % EtOH, then added 0.15 mol β-picoline or 3,4-lutidine dissolved in 15–20 ml EtOH. The oxidation was continued for 1 more hour. The resulted dark brown solution was filtered, and added to 100–100 ml filtered solution of 10–10 g KBr or KI,

dissolved in a small quantity of water. The dried crystallized brown product was filtered, washed with diluted alcoholic solution, and dried it on air. Details of the preparations, yields are given in Table 4.

Analysis

The studied complexes were characterized by N, X, H-microanalysis and their Co content was determined volumetrically with 0.01 m EDTA, using murexide indicator, after destruction of the samples (H_2SO_4 + KNO_3). The microscopic aspect, chemical analysis and IR-spectral measurement results for the studied compounds are given in tables 5, 6.

Table 5. Chemical analysis and microscopic aspect for $[Co(DioxH)_2(amine)_2]X$ type derivatives

Nr.	Compound	Mol-weigh	Chem. analysis		Color	Microscopic aspect
			Calc.	Found		
1.	$[Co(Me\text{-}Et\text{-}DioxH)_2(3,4\text{-}lutidine)_2]Br$	611.08	Co: 9.6 N: 13.7 Br: 49.3 H: 5.9	9.4 13.5 48.7 6.1	light brown	Rectangular, long, plates
2.	$[Co(Me\text{-}Et\text{-}DioxH)_2(3,4\text{-}lutidine)_2]I$	657.95	Co: 8.9 N: 12.8 I: 43.9 H: 5.4	9.1 13.1 44.2 5.0	light brown	Irregular crops
3.	$[Co(Me\text{-}Et\text{-}DioxH)_2(\beta\text{-}picoline)_2]Br$	538.38	Co: 10.1 N: 14.4 Br: 45.4 H: 5.4	9.8 14.7 44.9 5.7	reddish brown	Long, triangular based prisms
4.	$[Co(Me\text{-}Et\text{-}DioxH)_2(\beta\text{-}picoline)_2]I$	630.38	Co: 9.3 N: 13.3 I: 42.0 H: 5.0	9.7 12.9 43.2 4.7	light brown	Irregular, small plates

(β-picoline = 3-methyl-pyridine; 3,4-lutidine = 3,4-dimethyl-pyridine)

Table 6. FTIR-spectroscopic dates

Vibration (cm^{-1})	$[Co(Me\text{-}Et\text{-}DioxH)_2(3,4\text{-}lutidine)_2]Br$	$[Co(Me\text{-}Et\text{-}DioxH)_2(3,4\text{-}lutidine)_2]I$	$[Co(Me\text{-}Et\text{-}DioxH)_2(\beta\text{-}picoline)_2]Br$	$[Co(Me\text{-}Et\text{-}DioxH)_2(\beta\text{-}picoline)_2]I$
ν_{O-H}	3436 s	3437 s	3409 vs	3435 m
ν_{C-H}	3014 w 2983 s 2932 s 2871 m	3015 w 2982 m 2936 m	3115 m 2975 m 2932 m 2872 m	3116 m 3018 m 2973; 2935 2832 m
$\delta_{O-H\cdots O}$	1750 w	1740 w	1740 w	1733 w
ν_{C-C}	1616 s	1616 s	1611 m	1607 m
$\nu_{C=N}$	1547 vs	1547 vs	1551 vs	1547 vs
δ_{CH3}	1454 vs	1453 vs	1453 vs	1457 vs
δ_{CH2}	1384 m	1384 m	1384 m	1383 m

Vibration (cm^{-1})	$[Co(Me\text{-}Et\text{-}DioxH)_2(3,4\text{-}lutidine)_2]Br$	$[Co(Me\text{-}Et\text{-}DioxH)_2(3,4\text{-}lutidine)_2]I$	$[Co(Me\text{-}Et\text{-}DioxH)_2(\beta\text{-}picoline)_2]Br$	$[Co(Me\text{-}Et\text{-}DioxH)_2(\beta\text{-}picoline)_2]I$
ν_{NOH}	1280 vs	1229 vs	1229 vs	1228 vs
ν_{N-O}	1104 vs	1109 s	1108 vs	1109 vs
γ_{CH2}	722 s	721 s	701 vs	701 vs
ν_{Co-N}	512 vs	513 vs	514 vs	514 vs
δ_{N-Co-N}	379 m	380 m	383 m	383 m

s = strong; vs = very strong; m = medium; w = weak

Electronic spectra (UV–VIS)

The electronic-spectra were recorded for a few $[Co(Me\text{-}Et\text{-}DioxH)_2(amine)_2]X$ type complexes, and the observed absorption bands are summarized in table 7.

Table 7. Electronic spectra date

Compound	Absorption band (nm)	Observation
$[Co(Me\text{-}Et\text{-}DioxH)_2(3,4\text{-}lutidine)_2]Br$	201.5 vs 246.5 m	Internal absorption bands for the oxime- and pyridine-derivative ligands
$[Co(Me\text{-}Et\text{-}DioxH)_2(\beta\text{-}picoline)_2]Br$	204.0 vs 246.5 m	

vs = very strong; m = medium

Biological probes

The antimicrobial effects of our complexes were studied for Gram-negative and Gram-positive germs. The observation was made with the disk method. Filtering paper disks were impregnate with a concentrate probe solution, sterilized (with UV-radiation or in autoclave), then putted it on the germ substrate. After 24 hour incubation were observed whether the studied compound blocked the growth of the germ substrate. The case, when there was no growth of germ substrate around the disks, was called inhibition zone.

ACKNOWLEDGEMENT

The authors wish to express their thankfulness to the “Domus Hungarica Foundation” of Hungary for the several fellowships provided to Csaba Várhelyi jr.

REFERENCES

1. F.J. Welcher, “Organic Analytical Reagents”, Ed. D. van Nostrand Comp., New York, London, Toronto, **1955**, vol. III, p. 157.
2. V. M. Peskova, V. M. Savostina, E. K. Ivanova, “Oximi”, Izd. Nauka, Moskva, **1977**.
3. Houben-Weil, “Methoden der organischen Chemie”, G. Thieme Verl. Stuttgard, **1968**, Bd. VII/1, p. 455, 475, Bd. X/4, p. 7–320.
4. V.M. Bočkova, V.M. Peškova, *Zhur. neorg. Khim.*, **1958**, *3*, 1131.

5. S. Kinishita, J. Masuda, *Polyhedreon*, **1985**, *4*, 1245.
6. R. Hirota, Y. Yoshida, Y. Iida, H. Suezawa, T. Kogane, *Polyhedron*, **1993**, *12*, 1817.
7. L.M. Hansen, P.N. Kumar, D.S. Marynick, *Inorg. Chem.*, **1994**, *33*, 728.
8. C. Lopez, S. Alvarez, X. Solam, M. Font-Altabat, *Inorg. Chem.*, **1986**, *25*, 2962.
9. D. Mandal, B.D. Gupta, *Eur. J. Inorg. Chem.*, **2006**, 4086.
10. S. Reemers, U. Englert, *Inorg. Chem. Commun.*, **2002**, *5*, 829.
11. D. Xu, J. Gu, L. Xu, K. Liang, Y. Xu, *Polyhedron*, **1998**, *17*(2-3), 231.
12. M. J. Heeg, R. C. Elder, *Inorg. Chem.* **1980**, *19*, 932.
13. J. Gradinaru, S. Malinovskii, M. Gdaniec, S. Zecchin, *Polyhedron*, **2006**, *25*, 3417.
14. M. Özer, M. Kandaz, A.R. Özkaya, M. Bulut, O. Güney, *Dyes and Pigments*, **2008**, *76*, 125.
15. F. Karipcin, S. Ilican, Y. Caglar, M. Caglar, B. Dede, Y. Şahin, *J. Organomet. Chem.*, **2007**, *692*, 2473.
16. Z. Xin, H. Deyan, L. Yizhi, C. Huilan, *Inorg. Chim. Acta*, **2006**, *359*, 1121.
17. X. Zhang, Y. Li, Y. Mei, H. Chen, *J. Organomet. Chem.*, **2006**, *691*, 659.
18. B.D. Gupta, U. Tiwari, T. Barclay, W. Cordes, *J. Organomet. Chem.*, **2001**, *629*, 83.
19. B.D. Gupta, R. Yamuna, V. Singh, U. Tiwari, T. Barclay, W. Cordes, *J. Organomet. Chem.*, **2001**, *627*, 80.
20. B.D. Gupta, K. Qanungo, R. Yamuna, A. Pandey, U. Tewari, V. Vijaikanth, V. Singh, T. Barclay, W. Cordes, *J. Organomet. Chem.*, **2000**, *608*, 106.
21. B.D. Gupta, V. Singh, K. Qanungo, V. Vijaikanth, R. Yamuna, T. Barclay, W. Cordes, *J. Organomet. Chem.*, **2000**, *602*, 1.
22. T.M. Brown, A.T. Dronsfield, J.H. Fowler, S.W. Hill, *Inorg. Chim. Acta*, **2000**, *299*, 277.
23. V.Y. Kukushkin, A.J.L. Pombeiro, *Coord. Chem. Rev.*, **1999**, *181*, 147.
24. Y. Gök, H. Kantekin, *Polyhedron*, **1997**, *16*(14), 2413.
A. Treibs, A. Kuhn, *Chem. Ber.*, **1957**, *90*, 1691.
25. K. Nakamoto, "Infrared and Raman spectra of inorganic and coordination compounds", Part B, 5th Ed. J. Wiley, New York, **1997**.
26. J.T. Watson, "Introduction to Mass Spectrometry", Ed. Racon, New York, **1985**.
27. T.J. Beveridge, "Use of the gram stain in microbiology", Biotech Histochem, **2001**, *76*(3): 111. doi:10.1080/714028139. PMID 11475313.
28. E.J. Stewart, R. Madden, G. Paul, F. Taddei, **2005**, PLoS Biol 3(2): e45. DOI:10.1371/journal.pbio.0030045. PMID 15685293.
29. R. Bentley, R. Meganathan, *Bacteriol. Rev.*, **1982**, *46*(3), 241.
30. G. Reid, J. Howard, B.S. Gan, *Trends in Microbiology*, **2001**, *9(9),* 424.
31. N.A. Negm, M.F. Zaki, *Colloids and Surfaces B: Biointerfaces*, **2008**, *64*, 179.
32. A. Salyers, A. Gupta, Y. Wang, *Trends Microbiol.*, **2004**, *12*(9), 412.
33. L. Joshua, E.L. Tatum, *Nature*, **1946**, *158*, 558.
34. K.R. Matthews, J. Roberson, B.E. Gillespie, D.A. Luther, S.P. Oliver, *J. of Food Protection*, **1997**, *60*(6), 686.
35. J.R. Norris, J. Wolf, J, *J. Appl. Bacteriol*., **1961**, *24*, 42.
36. S. Vilain, et. al., *Appl. Environ. Microbiol*, **2006**, *72*, 4970.
37. S.S. Branda, et. al., *Proc. Natl. Acad. Sci. U.S.A.,* **2001**, *98*, 11621.
38. M. Szilágyi, A. Deák, Cs. Várhelyi Jr., J. Madarász, Gy. Pokol, Á. Gömöry, Cs. Várhelyi, *Polyhedron*, **2010**, *29*, 2185.

STUDIA UBB CHEMIA, LVI, 1, 2011

THE EFFECT OF SALICYLIC ACID ON THE BRIGGS-RAUSCHER OSCILLATING REACTION

LÉNÁRD-ISTVÁN CSEPEI[a,b], CSABA BOLLA[a]

ABSTRACT. Results concerning the effect of salicylic acid on the Briggs-Rauscher oscillating reaction in batch mode are presented. In contrast to the other phenolic and polyphenolic compounds studied before, this compound does not stop immediately the oscillations; however it reduces the amplitudes gradually. The time elapsed between the addition of the salicylic acid and the complete cessation of the oscillations is denominated as attenuation time. After the inhibition time the oscillations are restarted with low amplitude. The dependence of the amplitudes, attenuation time, inhibition time and period times on the salicylic acid is presented. Furthermore a new method for kinetic study of the unusual inhibitory effect is implemented. The reaction was followed potentiometrically, by means of an iodide ion selective electrode coupled to a double junction saturated calomel electrode. We derived the integrated rate equation that corresponds to the pseudo-first order reaction followed by a sensor with a nernstian transfer function. The hypothesis concerning the pseudo-first order kinetics of iodide ion production and consumption over a relatively long time within one period of oscillation is proven. The rate constants of iodide ion production and consumption are diminished gradually for the oscillations after the addition of salicylic acid. The fact that salicylic acid decreases the amplitudes and the rate constants of iodide ion formation and consumption during the attenuation period lead to the conclusion that this compound manifests a weak inhibitory effect in the attenuation period as well. However this inhibitory effect increases in time, until complete cessation of the oscillations.

Keywords: *Briggs-Rauscher oscillating reaction, salicylic acid, iodide ion selective electrode, Nernst equation, kinetics*

INTRODUCTION

The Briggs-Rauscher (BR) reaction is one of the most intensively investigated homogeneous phase oscillating reactions. It consists of oxidation and iodination of an organic substrate by hydrogen peroxide and iodate ion, catalyzed by Mn^{2+} and H^+ ions [1]. The organic substrate is usually malonic acid, but other enolic hydrogen atom containing organic compounds (i.e. acetone, methylmalonic acid, iodomalonic acid, phenylmalonic acid) can be used [2].

[a] *Universitatea Babeş-Bolyai, Facultatea de Chimie şi Inginerie Chimică, Str. Kogălniceanu, Nr. 1, RO-400084 Cluj-Napoca,Romania, csbolla@chem.ubbcluj.ro*

[b] *current address: Fritz Haber Institute der Max Planck Gesellschaft, Faradayweg 4-6, 14195 Berlin, Deutschland, cslenard@gmail.com*

The early mechanistic studies revealed the existence of 30 pseudo-elementary steps involving various oxygen and iodine containing species (i.e.: HOO•, HO•, $Mn(OH)^{2+}$ HIO, HIO_2, I•, IO•, IO_2•, I^-, and I_2) as intermediates [3, 4]. A set of 11 steps, known as skeleton mechanism, was proposed, which described qualitatively the nonlinear behavior of the system [5, 6]. The further studies led to a better mechanistic understanding of the reaction [2, 7].

Cervellati et al. studied the effect of different polyphenolic free radical scavengers (antioxidants) on the BR reaction [8-10]. All the studied polyphenolic compounds stopped immediately the oscillations for a certain time, denominated as inhibition time. A linear correlation was found between the inhibition time and the concentration of the antioxidant added to the mixture. Relative antioxidant activities have been determined. The qualitative mechanistic interpretation of the inhibitory effect was given: the antioxidant consumes the HOO• from the mixture in a fast step. When the antioxidant is completely consumed, the HOO• concentration increases above a critical value and the oscillations reappear. Reactions of antioxidant with other species than HOO• were also accounted for (i.e. oxidation and iodination by various oxy-iodine species) [10]. This method was claimed to be a validated analytical method for antioxidant activity determinations [9, 10]. More recent studies revealed the complexities of the reactions steps involving polyphenolic compounds in the BR-mixture [11, 12]. The effect of polyphenol was tested also in case of the BR reaction performed under flow conditions [13]. The analyte pulse perturbation technique applied in a CSTR showed that in contrast to the batch experiments, the resorcinol does not stop the oscillations, but decreases the period time and amplitude. Parabolic and reciprocal relationships were found between the concentration of resorcinol and the amplitude and the period time, respectively.

In our previous studies we reported that salicylic acid does not stop immediately the oscillations of the BR reaction operated in batch mode, like all the other phenolic compounds did [14-16]. In this work we present a more detailed phenomenological and kinetic study on the effect of salicylic acid on the BR reaction.

RESULTS AND DISCUSSION

The uninhibited Briggs-Rauscher reaction

Here we present the features of the uninhibited BR-reaction under the conditions described in the Experimental section. The reaction was followed using the iodide ion selective electrode and the bright platinum electrode simultaneously. The potential variation in time of these electrodes versus the reference electrode is presented in the Figure 1. It can be seen that the initial amplitudes monitored by the iodide ion selective electrode are large, approximately 250 mV. However the amplitudes monitored by the bright platinum electrode are lower by a factor of 8, approximately 30 mV. In our previous studies we used exclusively a bright platinum electrode coupled to

a reference electrode and we monitored only the redox potential change in time [14-15]. For the same composition of the BR-mixture we observed that the initial amplitudes were between 30 and 50 mV. The higher amplitude of the oscillations is a clear advantage of the application of the iodide-ion selective electrode. The second advantage and importance of the application of this electrode is related to the fact that it makes possible the kinetic study of iodide ion consumption and production [16]. This will be described in more detail in subsection entitled The potentiometric method for monitoring the BR-reaction.

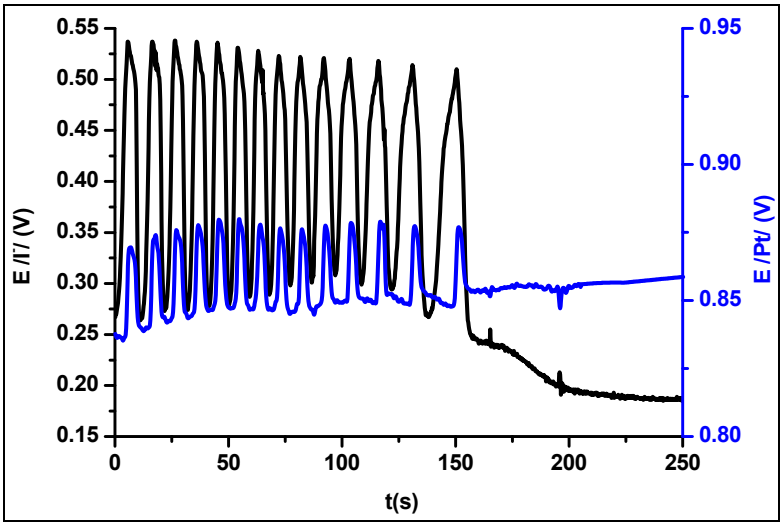

Figure 1. Simultaneous recording of the potentials of the iodide ion selective and the bright platinum electrodes versus the reference electrode immersed in the BR-mixture.

The shape of the first oscillations consists of four segments. The color changes observed during a single oscillation and the initial periods lengths are the same as reported previously [14, 15, 17]. Upon magnification it is notable that the peak maximum corresponding to the Pt-electrode is delayed in time by 0,6-1,0 s compared to the peak maximum on the iodide ion selective electrode. Szabó also reported a time-delay of 0,5-0,9 s between the peak maxima on the Pt-electrode and the iodide ion selective electrode for the first oscillations in the BR mixture [17].

The inhibition of the BR reaction with salicylic acid

When salicylic acid was added after the third oscillation in a relatively low concentration interval to the reacting BR mixture, the oscillations were not stopped at all (Figure 2).

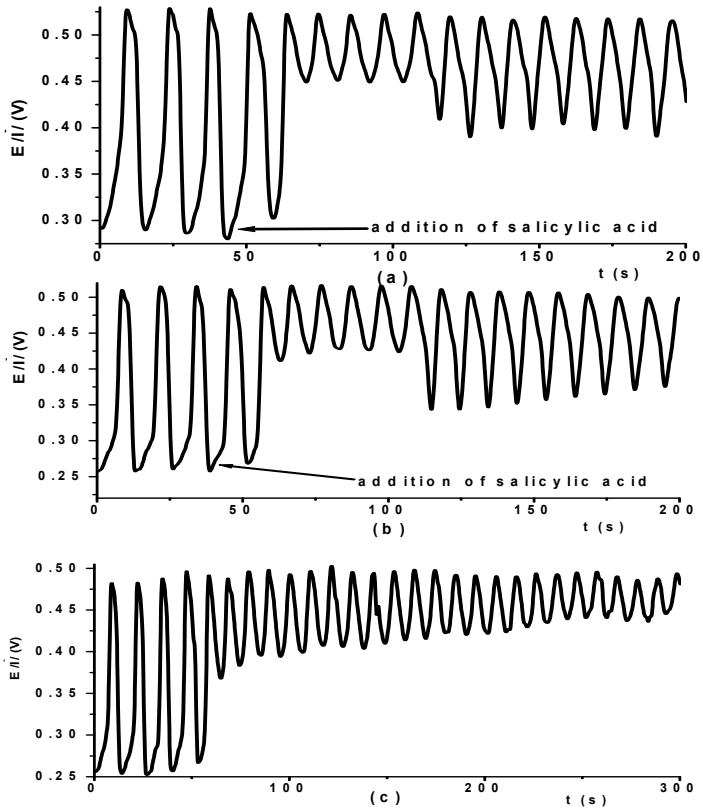

Figure 2. The effect of salicylic acid on the BR reaction in low concentrations, (a) - 0,28 mM, (b) - 0,31 mM, (c) - 0,34 mM.

The amplitude of the oscillation which appears right after the addition of the salicylic acid solution is not affected significantly. However the amplitude of the subsequent 5 and 6 oscillations are reduced considerably (Figure 2a and b, Figure 4), but then the amplitudes are increasing up to about half of the initial amplitudes.

When the salicylic acid concentration is higher than 0,34 mM, the amplitudes are reduced monotonically over the time (Figure 2.c, Figure 3. a-c and Figure 4). In accordance with the previous findings, the period times are not affected by the presence of salicylic acid [15]. It is also notable that after the addition of salicylic acid, the potential corresponding to the peak maxima are not changed significantly, however the minima are shifted considerably to more positive values. The shape of the oscillations after the addition of salicylic acid are also changed compared to the non-inhibited periods. In presence of salicylic acid, the shape of the oscillations resemble to sawtooth (when $c_{\text{salicylic acid}} \leq 0{,}31$ mM) and to damped sine wave (when $c_{\text{salicylic acid}} \geq 0{,}34$ mM).

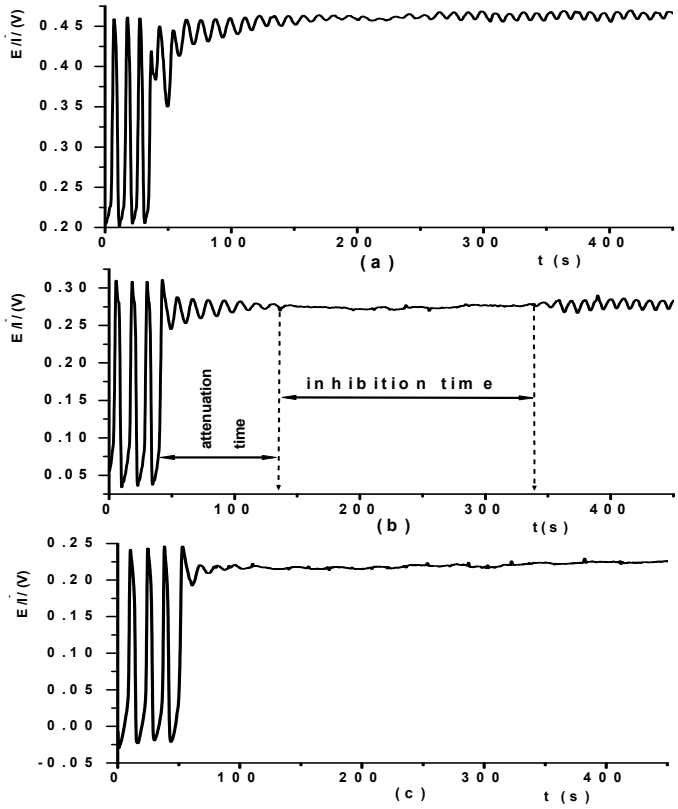

Figure 3. The effect of salicylic acid on the BR reaction in higher concentrations 0,69 mM, (b) - 0,85 mM, (c) - 1,16 mM.

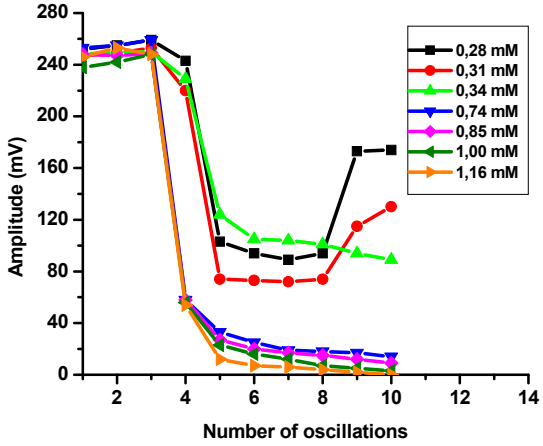

Figure 4. The effect of salicylic acid concentration on the amplitudes. The salicylic acid solution was injected after the third oscillation.

The mixture after the addition of salicylic acid was always transparent; therefore there was no indication that iodine was formed. The oscillatory time is longer than 700 seconds after addition of salicylic acid in low concentration. However the oscillatory time of the uninhibited BR-reaction is about 160 s, which is approximately 4,5 times shorter compared to the reaction inhibited by 0,28 mM salicylic acid.

We denominated the time elapsed between the addition of salicylic acid and the complete cessation of the oscillations as attenuation time [16]. The attenuation time decreases linearly with the concentration of salicylic acid (Figure 5). The equation of the straight line is the following:

$$t_{attenuation} = (266 \pm 11) - (189 \pm 12) \cdot c_{salicylic\,acid}, \quad R^2 = 0{,}9740, N = 8 \quad (eq.1)$$

At higher salicylic acid concentrations than 0,69 mM the oscillations are stopped after the attenuation time. The inhibitory time increased linearly with the salicylic acid concentration (Figure 5 and eq. 2). However at a concentration of 1,16 mM, the oscillations are not regenerated after a long inhibition time (more than 900 seconds).

$$t_{inh} = (-70 \pm 5) + (323 \pm 5) \cdot c_{salicylic\,acid}, \quad R^2 = 0{,}9986, N = 7 \quad (eq.2)$$

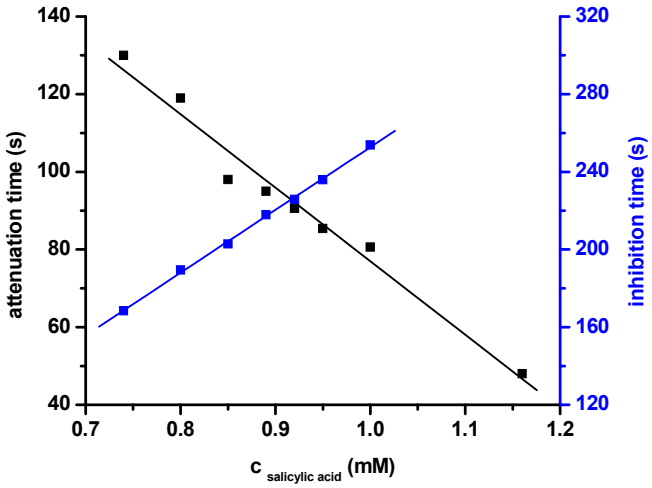

Figure 5. Plot of the attenuation time and inhibition time in function of the salicylic acid concentration.

Kinetic study on the BR-reaction inhibited by salicylic acid

Hypothesis

We assumed that one of the intermediates, the iodide ion presents pseudo-first order kinetics for a certain time interval, whithin one period of oscillation. To prove this assumption, it was necessary to monitor the iodide

ion concentration changes during the BR-reaction by means of a iodide ion selective electrode [16]. We present a method to obtain the rate constant of the iodide ion formation and consumption, respectively, directly from the variation in time of the potential difference between the iodide ion selective electrode and the reference electrode.

Instrumental methods (including spectroscopy and conductometry) for obtaining kinetic data are described in the literature. The transfer function of these instruments is linear. Upon changing the concentration variable with the instrument response variable (noted with P), the kinetic equation of a first order reaction becomes the following [18, 19]:

$$\ln \frac{P_\infty - P_t}{P_\infty - P_0} = -k_{obs} \cdot t \qquad (eq.3)$$

The above method has extensively been used for kinetic study of simple reactions. However only a few quantitative reports appeared about the employment of instrumental methods for kinetic study of complex reaction networks such as oscillating reactions. Some of these studies are briefly reviewed below.

The BR reaction has been followed by means of EPR [20], resonance Raman [21] and UV-Vis spectroscopy [2, 22]. Most of these studies lead to qualitative information concerning the intermediates [20-22]. An extensive quantitative kinetic study was presented by Furrow, who monitored the reaction spectrophotometrically and determined the rate of iodine production and consumption. He found that the iodine is consumed mainly in the iodination of the enol form of the organic substrate [2].

A less conventional coupling of instrumental analytical methods was employed by Fujieda and Ogata [23]. They monitored the reaction potentiometrically, calorimetrically and gasometrically in the same time. Semi-quantitative correlations were reported between the iodide ion concentration change, the total heat production, the heat production rate and the volume of the oxygen gas formation rate during the reaction.

Noszticzius et al. employed an experimental setup for the quantitation of the evolved CO and CO_2 end-products. N_2 carrier gas was bubbled through the reacting mixture, removing the CO and CO_2. Hydrogen was added to the gas mixture and the CO+CO_2 content was converted to methane over nickel catalyst. The formed methane was analyzed by a flame ionization detector. It was found that both the CO and CO_2 are products with oscillatory behavior [24, 25].

The potentiometric method for monitoring the BR-reaction

Potentiometry is an easier and more convenient method for the monitoring of the Briggs-Rauscher reaction compared to the spectrophotometric method. The difficulties concerning the spectrophotometric method of monitoring are the following:

- the BR reaction is strongly exothermic [9, 23] and in order to maintain the mixture under isothermal conditions, it needs to be well thermostated,
- during the reaction oxygen gas is evolved. The appearence of oxygen bubbles influences the absorbance of the mixture. Moreover, the oxygen is a triplet diradical and there are evidences that it inhibits the BR reaction [2]. Therefore the mixture needs to be stirred in order to facilitate the removal of the oxygen gas,
- the intermediates of the BR-reactions are photosensitive [2, 21]. The light beam of the spectrophotometer alters the oscillations. Strong light irradiation may stop the oscillations.

The potentiometric method can be applied easily under thermostated and stirred conditions. The method consists of recording of the potential difference between an indicator electrode and a suitable reference electrode. Frequently bright platinum electrode is employed as indicator electrode. However the platinum is a redox electrode. The measured potential is a mixed potential which depends on all the redox couples (i.e. $Mn^{2+}/Mn(OH)^{2+}$, I_2/I^-, HIO_2/HOI, etc.) existing in the solution. Therefore it is not possible to follow the concentration of a single species in time with a platinum electrode.

On the other hand the potential of a iodide ion selective electrode depends on the iodide ion concentration or activity, respectively. This depedence is given by the Nernst-equation (eq. 4). The main difference between the spectroscopic, conductometric methods and the potentiometric method is that the transfer function of the electrochemical sensor is not linear, but logarithmic.

Hence, by employing an iodide ion selective electrode for monitoring the BR reaction, it is possible to follow the concentration changes of the iodide ion. The knowledge of iodide ion concentration is of great interest, because the BR reaction is a iodide ion controlled oscillator.

$$\varepsilon_{I^-} = \varepsilon^0 + \frac{RT}{zF}\ln a_{I^-} = \varepsilon^{01} + \frac{RT}{zF}\ln c_{I^-} \qquad \text{(eq.4)}$$

where: - ε_{I^-} is the potential of the ionselective electrode,

- a_{I^-} is the activity and c_{I^-} is the concentration of iodide ion, respectively,
- ε^0 standard potential,
- ε^{01} standard formal potential.

The logarithm of the iodide ion concentration was explicited Nernst equation for the initial conditions t=0 and t=t (equations 7-8). Then by substituting these equations in the integrated rate law of a first order reaction and after performing the algebraic operations, we got the equation 9 [16].

$$E = \varepsilon_{I^-} - \varepsilon_{ref} \qquad \text{(eq.5)}$$

$$\mathrm{E} = \varepsilon^{01} + \frac{RT}{zF}\ln c_{I^-} - \varepsilon_{ref} \qquad (eq.6)$$

$$\ln c_{I^-,0} = \frac{zF}{RT}(E_0 - \varepsilon^{01} + \varepsilon_{ref}) \qquad (eq.7)$$

$$\ln c_{I^-,t} = \frac{zF}{RT}(E_t - \varepsilon^{01} + \varepsilon_{ref}) \qquad (eq.8)$$

$$\mathrm{E_t} = \mathrm{E_0} \pm \frac{RT}{zF}\cdot k_{obs}\cdot t \qquad (eq.9)$$

This latter linear equation 9 describes the variation in time of the electromotive force of an ion selective electrode-reference electrode couple, when the ion concentation follows a (pseudo)-first order kinetics. The ± sign means that the equation 9 is applicable either for the consumption or for the formation of the given ionic species. The (pseudo)-first order rate constant can be determined from the slope (noted here with b) of the E−t plots:

$$k_{obs} = \frac{zF}{RT}\cdot b \qquad \text{(eq.10)}$$

It can be concluded that the electrode response linearizes the integrated exponential rate law corresponding to the pseudo-first order reactions. For the determination of the rate constant, only a simple linear regression and a multiplication are needed. Because of the fact that this method for determination of rate constant requires less mathematical operations (only a linear regression and a multiplication, respectively) than those presented in the previous section, the error propagation is also lower [18].

The rate constants are accessible also when the logarithm of the iodide ion concentration calculated from the potential and is plotted against the time. According to the conventional kinetics, the linear segment on this plot also indicates that the iodide ion is involved in pseudo-first order steps within one period os oscillations. However for the calculation of the iodide ion concentration the knowledge of the standard formal potential (ε^{01}) is needed (eq. 9). Nevertheless this potential may change in long term measurements [26] or due to the corroding effect of the highly reactive iodide containing intermediates [27]. In such cases frequent calibration is recommended [26]. Otherwise due to the potential drifting phenomenon, the calculated concentrations will be also shifted severly (by one order of magnitude per 59 mV of potential drift).

The drifting phenomenon can also be observed in the present study: during the measurement series the potential interval of the first three non-inhibited oscillations were shifted gradually from 0,27 − 0,55 V to -0,025 − 0,25V (Figure 2 and 3). Nevertheless, the amplitudes of the first three non-inhibited oscillations are satisfactorily reproducible within the measurement

series (Figure 4). This suggests that the sensitivity of the electrode did not change; only the standard formal potential of the iodide ion selective electrode and/or the potential of the reference electrode (ε_{ref}) were drifting.

However if the rate constant is determined directly from the E-t plots according to the equation 9, neither the knowledge of the standard formal potential of the iodide ion selective electrode, nor the potential of the reference electrode is required. Since the sensitivity of the iodide ion selective electrode was found to be satisfactorily constant, we took the advantage of determining the rate constants according to the equation 9.

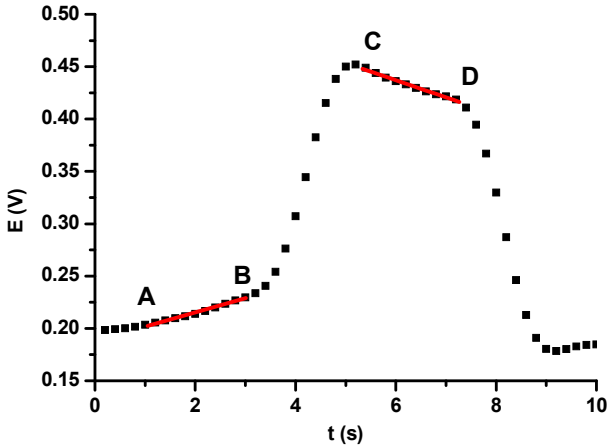

Figure 6. The variation of the electromotive force (E) during a single uninhibited oscillation.

Upon analyzing the shape of a single uninhibited oscillation, two relatively long linear segments can be observed (Figure 6). The AB segment with positive slope represents the iodide ion formation step. At the beginning of this segment the color of the mixture was brown due to the iodine. During the AB segment the brown color faded out gradually, the iodine was reacting with the enolic form of the organic substrate. The length of this segment was about 4,0 second, which represents 32-35% of the period time of the first oscillations. In order to determine the rate constant of iodine ion formation, a straight line was fitted to the most linear portion of the AB segment. The slope of the straight line was found to be 0,0132 ± 0,0006 V/s. The calculation of apparent rate constant and its standard deviation was done according to equation 11 and 12.

The potential increased rapidly between the B and C points, due to rapid reaction steps that are also producing iodide ions.

The decreasing CD segment represents the steps involving the consumption of the iodide ion.

$$k_{obs} = 0{,}01315 \cdot \frac{zF}{RT} = \frac{0{,}01315}{0{,}0257} = 0{,}51\,s^{-1} \qquad (eq.11)$$

$$\sigma_{kobs} = \sigma_b \cdot \frac{zF}{RT} = \frac{0{,}0006}{0{,}0257} = 0{,}02 s^{-1} \qquad (eq.12)$$

During the whole CD segment the mixture remained colorless. The length of this segment was about 2,0 seconds, which corresponds to approximately 16-18% of the period time. Linear fitting gave a slope of -0,01638±0,0006 V/s, therefore the apparent rate constant of iodide ion consumption was found to be k_{obs} = 0,64±0,02 s^{-1}.

After the CD segment the potential suddenly decreased due to fast reaction steps. The color of the mixture changed into brown and the cycle started again.

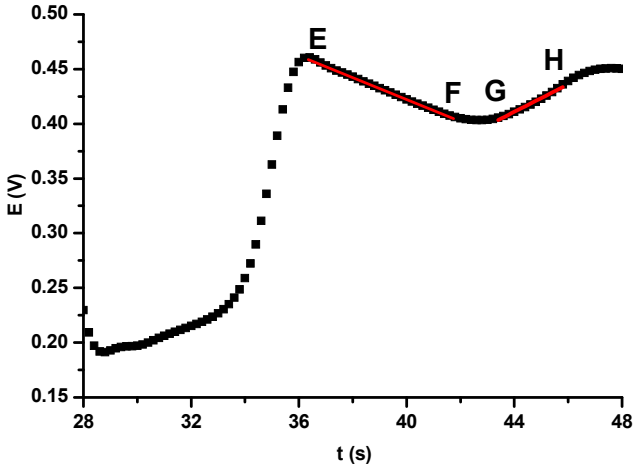

Figure 7. The segment where iodide ion is produced and consumed, respectively, in presence of 0,85 mM salicylic acid.

In the case of the inhibited reaction, the length of the straight line EF (see Figure 7) corresponding to the iodide ion consumption is increased significantly compared to the non-inhibited reaction. However the slope is smaller, consequently the observed rate constant of iodide ion consumption is also lower. Due to the fact that the shape of the oscillations in the attenuation period are different compared to the non-inhibited oscillations, the GH segment seems not to correspond to the AB segment of the first three non-inhibited oscillations.

The apparent rate constants corresponding to the iodide ion consumption and formation in the EF and GH portions are k_{obs} = 0,39±0,02 s^{-1} and k_{obs} = 0,41±0,02 s^{-1}, respectively.

The apparent rate constants of iodide ion formation and consumption corresponding to the successive periods of oscillations were represented in the Figure 8. It can be observed that after addition of the salicylic acid, the rate constant of iodide ion consumption is significantly reduced. Moreover, the rate constants decay in the successive periods until the oscillations are ceased. During the inhibitory time the potential is constant, therefore the concentration of iodide ions is also constant.

The salicylic acid also decreases progressively the rate constant of iodide ion formation in the attenuation period (Figure 8). The progressive decay of the iodide ion formation and consumption after salicylic acid addition suggests that this substance presents an inhibitory effect also during the attenuation period.

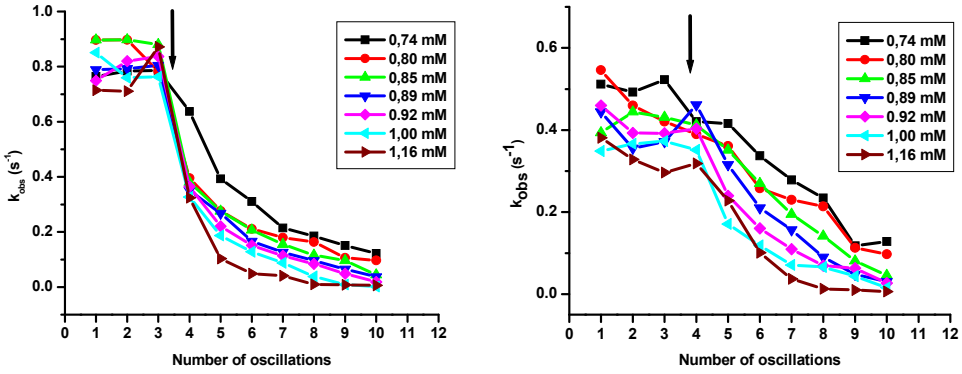

Figure 8. The effect of salicylic acid concentration on the apparent rate constants of iodide ion formation (top) and consumption (bottom) in the successive periods. The arrow indicated the addition of salicylic acid solution.

Up to our knowledge, the salicylic acid was the first organic compond reported which presents unusual inhibitory effect on the BR reaction operated in batch mode. The fact that this compound does not stop immediately the oscillations suggests that it is not a strong hydroperoxyl radical quencher. The antioxidant activity of salicylic acid determined by the TEAC method was found to be 0,04±0,01. This low value was explained by the steric hindrance and the electron withdrawing effect of the carboxylic group in the orto-position with respect to the hydroxyl-group [28].

However in presence of salicylic acid the oscillations are stopped after some time. A possible explanation is that some compound is formed in the reaction mixture, which is a more effective inhibitor of the BR reaction. The salicylic acid has been reported to be an effective hydroxyl radical quencher (spin trap). The hydroxyl radical is also an intermediate of the BR-reaction [2-4].

Upon hydroxylation of salicylic acid 2,3- and 2,5-dihydroxybenzoic acid isomers, catechol and hydroquinone are formed [29-31]. On the other hand, the dihydroxybenzoic acid isomers and catechol present a high antioxidant activity, i.e. they inhibit strongly the BR reaction even in micromolar concentration [9] (Table1).

Table 1. Comparison of the antioxidant activity of some polyphenols. Data collected from (a) Rice-Evans et al. [28], (b) Cervellati et al., relative antioxidant activity with respect to the slopes of the calibration graph, using resorcinol as stadard [9], and (c) this work. n.a.-data not available.

Compound	TEAC antioxidant Activity (a)	BR antioxidant Activity (b)
2-hydroxy-benzoic-acid	0,04±0,01	Unusual, low (c)
2,3-dihydroxy-benzoic-acid	1,46±0,01	n.a.
2,5-dihydroxy-benzoic-acid	1,04±0,03	0,092±0,003
o-catechol	n.a.	5,30±0,40

We did not find kinetic data concerning the hydroxylation of salicylic acid, but the cited literature data suggests that it is a relatively slow radical substitution reaction. The reaction time for the formation of well detectable amount of hydroxylated products spans from 30 seconds to 15 minutes, depending of the method of hydroxyl radical generation and the temperature. This would explain the observed attenuation period and the gradual decrease in the iodide formation and consumption rate constants as well.

It is also notable, that we also checked the effect of 4-sulfosalicylic acid on the BR-reaction. This derivative of the salicylic acid did not stop the oscillations, nor changed the amplitudes of the oscillations below 10 mM concentration. At a concentration of 20 mM the amplitudes were still unaffected, only the period time was slightly increased from 11-13 to about 14-15 seconds.

CONCLUSIONS

We studied the effect of salicylic acid on the Briggs-Rauscher oscillating reaction. This compound does not stop immediately the oscillations, in contrast to the other mono-and polyphenolic compounds which are effective inhibitors already in the micromolar concentration interval.

If the concentration of salicylic acid in the BR-mixture is lower than 0,69 mM, the oscillations are not stopped at all, only the amplitudes are reduced. However after a few periods of oscillations the amplitudes are increasing.

Added in higher concentration than 0.69 mM in the BR mixture, salicylic acid decreases the amplitudes gradually untill the oscillations are stopped. We denominated the time elapsed between the addition of salicylic acid and the cessation of the oscillations as attenuation time. The attenuation

time decreases linearly, the inhibition time increases linearly over a relatively narrow concentration of salicylic acid. However the period time is not affected by the presence of salicylic acid.

For the kinetic study the reaction was monitored by iodide ion selective electrode coupled to a reference electrode. We assumed that the iodide ion concentration follows pseudo-first order kinetics over a given time within one period of oscillations. We derived the equation that corresponds to the case when a first order reaction is followed by a sensor with nernstian transfer function. Based on this equation we validated the assumption concerning the reaction order of iodide ion formation and consumption. The rate constants were found to be decreased gradually from period to period in presence of salicylic acid, similarly to the decay of the amplitudes of the oscillations. This fact suggested that the studied compound manifests a weak inhibitory effect in the attenuation period as well. However the inhibitory effect enhances with the concentration and the reaction time as well, until the oscillations are stopped temporarily. These observations lead to a hypothesis that after adding the salicylic acid in the BR mixture, some compound is formed which is a better inhibitor of the oscillations. Since the hydroxyl radical is also an intermediate of the BR-reaction, it was plausible to suppose that the salicylic acid is hydroxylated to dihydroxybenzoic acid isomers. These latter compounds were reported to be efficient inhibitors of the BR-reaction. However the hypothesis is yet to be proven.

EXPERIMENTAL SECTION

The following stock solutions have been prepared according to the procedure described earlier [14-16]. The stock solutions and the double-walled glass reactor were thermostated to 25,0±0,1 ºC. Mixing of the stock solutions gave an oscillatory mixture with the following initial concentrations: $[H_2O_2]_0$=9,20·10^{-1} M, [malonic acid]$_0$=5,00·10^{-2} M, $[H_2SO_4]_0$=2,50·10^{-2} M, $[MnSO_4]_0$=6,50·10^{-3} M, $[KIO_3]_0$= 6,75·10^{-2} M. After the minimum of the third oscillation a given volume of the sodium salicilate was added to the reaction mixture using a Labsystems Finnpipette micropipette. Since the pH of the BR-mixture is sufficiently low (around 1,7), the salicilate ion was protonated quantitatively to salicylic acid.

The BR-reaction was monitored potentiometrically using an iodide ion selective electrode (Radelkis, Budapest) and a double junction saturated calomel reference electrode (Chemical Institute, Cluj-Napoca). For comparison a few experiments were performed using the iodide ion selective electrode and a bright platinum electrode simultaneously. A double junction calomel electrode was chosen as a reference electrode, because the conventional single junction electrodes contain saturated potassium-chloride electrolyte. When a single junction reference electrode is immersed into a solution, chloride ions diffuse

out through the fritt of the electrode in the solution. The contamination rate is approximately $0{,}2 \cdot 10^{-3}$ M/min [26]. Because of the fact that already traces of chloride ions inhibit the BR-reaction; any contamination with chloride ions must be avoided. For this purpose we used a double junction saturated calomel electrode, which contained 1,0 M KNO_3 electrolyte in the outer compartment.

The variation in time of the potential of the iodide ion selective electrode versus the reference electrode was recorded using a computer equipped with a National Instruments® data acquisition card. The acquisition frequency has been set to 5 s^{-1}.

ACKNOWLEDGMENTS

The author acknowledges the scholarship awarded by the PROFIL Group for the Cluj-Szeged Student Exchange Program to the University of Szeged, Hungary, Faculty of Natural Sciences. The author thanks Prof. Dr. I. C. Popescu (Dept. of Physical Chemistry, Faculty of Chemistry and Chemical Engineering, Babes-Bolyai University) for the iodide selective electrode.

REFERENCES

1. T.S. Briggs, W.C. Rauscher, *J. Chem. Educ.* **1973**, *50*, 496
2. S.D. Furrow, *J. Phys. Chem*, **1995**, *99*, 11131.
3. S.D. Furrow, R.M. Noyes, *J. Am. Chem. Soc*., **1982**, *104*, 38.
4. S.D. Furrow, R.M. Noyes, *J. Am. Chem. Soc*., **1982,** *104*, 42.
5. S.D. Furrow, R.M. Noyes, *J. Am. Chem. Soc*., **1982**, *104*, 45.
6. P. De Kepper, I.R. Epstein, *J. Am. Chem. Soc*., **1982**, *104*, 49.
7. S.D. Furrow, R. Cervellati, G. Amadori, *J. Phys. Chem. A,* **2002**, *106*, 5841
8. R. Cervellati, N. Crespi-Perrelino, S.D. Furrow, A. Minghetti, *Helv. Chim. Acta*, **2000**, *83*, 3179.
9. R. Cervellati, K. Höner, S.D. Furrow, C. Neddens, S. Costa, *Helv. Chim. Acta*, **2001**, *84*, 3533.
10. R. Cervellati, K. Höner, S.D. Furrow, F. Mazzanti, S. Costa, *Helv. Chim. Acta*, **2004**, *87*, 1, 133.
11. L. Onel, G. Bourceanu, M. Wittmann, Z. Noszticzius, G. Szabó, *J. Phys. Chem. A*, **2008**, *112*, 11649.
12. T. Lawson, J. Fülöp, M. Wittmann, Z. Noszticzius, N. Muntean, G. Szabó, L. Onel, *J. Phys. Chem. A*, **2009**, *113*, 14095.
13. N. Muntean, I Baldea, G. Szabó, Z. Noszticzius, *Studia UBB Chemia*, **2010**, *55(1),* 121.
14. L.I. Csepei, „A Briggs-Rauscher reakció oszcillációinak leállítása” („The Cessation of the Oscillations of Briggs-Rauscher Reaction”), Bachelor Diploma Thesis, supervisor: Cs. Bolla, Babes-Bolyai University, Faculty of Chemistry and Chemical Engineering, **2005**.

15. L.I. Csepei, Cs. Bolla*, Studia UBB Chemia*, **2009**, *54(II)*, 249.
16. L.I. Csepei, "Inhibiția reacției oscilante Briggs-Rauscher cu acid salicilic" ("Inhibition of Briggs-Rauscher Oscillating Reaction with Salycilic Acid"), Master Diploma Thesis, supervisor: Cs. Bolla, Babes-Bolyai University, Faculty of Chemistry and Chemical Engineering, **2006**.
17. E. Szabó, "A Briggs-Rauscher reakció tanulmányozása" ("Study on the Briggs-Rauscher reaction"), Bachelor Diploma Thesis, Supervisor Cs. Bolla, Babes-Bolyai University, Faculty of Chemistry and Chemical Engineering, **2000**, 53-66.
18. K.A. Connors, „Chemical Kinetics, The Study of Reaction Rates in Solution", VH Publishers, **1990**, 31-36.
19. I. Bâldea, „Cinetică chimică şi mecanisme de reacție, Baze teoretice şi aplicații", Presa Universitară Clujeană, Cluj-Napoca, **2002**, 26-40.
20. P.V. Lalitha, P. Sambasiva Rao, R. Ramaswamy, *Current Science*, **1991**, *61*, 5, 352.
21. B.Z. Chowdhry, A.P. Mendham, J. Tetteh, R. Withnall, *ChemPhysChem*, **2002**, *5*, 443.
22. M.J. Mahon, A.L. Smith, *J. Phys. Chem.* **1985***, 89,* 1215.
23. S. Fujieda, H. Ogata, *Talanta*, **1996**, *43*, 1989.
24. Sz. Nagygyörgy, M. Wittmann, Sz. Pintér, A. Visegrádi, A. Dancsó, B.T. Nguyen, Z. Noszticzius, L. Hegedűs, H.D. Försterling, *J. Phys. Chem. A*, **1999**, *103*, 4885.
25. G. Szabó, A. Csavdári, L. Onel, G. Bourceanu, Z. Noszticzius, M. Wittmann, *J. Phys. Chem. A*, **2007**, *111*, 610.
26. Orion Ionalyzer, Instruction Manual for Halide Electrodes, 5th Edition, Orion Research Inc., USA, **1973**.
27. Z. Noszticzius, E. Noszticzius, and Z.A. Schelly, *J. Am. Chem.* Soc., **1982**, *104,* 6194.
28. C.A. Rice-Evans, N.J. Miller, G. Paganga, *Free Rad. Biol. Med.*, **1996**, *20*, 7, 933.
29. R.A. Floyd, J.J. Watson, P.K. Wong, *J. Biochem. Biophys. Meth.*, **1984**, *10*, 221.
30. B. Halliwell, H. Kaur, M. Ingelman-Sundberg, *Free Rad. Biol. Med.*, **1991**, *10*, 439.
31. B.K. Glod, P. Grieb, *Acta Chromatographica*, **2006**, *15*, 258.